Spatio-Temporal, Multicellular and Monte Carlo Track-Based Model of Radiotherapy In Silico

JAKE CAMERON FORSTER

Principal Supervisor: Prof Eva Bezak

Co-Supervisors: Dr Wendy Phillips & Dr Michael Douglass

School of Physical Sciences

University of Adelaide

A thesis submitted for the degree of

Doctor of Philosophy

October 2018

For a thesis that contains publications:

I certify that this work contains no material which has been accepted for the award of any other degree or diploma in my name, in any university or other tertiary institution and, to the best of my knowledge and belief, contains no material previously published or written by another person, except where due reference has been made in the text. In addition, I certify that no part of this work will, in the future, be used in a submission in my name, for any other degree or diploma in any university or other tertiary institution without the prior approval of the University of Adelaide and where applicable, any partner institution responsible for the joint-award of this degree.

I acknowledge that copyright of published works contained within this thesis resides with the copyright holder(s) of those works.

I also give permission for the digital version of my thesis to be made available on the web, via the University's digital research repository, the Library Search and also through web search engines, unless permission has been granted by the University to restrict access for a period of time.

I acknowledge the support I have received for my research through the provision of an Australian Government Research Training Program Scholarship.

Acknowledgements

I am extremely grateful to my principal supervisor Professor Eva Bezak and co-supervisors Dr Wendy Phillips and Dr Michael Douglass. Their wisdom and guidance throughout this project were invaluable. I am thankful for the research skills they taught me and the professional advice they gave, which will benefit me for many years to come. A huge thank you to Eva for going above and beyond with her support for my conference attendance and publishing fees. I always felt I had the full support of my supervisors and we were on the same team, which made all the difference. They gave me the room to try, fail, learn and create, and supported me to take my work in directions that sparked my interest. I am also thankful that they restrained me when my inexperience lead me to overstate. I feel very fortunate to have had them supervise me and I hope I have the privilege of continuing to work with them in the future.

Special thank you to Dr Scott Penfold and Dr Alex Santos for their kindness, advice and encouragement. I enjoyed the camaraderie with the other postgraduate Medical Physics students, especially with Dr Julien Zhu, Annabelle Austin and Alexandra Chapsky (Sasha). Thanks also to the Medical Physics staff at the Royal Adelaide Hospital for being friendly and accommodating.

Thank you to the helpful and generous Phoenix HPC support staff, past and present, particularly Exequiel Sepulveda-Escobedo for the Geant4 support and Dr Fabien Voisin for helping me to finish my work on time.

Heartfelt thanks go to my Mum and Dad, my brother Brendan, sister Megan and brother-in-law James. Getting together (including Milla and Fletcher, and sometimes “Skype Brendan”) for dinner once-a-week helped me to rejuvenate. Special thanks also to my friends Jarrad, Jacques, Taylor and Dom.

Abstract

A notable short-coming in the way radiotherapy is currently practised is that patient-specific radiobiology is minimally and rarely accounted for in the treatment planning process. If this is to be remedied, *in silico* radiobiological models of radiotherapy will play an essential role. By increasing the complexity of such models, greater accuracy and utility are gained, along with opportunities for new radiobiological insights. A new computational model was developed called "Stochastic Squared Radiotherapy" (S^2RT). It is a spatio-temporal/four-dimensional radiotherapy model for head and neck squamous cell carcinoma (HNSCC), that uses stochastic modelling of tumour cells and Monte Carlo track structure simulations. The four main components of the model are tumour growth, tumour irradiation, DNA damage induction and cell death/survival.

The tumour growth module generates the initial multicellular tumour and evolves it spatio-temporally in-between dose fractions. Ellipsoidal tumour cells occupy randomised, non-overlapping locations. Cells are pushed outward and fall inward following cell division and cell death, respectively. An epithelial cell hierarchy of stem, transit and differentiated cells is modelled. A connected and chaotic network of blood vessels grows interwoven between the cells. Chronic hypoxia and necrotic cells are simulated at distances far from blood vessels. Hypoxic cells divide slower and necrotic cells are gradually resorbed. Accelerated repopulation may be simulated by increasing the symmetric division of cancer stem cells.

Dose fractions are delivered to the tumour in Monte Carlo simulations of radiation tracks. The multicellular tumour is voxelised into nucleus, cytoplasm and intercellular voxels of size 2 μm and imported into Geant4 to perform irradiation. A Geant4 application was developed that uses Geant4-DNA to simulate low-energy physical interactions and radiolytic chemical tracks to account for the indirect effect. The tracks through cell nuclei are converted to DNA damage, including double-strand breaks (DSBs). This was done by spatially clustering physical interactions such as ionisations and excitations and hydroxyl radical interactions into simulated DNA volumes, each of size 10 base pairs. The DNA damage was made dependent upon the cellular pO_2 by increasing the efficiency of DNA radical-to-strand break conversion with increasing pO_2.

In the model, complex DSBs (cDSBs) produced DNA free-ends that can misrejoin with one another and produce exchange-type chromosome aberrations. Complete

exchanges are assumed. The misrejoining probability is modelled as an exponential function of the initial distance between the two cDSBs involved. Cells die if they contain an asymmetric chromosome aberration.

Notable findings from the S^2RT model include: 1. Symmetric division of cancer stem cells may be as high as 50% during accelerated repopulation. 2. The decrease in the oxygen enhancement ratio for DSB induction with increasing LET can be attributed to spatial clustering alone; i.e., at higher LET, the additional strand breaks produced in the presence of oxygen seldom result in additional DSBs. Instead, they increase DSB complexity. 3. For MV x-rays, misrejoinings between cDSBs produced by the same primary x-ray (including its secondary electrons) do not contribute appreciably to the linear components of chromosome aberration production and cell killing. For HNSCC, which does have an appreciable linear component of cell killing, unrejoined DNA ends (i.e. incomplete exchanges and terminal deletions) may be important.

There is promise of accuracy and utility in S^2RT because it is predicated on simulating Monte Carlo tracks through a multicellular tumour and simulating cellular tumour growth in-between dose fractions. DNA damage induction and subsequent processes like DNA free-end misrejoining and cell death are modelled stochastically using the track structure. Simulated tumours have realistic spatial distributions of cellular pO_2 in relation to the blood vessels, so one can carefully investigate the effect of microscopic regions of tumour hypoxia on treatment efficacy. Since tumour irradiation is performed with track structure, the radiation quality modelled can easily be extended to high LET beams. Modelling a connected network of blood vessels in the tumour also enables consideration of vascular damages. In particular, the model may be used in the future to investigate the extent to which wide-spread vascular damages are responsible for the efficacy of high dose per fraction treatments such as stereotactic body radiotherapy.

Contents

x

Publications

Published and peer-reviewed

- Forster JC, Douglass MJ, Harriss-Phillips WM, Bezak E. Development of an in silico stochastic 4D model of tumor growth with angiogenesis. *Med Phys.* 2017; 44(4):1563-1576.
- Forster JC, Harriss-Phillips WM, Douglass MJ, Bezak E. A review of the development of tumor vasculature and its effects on the tumor microenvironment. *Hypoxia (Auckl).* 2017; 5:21-32.
- Forster JC, Douglass MJJ, Harriss-Phillips WM, Bezak E. Simulation of head and neck cancer oxygenation and doubling time in a 4D cellular model with angiogenesis. *Sci Rep.* 2017; 7(1):11037.
- Forster JC, Douglass MJJ, Phillips WM, Bezak E. Monte Carlo Simulation of the Oxygen Effect in DNA Damage Induction by Ionizing Radiation. *Radiat Res.* 2018; 190(3):248-261.

Unpublished and unsubmitted work written written in manuscript style

- Forster JC, Douglass MJJ, Phillips WM, Bezak E. Stochastic multicellular modeling of x-ray irradiation, DNA damage induction, DNA free-end misrejoining and cell death. 2018; Manuscript in preparation.

Grants and Awards

- **1st Place at Student Paper Night** SA/NT branch of Australasian College of Physical Scientists and Engineers in Medicine (ACPSEM) 2017.
- **Travel Grant from Cancer Council SA's Beat Cancer Project 2017** to attend Enigneering and Physical Sciences in Medicine (EPSM) Conference 2017.
- **1st Place at Student Paper Night** SA/NT branch of ACPSEM 2016.
- **Scholars-in-Training (SIT) Travel Award** Radiation Research Society (RRS) Annual Meeting 2016.
- **Young Investigator Award** 14th International Workshop on Radiation Damage to DNA (IWRDD) 2016.
- **Australian Postgraduate Award (APA)** March 2015 - August 2018.

Conference Presentations

- Forster JC, Douglass MJJ, Phillips WM, Bezak E. (2018, October) *4D cellular model of tumour growth, radiation track structures, DNA damage induction and cell death.* Talk presented at the Engineering and the Physical Sciences in Medicine (EPSM) Conference, Adelaide, Australia.

- Forster JC, Douglass MJ, Phillips WM, Bezak E. (2018, June) *4D cellular model of tumour growth, radiation track structures and DNA damage induction.* Talk presented at International Union for Physical and Engineering Sciences in Medicine (IUPESM) 2018 World Congress on Medical Physics and Biomedical Engineering, Prague, Czech Republic.

- Forster JC, Douglass MJ, Phillips WM, Bezak E. (2018, February) *Radiobiology modelling with Geant4.* Invited talk presented at Australia New Zealand Society of Nuclear Medicine (ANZSNM) Physics Special Interest Group (SIG) Symposium, Adelaide, Australia.

- Bezak E, Phillips W, Douglass M, Forster J, Reid P. (2017, November) *Development of 4D in-silico stochastic spatio temporal model of tumor growth with angiogenesis.* Invited talk presented (by Bezak E) at 38th Annual Conference of Association of Medical Physicists of India (AMPICON), Jaipur, India.

- Forster JC, Douglass MJ, Harriss-Phillips WM, Bezak E. (2017, October/November). *Simulation of DNA damage induction from Monte Carlo particle tracks (validation of radiochemistry).* Talk presented at EPSM Conference, Hobart, Australia.

- Forster JC, Harriss-Phillips WM, Douglass MJ, Bezak E. (2017, October). *The effect of LET and oxygen concentration on the induction of DNA damage by radiation in Monte Carlo track structure simulations using a spatial clustering algorithm.* Poster presented at the Radiation Research Society (RRS) Annual Meeting, Cancun, Mexico.

- Forster JC, Douglass MJ, Harriss-Phillips WM, Bezak E. (2016, November). *The effects of hypoxia on head and neck cancer growth in a 4D cellular growth model with angiogenesis.* Talk presented at EPSM Conference, Sydney, Australia.
- Forster JC, Harriss-Phillips WM, Douglass MJ, Bezak E. (2016, October). *The effects of hypoxia on tumour growth in a 4D cellular computational model.* Poster presented at RRS Annual Meeting, Hawaii, USA.
- Forster JC, Harriss-Phillips WM, Douglass MJ, Bezak E. (2016, March). *Development of a computational tumour growth model: cellular, temporal, spatial and includes tumour angiogenesis.* Talk presented at the 14th International Workshop on Radiation Damage to DNA (IWRDD), Melbourne, Australia.

List of Figures

NB: Does not include figures in publications.

List of Tables

NB: Does not include tables in publications.

List of Source Code Listings

List of Abbreviations

2D . . . . . Two-dimensional, referring to two spatial dimensions.

3D . . . . . Three-dimensional, referring to three spatial dimensions.

4D . . . . . Four-dimensional, referring to three spatial dimensions and one temporal dimension.

ACPSEM . . . Australasian College of Physical Scientists and Engineers in Medicine.

a.k.a . . . . . Also known as.

alt-NHEJ . . . Alternative-non-homologous end-joining.

AMPICON . . Annual Conference of Association of Medical Physicists of India.

a-MVD . . . . Average microvascular density.

ANZSNM . . Australian and New Zealand Society of Nuclear Medicine.

APA . . . . . Australian Postgraduate Award.

aq . . . . . Aqueous, in the context of an aqueous electron.

ATLAS . . . . A Toroidal LHC Apparatus.

BIANCA . . . Biophysical Analysis of Cell Death and Chromosome Aberrations (model).

bp . . . . . Base pair(s).

BSRT . . . . . Base-to-sugar radical transfer.

CA . . . . . Chromosome aberration.

CA9 . . . . . Carbonic anhydrase 9.

CCT . . . . . Cell cycle time.

cDSB . . . . . Complex DSB.

CERN . . . . . European Organization for Nuclear Research.

CL . . . . . Cluster lesion (referred to in the BIANCA model).

c-NHEJ . . . . Canonical-non-homologous end-joining.

CSC . . . . . Cancer stem cell.

CSV . . . . . Comma-separated values.

CTV . . . . . Clinical target volume.

DMSO . . . . . Dimethyl sulfoxide.

DNA . . . . . Deoxyribonucleic acid.

DSB . . . . . Double-strand break (referring to in DNA).

EGFR . . . . . Epidermal growth factor receptor.

EPSM . . . . . Engineering & Physical Sciences in Medicine.

GB . . . . . Gigabyte.

GUI . . . . . Graphical user interface.

h-MVD . . . . Highest microvascular density.

HNC . . . . . Head and neck cancer.

HNSCC . . . . Head and neck squamous cell carcinoma.

HPC . . . . . High-performance computing.

HPV . . . . . Human papillomavirus.

HR . . . . . Homologous recombination.

HUVEC . . . . Human umbilical vein endothelial cell.

HYP-RT . . . Hypoxic Radiotherapy (model).

ID . . . . . Identifier.

IRT . . . . . Independent reaction time method.

IUPESM . . . International Union for Physical and Engineering Sciences in Medicine.

IWRDD . . . . International Workshop on Radiation Damage to DNA.

LET . . . . . Linear energy transfer.

LHC . . . . . Large Hadron Collider.

LQ . . . . . Linear-quadratic (model).

MB . . . . . Modified base (referring to in DNA).

MS . . . . . Modified sugar (referring to in DNA).

MVD . . . . . Microvascular density.

OER . . . . . Oxygen enhancement ratio for cell killing.

$\mathbf{OER_{DSB}}$ . . . . Oxygen enhancement ratio for DSB induction.

PAL-E . . . . . Pathologische Anatomie Leiden-Endothelium.

PARTRAC . . Particle Tracks (model).

PTV . . . . . Planning target volume.

RADAMOL . Radiation Damage to Biomolecules (model).

RAM . . . . . Random access memory.

RITRACKS . Relativistic Ion Tracks (model).

RMSD . . . . . Root-mean-square displacement.

RRS . . . . . Radiation Research Society.

S^{2}RT . . . . . Stochastic Squared Radiotherapy (name of the model developed in this thesis).

SB . . . . . Strand break (referring to in DNA).

SBRT . . . . . Stereotactic body radiotherapy.

SBS . . . . . Step-by-step method.

SCC . . . . . Squamous cell carcinoma.

SD . . . . . Standard deviation.

SEM . . . . . Standard error of the mean.

SIG . . . . . Special Interest Group.

SIT . . . . . Scholar-in-training (term used by the RRS).

SSB . . . . . Single-strand break (referring to in DNA).

TAVAT . . . . Tumour anti-vascular alpha therapy.

TCP . . . . . Tumour control probability.

TNM . . . . . Tumour-node-metastasis.

vWF . . . . . von Willebrand factor.

Symbols

α	Linear component of cell killing (Gy^{-1}).
α_{ca}	Linear component of chromosome aberration production (Gy^{-1}).
$\alpha_{\text{killing}(lca)}$	Linear component of cell killing by lethal chromosome aberrations (Gy^{-1}).
$\alpha_{\text{killing}(mr)}$	Linear component of cell killing by DNA free-end misrejoining (Gy^{-1}).
α_{mr}	Linear component of DNA free-end misrejoining (Gy^{-1}).
β	Quadratic component of cell killing (Gy^{-2}).
β_{ca}	Quadratic component of chromosome aberration production (Gy^{-2}).
$\beta_{\text{killing}(lca)}$	Quadratic component of cell killing by lethal chromosome aberrations (Gy^{-2}).
$\beta_{\text{killing}(mr)}$	Quadratic component of cell killing by DNA free-end misrejoining (Gy^{-2}).
β_{mr}	Quadratic component of DNA free-end misrejoining (Gy^{-2}).
CCT_0	Cell cycle time under full oxia (pO_2 of 760 mmHg).
D	Total dose (Gy) or diffusion coefficient (m^2s^{-1}).
d	Dose per fraction (Gy).
d_1	Spatial clustering distance (nm).
D_{10}	Dose to achieve a surviving fraction of 10% (Gy).
D_{DNA}	Diameter of the DNA double helix (nm).
E_{min}	Minimum energy deposition for a direct event on DNA or its first hydration layer in order to produce a DNA radical (eV).
G_0	A cell cycle phase.
G_1	A cell cycle phase.
G_2	A cell cycle phase.

HP_x . . . . . Hypoxic proportion x, i.e., the proportion of viable cells with $pO_2 < x$ mmHg (%).

L_{DSB} . . . . . Maximum separation between two strand breaks on opposite strands of DNA that constitutes a DSB (nm). This is also the length of the simulated cylinders representing DNA volumes.

$L_{DSB,DSB}$ . . . Minimum distance between two DSBs for them to be counted as separate DSBs (nm).

N_{ca} . . . . . Number of chromosome aberrations per cell [dimensionless].

ND . . . . . Necrosis distance, i.e., the distance from a blood vessel to the onset of necrosis (μm).

N_{lca} . . . . . Number of lethal chromosome aberrations per cell [dimensionless].

N_{mr} . . . . . Number of DNA free-end misrejoining events in a cell [dimensionless].

OER_{dir} . . . . . Oxygen enhancement ratio for cell killing by the direct effect [dimensionless].

OER_{indir} . . . . Oxygen enhancement ratio for cell killing by the indirect effect [dimensionless].

$OER_{killing(mr)}$ . . Oxygen enhancement ratio for cell killing by DNA free-end misrejoining [dimensionless].

OF . . . . . Oxygen function [dimensionless].

p . . . . . Oxygen tension (mmHg).

p_0 . . . . . Blood oxygenation (mmHg).

P_{BSRT} . . . . . Probability of base-to-sugar-radical transfer for a base radical produced by an $^{\bullet}OH$ interaction [dimensionless].

P_{mr} . . . . . Probability of a DNA free-end misrejoining event [dimensionless].

P_{nlmr} . . . . . Probability that a DNA free-end misrejoining event is non-lethal [dimensionless].

pO_2 . . . . . Oxygen tension (mmHg).

$P_{SA,dir}$ . . . . . Probability that a direct event on DNA or its first hydration layer produces a sugar radical [dimensionless].

$P_{SA,^{\bullet}OH}$ . . . . . Probability that an OH interaction with DNA is on the sugar moiety, producing a sugar radical [dimensionless].

$P_{SB,dir}$ . . . . . Probability of a strand break from a direct event on DNA or its first hydration layer [dimensionless].

$P_{SB,^{\bullet}OH}$ . . . . . Probability of a strand break from an $^{\bullet}$OH interaction with DNA [dimensionless].

$P_{SB,SR,dir}$ . . . . Probability of a strand break from a sugar radical that was produced by a direct event (e.g. ionisation or excitation) on DNA or its first hydration layer [dimensionless].

$P_{SB,SR,^{\bullet}OH}$ . . . Probability of strand break from a sugar radical that was produced by an $^{\bullet}$OH interaction with DNA [dimensionless].

$P_{surv(mr)}$ . . . . Probability of cell survival from DNA free-end misrejoining [dimensionless].

r_0 . . . . . Characteristic interaction distance for DSBs (μm).

RVV . . . . . Relative vascular volume (%).

RVV_0 . . . . . Target relative vascular volume (%).

S . . . . . Surviving fraction (%).

SF_2 . . . . . Surviving fraction after a dose of 2 Gy (%).

$SF_{2(mr)}$ . . . . . Surviving fraction after a dose of 2 Gy due to cell killing by DNA free-end misrejoining (%).

S-phase . . . . . A cell cycle phase.

StO_2 . . . . . Microvascular oxygen saturation (%).

S_{lca} . . . . . Surviving fraction from lethal chromosome aberrations (%).

SDP . . . . . Symmetric division probability (referring to stem cells) (%).

t . . . . . Virtual time in radiation track simulation [time].

t_D . . . . . Minimum encounter time in the chemical stage [time].

T_{hyd} . . . . . Thickness of the first hydration layer of DNA (nm).

t_{limit} . . . . . Minimum time step in the chemical stage [time].

xxx

Computational irreducibility is the idea [proposed by Stephen Wolfram in [1]] that some systems can only be described by fully simulating them. The only way to determine the answer to a computationally irreducible question is to perform the computation. Thus it is not possible to know the outcome to a system at a future state without computing all states in between. These computations that cannot be reduced or sped up through any kind of shortcut are called computationally irreducible.

— *Complexity Labs* [2]

1 Introduction

Radiotherapy is a mainstay in the treatment of cancer. Delaney et al [3] estimated that optimally 52% of all cancer patients in Australia should receive external beam radiotherapy (the actual utilisation rate is unclear). The total cost of radiotherapy to the Government of Australia is less than 9 cents in every dollar spent on cancer [4], indicating that radiotherapy is cost-effective (assuming the actual utilisation rate is comparable to the estimated optimal rate).

One type of cancer whose treatment relies heavily upon radiotherapy is head and neck cancer (HNC). This chapter begins with general information about HNCs and their treatment. An issue is then raised with the standard practice of radiotherapy, which is not limited to radiotherapy of HNCs; namely, that radiotherapy treatments could be further individualised to improve patient outcomes. It is discussed how greater treatment individualisation could be achieved with use of predictive biomarkers and computational modelling. The work in this thesis is then introduced: the development of a new radiobiology-based computational model of HNC radiotherapy. The motivation for this model is to assist in further individualising HNC radiotherapy treatments, in particular to account for inter-patient variable tumour hypoxia, which is the main reason radiotherapy sometimes fails to cure HNCs.

1.1 Head and neck cancer

HNCs are those that occur in the throat (pharynx and larynx), nose, sinuses and mouth. More than 90% of these are squamous cell carcinomas (HNSCCs) [5]. For the Australian population in 2017, HNCs made up 5.0% (3,625/72,169) of all cancers diagnosed in men and 2.1% (1,330/62,005) in women [6]. They were responsible for 2.9% (777/27,076) of cancer deaths in men and 1.2% (249/20,677) in women. HNC incidence in Australia increased from 2,475 in 1982 to 3,896 in 2009 (4,955 in 2017) and deaths from HNC increased from 752 in 1982 to 944 in 2011 (1,026 in 2017) [7]. These increases were a reflection of Australia's increasing and ageing population, as age-standardised incidence and mortality rates decreased over the same periods. 5-year relative survival for HNC increased from 61.8% in 1982-87 to 68.2% (67.4% for males and 70.4% for females) in 2006-10 [7] and was 68.4% for males in 2009-13 [6]. Tobacco use and alcohol consumption are the primary risk factors [8]. Human papillomavirus (HPV) also contributes to HNCs, particularly of the oropharynx [9].

1.2 Treatment of head and neck cancer and the role of radiotherapy

Early tumour-node-metastasis (TNM) stage (stage I or II) HNCs are treated with either conservative surgery or radiotherapy (external beam radiotherapy or brachytherapy) [10, 11]. The majority of HNCs are locally advanced (stage III or IV) at the time of diagnosis [12]. Some locally advanced HNCs are treated with surgery, including reconstruction, plus post-operative (adjuvant) radiotherapy or adjuvant concurrent radiotherapy and chemotherapy (chemoradiotherapy). Here, the purpose of adjuvant radiotherapy is to eliminate any residual cancer cells and reduce the likelihood of recurrence, and adjuvant chemotherapy is necessary if there is distant metastatic disease. Radiotherapy and/or chemotherapy can also be administered before surgery (neoadjuvant) to shrink large tumours and make them easier to resect.

Some locally advanced HNCs are unresectable, or surgery will cause such great morbidity, including organ loss, that it is not justified; especially if the prognosis

is poor. In such cases, chemoradiotherapy is administered, either curatively or palliatively. Most deaths from HNC are due to locoregional failure. Clearly radiotherapy is an indispensable modality in the treatment of HNC.

For Australian men in 2014-15, HNC was the third most common cancer for which a radiotherapy course was provided (2,152 out of 28,649 radiotherapy courses) [6]. A study published in 2005 estimated that optimally 74% of all patients with HNC should receive radiotherapy, and found lower than optimal rates of radiotherapy utilisation in South Australia [3]. An advantage of radiotherapy over other modalities is that it seldom requires hospitalisation, which is burdensome for the patient, hospital and tax payer. In Australia in 2011-12, there were 3,725 surgery hospitalisations for HNC, 3,952 chemotherapy hospitalisations for HNC and just 124 radiotherapy hospitalisations for HNC [7].

1.3 Radiotherapy basics

Radiotherapy treats cancer by exposing it to ionising radiation. This radiation is conventionally in the form of an x-ray or electron beam, but there is also proton therapy available in many countries. There are even carbon ion therapy facilities in Japan, Germany, China and Italy. Protons and carbon ions may be advantageous in some patient subsets [13]. A proton therapy facility is planned for Adelaide by 2022 (the first in Australia), with a focus on treating paediatric cancer [14].

The aim of currative radiotherapy is to insult the malignant tissue enough to achieve a satisfactory tumour control probability (TCP) while minimising insult to the surrounding healthy tissue. Damage to normal tissue is responsible for side-effects, which can be particularly distressing when affecting organs in the head and neck [15].

While normal tissue damage is inevitable, there are two general tactics employed so that it is reduced. The first is dose conformation. The patient is imaged and a clinical target volume (CTV) is outlined that contains the extent of gross tumour plus a margin for microscopic disease. A treatment plan is devised that aims to

deliver the prescribed, tumouricidal dose to the planning target volume (PTV)[1] in such a way that the dose drops off as fast as possible outside of the PTV. The most basic way to achieve this conformal dose distribution is by varying the incident beam angle during treatment and shielding, so that the beam always passes through the PTV while passing through different volumes of healthy tissue. Technological advancements in treatment planning systems [16, 17] along with the inventions of image-guided radiotherapy, intensity-modulated radiotherapy and multi-leaf collimators have greatly improved dose conformation [18–20].

The second main way healthy tissue is spared is by exploiting differences between how tumours and healthy tissue respond to radiation. For this reason, the prescribed total dose is typically delivered in small dose fractions. For example, a standard course of radiotherapy for HNC consists of 33 fractions of 2 Gy each. One fraction is delivered per day, 5 days a week from Monday to Friday. The time in-between fractions allows both tumour and normal tissue time to repair some of the damage, but for HNC at least, the normal tissue receives a greater benefit. The study of the biological mechanisms underlying tumour and normal tissue response to radiation defines the field of *radiobiology*.

1.4 Treatment individualisation with biomarkers and computational modelling

Unlike the dose conformation in the treatment plan, which takes into account the patient's unique anatomy, the fractionation schedule is *not* individualised for the patient's unique radiobiology in current standard clinical practice. In standard practice, the clinician refers to a one-size-fits-all, population-based schedule (where population here refers to a type of cancer, e.g. HNC), like the one detailed above for HNC. Yet there is large intra-population variation in patient response to any fractionation schedule. For some patients, the standard total dose prescription is higher than necessary to achieve a satisfactory TCP and, as a result, there is

[1] The PTV is larger than the CTV and ensures that the prescribed, tumouricidal dose is actually delivered to the CTV, accounting for uncertainties in treatment planning and delivery.

superfluous normal tissue damage. Conversely, some other patients require a higher dose to achieve an adequate TCP. There are three main factors that affect the tumour response to radiotherapy: the intrinsic radiosensitivity of tumour cells, tumour hypoxia (volume and severity) and tumour repopulation [21].

Biomarkers have the potential to provide information about the effect of a treatment. Such a biomarker is said to have predictive value for that particular treatment.[2] There are a large number of promising biomarkers for HNC, including measurements of tumour hypoxia, HPV-status, gain-of-function in oncogenes (e.g. epidermal growth factor receptor; EGFR) and loss-of-function in tumour supressor genes (e.g. p53) [23–34]. Predictive value has been demonstrated for measurements of tumour hypoxia [33, 35] and measurements of certain gene expression [25] with respect to radiation-based therapies for HNC. Predictive biomarkers can also be used to anticipate the severity of normal tissue toxicity [36].

In a more ideal clinical practice, each patient would be radiobiologically assessed with multiple biomarkers prior to treatment in order to devise a more individualised, optimised treatment. For example, if EGFR is overexpressed, the EGFR inhibitor cetuximab may be beneficial in addition to chemoradiotherapy [26]. The radiotherapy part of treatment can be optimised in many ways. In addition to prescribing different total doses, the dose per fraction, number of fractions, total treatment time, dose rate and timing of combined therapies can all be adjusted in the optimisation.

The issue with biomarkers is that they require clinical trials to establish their predictive value. Without this evidence, it would not be worth the expense of using biomarkers. It could also be irresponsible, negligent and unsafe to alter a patient's treatment on the basis of an unproven biomarker. Unfortunately, clinical trials are expensive and time-consuming. Predictive value can also be difficult to demonstrate [29, 37]. Furthermore, even if a clinical trial is successful in demonstrating predictive value, it only demonstrates predictive value for one particular treatment. There are many vying biomarkers and many different types of treatment, so it seems that

[2]Not to be confused with prognostic value, which means the biomarker provides information about the overall cancer outcome [22]. Predictive biomarkers have greater utility.

an overwhelming number of clinical trials will be necessary before a substantial degree of biomarker-driven treatment optimisation can be achieved.

This is where radiobiological (computational) modelling can have an impact. Models can be developed to simulate the response of a tumour (or normal tissue) to different types of treatments, while taking into account those tumour properties (intrinsic radiosensitivity, hypoxia and repopulation) that affect the response. Accordingly, models can help to optimise treatments. While clinical trials are a mainstay, modelling can perform a complimentary role, suggesting which biomarkers could have the greatest impact and should be prioritised. Modelling is relatively cheap, and once a model is developed it can often be applied to investigate many different tumour properties and types of treatment simply by changing model parameters or making small modifications.

Radiobiological models are challenging to develop because the interactions between radiation and matter on the nanometre scale and the biological mechanisms involved in the cellular response to radiation are incredibly complex. Simple models exist that are accurate within a limited domain, but to increase the domain of applicability the model must be made more complex, either by accounting for more of the radiobiology involved or by simulating the radiobiology in a more fundamental way. In the latter case, not only does this increase the model's utility as a predictive tool, it can also provide unique insights into radiobiological processes that may be difficult to probe in experiment.

1.5 The current thesis

This thesis contains efforts in radiobiological modelling that build upon the impressive body of existing work. In particular, a spatio-temporal/four-dimensional (4D) model of HNC cellular kinetics and radiotherapy is developed, comprising four main components:

1. 4D cellular HNC tumour growth with angiogenesis,[3]

[3]Angiogenesis is the formation of new blood vessels.

2. Tumour irradiation using the Monte Carlo particle tracking toolkit Geant4 (version 10.4) [38–40], including simulation of the physicochemical and chemical stages with Geant4-DNA [41–43],

3. Induction of DNA damage, including double-strand breaks (DSBs), by track segments through cell nuclei, in a manner that takes into account the cellular oxygenation (pO_2), and

4. Simulation of DSB repair and misrepair and subsequent cell survival and death.

The model can be used to simulate a whole fractionated radiotherapy treatment by irradiating the tumour in multiple dose fractions and shrinking and regrowing the tumour in the time between fractions (Figure 1.1).

The essential novelty of this radiotherapy model lies in the combination of stochastic tumour cell modelling, meaning each cell is modelled individually with stochastic elements (e.g. spatial coordinates of cells, cell cycle times, asymmetric vs symmetric stem cell division), and modelling of the radiation effect starting from Monte Carlo track structure simulations through the multicellular tumour volume. For this reason, the model has been named "Stochastic Squared Radiotherapy" (S^2RT). It is hoped that this model foundation leads to greater accuracy and utility and the possibility of new insights into radiobiology.

For historical background, this Ph.D comes out of a medical physics group with members from the Royal Adelaide Hospital, University of Adelaide, University of South Australia and Adelaide Radiotherapy Centre who are recognised as leaders in radiobiological modelling and belonging to a laboratory with radiobiological modelling as its niche. There was previously a Ph.D by Michael Douglass in 2014 [44] that developed a purely spatial model of Monte Carlo tracks through a multicellular tumour. Before that, a Ph.D by Wendy Phillips in 2011 [45] developed a purely temporal model of cellular tumour growth and radiotherapy. The current work is a natural progression: an entirely new radiotherapy model is developed that

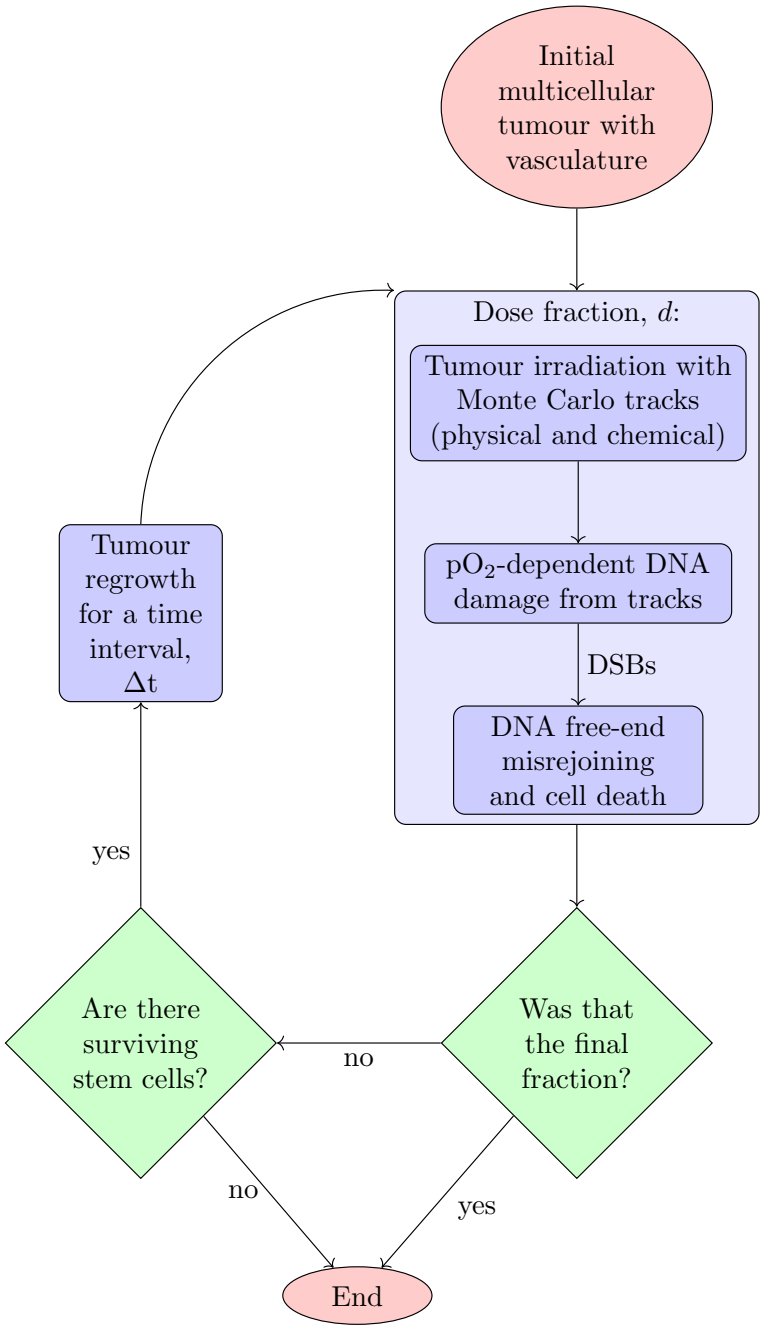

Figure 1.1: Schematic for the simulation of a fractionated radiotherapy treatment.

simulates spatio-temporal cellular tumour growth, including tumour angiogenesis, and irradiates the multicellular tumour with Monte Carlo tracks.

Other radiobiolgical models in the literature that simulate Monte Carlo tracks have typically focussed on simulating them through increasingly complex DNA geometries (nucleosome, chromatin and chromosome) within a single cell nucleus [46–53] or mitochondria [54]. The current work applies Monte Carlo tracks in a different context and at a different scale: to a multicellular tumour as part of a spatio-temporal radiotherapy model.

The underlying motivation for the model is the endeavour to further individualise HNC radiotherapy. Since locally advanced HNCs are often hypoxic [55] and measurements of tumour hypoxia have predictive value for HNC radiotherapy [33, 35], modelling tumour hypoxia and its effects are a central focus. To this end, simulated tumours are grown with a connected and chaotic tumour vasculature, so that realistic spatial distributions of cellular pO_2 are produced in relation to the blood vessels (chronic hypoxia). The simulated effects of hypoxia are i) the slowing of cell division during tumour growth and ii) the reduction of DNA damage and thus cell killing by radiation. To the authors' knowledge, this work is the first to model the latter effect at the level of DNA radical chemistry in the framework of a radiation track structure model. DNA damage is simulated from both direct-type effects (whereby radiation interacts directly with DNA or its primary hydration layer) and the indirect effect (whereby radiation interacts with bulk water to produce hydroxyl radicals which in turn interact with DNA). The indirect effect is more sensitive to cellular pO_2 and necessitated simulation of physicochemical and chemical stages of irradiation.

The aim of this thesis is to develop and validate the four components of the S^2RT model (namely tumour growth, tumour irradiation, DNA damage induction and cell death). The remainder of the thesis content is as follows:

Chapter 2 is a literature review regarding i) the development of tumour vasculature and why hypoxia arises in some tumours and ii) quantitative data for the amount of vascularisation measured in human HNCs.

Chapter 3 contains a brief review of radiobiological modelling, focussing mainly on Geant4-DNA and particularly its chemistry module.

Chapter 4 is a research paper describing the in-house development of a 4D cellular HNC tumour growth model with angiogenesis. This includes a brief review of other radiotherapy models in the literature.

Chapter 5 is a research paper that describes the behaviour of the developed tumour growth model in more depth and provides results pertaining to HNC tumour growth.

Chapter 6 is a research paper describing the in-house development of an algorithm to predict DNA damage from Geant4-DNA physical and chemical tracks through a nucleus, taking into account the cellular pO_2. This includes a brief literature review regarding the mechanisms of the oxygen enhancement effect.

Chapter 7 is a research paper describing an in-house developed Geant4 application for irradiating a multicellular tumour with Monte Carlo tracks, followed by translation of track segments through cell nuclei into DNA damage and simulation of DNA-free end misrejoining and cell death. This includes a brief literature review regarding the mechanisms of cell death from DNA damage.

Chapter 8 contains concluding remarks, including possible future directions.

2

A review of the development of tumor vasculature and its effects on the tumor microenvironment

The publication [56] forms the basis of this chapter:

Forster JC, Harriss-Phillips WM, Douglass MJ, Bezak E. A review of the development of tumor vasculature and its effects on the tumor microenvironment. *Hypoxia (Auckl).* 2017 Apr 11; 5:21-32. doi: 10.2147/HP.S133231.

2.1 Introduction and Motivation

A primary objective of this work was to model the growth of blood vessels in the tumour (tumour angiogenesis). The tumour vasculature supplies the tumour with oxygen and other nutrients. Accordingly, tumour hypoxia may be attributed to deficiencies in the tumour vasculature. A literature review was conducted to investigate what goes awry with the vasculature in tumours compared to in normal tissue, as well as to compile quantitative data of the vasculature morphology in human head and neck cancer. Insights were gained that were utilised in the development of the tumour growth model with angiogenesis.

2.2 Statement of Contribution

2.2.1 Conception

The idea to review tumour angiogenesis was from Eva Bezak. The specific scope of the review and search methodology were conceptualised by Jake Forster with input from Wendy Phillips, Michael Douglass and Eva Bezak.

2.2.2 Realisation

The review was conducted by Jake Forster, with general supervision and guidance provided by Wendy Phillips, Michael Douglass and Eva Bezak. The manuscript was evaluated by Eva Bezak, Wendy Phillips and Michael Douglass for data accuracy, critical appraisal, conclusions reached and general structure and flow.

2.2.3 Documentation

The manuscript was primarily written by Jake Forster. Wendy Phillips, Michael Douglass and Eva Bezak provided input, feedback and revisions.

Statement of Authorship

Title of Paper	A review of the development of tumor vasculature and its effects on the tumor microenvironment
Publication Status	☑ Published ☐ Accepted for Publication ☐ Submitted for Publication ☐ Unpublished and Unsubmitted w ork w ritten in manuscript style
Publication Details	Forster JC, Harriss-Phillips WM, Douglass MJ, Bezak E. *Hypoxia (Auckl)*. 2017; 5:21-32. doi: 10.2147/HP.S133231.

Principal Author

Name of Principal Author (Candidate)	Jake Cameron Forster		
Contribution to the Paper	Conceived of the scope of the literature review, conducted the literature review, wrote the manuscript and acted as the corresponding author.		
Overall percentage (%)	80%		
Certification:	This paper reports on original research I conducted during the period of my Higher Degree by Research candidature and is not subject to any obligations or contractual agreements with a third party that would constrain its inclusion in this thesis. I am the primary author of this paper.		
Signature		Date	3-10-2018

Co-Author Contributions

By signing the Statement of Authorship, each author certifies that:

i. the candidate's stated contribution to the publication is accurate (as detailed above);

ii. permission is granted for the candidate in include the publication in the thesis; and

iii. the sum of all co-author contributions is equal to 100% less the candidate's stated contribution.

Name of Co-Author	Prof. Eva Bezak		
Contribution to the Paper	Initial idea, general supervision and guidance and manuscript revision.		
Overall percentage (%)	10%		
Signature		Date	3-10-2018

Name of Co-Author	Dr Wendy Phillips		
Contribution to the Paper	General supervision and guidance and manuscript revision.		
Overall percentage (%)	5%		
Signature		Date	3-10-2018

Name of Co-Author	Dr Michael Douglass		
Contribution to the Paper	General supervision and guidance and manuscript revision.		
Overall percentage (%)	5%		
Signature		Date	4-10-2018

Hypoxia

Dovepress
open access to scientific and medical research

Open Access Full Text Article

REVIEW

A review of the development of tumor vasculature and its effects on the tumor microenvironment

Jake C Forster[1,2]
Wendy M Harriss-Phillips[1,2]
Michael JJ Douglass[1,2]
Eva Bezak[1,3]

[1]Department of Physics, University of Adelaide, [2]Department of Medical Physics, Royal Adelaide Hospital, [3]Sansom Institute for Health Research and the School of Health Sciences, University of South Australia, Adelaide, SA, Australia

Background: The imbalance of angiogenic regulators in tumors drives tumor angiogenesis and causes the vasculature to develop much differently in tumors than in normal tissue. There are several cancer therapy techniques currently being used and developed that target the tumor vasculature for the treatment of solid tumors. This article reviews the aspects of the tumor vasculature that are relevant to most cancer therapies but particularly to vascular targeting techniques.
Materials and methods: We conducted a review of identified experiments in which tumors were transplanted into animals to study the development of the tumor vasculature with tumor growth. Quantitative vasculature morphology data for spontaneous human head and neck cancers are reviewed. Parameters assessed include the highest microvascular density (h-MVD) and the relative vascular volume (RVV). The effects of the vasculature on the tumor microenvironment are discussed, including the distributions of hypoxia and proliferation.
Results: Data for the h-MVD and RVV in head and neck cancers are highly varied, partly due to methodological differences. However, it is clear that the cancers are typically more vascularized than the corresponding normal tissue. The commonly observed chronic hypoxia and acute hypoxia in these tumors are due to high intratumor heterogeneity in MVD and lower than normal blood oxygenation levels through the abnormally developed tumor vasculature. Hypoxic regions are associated with decreased cell proliferation.
Conclusion: The morphology of the vasculature strongly influences the tumor microenvironment, with important implications for tumor response to medical intervention such as radiotherapy. Quantitative vasculature morphology data herein may be used to inform computational models that simulate the spatial tumor vasculature. Such models may play an important role in exploring and optimizing vascular targeting cancer therapies.
Keywords: cancer, head and neck, vasculature morphology, hypoxia, radiotherapy response

Introduction

In cancer therapy, techniques continue to be used and developed that target the tumor vasculature for the treatment of solid tumors. The tumor vasculature is essential for keeping the tumor alive and facilitating its growth. Tumor cells must be within a certain distance of a perfused blood vessel to receive sufficient oxygen and nutrients to survive and proliferate. It is for this reason that solid tumors must become angiogenic and recruit their own vasculature to grow beyond 1–2 mm in diameter.[1]

Various approaches of vascular targeting are currently being explored, including antiangiogenic agents that disrupt the formation of new blood vessels and vascular targeting agents that shut down the existing tumor blood flow.[2] In the radiotherapy domain, the tumor response to high doses of radiation includes widespread damages

Correspondence: Jake C Forster
Department of Physics, University of Adelaide, Physics Building, Room G16, North Terrace, Adelaide, SA 5005, Australia
Tel +61 8 8313 5996
Fax +61 8 8313 4380
Email jake.forster@adelaide.edu.au

submit your manuscript | www.dovepress.com
Dovepress
http://dx.doi.org/10.2147/HP.S133231

to the vasculature.[3,4] High dose per fraction treatments such as stereotactic body radiation therapy (SBRT) are finding increasing clinical use worldwide for small- to medium-sized primary and metastatic disease,[5,6] although the extent to which vascular damage is responsible for the success of SBRT is not clear.[7] There is also tumor antivascular alpha therapy (TAVAT), in which alpha-emitting radionuclides are delivered to the tumor vasculature to disrupt the tumor vessels.[8]

The tumor vasculature plays an indirect role in other cancer treatment modalities. In chemotherapy, the tumor vasculature is relied upon to deliver the drugs to the tumor cells. The tumor vasculature performs the same role in the technique of tumor radiosensitization using nanoparticles such as gold.[9] There is also interest in radiosensitizing the tumor vessels themselves – as opposed to the tumor cells – by irradiating shortly after ingestion of nanoparticles while they are still concentrated in the tumor vasculature.[10]

With several treatment modalities currently being explored that target the tumor vasculature primarily or secondarily, a topical review is presented herein on the tumor vasculature, focusing on the aspects that are relevant to most cancer therapies and especially to vascular targeting techniques. The first part of this article is a review of the process of tumor vascularization and how the vasculature develops during tumor growth. Experiments are revisited in which tumors were transplanted into rats and mice for the purpose of studying the development of the tumor vasculature. In some experiments, transparent chambers were used to observe changes to the tumor vasculature in real time, while others grew tumors to different sizes and then compared the vasculature between them. The vasculature morphology in tumors, like in normal tissue, can be described quantitatively with parameters such as the average vessel diameter, the vascular density, and the relative vascular volume (RVV). The second part of this article provides a compilation of tumor vasculature morphology data from the literature for spontaneous head and neck cancers in humans. Head and neck cancers were chosen because they are often poorly oxygenated.[11] Finally, there is a review of the effects of the tumor vasculature on the tumor microenvironment. More recently, this has been explored by staining tumor sections with markers for blood vessels, perfusion, hypoxia, and proliferation. Studies of head and neck cancers were exemplary.

The scope of the biology content in this review is intended for a medical physics audience. It is written from a historical perspective, discussing the key findings made. Quantitative vasculature morphology data are emphasized, which may be used to inform computational models that simulate the spatial tumor vasculature. Such models may play an important role in exploring and optimizing vascular targeting cancer therapies.

Materials and methods

The following search strategy and selection criteria were used. Three separate searches were performed using the PubMed database, one for each section of the review. Each search was across all years, and only publications in English were considered.

For the first section, studies of the development of the vasculature in tumor transplants were found by a search of the following keywords: "tumor AND vasculature AND transplant AND quantitative". To be considered, publications had to present findings pertaining to the morphology or functionality of the vasculature at different stages of tumor growth. From the search results and references therein, 57 such publications were found, 15 of which were deemed representative and were discussed in the review.

In the second section, to find vasculature morphology data for spontaneous human cancers of the head and neck, a search was conducted using the keywords: "tumor AND vasculature AND human AND (oral OR laryngeal OR tongue OR pharyngeal OR salivary OR cheek) AND ([vessel density] OR [vessel volume] OR [vessel diameter])". Importantly, due to the large variation in measurements from using different methodologies, publications were only included if they reported measurements on the corresponding normal tissue and on the cancer. In addition, measurements had to be presented as mean ± standard deviation, for vessel densities, there had to be sufficient information to convert the value to mm^{-2} and finally a reasonable sample size was required. Of the 87 publications, 9 met these criteria. The data were tabulated for comparison of measurements between different groups.

For the third section regarding the effects of the tumor vasculature on the tumor microenvironment, a search was conducted using the following keywords: "tumor AND vasculature AND distance AND (proliferation OR hypoxia OR necrosis)". Nine publications were selected for discussion from the search results and references therein. Aside from historically significant publications, the most insightful studies were those conducted on head and neck cancers.

Results and discussion

Development of tumor vasculature with tumor growth

The first group to quantitate changes in the tumor vasculature morphology during tumor growth was Algire and

Chalkley.[12] They transplanted tumors of mammary gland carcinoma and sarcoma 37 into transparent skin flap chambers in mice to grow in the subcutaneous connective tissue. The tumors became vascularized by eliciting the sprouting of new capillaries from the vessels in the surrounding host tissue. This process is called angiogenesis.[13] Angiogenesis also occurred with implants of subcutaneous tissue and at the site of a wound. However, for tumors, it occurred 3 days after implantation, whereas it began 6 days after implantation of subcutaneous tissue or the infliction of a wound. The tumors only increased in size once they became pervaded by capillaries. The tumor vascularity increased, and angiogenesis continued to occur at the tumor edge to facilitate the increasing tumor size. The RVV, which was the relative proportion of the tumor area in the chamber covered by blood vessels, was measured daily using a method devised by Chalkley.[14] Briefly, an eyepiece graticule is randomly placed several times, and the proportion of coincidences with vessels yields the RVV. The RVV increased and reached 50% only 7 days after implantation and maintained this level thereafter, which was twice the value in control chambers containing normal subcutaneous tissue. The tumor vasculature was a sinusoid-like plexus of vessels with large marginal draining vessels. There was no evidence that the new tumor vessels differentiated into venules or arterioles. They retained their capillary-like structure, having walls that contained only a single layer of endothelium, but their diameters were much larger than the capillaries in normal subcutaneous tissue. Such observations revealed that the vasculature in tumors is chaotic compared to that in normal tissue (Figure 1).

The formation of the tumor vasculature was described in more detail by Eddy and Casarett.[16] They studied the development of the vasculature in tumors of a malignant neurilemmoma of the Syrian hamster as they grew in a transparent cheek pouch chamber. After tumor implantation, the veins and venules in the surrounding host tissue dilated and become tortuous. The arterial vessels were largely unaffected in comparison. The capillary sprouts of angiogenesis were seen to originate from the host venous vessels, although the magnitude of this activity may have obscured a similar activity in the host capillary bed. The capillary sprouts elongated and anastomosed with each other to establish a capillary-like network in the tumor. As soon as a tumor capillary anastomosed with the arterial end of a host capillary, the direction of blood flow changed so that the host arterial supply flowed through the tumor capillary network to the host venous system. Anastomoses between the tumor capillaries and the host arterioles were seemingly random and occasionally resulted in inefficient blood distribution. For example, a single short capillary could conduct blood from a host arteriole directly to a wide capillary-like vessel, which drained to the tumor perimeter. As the tumor increased in size, the host venous vessels were remodeled and pushed away until finally being incorporated into the tumor. In contrast, the host arterial vessels remained in about the same location as the tumor grew around them. The tumor vessels maintained a capillary-like structure, including a number that progressively dilated and reached diameters as large as 200 μm in some cases (capillaries normally have diameters less than 12 μm). In the later stages of tumor growth, it was apparent that some vessels had become occluded. Blood flow was restored if the chamber walls were separated by even a fraction of a millimeter.

Yamaura and Sato[17] further quantitated the development of the tumor vasculature morphology in tumors of rat ascites hepatoma growing in transparent chambers. At various days after tumor implantation, they measured the frequency distribution of vessel diameters and the RVV using Chalkley's method in the whole chamber. They also used these measurements to calculate the vascular length and surface area per unit volume of tissue. Tumor angiogenesis began after 3 to 5 days. The sprouting of capillaries resulted in an increase in the proportion of vessels with diameters less than 10 μm

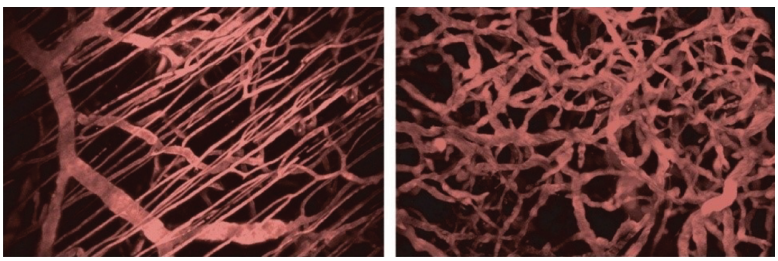

Figure 1 Organized vasculature in normal tissue contrasted with chaotic vasculature in tumors.
Note: Adapted with permission from Macmillan Publishers Ltd.: *Nature Medicine*, Jain RK, Molecular regulation of vessel maturation, 2003;9(6):685–693,[15] copyright (2003).

from 40 to 70%. The vascular length increased from 30 to 160 cm/mm^3, the vascular surface area increased from 20 to 63 mm^2/mm^3, and the RVV increased from 20 to 50%. On day 10, the tumor capillaries began to dilate, causing the frequency distribution of vessel diameters to become low and wide. This was associated with decreases in the vascular length and surface area, but the RVV was unchanged. There were changes to the host arterial vessels around this time. Their walls became thin and ragged, their lumina widened at branching sites, they took on a zigzag pattern and vasomotion eventually disappeared. After 14 days, necrosis appeared near the center of the tumor and spread outward, seemingly due to prolonged vessel occlusion. The smallest vessels were the first to close, resulting in cords of viable tissue surrounding the remaining larger vessels, beyond which there was necrosis. Eventually, even the widest vessels were forced shut and the tumor became completely necrotic. Necrosis was associated with the disappearance of blood vessels and thus coincided with decreases in the vascular length, vascular surface area, and RVV to zero.

It is worth briefly mentioning the findings of a few other experiments in which tumors were grown in transparent chambers. Peters et al[18] observed that in normal tissue, the capillary perfusion was uniform and orderly. Conversely, in a mammary adenocarcinoma, red blood cells were often densely packed and slowly squeezed single file through windy capillaries. Capillaries could alternate between very fast and very slow perfusion. Boucher et al[19] demonstrated that the interstitial fluid pressure increased over time in human colon adenocarcinoma and mouse mammary adenocarcinoma growing in a skin fold chamber in mice. Endrich et al[20] found that the mean blood flow to amelantotic melanoma growing in a chamber decreased from 40.4 mL/min/100 g on day 4 to 21.1 mL/min/100 g on day 12. Central necrosis appeared in these tumors after just 5 days. Vajkoczy et al[21] showed for gliomas growing in a skin fold chamber in mice that the onset of central necrosis on day 22 coincided with a significant decrease in the vessel perfusion index in the central region of the tumor compared to that in the marginal region. Each of these findings suggests that blood vessels may become occluded during tumor growth in chambers, which if prolonged could cause necrosis from blood stasis.

The transparent chamber technique allowed for observation of the development of the tumor vasculature in real time. In particular, it provided unique insight into the process of tumor vascularization as discussed earlier. However, this technique has limitations. Recall in the experiment by Eddy and Casarett,[16] it was shown that permanent and widespread vessel occlusion can occur in tumors that grow within the confines of a chamber due to pressure from the chamber itself. This quickly leads to massive necrosis, making it difficult to study the development of the tumor vasculature after the earliest stages of growth. Therefore, the discussion now moves to experiments that grew tumor transplants to different sizes without being confined to a chamber, then internally examined them to view the state of the tumor vasculature at various stages of growth.

Although prolonged vessel occlusion and thus necrosis may be produced artificially in chamber experiments, these processes occur naturally in tumors as well. Large interstitial pressures develop in tumors due to a combination of the high tumor cell density (10^8–10^9 cells/cm^3), high blood vessel permeability, and poor lymphatics.[22] Goldacre and Sylven[23] found that for various unicentric mouse and rat tumors transplanted subcutaneously or intramuscularly, central necrosis appeared when tumors reached a diameter of 1 cm. It was found by injection of a dye that there was no blood flow to the necrotic zone, but there were blood vessels in the necrotic zone that contained undamaged red blood cells. These findings indicated that vessel occlusion resulting in blood stasis was responsible for the central necrosis. For tumor transplants of rat fibrosarcoma in which necrosis tended to develop centrally, Tozer et al[24] showed that the mean blood flow (mL/min/100 g) decreased with increasing tumor size. Furthermore, the blood flow was constant in the tumor periphery, it was in the center that it decreased. In all but the smallest tumors, blood flow was lower in the center than the periphery, even when only considering viable tissue.

Tannock and Steel[25] found that the relative necrotic volume (the relative proportion of the tumor section covered by necrosis, measured using Chalkley's method) in equatorial sections of transplanted rat mammary tumors increased with tumor weight from 0% at 0.5 g to 50% at 10 g. By labeling red blood cells with chromium-51 and observing that only a small fraction of the red blood cells in necrotic regions were labeled compared to that in viable regions, it was concluded that the cause of necrosis was again stasis in tumor blood vessels caused by vessel occlusion.

Fallowfield[26] reported that for murine melanoma B16 and human melanoma Mel-mo transplanted subcutaneously in mice, the relative perfused vascular volume (as determined by staining with Hoechst 33342) in all tumor tissue, both viable and necrotic, decreased with the logarithm of tumor weight, while the relative necrotic volume increased with the logarithm of tumor weight. These relationships suggest that necrosis appeared when the blood vessels became occluded.

In Mel-mo tumors weighing between 37 and 2050 mg, the relative perfused vascular volume decreased from 12.6 to 4.1% and the relative necrotic volume increased from 24 to 48.8%. In B16 tumors weighing between 80 and 3612 mg, the relative perfused vascular volume decreased from 20 to 8.7% and the relative necrotic volume increased from 2.8 to 30%.

Different tumor types can elicit entirely different patterns of vasculature from the host subcutaneous tissue. Rubin and Casarett[27] used angiography to study the development of the vasculature in tumors of Walker carcinosarcoma and Murphy lymphosarcoma transplanted into rats. Walker carcinosarcoma induced "peripheral vascularization", which consisted of vessels corkscrewing radially into the tumor. Once these tumors reached 1.5 to 3 cm in diameter, central necrosis appeared and the radial vessels abruptly terminated at the necrotic edge. Murphy lymphosarcoma induced a contrasting pattern of "central vascularization". Major vessels penetrated into the tumor center and formed an axial trunk from which smaller vessels branched out to the periphery in an arborescent fashion. Central necrosis did not develop in these tumors.

Gliomas induce a distinct vasculature that differs systematically from the tumor center to periphery. The development of the glioma vasculature was best described by Deane and Lantos[28] who induced gliomas in rats by intracerebral injection of neoplastic glial cells, but similar findings have been reported for gliomas growing subcutaneously.[21] The gliomas remained avascular to sizes up to 1 mm in diameter. In larger tumors up to 4 mm in diameter, the core remained avascular and occasionally developed necrosis, while at the tumor periphery, there were capillary buds and capillaries up to 5 μm in diameter corresponding to early angiogenesis. In tumors larger than 4 mm, there was a third zone in between the central avascular necrotic zone and the peripheral zone of early angiogenesis. This intermediate zone contained tortuous vessels with diameters ranging from 3 to 40 μm. The wider vessels were unusually large sinusoidal capillaries lined by up to 15 endothelial cells. It was deemed that the vasculature in the intermediate zone was in the "late vascular stage".

Perhaps the most quantitative study of the development of tumor vasculature morphology was conducted by Vogel.[29] Tumors of mammary adenocarcinoma 72j were transplanted subcutaneously in mice and permitted to grow for 6, 17, or 23 days to produce a range of tumor weights from 5 to 2700 mg. Necrotic regions were randomly scattered throughout tumors weighing more than 300 mg and occupied between 5 and 15% of the tumor cross section. Vessels were stained by injection of India ink so the vasculature morphology was only measured in viable regions. The vasculature morphology was quantitated by measuring the frequency distribution of vessel diameters and the RVV using Chalkley's method. The vascular length and surface area per unit volume of tissue were also calculated. Viable regions in the center showed no significant differences in vasculature morphology compared to viable regions in the periphery. In the smallest tumors between 5 and 30 mg, vascular length was 820 mm/mm^3 and vascular surface area was 34 mm^2/mm^3. In the largest tumors weighing between 1.1 and 2.7 g, the vascular length and surface area in viable tissue were drastically reduced. The vascular length was 47 mm/mm^3, and the vascular surface area was 7 mm^2/mm^3. The RVV increased only slightly from 16 to 18% in the viable tissue from the smallest tumors to the largest. The frequency distribution of vessel diameters revealed that 70% of vessels had a diameter less than 12 μm for tumors weighing between 5 and 30 mg, but as the tumors increased in size, there was a familiar widening and flattening of the distribution. In tumors weighing between 1.1 and 2.7 g, only 27% of the vessels had a diameter less than 12 μm. Vogel reported that tumor growth was accompanied by an increase in sinusoidal areas compared to capillary areas. Typical capillary areas had 97% of vessel diameters less than 12 μm, an RVV of 12%, an average vessel diameter of 6.7 μm, a vascular length of 1700 mm/mm^2, and a vascular surface area of 45 mm^2/mm^3. Contrastingly, sinusoidal areas had 11% of vessel diameters less than 12 μm, an RVV of 32%, an average vessel diameter of 53 μm, a vascular length of 50 mm/mm^3, and a vascular surface area of 11 mm^2/mm^3.

A similar experiment was conducted by Hilmas and Gillette[30] on mouse mammary carcinoma grown in gastrocnemius muscle. Tumors ranged between 4 mm in diameter (volume 35 mm^3) and 14 mm in diameter (volume 1500 mm^3). Again vessels were stained by injection of a contrast agent, in this case colloidal carbon, and the vasculature morphology was quantitated in the viable tissue. The vascular length decreased rapidly from 850 to 350 mm/mm^3 with increasing tumor volume between 35 and 100 mm^3. In tumors larger than 500 mm^3, the vascular length was 150 mm/mm^3 or less. The vascular surface area was 26.5 mm^2/mm^3 in the smallest tumors and 15 mm^2/mm^3 or less for tumor volumes of 500 mm^3 or greater. An increase in the average vessel diameter was again observed with increasing tumor size. The RVV in viable tissue was a constant 17% for all tumor sizes. The relative necrotic volume was less than 5% for tumor volumes of 35 mm^3 and increased to over 40% in tumors with volumes over 1500 mm^3.

In summary, tumors become vascularized by inducing angiogenesis in the veins, venules, and capillaries of the host tissue. Capillaries sprout toward the tumor and anastomose with each other and the host vessels to form a capillary network through the tumor. Angiogenesis continues to occur beyond the tumor periphery to facilitate its increase in size. The host venous vessels are pushed away and remodeled before being incorporating into the growing tumor, while the patterns of the arterial vessels are unchanged as they are incorporated. The tumor capillaries develop abnormally. They dilate and become tortuous while retaining their capillary-like structure and not properly differentiating into arterials and venules. Associated with these changes are decreases in the vascular length and vascular surface area per unit volume of tissue but the RVV remains about the same. The host vessels that become incorporated in the tumor become disfigured too. They dilate and the arterial vessels become thin and ragged and eventually lose vasomotion. The tortuosity of tumor vessels causes vessel perfusion to fluctuate. When tumors become larger, the interstitial fluid pressure can become so great that small vessels become permanently occluded. This leads to blood stasis and the formation of necrotic regions, typically near the tumor center.

It must be noted that these observations are from tumors growing in rats and mice (and generally in the subcutaneous tissue), since only in such animal models has the development of tumor vasculature been closely observed (for ethical and practical reasons). However, it is reasonable to assume that the development of vasculature in spontaneous human tumors shares similarities with the development in animal models.

Vasculature morphology in spontaneous human tumors

In the past few decades, the vasculature morphology has been quantitated in spontaneous tumors presenting in human patients. This has typically been done by staining the blood vessels in resected specimens using a marker such as von Willebrand factor (vWF), CD34, or CD31. A compilation of the vasculature morphology data from the literature for various head and neck cancers is presented in Table 1. There are six publications for squamous cell carcinoma (SCC) of the oral cavity, two for laryngeal SCC and one for mucoepidermoid carcinoma of the salivary glands. Vasculature morphology parameters include the highest microvascular density (h-MVD), the RVV, and the mean vessel diameter. For every measurement on carcinoma, the measurement on the corresponding normal tissue is also presented. Measurements on dysplasia were included too. The table contains a description of the method used for each measurement.

There is usually large intratumoral heterogeneity in the MVD. For example, Wijffels et al[31] found that for various human head and neck SCCs, the values for h-MVD were a factor of 1.5 to 6 times higher than the vascular density across the whole tumor section, referred to as the average MVD (a-MVD). Most groups[32–39] report on the h-MVD. They do so by staining vessels and measuring the vascular density in the most vascularized areas or "hotspots" in the tumor, an approach pioneered by Weidner et al.[40] The findings in the table demonstrate that for oral SCC, laryngeal SCC, and mucoepidermoid carcinoma of salivary glands, the h-MVD is significantly higher in carcinoma than in the corresponding normal tissue, i.e., tumors contain regions that are more vascularized than anywhere in the normal tissue. Further, a significant increase from normal to dysplasia was found by Pazouki et al,[32] Pignataro et al,[34] Shieh et al,[35] and Mohtasham et al[39] but not by Li et al.[36] From dysplasia to cancer, Li et al[36] and Mohtasham et al[39] found a significant increase, while Pazouki et al,[32] Pignataro et al,[34] and Shieh et al[35] did not.

There is enormous variation in the values of h-MVD for oral SCC presented by different groups. On opposite extremes, Mohtasham et al[39] reported a value of 57.8 ± 10.8 mm^{-2}, while Sharma et al[38] found it to be 240.53 ± 92.3 mm^{-2}. Elsewhere, Davey et al[41] reported a median h-MVD of over 1000 mm^{-2} (and a median of ~400 mm^{-2} for normal tissue). Schor et al[42] demonstrated that measurements of h-MVD are highly subject to the methodology used, including the staining factor, the pretreatment, and the size of the subset area. There is also variation due to interobserver bias. For this reason, it was essential that normal tissue values be provided to serve as a reference point for the measurement on cancer.

The data also indicate that progression of oral SCC is accompanied by increasing RVV, which means tumors are overall more vascularized than normal tissue. This should also be reflected in the parameter a-MVD, but unfortunately there are limited data available. Davey et al[41] reported that the a-MVD was significantly higher (p=0.01) in oral SCC than in normal oral mucosa for six specimens when staining vessels with vWF. Nevertheless, given the high degree of intratumor heterogeneity in vascularity, there can still be regions of a tumor, in which the vascularity is comparable to or even less than that in normal tissue.

Li et al[36] commented that for oral SCC, high concentrations of vascularization were most commonly found at the

Table 1 Vasculature morphology data for spontaneous human head and neck cancers

Reference (year)	Cancer type	Number of specimens	Method	Measurements
Pazouki et al[32] (1997)	Oral SCC	16 of normal oral mucosa, 30 of dysplasia (10 mild, 9 moderate, and 11 severe), and 30 of cancer (14 early and 16 late)	Vessels were stained for vWF, h-MVD was measured using the hotspot method and RVV was measured using Chalkley's method	h-MVD (mm^{-2}): normal 88±35, severe dysplasia 164±58,* and late SCC 148±53* RVV (%): normal 3.7%±0.5%, increased linearly with severity of dysplasia, and SCC to 10.0%±2.5% for late SCC* (values for RVV were taken by reading off a graph)
Sawatsubashi et al[33] (2000)	Laryngeal SCC	10 of normal, 54 of invasive cancer	Vessels were stained for CD34, and h-MVD was measured using the hotspot method	h-MVD (mm^{-2}): normal 21.67±3.00 and cancer 37.34±2.64*
Pignataro et al[34] (2001)	Laryngeal SCC	20 of normal mucosa, 20 of dysplasia, and 20 of infiltrating carcinoma	Vessels were stained for CD34, and h-MVD was measured using the hotspot method	h-MVD (mm^{-2}): normal 35.1±11.5, dysplasia 60.9±19.8,* and cancer 74.8±19.0*
Shieh et al[35] (2004)	Oral SCC	12 of normal mucosa, 28 of dysplasia, and 50 of T2 cancer	Vessels were stained for CD34, and h-MVD was measured using the hotspot method	h-MVD (mm^{-2}): normal 84±21, dysplasia 212±56,* cancer intratumoral 226±50,* and cancer peritumoral 240±58*
Li et al[36] (2005)	Oral SCC	12 of normal mucosa, 26 of mild dysplasia, 16 of moderate dysplasia, 10 of severe dysplasia, and 98 of cancer	Vessels were stained for CD31, and h-MVD was measured using the hotspot method	h-MVD (mm^{-2}): normal 31.0±13.4, mild dysplasia 37.4±10.8, moderate dysplasia 42.1±23.8, severe dysplasia 48.1±19.6, and cancer 79.6±38.2*
Amelink et al[44] (2008)	Oral SCC	16+ of normal mucosa and 24+ of cancer	Noninvasive differential path-length spectroscopy in vivo	Mean vessel diameter (μm): normal 24±14 and cancer 25±12 RVV (%): normal 1.0±0.9 and cancer 2.2±2.3*
Shieh et al[37] (2009)	Mucoepidermoid carcinoma of salivary glands	35 of normal tissue and 35 of cancer	Vessels were stained for CD34, and h-MVD was measured using the hotspot method	h-MVD (mm^{-2}): normal 18.7±5.2 and cancer intratumoral 63.9±23.2*
Sharma et al[38] (2010)	Oral SCC	10 of normal mucosa and 30 of cancer	Vessels were stained for vWF, and h-MVD was measured using the hotspot method	h-MVD (mm^{-2}): normal 64.4±13.53 and cancer 240.53±92.3*
Mohtasham et al[39] (2010)	Oral SCC	6 of normal mucosa, 22 of dysplasia, and 42 of cancer	Vessels were stained for CD34, and h-MVD was measured using the hotspot method	h-MVD (mm^{-2}): normal 27.5 ± 12.5, dysplasia 41.5±8.5,* and cancer 57.8±10.8*

Note: *Significantly different to normal tissue ($p<0.05$).
Abbreviations: SCC, squamous cell carcinoma; h-MVD, highest microvascular density; RVV, relative vascular volume; vWF, von Willebrand factor.

margins of invasive regions. The same has been reported elsewhere.[43] Li et al also noted that the vessels in normal oral mucosa were regularly distributed and had regular courses and cross-sectional shapes, whereas at the margin of oral SCC, the vessels had irregular courses and elongated cross-sectional shapes.

The method of differential path length spectroscopy used by Amelink et al[44] also enabled measurement of the microvascular oxygen saturation (StO_2). They reported that the vessels were significantly less oxygenated in oral SCC than that in normal oral mucosa ($p<0.05$), with StO_2 values of 81±21 and 95±5%, respectively. They also found that this was the case for bronchial carcinoma compared with normal bronchial mucosa.[45] These findings suggest that the tumors contained poorly perfused vessels and thus blood depleted of oxygen.

Effects of the tumor vasculature on the tumor microenvironment

Ultimately, the tumor vasculature must be judged by how well it nourishes the tumor cells. In a study of surgical resections of human bronchial carcinoma, Thomlinson and Gray[46] discovered how the vasculature in spontaneous human tumors sometimes fails in this sense. They found that the tumor cells were located in cords, where each cord had a single blood vessel along its axis and outside of the cords there was necrosis. The obvious explanation for their discovery was that the availability of oxygen and nutrients decreases with increasing distance from the blood vessels and only tumor cells within the cords were close enough to a blood vessel to survive. A similar corded structure was observed in Yamaura and Sato's chamber experiment,[17] which was discussed in the first section of this review, but in that instance the cords appeared because only the largest vessels were still perfused after all of the smaller vessels had become occluded from the high interstitial pressure. In the present case, all of the vessels were perfused but apparently the vessel density was insufficient for the amount of oxygen available in the blood. Thomlinson and Gray recognized that there must be a large fraction of hypoxic cells in corded tumors, particularly in the outer regions of the cords bordering necrosis. Hypoxia of this nature is called "chronic hypoxia". It is sometimes misleadingly referred to as "diffusion limited". "Consumption limited" would be a more accurate term.

An example of an animal tumor that has an innate corded structure is the mouse mammary tumor BICR/SA1 studied by Tannock.[47] Necrosis and cords of viable tissue were evident even in the smallest tumors examined weighing 0.1 g. For tumors weighing between 0.5 and 3 g, the relative necrotic volume was 60 to 70% and increased slightly with tumor weight. Tumor cords had radii in the range 60 to 120 μm, and there was no systematic variation in the mean cord radius with tumor weight. It was found that for animals breathing only 10% oxygen, the mean tumor cord radius decreased from 85.1±2.2 to 75.5±8.8 μm. Tannock also investigated the patterns of cell proliferation in this tumor using tritiated thymidine. He found that proliferation in the tumor cords decreased with increasing distance from the blood vessels. He reported that this was due to a decrease in the fraction of cycling cells and that the cell cycle time did not vary. The growth fraction was 100% in the inner zone, 80% in the middle zone, and 50% in the outer zone of the cords. He noted that tumor cells must migrate centrifugally through the tumor cords. When a tumor cell divides, its daughter displaces neighboring cells further toward the cord periphery and finally into the necrotic zone. He suggested that for every tumor cell produced by mitosis, on average one tumor cell becomes necrotic (neglecting longitudinal cord growth). Therefore in tumor cords, there is constant cell renewal. It was estimated that cells in the inner and middle zones took 36 and 16 hours, respectively, to migrate to the outer zone.

A similar experiment was conducted by Hirst and Denekamp[48] on the corded tumors of another transplantable mouse mammary carcinoma KHH. They reported that proliferation in this tumor did not vary between center and periphery, it only decreased with increasing distance from blood vessels. Unlike Tannock, they found that the cell cycle time did increase with increasing distance from the vessel, mainly due to the duration of the G_1 phase, which was 7.2 hours in the inner zone, 11.8 hours in the middle zone, and 17.1 hours in the outer zone. The growth fraction decreased from 100% in the inner and middle zones to 58% in the outer zone of the cords. They too estimated that a cell labeled next to a vessel transversed the 90 μm to the outer zone in ~36 hours. In both this study and Tannock's study, it was estimated that the growth fraction in the outer zone of the cord, which neighbored the necrotic region and presumably contained hypoxic cells, was over 50%. This large population of radioresistant cells with the ability to repopulate the tumor would make these tumors difficult to eradicate with radiotherapy.

More recently, the effects of the vasculature on the tumor microenvironment have been explored in human tumors, particularly those of head and neck cancers, by staining tumor sections with markers for blood vessels and hypoxia. Wijffels et al[31] studied the spatial relationship between hypoxia and blood vessels in 22 specimens of human SCC of the oropharynx, larynx, and hypopharynx. Blood vessels were stained by Pathologische Anatomie Leiden-Endothelium (PAL-E), and hypoxia was stained by pimonidazole. Pimonidazole binding occurs at oxygen tensions less than 10 mmHg.[49,50] The fraction of the tumor section stained by pimonidazole, called the hypoxic fraction, varied between 2 and 29% across the entire tumor surface. Of the 22 tumors, 16 had a total hypoxic fraction above 5%. For these tumors, to quantitate the distribution of hypoxia in relation to the vasculature, the hypoxic fraction was calculated in zones at increasing distance from the nearest blood vessel (0–50, 50–100, 100–150 μm, etc.). Accordingly, tumors were separated into three categories. One category of tumors had hypoxia between 50 and 200 μm from vessels and small areas of necrosis beyond 150–200 μm. These tumors possessed a typical corded structure (Figure 2). Another category of tumors had very little hypoxia within

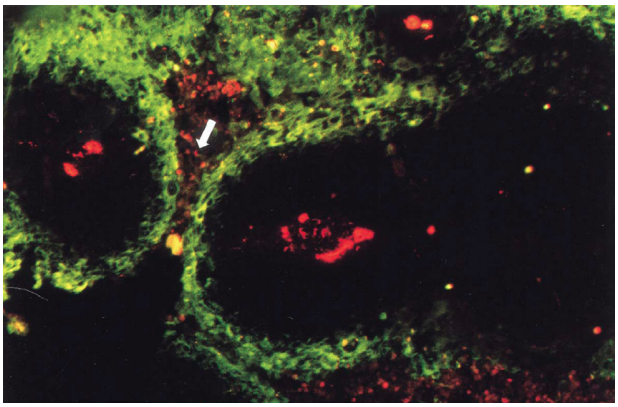

Figure 2 Fluorescence microscopic image of a tumor section after staining for hypoxia (green) and vessels (red).
Notes: A typical corded structure is recognizable. There are well-oxygenated areas directly adjacent to vessels, further out there is hypoxia and at even greater distances there is necrosis (white arrow). Adapted with permission from Macmillan Publishers Ltd on behalf of Cancer Research UK: *British Journal of Cancer*, Wijffels KIEM, Kaanders JHAM, Rijken PFJW, et al, Vascular architecture and hypoxic profiles in human head and neck squamous cell carcinomas, 2000;83(5):674–683,[31] copyright 2000.

100 μm of vessels and significant amounts of viable, hypoxic tissue at distances greater than 200 μm. The stark contrast between these categories suggests that oxygen consumption and delivery varied considerably between tumors. In the last category, tumors had considerable amounts of hypoxia within 50 μm of blood vessels, where there are ordinarily normoxic cells. Hypoxia this close to blood vessels is caused by a temporary absence of vessel perfusion and is termed "acute hypoxia" to distinguish it from consumption-limited, chronic hypoxia. In each category, the tumors showed an increase in the hypoxic fraction in zones at increasing distance from blood vessels (at least before the onset of necrosis).

An alternative hypoxia marker to pimonidazole is carbonic anhydrase 9 (CA9). CA9 is typically expressed at oxygen tensions less than 20 mmHg.[51] Since it has a higher threshold than pimonidazole, it should stain closer to blood vessels. Hoogsteen et al[52] found this was the case in a study of 103 human biopsies of laryngeal SCC. For 18 tumors of assorted human head and neck SCCs, Beasley et al[53] found that the distance from blood vessels (stained by CD34) to the start of CA9 expression was between 40 and 140 μm (median 80 μm) and the distance from blood vessels to the onset of necrosis was between 80 and 200 μm (median 130 μm).

Further insights have been gained from staining tumor sections with markers for perfusion and proliferation in conjunction with markers for vessels and hypoxia. By staining vessels with 9F1, perfusion with Hoechst 33342, and proliferation with S-phase marker BrdUrd, Bussink et al[54] showed that proliferation staining decreased in zones at increasing distance from both perfused and nonperfused vessels in xenografts of human laryngeal SCC grown subcutaneously in mice. Proliferation was higher near perfused than nonperfused vessels, but proliferation close to nonperfused vessels was comparable to or greater than it was at larger distances from perfused vessels. This indicated that the nonperfused vessels were recently perfused and thus vessel perfusion fluctuated in these tumors.

In a study of xenografts of human head and neck SCCs grown subcutaneously in mice, Ljungkvist et al[55] found that different vasculature structures give rise to different distributions of hypoxia. By staining blood vessels with 9F1 and hypoxia with pimonidazole, two distinct patterns of hypoxia were identified. Patchy hypoxia was associated with a typical tumor cord structure. Ribbon-like hypoxia occurred when the vessels were in sheet structures that formed concentric lobe shapes. In both cases, the hypoxic fraction increased and proliferation staining with BrdUrd decreased in zones at increasing distance from blood vessels. They found that there was considerable overlap between hypoxia and proliferation, particularly at 100–150 μm from vessels.

Some human head and neck cancers are well oxygenated. Wijffels et al[56] conducted a study of eight specimens of human salivary gland carcinoma and found that none contained any hypoxia according to staining with pimonidazole and CA9. They also stained blood vessels with PAL-E, and it was apparent that the MVD was high across the entire tumor sections. The a-MVD varied from 209 to 546 mm^{-2} (median 285 mm^{-2}). There were no measurements on normal tissue to compare with, but they reported in the aforementioned study of oropharyngeal, laryngeal, and hypopharyngeal SCCs (again staining vessels with PAL-E) that the a-MVD varied between 11 and 67 mm^{-2} (median 42 mm^{-2}). Assuming they used similar methodologies between studies, it is safe to conclude that these salivary gland carcinomas were extremely vascularized. Along with the lack of hypoxia, there was no clear spatial relationship between proliferation staining with IdUrd (another S-phase marker) and vessel structures.

Conclusion

Studies of tumor transplants growing subcutaneously in rats and mice reveal that the tumor vasculature develops inefficiently under the imbalance of angiogenic regulators. The tumor vessels are unorganized and become increasingly tortuous and disfigured, hindering vessel perfusion. When tumors become large, high interstitial fluid pressures can develop, which cause vessels in the tumor to permanently shut, resulting in blood stasis and the development of macroscopic necrosis.

Data from spontaneous human head and neck cancers show that there are typically regions in the tumor that are more vascularized than any region in the normal tissue. Although the data are limited, it seems that tumors are also more vascularized overall. This is not trivial – the opposite has been reported for esophageal SCC[57] and lung cancer.[58] However, tumor vascularity is highly heterogeneous, and there can still be regions of head and neck cancers, in which the vascularity is comparable to or even less than that in normal tissue. Vascular hotspots are most commonly observed in invasive regions of the carcinoma. Like in animal models, the vessels in spontaneous human carcinomas are observed to be irregular and tortuous compared to those in the normal tissue, thus hindering perfusion and reducing the oxygenation levels in the blood, as evidenced by StO_2 measurements.

By staining tumor sections of head and neck cancers with markers for vessels, perfusion, hypoxia, and proliferation, it becomes apparent that the tumor vasculature intimately shapes the microenvironment. Acute hypoxia is observed near vessels that were not recently perfused (though perfusion fluctuates and the acute hypoxia soon moves elsewhere), and chronic hypoxia is observed at a distance from perfused blood vessels. Chronic hypoxia according to staining of pimonidazole began at distances between 75 and 125 μm from vessels, while chronic hypoxia according to CA9 expression began at distances between 40 and 140 μm from vessels, with the difference largely reflecting their different oxygen tension thresholds for binding and expression. The distance from blood vessels to the onset of necrosis varied from 80 to 300 μm. The distance from blood vessels to the onset of chronic hypoxia, observed by staining or expression of a hypoxic marker, depends on the blood oxygenation and the metabolic demands of the tumor cells. The distance from blood vessels to the onset of necrosis depends on these factors and the tolerance of the tumor cells to hypoxia. Chronic hypoxia and necrosis are observed closer to vessels in tumors than in normal tissue because the blood oxygenation is less in tumors, and tumor cells typically have increased metabolic demands. Thus, the vascular density in the tumor does not need to be less than that in normal tissue for chronic hypoxia to occur.

In practice, acute hypoxia and chronic hypoxia are limited to the least vascularized regions of tumors for head and neck cancers. In these regions, there was an increase in staining of hypoxia markers and a corresponding decrease in staining of proliferation markers with increasing distance from the vessels. Microscopic regions of necrosis were also observed at large distances from vessels. The decrease in proliferation may possibly be attributed to a decreasing growth fraction (as hypoxic cells are held up at cell cycle checkpoints) and lengthening of the duration of the G_1 phase of the cell cycle. Thus, tumor cells become more radioresistant further from the vessels as more of them are hypoxic and more are found in the relatively radioresistant G_1 phase. Contrastingly, in vascular hotspots, there was little hypoxia staining and no clear spatial relationship between proliferation staining and the vessels.

Since the morphology of the tumor vasculature strongly affects the tumor microenvironment, the tumor vasculature should ideally be included in models that simulate tumor growth and tumor response to irradiation. This is especially necessary when modeling poorly oxygenated tumors like those of head and neck cancers. Such radiotherapy models are highly valuable for their insight, utility, and predictive powers. They may be used to determine the most effective radiotherapy treatment schedule for a given set of tumor properties. It is hoped they will lead to better customization of radiotherapy treatment plans on an individual patient basis by accounting for interpatient variations in tumor properties. Indeed, some radiotherapy models have been developed that include a basic representation of the tumor vasculature,[59,60] but since the vasculature can have such a strong effect, it is important that it be modeled as realistically as possible. Accurate simulation of the tumor vasculature will also be important in exploring and optimizing vascular targeting treatment techniques. It is hoped that the quantitative vasculature morphology data compiled within will assist with the modeling efforts to come.

Disclosure

The authors report no conflicts of interest in this work.

References

1. Gimbrone MA Jr, Leapman SB, Cotran RS, Folkman J. Tumor dormancy in vivo by prevention of neovascularization. *J Exp Med*. 1972;136(2):261–276.
2. Pilat MJ, McCormick J, LoRusso PM. Vascular targeting agents. *Curr Oncol Rep*. 2004;6(2):103–110.
3. Park HJ, Griffin RJ, Hui S, et al. Radiation-induced vascular damage in tumors: implications of vascular damage in ablative hypofractionated radiotherapy (SBRT and SRS). *Radiat Res*. 2012;177(3):311–327.
4. El Kaffas A, Giles A, Czarnota GJ. Dose-dependent response of tumor vasculature to radiation therapy in combination with sunitinib depicted by three-dimensional high-frequency power Doppler ultrasound. *Angiogenesis*. 2013;16(2):443–454.
5. Franks KN, Jain P, Snee MP. Stereotactic ablative body radiotherapy for lung cancer. *Clin Oncol (R Coll Radiol)*. 2015;27(5):280–289.
6. Musunuru HB, Loblaw A. Clinical trials of stereotactic ablative radiotherapy for prostate cancer: updates and future direction. *Future Oncol*. 2015;11(5):819–831.
7. Karam SD, Bhatia S. The radiobiological targets of SBRT: tumor cells or endothelial cells? *Ann Transl Med*. 2015;3(19):290.

8. Allen BJ, Huang C-Y, Clarke RA. Targeted alpha anticancer therapies: update and future prospects. *Biologics*. 2014;4(8):255–267.
9. Butterworth KT, McMahon SJ, Currell FJ, Prise KM. Physical basis and biological mechanisms of gold nanoparticle radiosensitization. *Nanoscale*. 2012;4(16):4830–4838.
10. Lin Y, Paganetti H, McMahon SJ, Schuemann J. Gold nanoparticle induced vasculature damage in radiotherapy: comparing protons, megavoltage photons, and kilovoltage photons. *Med Phys*. 2015;42(10):5890–5902.
11. Becker A, Hänsgen G, Bloching M, Weigel C, Lautenschläger C, Dunst J. Oxygenation of squamous cell carcinoma of the head and neck: comparison of primary tumors, neck node metastases, and normal tissue. *Int J Radiat Oncol Biol Phys*. 1998;42(1):35–41.
12. Algire GH, Chalkley HW. Vascular reactions of normal and malignant tissues in vivo. I. Vascular reactions of mice to wounds and to normal and neoplastic transplants. *J Natl Cancer Inst*. 1945;6(1):73–85.
13. Folkman J. Tumor angiogenesis. *Adv Cancer Res*. 1985;43(1):175–203.
14. Chalkley HW. Method for the quantitative morphologic analysis of tissues. *J Natl Cancer Inst*. 1943;4(1):47–53.
15. Jain RK. Molecular regulation of vessel maturation. *Nat Med*. 2003;9(6):685–693.
16. Eddy HA, Casarett GW. Development of the vascular system in the hamster malignant neurilemmoma. *Microvasc Res*. 1973;6(1):63–82.
17. Yamaura H, Sato H. Quantitative studies on the developing vascular system of rat hepatoma. *J Natl Cancer Inst*. 1974;53(5):1229–1240.
18. Peters W, Teixeira M, Intaglietta M, Gross JF. Microcirculatory studies in rat mammary carcinoma. I. Transparent chamber method, development of microvasculature, and pressures in tumor vessels. *J Natl Cancer Inst*. 1980;65(3):631–642.
19. Boucher Y, Leunig M, Jain RK. Tumor angiogenesis and interstitial hypertension. *Cancer Res*. 1996;56(18):4264–4266.
20. Endrich B, Hammersen F, Götz A, Messmer K. Microcirculatory blood flow, capillary morphology, and local oxygen pressure of the hamster amelanotic melanoma A-Mel-3. *J Natl Cancer Inst*. 1982;68(3):475–485.
21. Vajkoczy P, Schilling L, Ullrich A, Schmiedek P, Menger MD. Characterization of angiogenesis and microcirculation of high-grade glioma: an intravital multifluorescence microscopic approach in the athymic nude mouse. *J Cereb Blood Flow Metab*. 1998;18(5):510–520.
22. Leu AJ, Berk DA, Lymboussaki A, Alitalo K, Jain RK. Absence of functional lymphatics within a murine sarcoma: a molecular and functional evaluation. *Cancer Res*. 2000;60(16):4324–4327.
23. Goldacre RJ, Sylven B. On the access of blood-borne dyes to various tumour regions. *Br J Cancer*. 1962;16(1):306–322.
24. Tozer GM, Lewis S, Michalowski A, Aber V. The relationship between regional variations in blood flow and histology in a transplanted rat fibrosarcoma. *Br J Cancer*. 1990;61(2):250–257.
25. Tannock IF, Steel GG. Quantitative techniques for study of the anatomy and function of small blood vessels in tumors. *J Natl Cancer Inst*. 1969;42(5):771–782.
26. Fallowfield ME. Vascular volume in B16 allografts and human melanoma xenografts estimated by means of Hoechst 33342. *J Pathol*. 1989;157(3):249–252.
27. Rubin P, Casarett G. Microcirculation of tumors part I: anatomy, function, and necrosis. *Clin Radiol*. 1966;17(3):220–229.
28. Deane BR, Lantos PL. The vasculature of experimental brain tumours. Part 1. A sequential light and electron microscope study of angiogenesis. *J Neurol Sci*. 1981;49(1):55–66.
29. Vogel AW. Intratumoral vascular changes with increased size of a mammary adenocarcinoma: new method and results. *J Natl Cancer Inst*. 1965;34(5):571–578.
30. Hilmas DE, Gillette EL. Morphometric analyses of the microvasculature of tumors during growth and after x-irradiation. *Cancer*. 1974;33(1):103–110.
31. Wijffels KIEM, Kaanders JHAM, Rijken PFJW, et al. Vascular architecture and hypoxic profiles in human head and neck squamous cell carcinomas. *Br J Cancer*. 2000;83(5):674–683.
32. Pazouki S, Chisholm DM, Adi MM, et al. The association between tumour progression and vascularity in the oral mucosa. *J Pathol*. 1997;183(1):39–43.
33. Sawatsubashi M, Yamada T, Fukushima N, Mizokami H, Tokunaga O, Shin T. Association of vascular endothelial growth factor and mast cells with angiogenesis in laryngeal squamous cell carcinoma. *Virchows Arch*. 2000;436(3):243–248.
34. Pignataro L, Carboni N, Midolo V, et al. Clinical relevance of microvessel density in laryngeal squamous cell carcinomas. *Int J Cancer*. 2001;92(5):666–670.
35. Shieh YS, Lee HS, Shiah SG, Chu YW, Wu CW, Chang LC. Role of angiogenic and non-angiogenic mechanisms in oral squamous cell carcinoma: correlation with histologic differentiation and tumor progression. *J Oral Pathol Med*. 2004;33(10):601–606.
36. Li C, Shintani S, Terakado N, et al. Microvessel density and expression of vascular endothelial growth factor, basic fibroblast growth factor, and platelet-derived endothelial growth factor in oral squamous cell carcinomas. *Int J Oral Maxillofac Surg*. 2005;34(5):559–565.
37. Shieh YS, Hung YJ, Hsieh CB, Chen JS, Chou KC, Liu SY. Tumor-associated macrophage correlated with angiogenesis and progression of mucoepidermoid carcinoma of salivary glands. *Ann Surg Oncol*. 2009;16(3):751–760.
38. Sharma B, Sriram G, Saraswathi TR, Sivapathasundharam B. Immunohistochemical evaluation of mast cells and angiogenesis in oral squamous cell carcinoma. *Indian J Dent Res*. 2010;21(2):260–265.
39. Mohtasham N, Babakoohi S, Salehinejad J, et al. Mast cell density and angiogenesis in oral dysplastic epithelium and low- and high-grade oral squamous cell carcinoma. *Acta Odontol Scand*. 2010;68(5):300–304.
40. Weidner N, Semple JP, Welch WR, et al. Tumor angiogenesis and metastasis – correlation in invasive breast carcinoma. *N Engl J Med*. 1991;324(1):1–8.
41. Davey KJ, Perrier S, Ohe G, et al. Assessment of vascularity as an index of angiogenesis in periradicular granulomas. Comparison with oral carcinomas and normal tissue counterparts. *Int Endod J*. 2008;41(11):987–996.
42. Schor AM, Pendleton N, Pazouki S, et al. Assessment of vascularity in histological sections: effects of methodology and value as an index of angiogenesis in breast tumours. *Histochem J*. 1998;30(12):849–856.
43. Hagedorn HG, Nerlich AG. Microvessel density and endothelial basement membrane composition in laryngeal squamous cell carcinomas. *Acta Otolaryngol*. 2000;120(7):891–898.
44. Amelink A, Kaspers OP, Sterenborg HJ, van der Wal JE, Roodenburg JL, Witjes MJ. Non-invasive measurement of the morphology and physiology of oral mucosa by use of optical spectroscopy. *Oral Oncol*. 2008;44(1):65–71.
45. Amelink A, Sterenborg HJ, Bard MP, Burgers SA. In vivo measurement of the local optical properties of tissue by use of differential path-length spectroscopy. *Opt Lett*. 2004;29(10):1087–1089.
46. Thomlinson RH, Gray LH. The histological structure of some human lung cancers and the possible implications for radiotherapy. *Br J Cancer*. 1955;9(4):539–549.
47. Tannock IF. The relation between cell proliferation and the vascular system in a transplanted mouse mammary tumour. *Br J Cancer*. 1968;22(2):258–273.
48. Hirst DG, Denekamp J. Tumour cell proliferation in relation to the vasculature. *Cell Tissue Kinet*. 1979;12(1):31–42.
49. Gross MW, Karbach U, Groebe K, Franko AJ, Mueller-Klieser W. Calibration of misonidazole labeling by simultaneous measurement of oxygen tension and labeling density in multicellular spheroids. *Int J Cancer*. 1995;61(4):567–573.
50. Chou SC, Azuma Y, Varia MA, Raleigh JA. Evidence that involucrin, a marker for differentiation, is oxygen regulated in human squamous cell carcinomas. *Br J Cancer*. 2004;90(3):728–735.
51. Wykoff CC, Beasley NJ, Watson PH, et al. Hypoxia-inducible expression of tumor-associated carbonic anhydrases. *Cancer Res*. 2000;60(24):7075–7083.

52. Hoogsteen IJ, Lok J, Marres HA, et al. Hypoxia in larynx carcinomas assessed by pimonidazole binding and the value of CA-IX and vascularity as surrogate markers of hypoxia. *Eur J Cancer*. 2009;45(16):2906–2914.
53. Beasley NJ, Wykoff CC, Watson PH, et al. Carbonic anhydrase IX, an endogenous hypoxia marker, expression in head and neck squamous cell carcinoma and its relationship to hypoxia, necrosis, and microvessel density. *Cancer Res*. 2001;61(13):5262–5267.
54. Bussink J, Kaanders JH, Rijken PF, Martindale CA, van der Kogel AJ. Multiparameter analysis of vasculature, perfusion and proliferation in human tumour xenografts. *Br J Cancer*. 1998;77(1):57–64.
55. Ljungkvist AS, Bussink J, Rijken PF, Kaanders JH, van der Kogel AJ, Denekamp J. Vascular architecture, hypoxia, and proliferation in first-generation xenografts of human head-and-neck squamous cell carcinomas. *Int J Radiat Oncol Biol Phys*. 2002;54(1):215–228.
56. Wijffels KIEM, Hoogsteen IJ, Lok J, et al. No detectable hypoxia in malignant salivary gland tumors: preliminary results. *Int J Radiat Oncol Biol Phys*. 2009;73(5):1319–1325.
57. Porschen R, Classen S, Piontek M, Borchard F. Vascularization of carcinomas of the esophagus and its correlation with tumor proliferation. *Cancer Res*. 1994;54(2):587–591.
58. Schor AM, Pazouki S, Morris J, Smither RL, Chandrachud LM, Pendleton N. Heterogeneity in microvascular density in lung tumours: comparison with normal bronchus. *Br J Cancer*. 1998;77(6):946–951.
59. Borkenstein K, Levegrun S, Peschke P. Modeling and computer simulations of tumor growth and tumor response to radiotherapy. *Radiat Res*. 2004;162(1):71–83.
60. Harting C, Peschke P, Borkenstein K, Karger CP. Single-cell-based computer simulation of the oxygen-dependent tumour response to irradiation. *Phys Med Biol*. 2007;52(16):4775–4789.

2.3 Discussion and Conclusion

It was interesting to find that hypoxia does not typically arise in tumours of HNSCC due to a diminished vessel density; conversely, the vessel density is usually greater in tumours than in normal tissue. Rather, it is due to decreased oxygen levels in the blood (chronic hypoxia) and temporally inhibited blood flow (acute hypoxia). This occurs because there are imbalanced factors (e.g. vascular endothelial growth factor), producing immature and deformed vessels, with no proper system of flow through artery→arteriole→capillary→venule→vein, and there are high interstitial pressures that squash and occlude vessels. The tumour growth model developed in Chapter 4 makes particular use of the findings that, in tumours of HNSCC, the relative vascular volume (RVV) varies from 2 to 10% and the distance from vessels to the onset of necrosis (necrosis distance; ND) varies from 80 to 300 μm.

3

Background on radiobiological modelling and the Geant4 Monte Carlo toolkit

3.1 Introduction

This chapter provides background for the computational models developed in this thesis, with which we aim to predict the response of a tumour to a course of radiotherapy, taking into account properties of the tumour (e.g. hypoxia) and details of the treatment (e.g. fractionation schedule). Since the modelling must incorporate radiobiological mechanisms, a glossary of the most important radiobiological effects is provided for completeness. Justification is then given for a transition from deterministic to stochastic models of radiotherapy. One way to incorporate a stochastic element is by performing the irradiation using Monte Carlo track structure simulations. This was done in the current work (see Chapters 6 and 7) using the Geant4 toolkit. Relevant background is provided on Geant4 and its low-energy extension Geant4-DNA. Particular attention is paid to the chemistry module of Geant4-DNA, which was used to simulate water radiolysis and the indirect effect of ionising radiation.

3.2 The Rs of radiobiology

Predicting clinical outcomes of radiotherapy treatments is a challenging endeavour that implores the simulation of many complicated physical, chemical and biological mechanisms. The principle biological mechanisms involved in the radiation response are captured in the "Rs of radiobiology" [57–60]:

- **Repair** of sub-lethal DNA damage in tumour stem cells (and normal stem cells).
- **Repopulation** as surviving stem cells divide and regrow the tumour (and normal tissue), e.g., by loss of asymmetry in stem cell division.
- **Redistribution** of cells in the cell cycle. In tumour cells, genes, such as p53, that regulate cell cycle checkpoints may be mutated and the checkpoints absent. This, combined with the phase of the cell cycle affecting radiosensitivity, may give rise to different distributions of cell cycle phases between tumour and normal cell populations. This may affect tumour and normal tissue radiosensitivities to a subsequent fractional dose.
- **Reoxygenation** of the tumour after irradiation. The tumour shrinks and surviving (radioresistant) hypoxic cells gain better access to the oxygen and other nutrients in the blood.
- **Radiosensitivity** of cells, which is dictated by exogenous factors such as pO_2 as well as endogenous factors pertaining to the genome (e.g. mutated DNA repair pathways, cell cycle checkpoints, signal transduction) and the cell cycle phase (cells in S-phase are more radioresistant than cells in G_2 or mitosis).

Additional Rs have also been proposed, including [61, 62]:

- **Dose-rate effect**, which denotes the increase in isoeffective dose with decreasing dose rate. This is because at low dose rates, repair of DNA damage (and other biological processes; the first four Rs) occurs during irradiation.

- **(Remote) bystander effects**, referring to the observation that cells can die from irradiation of neighbouring cells, possibly because irradiated cells secrete factors and transfer harmful molecules (long-lived reactive oxygen species) via gap-junctions.

3.3 Deterministic versus stochastic radiobiological models

Radiobiological models may broadly be categorised as deterministic or stochastic. Deterministic models (a.k.a. analytic models) solve for a set of equations and are typically fast. Stochastic models take a different approach that involves sampling from one or more random probability distributions. A stochastic approach is more appropriate when the process being modelled is itself stochastic in nature, as is the case for radiation interactions with matter, for example. While stochastic models of stochastic phenomena can achieve greater accuracy and utility than deterministic models, it is at the expense of increased computation time.

The most renowned radiobiological model, the Linear Quadratic (LQ) model, is deterministic. It relates the surviving fraction of cells, S, to the dose delivered, D:

$$S = e^{-\alpha D - \beta D^2} \tag{3.1}$$

The LQ model often provides a good fit to experimental data of clonogenic cell survival for certain values of the α and β parameters. Note that this is a macroscopic model that arose from curve fitting [63], but there can be radiobiological meaning attached to it relating to microscopic processes (see Chapter 7). It overestimates the effect at high doses ($\gtrsim$ 10 Gy), where the true response becomes linear (possibly associated with vasculature damage, immunological effects or breakdown of the Poisson assumption) [64–68].

If the dose is delivered in n fractions, each of dose d ($D = nd$), the LQ model becomes:

$$S = e^{-n(\alpha d + n\beta d^2)} \tag{3.2}$$

This allows for tentative comparison between different fractionation schedules, but noting that repopulation between dose fractions is neglected. Improvements have been suggested in the form of a time parameter and additional terms to account for repair, repopulation, redistribution and reoxygenation [45, 69]. However, a purely deterministic model may be too restrictive and inappropriate for tackling the highly complex and inherently stochastic processes in radiotherapy.

A radiobiological model of radiotherapy is an excellent candidate for stochastic methods. In this thesis, such a model is developed that is stochastic in tumour cell modelling, meaning each cell is modelled individually with stochastic elements (e.g. spatial coordinates of cells, cell cycle times, asymmetric vs symmetric stem cell division), and uses Monte Carlo track structure simulations for modelling the radiation effect. The remainder of this chapter describes how Monte Carlo (stochastic) track structure is simulated in Geant4.

3.4 The Geant4 Monte Carlo toolkit

Simulating the passage of a particle (e.g. an electron) through matter (e.g. water) using Monte Carlo methods generally consists of calculating the probability of interaction for all of the possible physics processes available to it given the material it is in (e.g. electron ionisation in water), and then selecting one of these processes to occur based on randomly sampling the interaction probabilities [44]. This is repeated for the next physics process and so on, tracking the particle until it stops or leaves the simulation volume. Some physics processes generate secondary particles and these are tracked in the same way.

The prototypical code for Monte Carlo track structure simulation in the low-energy domain of radiobiology/medical physics is Friedland et al's PARTRAC (Particle Tracks) [46, 54, 70, 71]. However, this code is not publically available. Another excellent code in the field of radiobiology is RITRACKS (Relativistic Ion Tracks), developed by I. Plante [72, 73], which can be used but not developed.[1]

[1]RITRACKS may be obtained in black box form from NASA upon request: `https://software.nasa.gov`

The (private) KUBEC code is also eminent in the radiobiological domain [74]. Other codes include PITS [75], NOREC [76], MC4 [77], TRIOL [78], CPA100 [79], MOCA [80], PROTON and DELTA [81].

The track structure simulations in this project were performed using the Monte Carlo toolkit Geant4 [38–40, 82]. Geant4 is open-source (all of its code is accessible), free to download, regularly updated and routinely verified. It is written in C++ and, thanks to its object-oriented modular structure, it is easy for users to develop their own unique applications to meet their specific needs. While it was originally developed for high energy physics, it has found application in other fields including space radiation and medical physics.

The basic structure of Geant4 is as follows. Please refer to the user and developer guides available on the official Geant4 website [82] for more comprehensive details. Note that names of C++ classes will be written in purple and names of C++ functions will be written in orange. A Geant4 application requires, at minimum, the following classes (in addition to the main() function):

- **DetectorConstruction**: Constructs the simulation geometry by placing volumes of different shapes and materials in different positions and orientations. Geometries from atomistic DNA structure to a high energy physics detector can be achieved in this way (Figure 3.1).

- **PhysicsList**: Defines the physics processes to mediate particle interactions with materials. For each process (e.g. electron ionisation in water), there are multiple models to choose from; some alternative and some complementary (e.g. Moller-Bhabha, Livermore, Penelope, Born, Emfietzoglou and CPA100 ionisation models). The physics list can be constructed piece-wise from scratch or there are pre-made physics lists to choose from depending on the application (the energy range).

- **PrimaryGeneratorAction**: Specifies the source(s) of particles, including the particle type, energy distribution, position, direction and shape.

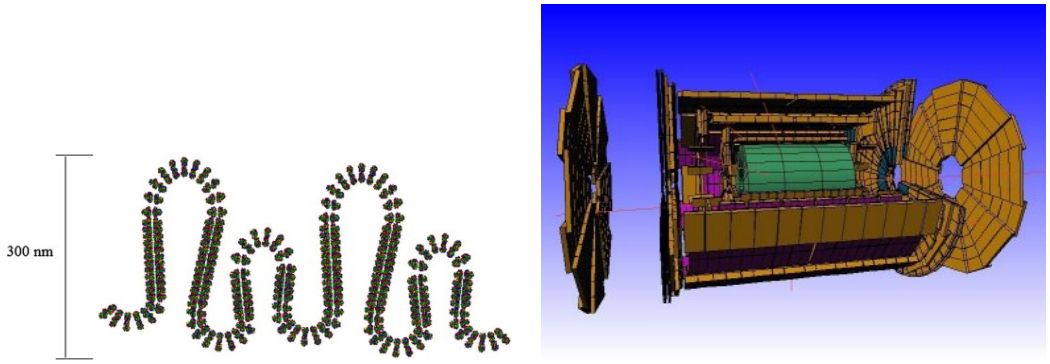

(a) (b)

Figure 3.1: Examples of geometries simulated in Geant4. (a) Atomistic chromatin fibre loop. Reprinted from Nuclear Instruments and Methods in Physics Research B, 346, Tajik M, Rozatian ASH, Semsarha F, Calculation of direct effects of ^{60}Co gamma rays on the different DNA structural levels: A simulation study using the Geant4-DNA toolkit, pp 53-60, Copyright 2015 [50], with permission from Elsevier. (b) ATLAS detector at the Large Hadron Collider, CERN [83].

- **ActionInitialization**: Defines the user action classes (see below) to be invoked during the simulation (including the mandatory PrimaryGeneratorAction).

As alluded to, there are several optional user action classes, which are useful for extracting information about the simulation. They include:

- **RunAction:** The "run" refers to the sum of all the primary particles, i.e., the whole simulation. The RunAction class has member functions PreUserRunAction and PostUserRunAction. They enable user actions before and after the run, respectively (e.g. initialise a data analysis tool in Pre and write the data to a file in Post).

- **EventAction:** Each primary particle is called an "event". The Pre & PostUserEventAction functions enable user actions before and after each event (e.g. query the state of the random number generator engine for the upcoming event in Pre).

- **TrackingAction:** A "track" stores the current information of a particle, including dynamic quantities (energy, momentum, position, time, etc.) and static quantities (charge, mass, etc.). The Pre & PostUserTrackingAction

functions enable user actions at the beginning and end of tracks (e.g. accessing the initial and final energies of particles).

- **SteppingAction:** A track can only be changed by a process and each change occurs in a "step". A step contains information about which process is responsible for it, the coordinates and volumes at the beginning and the end of the step and the changes in energy and momentum in the step. The UserSteppingAction function enables user actions during each step (e.g. accessing any of the above information about steps).

The free-to-download Geant4 software includes a large number of example applications. These range from beginner to advanced level and perform different tasks. They demonstrate the impressive capabilities of Geant4 and how to make use of them in your own application. The examples often include visualisation, achieved with software such as OpenGL [84] and DAWN [85]. Note that names of example applications will be written as ≪**example**≫.

3.5 The low energy extension Geant4-DNA

Geant4-DNA is the low energy extension of Geant4, developed for modelling early biological damage induced by ionising radiation at the DNA scale [41–43, 86]. It uses many of the same interaction cross sections as PARTRAC and similar simulation techniques. Geant4-DNA is divided into physics and chemistry compartments.

3.5.1 Geant4-DNA physics

Geant4-DNA physics is unique (compared to the other physics lists in Geant4) in that it uses discrete, step-by-step (a.k.a event-by-event) processes, as opposed to condensed history processes, and electrons are tracked in this manner down to eV energies. Figure 3.2 illustrates the difference between the Livermore physics list (which is relatively low energy) and Geant4-DNA physics. The difference is critical, as there is biological effect at the end of the electron track (the "sting in the tail" [87]). A limitation of Geant4-DNA, however, is that it currently only simulates interactions

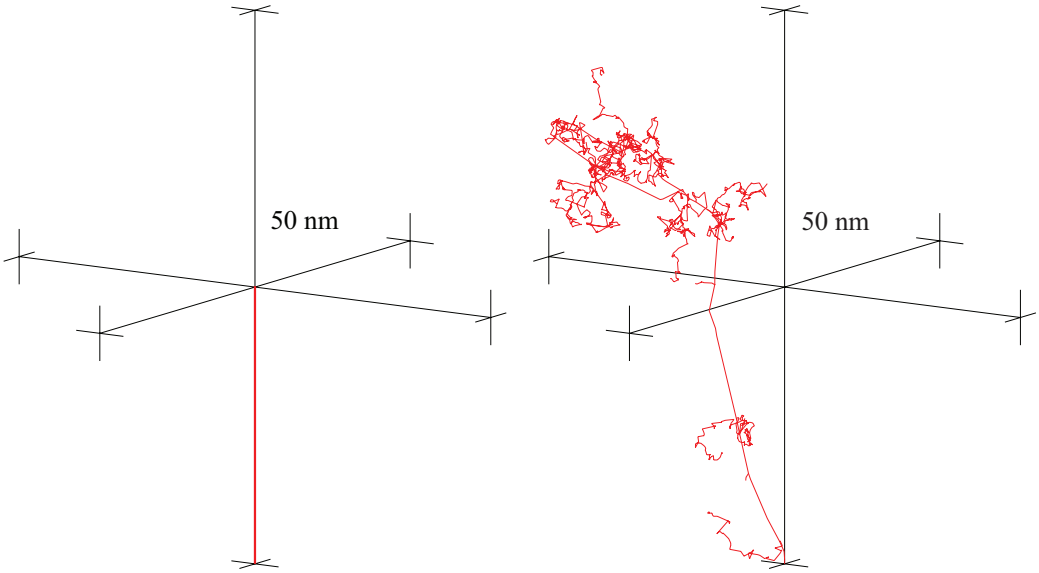

(a) Livermore physics **(b)** Geant4-DNA physics

Figure 3.2: Comparison of Livermore versus Geant4-DNA physics lists for tracking an electron (red) in water, with initial energy 1 keV and initial direction up the page. The three scale bars are mutually orthogonal and each 50 nm long.

in liquid water (of variable density). In other words, real biological molecules and proteins, such as DNA, cannot yet be modelled. Instead, geometries representing these molecules and proteins but containing liquid water are typically modelled.

Geant4-DNA physics can be used to simulate ionisations and excitations of water molecules in a DNA geometry (the so-called "direct effect" of ionising radiation) and of bound water molecules in the first hydration layer of DNA (the "quasi-direct effect"). The direct and quasi-direct effects are collectively termed "direct-type effects". There is also the "indirect effect", whereby radiation interacts with water to produce radical[2] species that in turn react with DNA (more in Chapter 6). The chemistry module of Geant4-DNA simulates water radiolysis, allowing for consideration of the indirect effect.

3.5.2 Geant4-DNA chemistry

Water radiolysis is simulated in Geant4-DNA in temporal stages [88]. Virtual time is denoted by t.

[2]A radical is an atom or molecule with an unpaired electron and is highly reactive.

Physical stage ($t < 10^{-16}$ s)

Electrons are tracked through the water medium as they undergo physical interactions including elastic scattering, ionisation ($H_2O \longrightarrow H_2O^+ + e^-$), electronic excitation ($H_2O \longrightarrow H_2O^*$) and dissociative attachment ($H_2O + e^- \longrightarrow H_2O^-$). The result is a spatial distribution of H_2O^+, H_2O^*, H_2O^- and e^- as spheres or point-like objects along the electron track.

Physicochemical stage ($10^{-16} < t < 10^{-12}$ s)

Disocciation or relaxation of water ions and molecules (process name "H2O_DNAMolecularDecay" of class G4DNAMolecularDecay) produces various radical species, e.g.:

$$H_2O^+ \longrightarrow H_3O^+ + {}^\bullet OH \tag{3.3}$$

$$H_2O^* \longrightarrow {}^\bullet OH + H^\bullet \tag{3.4}$$

$$H_2O^- \longrightarrow {}^\bullet OH + OH^- + H_2 \tag{3.5}$$

H_2O^* and H_2O^+ may also undergo electron hole recombination (process class G4DNAElectronHoleRecombination). Each e^- is surrounded by a cage of water ($e^- + H_2O \longrightarrow e^-_{aq}$) becoming a "solvated" or "aqueous" (aq) electron. The result is a spatial distribution of ${}^\bullet OH$, e^-_{aq}, $H^\bullet$, OH^-, H_3O^+ and H_2 as spheres or point-like objects along the electron track.

Chemical stage ($10^{-12} < t < 10^{-6}$ s)

The various chemical species diffuse away from the initial electron track under Brownian motion (process class G4DNABrownianTransportation) (Figure 3.3). For Brownian motion in 3D, the root-mean-square displacement (RMSD) after a time t is:

$$\text{RMSD} = \sqrt{6Dt} \tag{3.6}$$

where D is the diffusion coefficient. The diffusion coefficients used in Geant4-DNA for the various chemical species are shown in Table 3.1. If two molecules are potential

Table 3.1: Difussion coefficients in Geant4-DNA [88].

Chemical species	Diffusion coefficient D (10^{-9} m^2s^{-1})
e^-_{aq}	4.9
$^\bullet OH$	2.8
$H^\bullet$	7.0
H_3O^+	9.0
H_2	4.8
OH^-	5.0
H_2O_2	2.3

reactants and the distance between them becomes less than the reaction radius, a chemical reaction occurs. The possible reactions modelled in Geant4-DNA are:

$$^\bullet OH + {}^\bullet OH \longrightarrow H_2O_2 \tag{3.7}$$

$$^\bullet OH + e^-_{aq} \longrightarrow OH^- \tag{3.8}$$

$$^\bullet OH + H^\bullet \longrightarrow \text{no product} \tag{3.9}$$

$$H_3O^+ + e^-_{aq} \longrightarrow H^\bullet \tag{3.10}$$

$$e^-_{aq} + e^-_{aq} \longrightarrow OH^- + OH^- + H_2 \tag{3.11}$$

$$e^-_{aq} + H^\bullet \longrightarrow OH^- + H_2 \tag{3.12}$$

$$H^\bullet + H^\bullet \longrightarrow H_2 \tag{3.13}$$

$$H_3O^+ + OH^- \longrightarrow \text{no product} \tag{3.14}$$

$$e^-_{aq} + H_2O_2 \longrightarrow OH^- + {}^\bullet OH \tag{3.15}$$

Note that these reactions tend to decrease the number of radicals over time. Colliaux et al [89], using a different code, also simulated molecules of O_2 and reactions involving O_2.

The simulation technique for the chemical stage

As mentioned above, molecules diffuse during the chemical stage according to Brownian motion. The transportation method implemented in Geant4-DNA is [90]:

$$x(t_0 + \tau) = x_0 + \left.\frac{F(x_0)}{m\gamma}\right|_{t_o} \cdot \tau + \sqrt{2D\tau} \cdot N(0,1) + \mathcal{O}(\tau^2) \tag{3.16}$$

where:

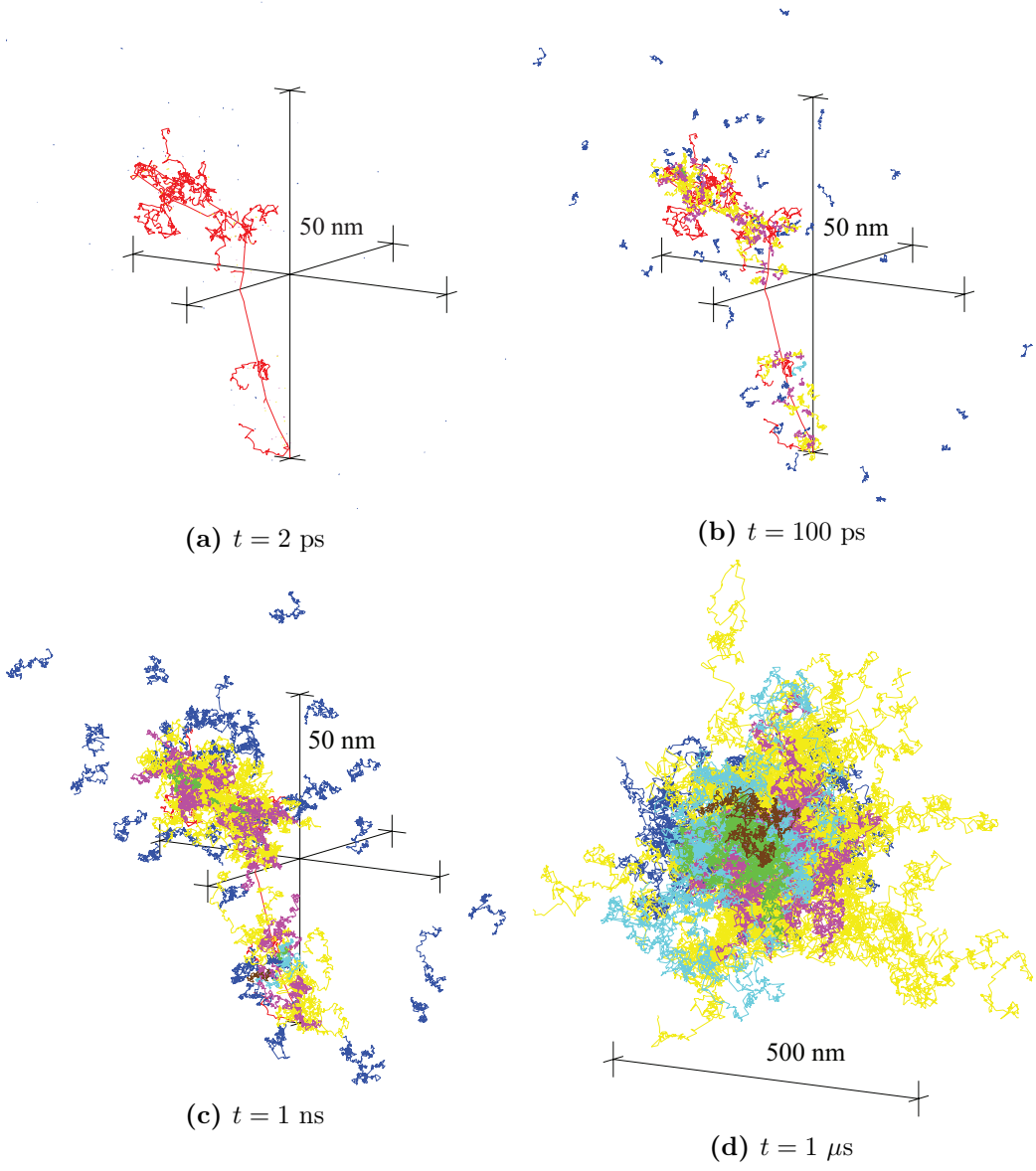

(a) $t = 2$ ps **(b)** $t = 100$ ps

(c) $t = 1$ ns **(d)** $t = 1$ μs

Figure 3.3: Time evolution of the chemical stage in Geant4-DNA for a 1 keV electron track (red) in water. The chemical species diffuse away from the electron track as virtual time progresses. Chemical species shown: $^{\bullet}OH$ (magenta), H_3O^+ (yellow), e^-_{aq} (blue), H_2O_2 (green), $H^{\bullet}$ (cyan) and H_2 (brown) (OH^- not shown).

- t_0 is the initial time,
- τ is the time interval,
- x_0 is the initial position,
- F is the external force,
- m is the mass,
- γ is the friction constant,
- D is the diffusion coefficient, and
- $N(0,1)$ is a random number described by a Gaussian distribution of mean 0 and variance 1.

The simulation of the chemical stage uses the Step-By-Step (SBS) method. Using this method, all chemical species are stepped (with randomised Brownian transport) in the same (virtual) time steps. After a time step, if two reactants are separated by less than the reaction radius, a reaction occurs.

The question then arises as to what time steps to use? With larger time steps, there is more chance of missing reactions, while smaller time steps require more computation time (and the Smoluchowski equation is not valid if the time step is less than the relaxation time of velocity - see [90]). The developers of PARTRAC noted that the molecules are closest together at the beginning of the chemical stage and move further apart as time goes on, so reactions become less likely over time [71]. Accordingly, they proposed time steps that start small and get larger as the virtual time progresses.

To improve upon this approach of static time steps, a method of dynamic time steps was developed. A time step, t_D, is defined for a given pair of reactants as the time during which no reaction will occur, with 95% confidence. This is referred to as the "maximum diffusion time without reaction" or the "minimum encounter time". The minimum encounter time is calculated for each possible reaction using the closest pair of reactants, and the smallest t_D is used for the time step. With

Table 3.2: Conventional minimum time steps for the chemical stage in Geant4-DNA.

Virtual time (ps)	Minimum time step (ps)
$1 - 10$	0.1
$10 - 10^2$	1
$10^2 - 10^3$	3
$10^3 - 10^4$	10
$10^4 - 10^6$	10^2

this approach of dynamic time steps, the time steps should naturally become larger as virtual time goes on and it is unlikely that reactions will be missed.

The downside of dynamic time steps is that before a reaction occurs, there will be smaller and smaller time steps as the pair of reactants move closer and closer together, thus increasing the computation time. To overcome this limitation, Geant4-DNA uses a combination of dynamic and static time steps, as follows. It introduces a minimum time step, t_{limit}, which is a function of the virtual time (Table 3.2). If the smallest t_D is less than t_{limit}, all pairs of reactants with $t_D < t_{limit}$ are recorded and then all molecules are diffused for a time step of t_{limit}. For those pairs of reactants that previously had $t_D < t_{limit}$, if after the time step their separation distance is (again) greater than the reaction radius, there is a possibility that their separation distance was less than the reaction radius for some time during the time step. The likelihood of this is calculated using the Brownian bridge technique (see [90] for details) and a reaction may be simulated in retrospect.

The Independent Reaction Time (IRT) method is an alternative to the Step-By-Step method. It is an event-driven simulation in which a reaction occurs at every time step. Reactions are decided at the creation of molecules, without modelling diffusion. RITRACKS offers both SBS and IRT [72].

3.5.3 How to implement Geant4-DNA

To use DNA physics and chemistry in a Geant4 application requires the following (as demonstrated in example ≪**chem1**≫):

1. Register DNA physics and chemistry in the PhysicsList.cc file, as shown in Listing 3.1.

   Listing 3.1: Registering Geant4-DNA physics and chemistry in PhysicsList.cc (C++).

```
#include <PhysicsList.hh>
#include <G4EmDNAPhysics.hh>
#include <G4EmDNAChemistry.hh>
...
PhysicsList::PhysicsList()
: G4VModularPhysicsList()
{
  ...
  RegisterPhysics(new G4EmDNAPhysics());
  RegisterPhysics(new G4EmDNAChemistry());
}
```

   Alternatively, activate DNA physics and chemistry only in a given G4Region using the member function AddDNA of class G4EmParameters (see example ≪**neuron**≫).

2. Implement a StackingAction that instructs the program to begin simulating chemistry (the physicochemical and chemical stages) when the physical stage ends, as shown in Listing 3.2.

   Listing 3.2: The necessary StackingAction.cc to use Geant4-DNA chemistry (C++).

```
#include <StackingAction.hh>
#include <G4StackManager.hh>
#include <G4DNAChemistryManager.hh>
...
void StackingAction::NewStage()
{
  if(stackManager->GetNTotalTrack() == 0) //all physical tracks
    have been processed
  {
    G4DNAChemistryManager::Instance()->Run(); //begin chemistry
  }
}
```

3. Notify your program of the StackingAction by including it in your ActionInitialization (Listing 3.3).

   Listing 3.3: Modifying the ActionInitialization.cc to use Geant4-DNA chemistry (C++).

```
#include <ActionInitialization.hh>
```

```
#include <StackingAction.hh>
...
void ActionInitialization::Build() const
{
  ...
  SetUserAction(new StackingAction());
  ...
}
```

The user may change the minimum time steps used in the chemical stage in a TimeStepAction.cc file (Listing 3.4).

Listing 3.4: Setting the minimum time steps for the chemical stage in TimeStepAction.cc (Geant4-DNA) (C++).

```
#include <TimeStepAction.hh>
...
TimeStepAction::TimeStepAction() : G4UserTimeStepAction()
{
  AddTimeStep(1*picosecond, 0.1*picosecond);
  AddTimeStep(10*picosecond, 1*picosecond);
  AddTimeStep(100*picosecond, 3*picosecond);
  AddTimeStep(1000*picosecond, 10*picosecond);
  AddTimeStep(10000*picosecond, 100*picosecond);
  /*
   * E.g. from 1 picosecond to 10 picosecond, the minimum time
   * step is 0.1 picosecond.
   */
}
```

The user can also change the duration of the chemical stage in the ActionInitialization (Listing 3.5):

Listing 3.5: Adjusting the duration of the chemical stage in ActionInitialization.cc (Geant4-DNA) (C++).

```
#include <ActionInitialization.hh>
#include <G4DNAChemistryManager.hh>
#include <G4Scheduler.hh>
...
void ActionInitialization::Build() const
{
  ...
  if(G4DNAChemistryManager::IsActivated())
  {
    ...
    // Uncomment to stop the chemical stage after
    // ...a given number of time steps:
    //G4Scheduler::Instance()->SetMaxNbSteps(50);

    // ...or reaching this virtual time:
    G4Scheduler::Instance()->SetEndTime(1*nanosecond);
  }
}
```

The example ≪**chem3**≫ demonstrates user interactivity with the chemical tracks via TimeStepAction.cc, ITTrackingAction.cc and ITSteppingAction.cc files. The TimeStepAction class permits user interaction in-between time steps and after chemical reactions with its member functions UserPostTimeStepAction and UserReactionAction, respectively. The ITTrackingAction and ITSteppingAction classes are analogous to TrackingAction and SteppingAction for chemical tracks rather than physical tracks.

Finally, some miscellaneous pieces of advice relating to Geant4-DNA chemistry:

- If the user wishes to unnaturally kill a chemical track (e.g., to simulate additional scavenging), they may do so in the ITTrackingAction or ITSteppingAction. It was this user's experience (using Geant4 version 10.4) that chemical tracks are best killed in the PreUserTrackingAction of ITTrackingAction to avoid a G4Exception or segmentation fault, as demonstrated in Listing 3.6.

  Listing 3.6: Safely killing a chemical track in ITTrackingAction.cc (Geant4-DNA) (C++).

```
#include <ITTrackingAction.hh>
#include <G4Track.hh>
...
void
ITTrackingAction::
PreUserTrackingAction(const G4Track* track)
{
//if( /*some condition is met*/ )
//{
    G4Track* tr = (G4Track*) track;
    tr->SetTrackStatus(fKillTrackAndSecondaries);
//}
}
```

- Energy deposition should be scored in the (physical) SteppingAction or via a primitive scorer (like in example ≪**RE02**≫). These two methods give the same result and they do not receive a contribution from DNA chemistry. Energy deposition should not be scored in the ITSteppingAction, where there will very rarely be energy deposited due to non-dissociative relaxation of H_2O.

- Colleagues and I have had issues with a G4Exception occasionally occurring called "Outside of mother volume". It reports that a "Product has been

placed outside of the volume containing the mother molecule". This can be commented out in G4DNAMolecularDisssociation.cc, seemingly without detriment.

3.6 Summary

The current chapter has provided an overview of the radiobiological principles and software tools employed in the computational models that follow. The principal radiobiological effects described were carefully considered in the development of the cellular tumour growth model, described in Chapters 4 and 5, and impacted the DNA damage and radiation-induced cell kill modelling in Chapters 6 and 7. Background was provided on the simulation of ionising radiation from first principles with Monte Carlo track structure. The elegant structure of Geant4 was described, along with the sophisticated simulation of physical tracks and radiolytic chemical tracks in Geant4-DNA. These technical details should assist the reader in Chapters 6 and 7, where the Geant4-DNA software is applied.

4

Development of an in silico stochastic 4D model of tumor growth with angiogenesis

The publication [91] forms the basis of this chapter:

Forster JC, Douglass MJ, Harriss-Phillips WM, Bezak E. Development of an in silico stochastic 4D model of tumor growth with angiogenesis. *Med Phys.* 2017 Apr; 44(4):1563-1576. doi: 10.1002/mp.12130.

4.1 Introduction and Motivation

This is the first of two publications on the HNSCC tumour growth model. The model is spatio-temporal, multicellular and includes tumour angiogenesis. This paper describes the development of the model, including a detailed description of the computational methods. Other tumour growth models in the literature are briefly reviewed in the Introduction. The main goals for the model were: randomised cell positions, tumour growth by cell division (including an epithelial cell hierarchy), and growth of a connected network of blood vessels interwoven between the cells. Chronic hypoxia and necrosis were simulated in the tumour.

4.2 Statement of Contribution

4.2.1 Conception

The model methods were conceived by Jake Forster under the supervision of Michael Douglass, Wendy Phillips and Eva Bezak, based on their previous work and the idea of a spatial-temporal multicellular tumour model.

4.2.2 Realisation

Jake Forster developed the model (i.e. wrote the code), wrote the code to run the simulations to acquire data, wrote the code to run the simulations on a supercomputer, ran the simulations on a supercomputer, analysed the data and made the plots for visualising data. The manuscript was evaluated by Eva Bezak, Wendy Phillips and Michael Douglass for data accuracy, critical appraisal, conclusions reached and general structure and flow.

4.2.3 Documentation

The manuscript was primarily written by Jake Forster, who also prepared the figures. Wendy Phillips, Michael Douglass and Eva Bezak provided input, feedback and revisions.

Statement of Authorship

Title of Paper	Development of an in silico stochastic 4D model of tumor growth with angiogenesis
Publication Status	☑ Published ☐ Accepted for Publication ☐ Submitted for Publication ☐ Unpublished and Unsubmitted work written in manuscript style
Publication Details	Forster JC, Douglass MJ, Harriss-Phillips WM, Bezak E. *Med Phys*. 2017; 44(4):1563-1576. doi: 10.1002/mp.12130.

Principal Author

Name of Principal Author (Candidate)	Jake Cameron Forster		
Contribution to the Paper	Conceived of the model methods, developed the model (i.e. wrote the code), wrote the code to run the simulations to acquire data, wrote the code to run the simulations on a supercomputer, ran the simulations on a supercomputer, analysed the data, made the plots for visualising data, wrote the manuscript, prepared the figures and acted as the corresponding author.		
Overall percentage (%)	80%		
Certification:	This paper reports on original research I conducted during the period of my Higher Degree by Research candidature and is not subject to any obligations or contractual agreements with a third party that would constrain its inclusion in this thesis. I am the primary author of this paper.		
Signature		Date	3-10-2018

Co-Author Contributions

By signing the Statement of Authorship, each author certifies that:

i. the candidate's stated contribution to the publication is accurate (as detailed above);

ii. permission is granted for the candidate in include the publication in the thesis; and

iii. the sum of all co-author contributions is equal to 100% less the candidate's stated contribution.

Name of Co-Author	Prof. Eva Bezak		
Contribution to the Paper	Initial idea, general supervision and guidance and manuscript revisions.		
Overall percentage (%)	10%		
Signature		Date	3-10-2018

Name of Co-Author	Dr Wendy Phillips		
Contribution to the Paper	Initial idea, general supervision and guidance and manuscript revisions.		
Overall percentage (%)	5%		
Signature		Date	3-10-2018

Name of Co-Author	Dr Michael Douglass		
Contribution to the Paper	Initial idea, general supervision and guidance and manuscript revisions.		
Overall percentage (%)	5%		
Signature		Date	4-10-2018

Development of an *in silico* stochastic 4D model of tumor growth with angiogenesis

Jake C. Forster,[a] Michael J.J. Douglass, and Wendy M. Harriss-Phillips
Department of Physics, University of Adelaide, North Terrace, Adelaide, South Australia 5005, Australia
Department of Medical Physics, Royal Adelaide Hospital, North Terrace, Adelaide, South Australia 5000, Australia

Eva Bezak
Sansom Institute for Health Research and School of Health Sciences, Division of Health Sciences, University of South Australia, Adelaide, South Australia 5001, Australia
Department of Physics, University of Adelaide, North Terrace, Adelaide, South Australia 5005, Australia

(Received 4 October 2016; revised 10 December 2016; accepted for publication 18 January 2017; published 22 March 2017)

Purpose: A stochastic computer model of tumour growth with spatial and temporal components that includes tumour angiogenesis was developed. In the current work it was used to simulate head and neck tumour growth. The model also provides the foundation for a 4D cellular radiotherapy simulation tool.
Methods: The model, developed in Matlab, contains cell positions randomised in 3D space without overlap. Blood vessels are represented by strings of blood vessel units which branch outwards to achieve the desired tumour relative vascular volume. Hypoxic cells have an increased cell cycle time and become quiescent at oxygen tensions less than 1 mmHg. Necrotic cells are resorbed. A hierarchy of stem cells, transit cells and differentiated cells is considered along with differentiated cell loss. Model parameters include the relative vascular volume (2–10%), blood oxygenation (20–100 mmHg), distance from vessels to the onset of necrosis (80–300 μm) and probability for stem cells to undergo symmetric division (2%). Simulations were performed to observe the effects of hypoxia on tumour growth rate for head and neck cancers. Simulations were run on a supercomputer with eligible parts running in parallel on 12 cores.
Results: Using biologically plausible model parameters for head and neck cancers, the tumour volume doubling time varied from 45 $\pm$ 5 days (n = 3) for well oxygenated tumours to 87 $\pm$ 5 days (n = 3) for severely hypoxic tumours.
Conclusions: The main achievements of the current model were randomised cell positions and the connected vasculature structure between the cells. These developments will also be beneficial when irradiating the simulated tumours using Monte Carlo track structure methods. © *2017 American Association of Physicists in Medicine* [https://doi.org/10.1002/mp.12130]

Key words: cancer, cancer stem cell, doubling time, head and neck, hypoxia, stochastic

1. INTRODUCTION

Models of tumor growth can be broadly classified as analytic or stochastic. Analytic models[1–3] are relatively fast computationally, but have limitations when modeling inherently stochastic processes. Stochastic models typically treat each cell in the tumor individually and the tumor grows by cell division. Stochastic models have been the models of choice in the last two decades following advancements in computing power.

Stochastic models of tumor growth may be purely temporal, i.e., without a spatial component. This can save greatly on computation time while still enabling important features of tumor growth to be simulated. For example, the stochastic temporal model of head and neck squamous cell carcinoma (HNSCC) by Harriss-Phillips et al.[4–6] featured a hierarchy of different cell types including stem cells, transit cells, and differentiated cells and a sophisticated system of transitions to progress cells through the hierarchy. It simulated both symmetric and asymmetric division of stem cells and loss of differentiated cells from the tumor. The model also simulated each phase of the cell cycle as well as quiescence due to hypoxia. The model by Appleton et al.[7] is another example of a purely temporal stochastic growth model that simulated the phases of the cell cycle and a hierarchy of cell types for the mouse oral epithelium.

Spatial stochastic models, on the other hand, generate a tumor composed of a two-dimensional (2D) or three-dimensional (3D) spatial distribution of tumor cells. The simplest form of distribution is a regular cubic lattice of cell positions. This approach has been common in tumor growth models.[8–15] However, the lattice method produces artificial anisotropies in space. For example, there are straight line paths from one end of the geometry to the other that pass through practically no cellular material. This could be a limitation for certain applications. For example, it could produce artifacts if the simulated tumors are spatially irradiated in Monte Carlo particle tracking simulations. A purely spatial and spatially isotropic tumor model was developed by Douglass et al.[16–18] which modeled ellipsoid shaped cells of different sizes randomly distributed in

3D space without overlap. Another spatially isotropic approach was employed in the tumor growth model by Kansal et al.,[19] in which the tumor was partitioned into cells according to a Voronoi diagram.

Additional properties of tumors that tumor growth models have endeavored to incorporate are hypoxia and necrosis. Hypoxia has been observed to reduce cell proliferation in tumors by decreasing the proportion of cycling cells and increasing the cell cycle time (CCT).[20,21] Severely hypoxic cells become necrotic and are eventually resorbed. The previously mentioned temporal model by Harriss-Phillips et al.[4–6] included the simulation of hypoxia. It adjusted the CCT for hypoxic cells and induced cell quiescence below a threshold cellular oxygenation (pO_2). However, it is desirable for tumor models to be spatial in order to model hypoxia and necrosis from a more fundamental standpoint.

In living tissue, hypoxic cells are typically located beyond some distance from the blood vessels and necrotic cells are located further again. Accordingly, tumor cell pO_2 is often treated in models as a function of distance from the nearest blood vessel.[22–25] Therefore to model tumor growth with hypoxia and necrosis, models should ideally possess both temporal and spatial components (i.e., spatio-temporal models) and include tumor angiogenesis to dynamically generate a spatial tumor vasculature.

For example, a stochastic spatio-temporal tumor growth model with angiogenesis was developed by Kocher et al.,[10] with tumor cells and blood vessel units confined to positions in a regular 3D lattice. Hypoxia was simulated 100 μm from the vessels. New vessel units formed by angiogenesis from existing ones in order to maintain a certain vessel density in the tumor. However, the vessel units were scattered incoherently rather than forming continuous vessel structures in the tumor. One limitation this presents is that the degree of vascularity in the tumor does not relate to the amount of hypoxia in the same way as it would if the vessel units were in a connected vasculature structure, like in real tumors.

Another spatio-temporal model with angiogenesis was developed by Borkenstein et al.[13] and later adapted by Harting et al.[14] This model had similar limitations as the Kocher et al. model, namely cell and vessel units were in a regular lattice and the vessel units were randomly scattered. But rather than angiogenesis occurring in response to diminished vessel density, it occurred in response to hypoxia. Hypoxic cells excreted vascular endothelial growth factor and angiogenesis occurred after a certain amount of factor accumulated at a vessel unit.

Cai et al.[15] developed a model that likewise simulated angiogenesis in response to hypoxia. In addition, the vessel units formed continuous vessels in a connected vasculature structure. However, the tumor cells and the vasculature were generated in two different spaces and were effectively overlaid as if they were transparent. This is a limitation for certain applications (e.g., if the intention is to irradiate the simulated tumors using Monte Carlo track structure methods). Cells and vessel units were also confined to regular lattice positions.

In this work, we describe the development of a new stochastic spatio-temporal tumor growth model with a novel approach to angiogenesis. The model is designed to simulate HNSCC. It extends the work of previous models[26,27] and addresses some of the limitations of existing spatio-temporal models. In particular, in this work, ellipsoid-shaped cells occupy randomized positions in 3D and a connected vasculature structure grows between the cells. These developments will also be beneficial in future work when the tumors generated are spatially irradiated using Monte Carlo track structure methods. Herein we describe the computational methods employed in the model and present its first results, including tumor doubling times for well-oxygenated and severely hypoxic tumors of HNSCC.

2. MATERIALS AND METHODS

2.A. Model features and biological background

The tumor growth model presented in this work was developed in Matlab and is designed to model HNSCC. While some features of the model are specific to HNSCC, the model is capable of simulating other cancer types after making appropriate parameter modifications. The flow chart in Fig. 1 outlines the various spatial and temporal features of the model and how they are interconnected. In this section, each of these features are described and justified with the relevant biological background. The details of how they were implemented in the tumor growth algorithm are described in the computational methods section (Section 2) that follows.

2.A.1. 3D placement of cells

In the model, 3D tumor cells are packed into randomized positions in 3D space without overlap. Ellipsoids are used for the cell shape, consistent with the shape of squamous cells. Cells have major axis sizes ranging from 14 to 20 μm (FaDu HNSCC cell line[28]) and contain internal structures including the cytoplasm and nucleus, as shown in Fig. 2. The ellipsoidal cells have randomized orientations. The internal structures are coaxial with the cell and their sizes are fixed proportions of the cell size. The nucleus volume is 8% of the cell volume.[29]

2.A.2. Cell division and cell hierarchy

Tumor growth is simulated through cell division. Each cell is allocated a CCT which is the time between divisions. Upon division, one daughter cell occupies the position of the parent cell and the other daughter cell occupies an adjacent position, which usually involves pushing neighboring cells outwards towards the tumor periphery. Cell division is typically accompanied by cellular differentiation, whereby cells become more specialized in their functionality but lose proliferative potential. A basic epithelial cell hierarchy is implemented consisting of stem cells (S), three generations of transit cells

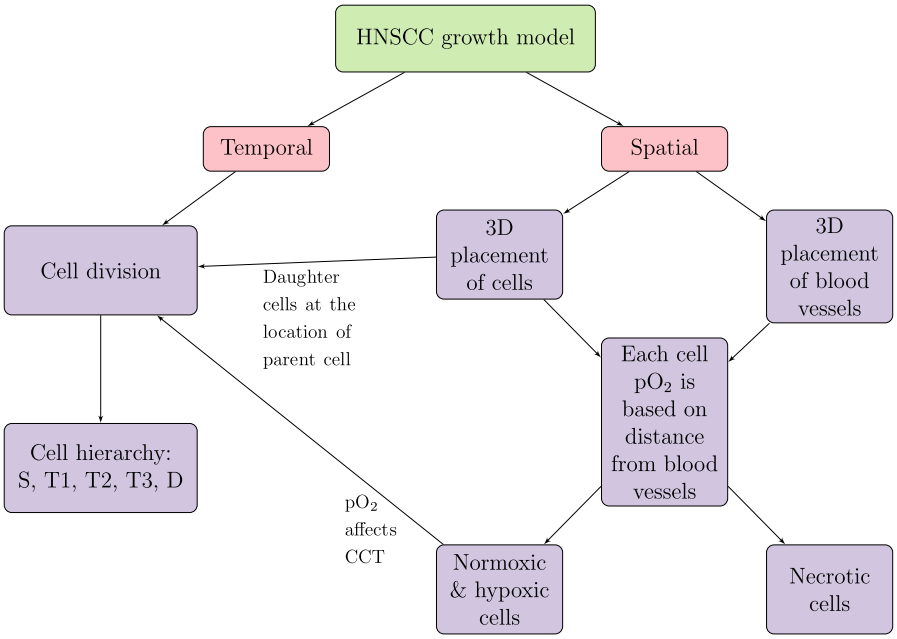

FIG. 1. Main features of the newly developed HNSCC tumour growth model. [Color figure can be viewed at wileyonlinelibrary.com]

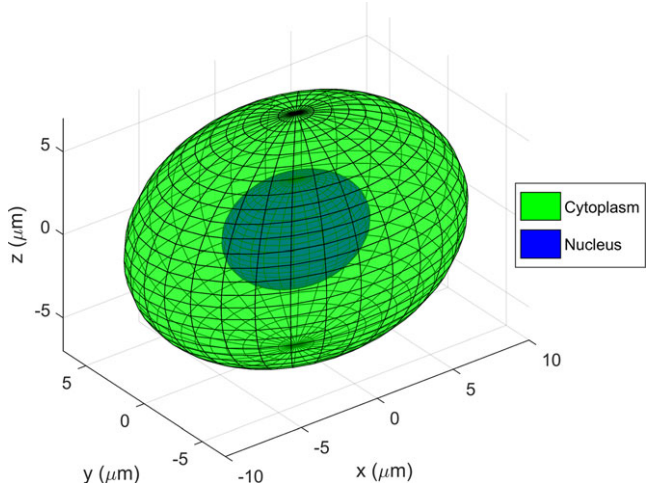

FIG. 2. Tumor cells are modeled as ellipsoids to represent squamous cells. The cells contain internal structures with different chemical compositions.[27] [Color figure can be viewed at wileyonlinelibrary.com]

(T1, T2, and T3), and differentiated cells (D).[26] An S may either divide into two Ss (symmetric division) or one S and one T1 (asymmetric division). The probability for stem cells to undergo symmetric division is set to 2%,[26] but this may become higher than 50% for HNSCCs regrowing after irradiation during accelerated repopulation.[30–32] A T1 divides into two T2s, a T2 into two T3s and a T3 into two Ds (Fig. 3). This is at present a basic system of cell hierarchy. With HNSCC, the loss of differentiated cells due to cell death (natural sloughing or apoptosis) is simulated using an *in vivo* reported differentiated cell loss factor of 80%.[26,33,34] This means that after a time equivalent to the CCT, a differentiated cell has an 80% chance of dying and being removed from the tumor. If it survives, it has the same likelihood of dying after another CCT passes.

2.A.3. 3D placement of blood vessels

The simulated tumor contains a network of blood vessels growing between the tumor cells. Vessels are represented by "strings" of discrete spherical vessel units. The diameter of the vessel units ranges from 14 to 20 μm, in line with the diameters of the dilated capillary-like vessels observed in tumors.[35,36] The vasculature structure that develops is chaotic, as is the case in real tumors, in contrast with the spatially regular, organized, and efficient vasculature found in normal tissue.[37] Various degrees of tumor vascularity may be simulated, i.e., different amounts of vessel branching. The relative vascular volume (RVV) in the tumor is manipulated via the model parameter RVV_0. Measurements of the RVV in human HNSCC have yielded values between 2 and 10%.[36,38]

2.A.4. Hypoxia and its effect on the CCT

Chronic hypoxia is simulated beyond a certain distance from the blood vessels as follows. The cellular pO_2 is taken to be the oxygen tension at the center of the cell. The oxygen tension, p, is calculated using the distance, r, to the nearest blood vessel unit:[23,25]

$$p(r) = p_0 \frac{\mathrm{ND}^2}{R_0^2}\left(2\ln\left(\frac{\mathrm{ND}}{r}\right) - 1 + \frac{r^2}{\mathrm{ND}^2}\right) \quad (1)$$

where p_0 is the oxygen tension at the vessel wall, the necrosis distance, ND, is the distance between vessels and the onset of necrosis and R_0 is a constant defined by:

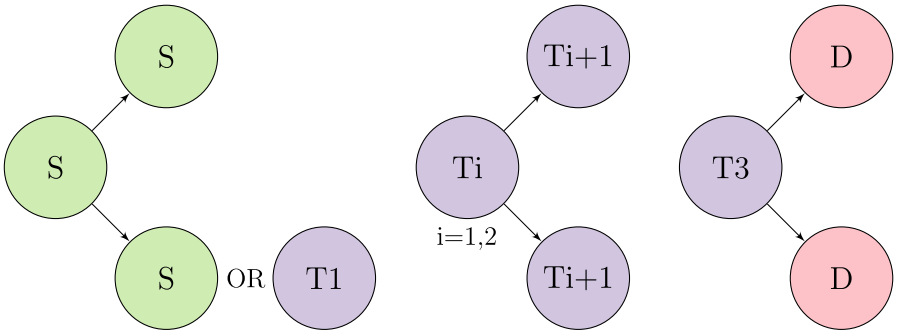

FIG. 3. Cell division and progression through the cell hierarchy. S denotes a stem cell, T1, T2, and T3 are three generations of transit cells and D denotes a differentiated cell. [Color figure can be viewed at wileyonlinelibrary.com]

$$R_0^2 = \mathrm{ND}^2\left(2\ln\left(\frac{\mathrm{ND}}{a}\right) - 1\right) \tag{2}$$

The parameter a is the vessel radius and is set to 10 μm (the maximum radius of vessel units). Studies of HNSCC have reported observing values of ND from 80 to 300 μm.[24,39] Values of blood oxygenation, p_0, from 20 to 100 mmHg are considered, noting that the oxygenations of healthy artery and venule blood are 100 and 40 mmHg, respectively,[40] and blood vessels in tumors can suffer from sluggish flow resulting in lower than normal blood oxygenation.[35,36]

Hypoxic cells have an increased CCT in the model.[41–44] For HNSCC, the CCT under normoxic conditions follows the Gaussian distribution:[26,34]

$$\mathrm{CCT}_0 = 33 \pm 5.9 \text{ h} \tag{3}$$

The CCT is increased for hypoxic cells according to the following adjustment factor y, which is a function of the cellular pO_2:[21,26,45]

$$y(\mathrm{pO}_2) = 1 + 1.8\, e^{-0.2\mathrm{pO}_2} \tag{4}$$

where the cellular pO_2 is in units of mmHg. That is, the CCT is:

$$\mathrm{CCT}(\mathrm{pO}_2) = \mathrm{CCT}_0 \times y(\mathrm{pO}_2) \tag{5}$$

Studies have also shown that cells may enter the quiescent G_0 phase under severely hypoxic conditions, e.g., below 1 mmHg.[46–48] This is accounted for in the model by making the CCT infinite at cellular $\mathrm{pO}_2 < 1$ mmHg. The CCT adjustment factor then becomes:

$$y(\mathrm{pO}_2) = \begin{cases} 1 + 1.8\, e^{-0.2\mathrm{pO}_2}, & \mathrm{pO}_2 \geq 1 \\ \infty, & 0 < \mathrm{pO}_2 < 1 \end{cases} \tag{6}$$

Note that a cell in a quiescent position with infinite CCT does not stay there for long before being pushed into a different position, often moving further from vessels and becoming necrotic (see Section 4). Fig. 4 illustrates the cellular pO_2 and CCT adjustment factor as a function of distance from the nearest blood vessel, calculated using Eqs. (1)–(6).

Before tumor growth is simulated by cell division, the structure of the vasculature that will grow out during tumor growth is established (with a unique randomized vasculature

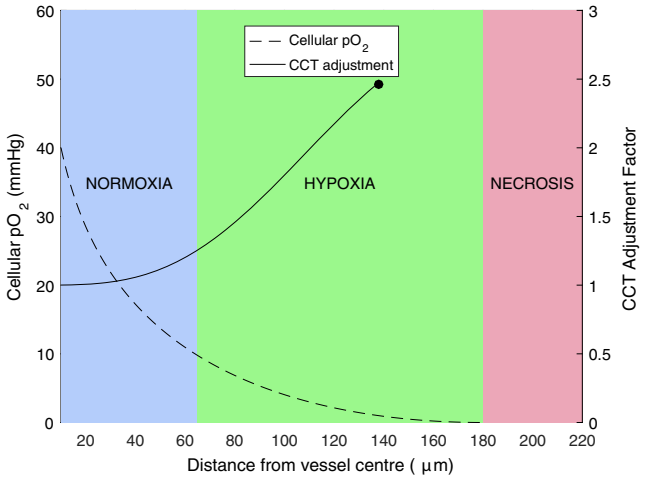

FIG. 4. Cellular pO_2 decreases and CCT increases with increasing distance from the nearest blood vessel. In this example using $p_0 = 40$ mmHg and ND = 180 μm, the increase in CCT becomes noticeable when cells are further than 65 μm from a vessel and cells become quiescent beyond 140 μm. Cells in the region labeled "hypoxia" are viable but have $\mathrm{pO}_2 < 10$ mmHg and would likely stain positive for the hypoxia marker pimonidazole.[49,50] [Color figure can be viewed at wileyonlinelibrary.com]

structure generated in each simulation). That is, the tumor cells move positions during the simulation but the vessel units do not. Thus, it is possible to precalculate the oxygen tension at each cell position and, in turn, the CCT at each cell position. When a cell moves positions relative to the blood vessels, its pO_2 changes and its CCT changes accordingly, but it retains its age. So the time remaining before it divides (= CCT−age) will have changed. In this way, cells have a dynamic CCT in the model that reflects their instantaneous pO_2.

2.A.5. Necrotic cells

If during the tumor growth simulation a cell is pushed to a distance beyond ND from a blood vessel to where the oxygen tension is insufficient to keep it alive, the cell becomes necrotic. After a time, the necrotic cell is resorbed by the tumor. The time taken for the necrotic cell to be resorbed depends on the local necrotic volume, defined as the proportion of the cell positions within a 28 μm radius that are likewise occupied by necrotic cells (i.e., the number of necrotic cells within

TABLE I. Model input parameters and values for HNSCC.

Input parameter	Values	Type	References
Cell (and blood vessel) diameter	14–20 μm	Distribution	[28]
RVV	2–10%	Single value	[36,38]
Oxygen tension	$p(r) = p_0 \frac{\mathrm{ND}^2}{R_0^2}(2\ln(\frac{\mathrm{ND}}{r}) - 1 + \frac{r^2}{\mathrm{ND}^2})$	Distribution	[23,25]
p_0	20–100 mmHg	Single value	[36,40]
ND	80–300 μm	Single value	[24,39]
CCT under normoxia	33 $\pm$ 5.9 h (Gaussian)	Distribution	[26,34]
CCT adjustment factor with hypoxia	$y(\mathrm{pO_2}) = 1 + 1.8\,e^{-0.2\mathrm{pO_2}}$	Distribution	[21,26,45]
Hypoxia-induced quiescence	<1 mmHg	Single value	[46–48]
Necrotic cell resorption time	3–6 d depending on local necrotic volume	Distribution	[13,14]
S symmetric division probability	$\sim$ 2% before irrad., possibly > 50% after	Single value	[26]
Differentiated cell loss factor	80%	Single value	[26,34]

28 μm divided by the number of cell positions within 28 μm $\times$ 100%). The necrotic cell resoprtion time follows Gaussian distributions with means of 3, 4, 5, and 6 days for local necrotic volumes between 0–25%, 25–50%, 50–75%, and 75–100% respectively, and in each case, the standard deviation is an eighth of the mean.[13,14] This means that necrotic cells in large volumes of necrosis take longer to be resorbed than those interspersed among living cells. When a necrotic cell moves positions during tumor growth (e.g., it may be pushed outwards due to cell division), its resorption time is recalculated based on the new local necrotic volume but it retains its age.

The model parameters and their values for HNSCC are summarized in Table I.

2.B. Computational methods

This section describes the computational methods employed in the model to achieve spatial and temporal cellular tumor growth with angiogenesis. The layout of the program is shown in Fig. 5.

2.B.1. Generate 3D mesh

To begin, a 3D coordinate mesh containing all positions that tumor cells and blood vessel units may occupy is established. During the tumor growth simulation, the tumor grows larger as more positions in the mesh become occupied by cells and vessel units. Rather than confining mesh positions to a regular lattice, they are randomized while ensuring that cells and vessel units do not overlap with one another.

The following algorithm was developed to fill a given volume with nonoverlapping cell/vessel unit positions:

1. X, Y and Z coordinates are randomly chosen within the volume to be filled.
2. If a sphere of radius $R_{\mathrm{cell,min}} = 7\,\mu$m could be placed at that position without overlapping with the spheres at positions already placed, this is a successful placement.
3. If the placement has been successful, the sphere radius is then increased in increments of 0.1 μm up to a maximum radius of $R_{\mathrm{cell,max}} = 10\,\mu$m. After each increment, it is checked whether the sphere now overlaps with any of the spheres at positions already placed. If overlap has occurred, the sphere radius is reduced to its previous value at which there is no overlap. The final sphere radius is then stored along with the position coordinates.
4. Steps 1–3 are repeated until there fails to be a successful placement for a certain number of consecutive attempts (see below), indicating that a sufficient density has been reached.

The computation time for this algorithm increases dramatically with the size of the volume being filled. Consequently, the total spherical tumor volume of radius $R_{\mathrm{tum,max}}$ is divided into shells of thickness:

$$\Delta R_{\mathrm{shell}} = 2R_{\mathrm{cell,max}} + 1 = 21\mu\mathrm{m} \tag{7}$$

Shells are filled with cell/vessel unit positions one at a time from the origin outward. This shell thickness is chosen so that when placing a position in the shell, overlap need only be checked with existing positions in the current shell and in the previous shell. As the shell volume grows larger further from the origin, shells are further divided into increments of polar angle, θ, and azimuthal angle, ϕ, such that the outer arc lengths are Δl = 11 μm, as shown in Fig. 6. Thus ultimately cell/vessel unit positions are placed in subvolumes of size:

$$V \lesssim \Delta R_{\mathrm{shell}} \Delta l^2 = 2541\ \mu\mathrm{m}^3 \tag{8}$$

The following formula is used to set the maximum number of consecutive failed position placements before moving on to the next subvolume:

$$n = \mathrm{ceil}\left(10 \times \left(\frac{\text{subvolume size}}{\text{minimum sphere volume}}\right)\right) \tag{9}$$

$$= \mathrm{ceil}\left(10 \times \left(\frac{\Delta R_{\mathrm{shell}} \Delta l^2}{\frac{4}{3}\pi R_{\mathrm{cell,min}}^3}\right)\right) = 18 \tag{10}$$

where ceil is the ceiling function.

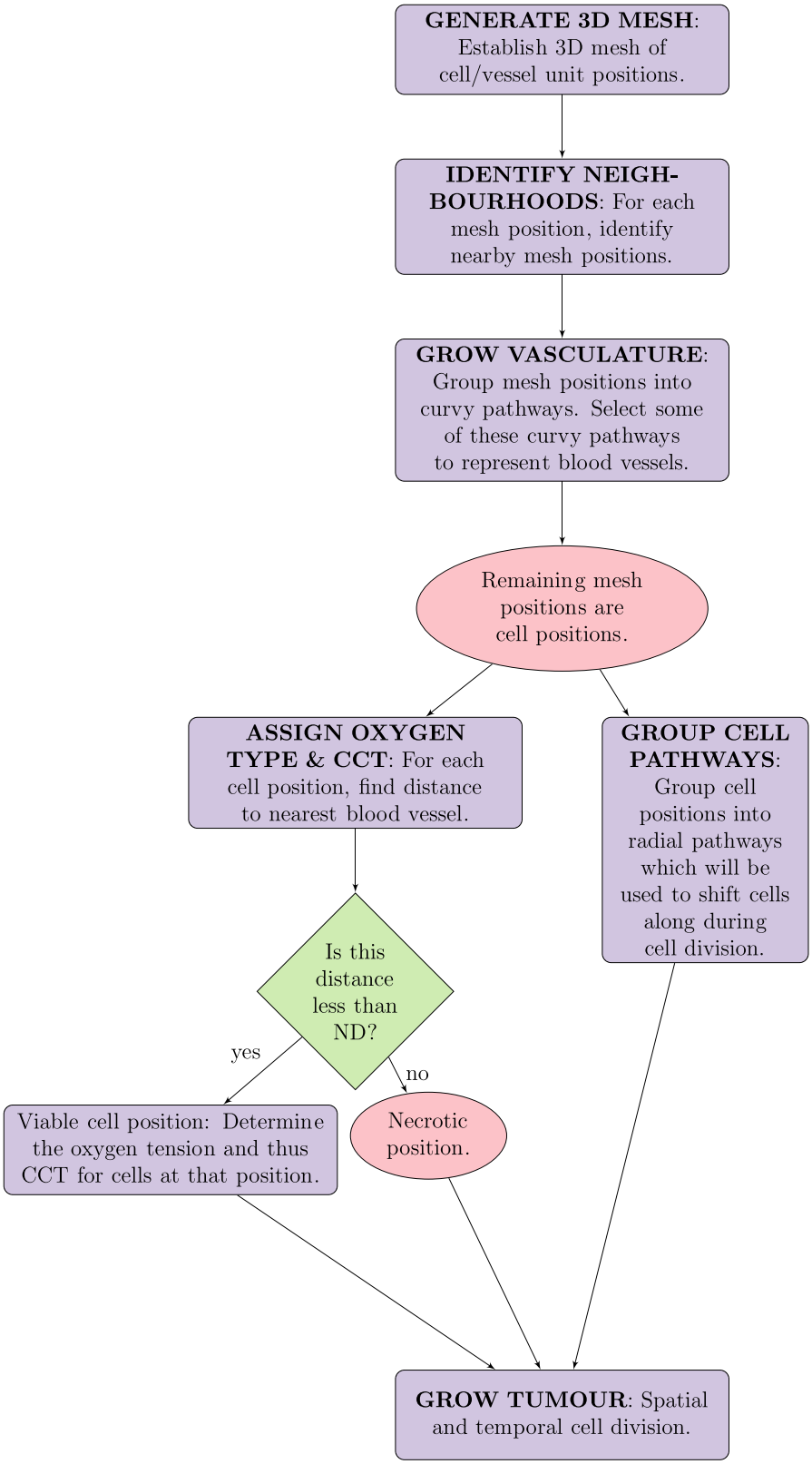

FIG. 5. Overview of the program structure. [Color figure can be viewed at wileyonlinelibrary.com]

The result is a 3D mesh of randomized cell/vessel unit positions, each with an assigned cell/vessel unit radius which limits the size of the ellipsoidal cell or spherical vessel unit that occupies that position, thereby ensuring no overlap occurs (Fig. 7). For ellipsoidal cells the semimajor axis of the ellipsoid is equal to the radius assigned to that position and the other semi-axes lengths are randomly assigned between 7 μm and the semimajor axis length.

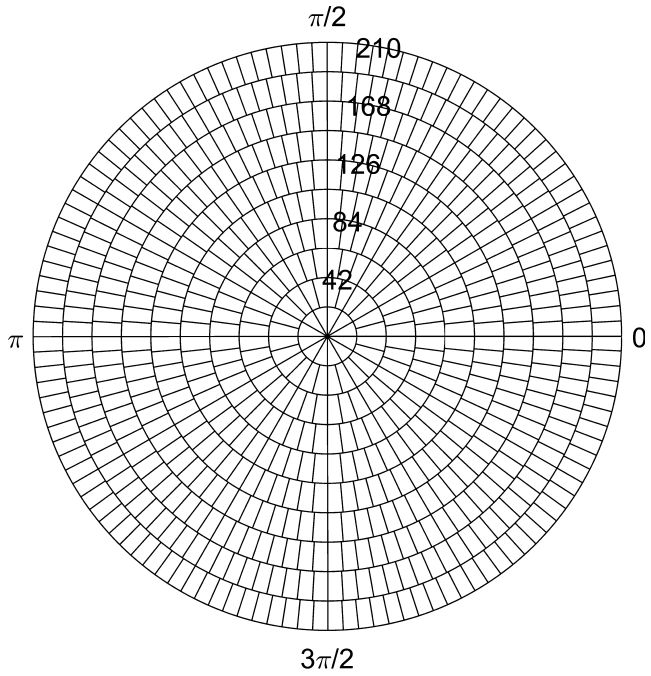

FIG. 6. A 2D representation of the placement subvolumes for the first 10 shells. The spherical tumor volume is divided into subvolumes of approximately equal size, which are filled with cell/vessel unit positions one at a time.

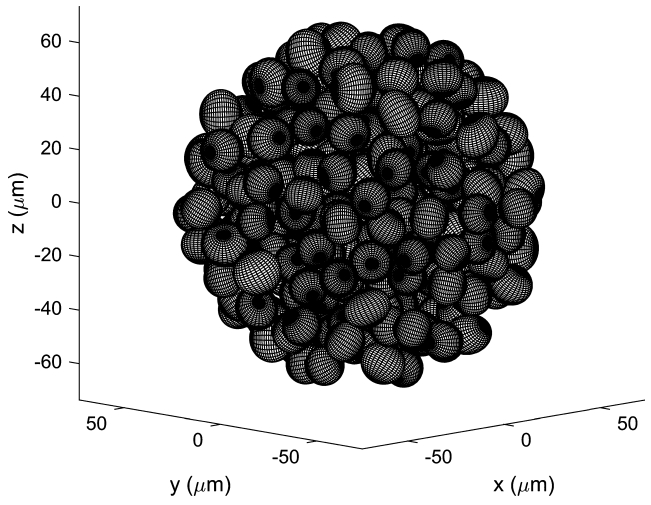

FIG. 7. A 3D mesh of cell/vessel unit positions filled with ellipsoids representing tumor cells.

2.B.2. Identify neighborhoods

For each mesh position, nearby mesh positions are identified. In later stages of the program, this information is used to perform vessel branching and to shift cells out to make room when a cell divides. Mesh positions within a distance of $4R_{\text{cell,min}} = 28\mu\text{m}$ are considered to be in the "neighborhood". This distance is chosen to ensure no more than one position would be included in the neighborhood along the same direction in space.

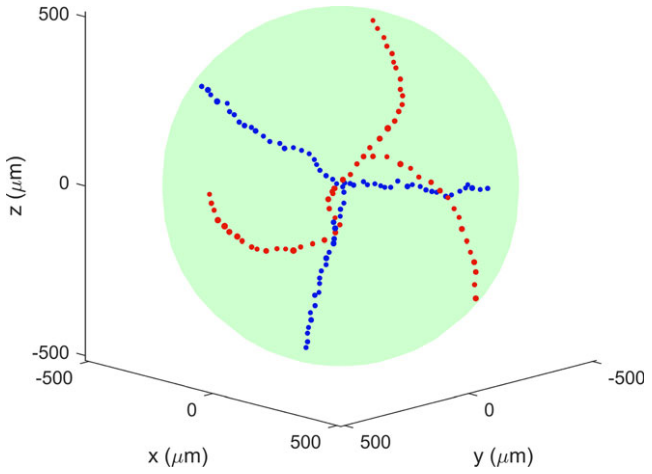

FIG. 8. Examples of radial pathways (blue) and curvy pathways (red). Radial pathways are used to shift cells along to make room for an additional daughter cell when a cell divides, while curvy pathways are used to direct the growth of blood vessels. [Color figure can be viewed at wileyonlinelibrary.com]

2.B.3. Grow vasculature

The structure of the tumor vasculature that grows out during tumor growth is established before tumor growth is simulated. To achieve this, all mesh positions are initially grouped into curvy "pathways" that start at different distances from the center and extend out to the periphery of the tumor volume. The total spherical tumor volume is divided into shells of thickness $\Delta R_{\text{shell}} = 21\ \mu$m, then a curvy pathway is formed by starting at one shell and taking one position per shell out to the periphery. Positions are chosen that have the most similar θ and ϕ coordinates to the previous position in the pathway after both θ and ϕ are offset by an amount corresponding to an arc length of $\Delta R_{\text{shell}} = 21\ \mu$m, which is slightly larger than the diameter of a cell. This has the effect of moving to the next position across in the shell and thus produces curvature in the pathway (Fig. 8). The offset in θ and ϕ is in the same direction (the same sign + or −) for the whole pathway, so the pathway has a consistent curvature. Pathways that begin in one shell are made to have the opposite curvature to pathways beginning in the previous shell.

A small number of these curvy pathways are then selected to be "vessel pathways", which blood vessels will grow along during tumor growth. That is, the mesh positions in these pathways will become occupied by blood vessel units. First, six curvy pathways are chosen to be the initial vessels growing in 3D. These curvy pathways are selected from those that begin in either the first or second shell, so that they roughly emanate from the origin, and on the basis that the last position in the pathway lies the closest to one of the positive or negative Cartesian axes, thereby ensuring the tumor grows in all directions even in the absence of vessel branching.

Next, additional curvy pathways are chosen to be vessel pathways on the basis that the new vessels appear to branch from existing ones. The amount of vessel branching that

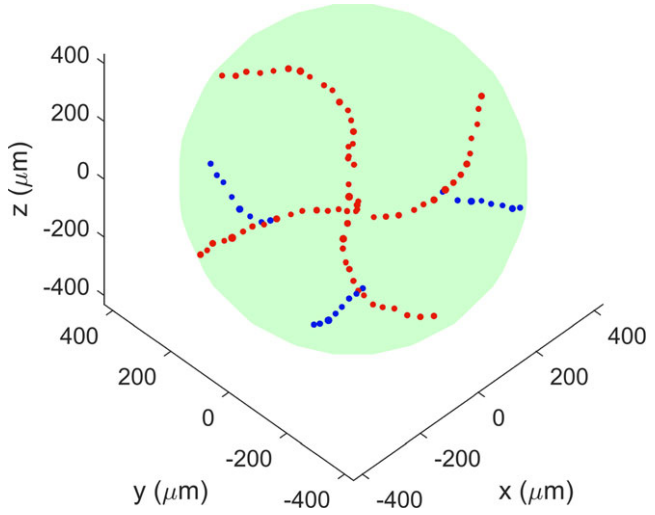

FIG. 9. Illustration of four initial blood vessels (red) emanating from the origin in opposite directions and three additional blood vessels (blue) branching from them. [Color figure can be viewed at wileyonlinelibrary.com]

occurs is dictated by the model parameter RVV_0. Starting with the third shell, the RVV in the previous shell is calculated. The RVV is calculated by the ratio of the number of positions occupied by blood vessel units to the total number of positions in that shell. If the RVV in the previous shell is less than the desired value for the tumor (RVV_0), an attempt is made to branch new vessels from existing ones at the current shell as follows. For each vessel pathway, the position in the pathway in the current shell has its neighborhood searched. If any of the neighboring positions is the first position in its own pathway, that pathway is selected as a new vessel pathway. The result is vessel branching as illustrated in Fig. 9. This is repeated for the next shell and so on to establish the complete tumor vasculature and achieve approximately the desired tumor RVV.

The remaining mesh positions that are not in vessel pathways are cell positions, meaning that cells may occupy them during tumor growth.

2.B.4. Assign oxygen type & CCT

With the structure of the vasculature predetermined, the distance from each cell position to the nearest blood vessel unit is calculated. If this distance is less than ND, the cell position is viable, otherwise it is a necrotic position. For viable cell positions, the distance is used to calculate the cellular pO_2 using Eq. (1). Each viable cell position is then assigned a CCT which cells will adopt while occupying that position. To obtain the CCT, a normoxic CCT is randomly sampled from the distribution in Eq. (3) and multiplied by the CCT adjustment factor in Eq. (6) which is a function of the cellular pO_2.

2.B.5. Group cell pathways

Cell positions are grouped into radial "cell pathways" which cells will shift along when a cell divides, a differentiated cell dies, or a necrotic cell is resorbed. The total spherical tumor volume is divided into shells of thickness $\Delta R_{\text{shell}} = 21\ \mu$m, then a pathway is formed by starting at one shell and taking one position per shell out to the periphery. Positions are chosen that have the most similar θ and ϕ coordinates to the previous position in the pathway (Fig. 8).

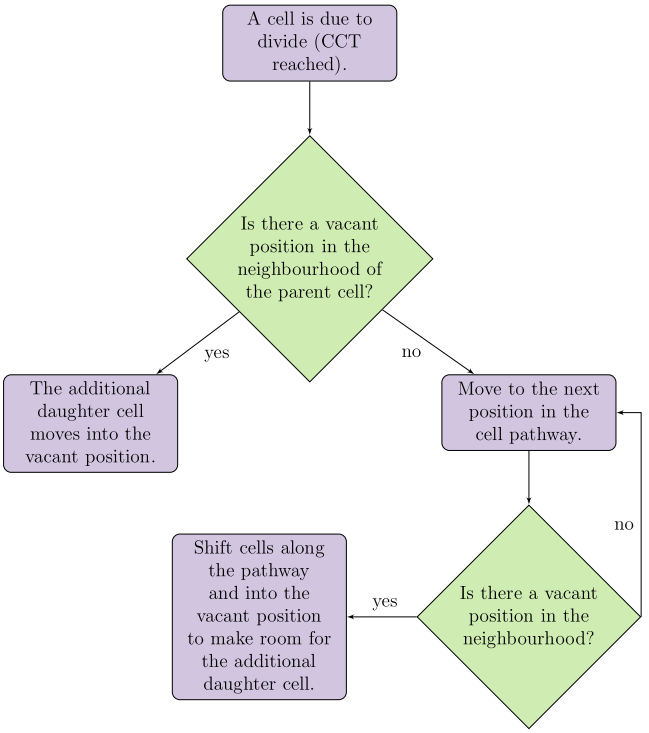

FIG. 10. Tumor growth: placement of daughter cells after a cell divides. [Color figure can be viewed at wileyonlinelibrary.com]

During the tumor growth simulation, when a cell divides giving rise to two daughter cells, one daughter cell occupies the parent cell's position and the other daughter cell occupies an adjacent position. When there are no vacant positions adjacent to the parent cell, cells are shifted out along the cell pathway to make room (Fig. 10). Similarly, when a differentiated cell dies or a necrotic cell is resorbed, cells are shifted inward along the cell pathway to fill the vacant position left behind.

The tumor growth simulation is terminated when a cell position at the end of a cell pathway becomes occupied, as it means that soon there will be no vacancies available when a cell in that pathway next divides. If cells divide more rapidly in one pathway than in others (e.g., as a result of pO_2), an irregular tumor shape develops rather than a spherical one.

2.B.6. Grow tumor

The initial tumor size is set by the number of 21 μm shells that tumor cells occupy to begin with. The user sets the initial proportions of each cell type (S, T1, T2, T3, and D). Each cell starts with an age that is a random fraction of its CCT. Vessel units in the preestablished vessel pathways are activated out to two shells beyond the tumor cells and this relative lead is maintained throughout the tumor growth simulation. Thus, vessel branching occurs just beyond the

tumor margin before cells move into the space, simulating new tumor vessels originating from the surrounding normal tissue vasculature.[51,52]

Simulation time is progressed until the first action is to be taken. Action is taken when a cell's age reaches its CCT or a necrotic cell's age reaches its resorption time. If a cell's age reaches its CCT and it is an S, T1, T2, or T3, the action taken is cell division. When a differentiated cell's age reaches its CCT, it either dies (80% chance) or survives for at least one more CCT. When a necrotic cell's age reaches its resorption time it is resorbed.

If the action taken involves a shift of cells and/or necrotic cells, the cells and necrotic cells involved in the shift will be affected and this may trigger further action. For example, the shift may cause a cell to move to a necrotic position and therefore become a necrotic cell. A cell shifted to another viable position will adopt the CCT at the new position and a necrotic cell shifted will have its resorption time recalculated. In each case, the age of the (necrotic) cell is retained. If a cell moves to a viable position with a shorter CCT and its age now exceeds its CCT, it immediately divides, or in the case of a differentiated cell, it has a chance to die. Likewise, if the resorption time of a necrotic cell becomes less than its age, the necrotic cell is resorbed. These actions and consequent shifts may themselves trigger more actions, and so on. Once there are no more actions to perform at this instant, simulation time is progressed until the next action is due to be performed, and so on.

2.B.7. Simulations performed

Tumor growth simulations were performed varying key input parameters RVV_0, p_0 and ND between biologically plausible limits (Table I) to observe the effects of different amounts of hypoxia on the tumor growth rate. Hypoxia was assessed by the hypoxic fractions HF10, HF5, HF2, and HF1 (the fractions of cells with $pO_2 < 10$, 5, 2, and 1 mmHg, respectively). The stem cell symmetric division probability was also varied. Computation times were reported. The segments of code "IDENTIFY NEIGHBORHOODS" and "ASSIGN OXYGEN TYPE & CCT" were eligible to run in parallel on multiple cores. Simulations were performed on the Phoenix supercomputer[53] using as many as 12 cores and 4 GB of memory.

3. RESULTS

3.A. Visualization of tumor growth simulation

A tumor growth simulation is visualized in Fig. 11. As cells divided, the tumor margin expanded and new vessels branched from existing ones to maintain the desired RVV (set by the model parameter RVV_0). Cells near vessels were normoxic, whereas cells pushed further out were hypoxic with longer CCTs and cells pushed further than ND from a vessel became necrotic. Note that vessels only appear open-ended because the surrounding normal tissue is not modeled. In reality, these vessels connect with the normal tissue vasculature. Vessel branching occurs just beyond the tumor margin to simulate new vessels originating from the normal tissue vasculature.

3.B. Variation of tumor oxygenation

The amount of hypoxia and necrosis in the simulated tumor depends on the model parameters RVV_0, p_0 and ND. Figure 12 compares sections of tumors with the same RVV but different p_0 and ND. The tumor oxygenation can be described quantitatively by the distribution of cellular pO_2, as shown in Fig. 13.

3.C. Tumor volume doubling times for HNSCC

The tumor growth rate was reduced by the presence of hypoxia and necrosis (Fig. 14). With a stem cell symmetric division probability of 2% and differentiated cell loss factor of 80%, well-oxygenated tumors ($RVV_0 = 10\%$, $p_0 = 100\,\text{mmHg}, \text{ND} = 300\,\mu\text{m}$) had a volume doubling time of 45±5 days ($n = 3$ simulations). Conversely, the volume doubling time for severely hypoxic tumors ($RVV_0 = 2\%, p_0 = 20\,\text{mmHg}, \text{ND} = 80\,\mu\text{m}$) was 87±5 days ($n = 3$ simulations). Well-oxygenated tumors contained no hypoxia or necrosis and had a median cellular pO_2 of 69±1 mmHg and a mean cellular pO_2 of 67±1 mmHg, while severely hypoxic tumors contained hypoxic fractions of HF10 = 0.79±0.01, HF5 = 0.54±0.01, HF2 = 0.31±0.01, and HF1 = 0.21±0.01 (also the quiescent fraction), a necrotic volume of 4.5±0.5%, a median cellular pO_2 of 4.4±0.2 mmHg, and a mean cellular pO_2 of 5.6±0.1 mmHg. The composition of the tumor rapidly equilibrated to 6% S, 6% T1, 11% T2, 22% T3, and 55% D for both oxic and hypoxic cases. The reduction in the stem cell proportion from 100% to 6%, as a result of cell differentiation during tumor growth, is responsible for the shoulder in both curves in Fig. 14.

With the stem cell symmetric division probability increased from 2% to 50% to simulate possible conditions during accelerated repopulation, the tumor volume doubling time decreased to 2.2±0.1 days ($n = 3$ simulations) for well-oxygenated tumors and 4.0±0.4 days ($n = 3$ simulations) for severely hypoxic tumors.

3.D. Computation time

The computation time for simulations beginning with the first two 21 μm shells filled with stem cells and ending in a final tumor diameter of 1.5 mm, containing 33×10^5 cell/vessel unit positions, is shown in Table II. 4 GB of memory was sufficient for all parts.

4. DISCUSSION

A spatio-temporal stochastic tumor growth model with angiogenesis has been developed. One of the main achievements of the current model was to position cells and vessel units into randomized positions in 3D, whereas most spatio-temporal models in the past have used a regular lattice.[8–15]

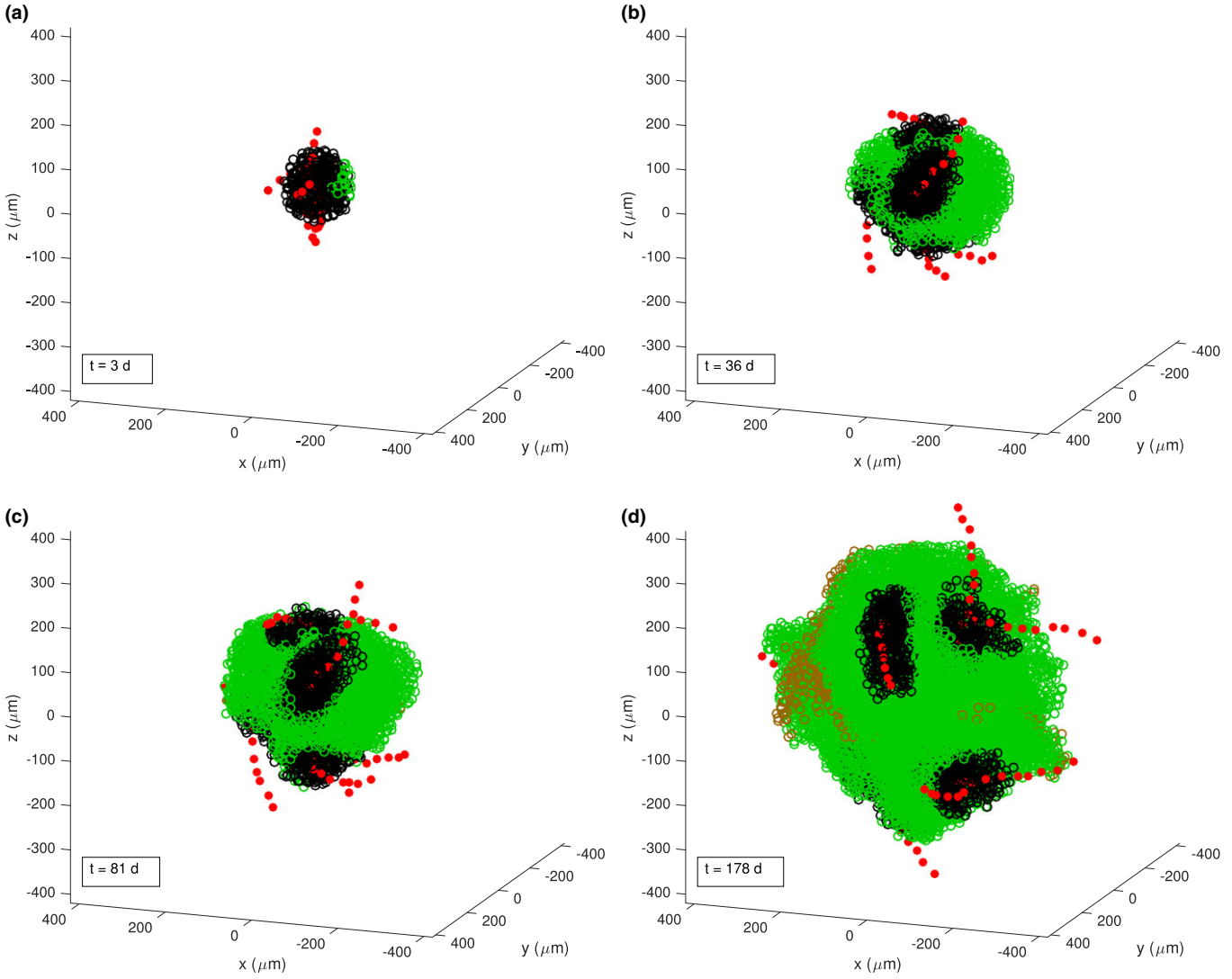

FIG. 11. Snapshots during a tumor growth simulation. Blood vessel units are shown in red, normoxic cells in black, hypoxic cells ($pO_2 < 10$ mmHg) in green, and necrotic cells in brown. The simulation began with approximately 70 stem cells occupying the first two 21 μm shells of the tumor volume. The different initial vessels are easily distinguishable in (b), these vessels recently underwent branching in (c), and in (d), some cells had necrosed. The tumor RVV was only 0.5% and the simulation used $p_0 = 40$ mmHg, ND = 180μm, stem cell symmetric division probability = 2%, and differentiated cell loss factor = 80%. [Color figure can be viewed at wileyonlinelibrary.com]

This was an important development because a lattice can produce artifacts in certain applications (e.g., in Monte Carlo particle tracking simulations). With randomized cell positions, to implement cell division (and differentiated cell loss and necrotic cell resorption), the concept of the cell pathway was devised. One drawback of randomized cell positions was having to accept a slightly lower cell density. The cell density obtained was 2×10^8 positions/cm^3 (cells and vessels). While 10^9 cells/cm^3 is the textbook standard tumor density, it is becoming recognized that 10^8 cells/cm^3 may be more accurate after accounting for the vasculature and the extracellular matrix.[54]

Another achievement was having the vessel units connected to form a coherent vasculature structure in the tumor. This had been done previously by Cai et al.,[15] but in their model, the tumor cells and blood vessels were generated in two separate spaces and then coupled. In the current model, the vessels coexist with the tumor cells, extending between them without overlapping. One advantage of having a connected vasculature as opposed to scattered vessel units is that the tumor vascularity will relate to the amount of hypoxia in a similar way as it does in real tumors.

The model also achieved a dynamic CCT for the cells. This was made possible by preventing the vessel units from moving around during tumor growth (even though the vessels grew and branched). Thus, it was possible to predetermine the oxygen tension at each cell position and, in turn, the CCT that cells would have while occupying that position.

Angiogenesis was simulated to maintain the desired tumor vascularity (RVV between 2 and 10%) via the model parameter RVV_0. A similar criteria for triggering angiogenesis was used in the model by Kocher et al.[10] Some models instead simulated angiogenesis in response to hypoxia, i.e., hypoxic cells released factors that were received by vessel units and

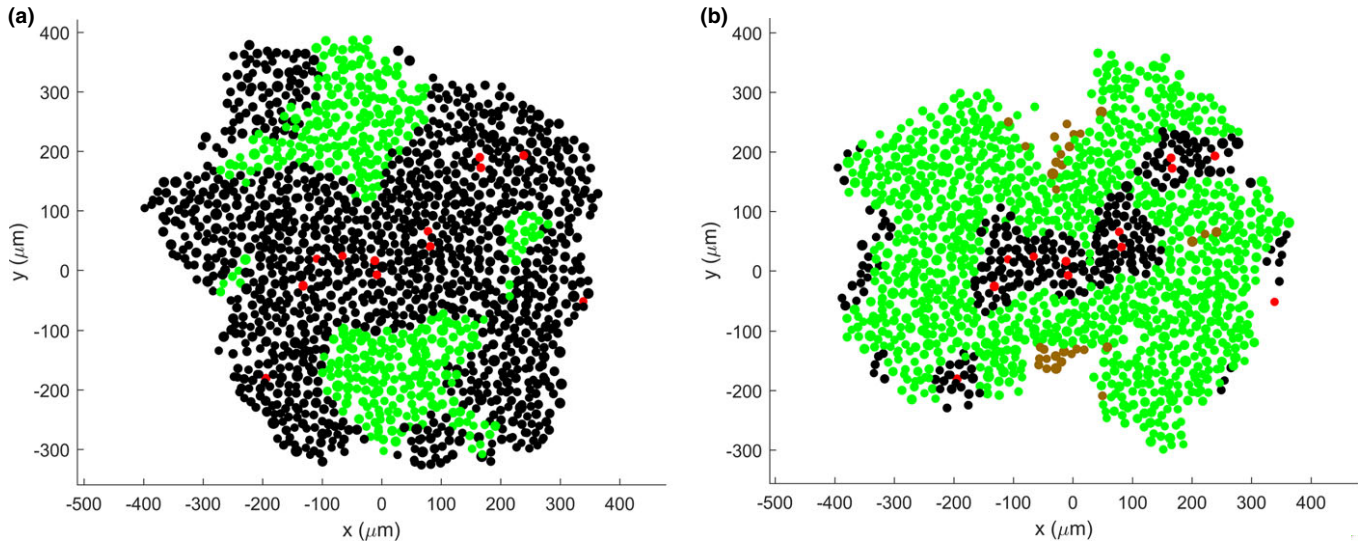

$\mathrm{RVV}_0 = 2\%$, $p_0 = 60$ mmHg, $\mathrm{ND} = 220\,\mu$m. $\mathrm{RVV}_0 = 2\%$, $p_0 = 30$ mmHg, $\mathrm{ND} = 120\,\mu$m.

FIG. 12. Sections of tumors with the same vasculature structure but different p_0 and ND. Blood vessel units are shown in red, normoxic cells in black, hypoxic cells ($pO_2 < 10$ mmHg) in green, and necrotic cells in brown. [Color figure can be viewed at wileyonlinelibrary.com]

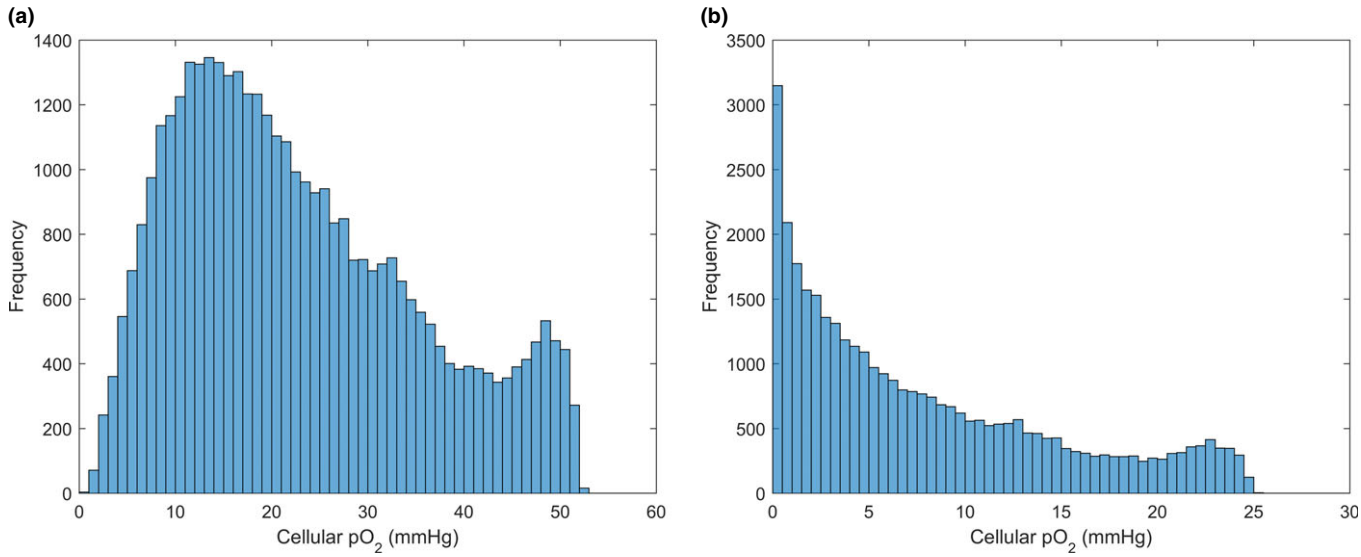

$\mathrm{RVV}_0 = 2\%$, $p_0 = 60$ mmHg, $\mathrm{ND} = 220\,\mu$m. $\mathrm{RVV}_0 = 2\%$, $p_0 = 30$ mmHg, $\mathrm{ND} = 120\,\mu$m.

FIG. 13. Distributions of cellular pO_2 for tumors with the same vasculature structure but different p_0 and ND. [Color figure can be viewed at wileyonlinelibrary.com]

stimulated angiogenesis.[13–15] This approach was not implemented in the current model because it would require that vessel units have access to the same positions as cells and thus be capable of moving around during the simulation (e.g., in response to cell division). If vessel units were permitted to move around, it would be difficult to keep them connected to form whole vessels and a coherent vasculature structure. It would also mean regularly recalculating the oxygen tension and CCT at each cell position, which would make the model far more computationally intensive. While angiogenesis is not driven by cell signaling in the current model, realistic vasculature structures, cellular pO_2 distributions and tumor growth rates are achieved, which are the most important factors for future applications in radiotherapy simulations.

The vessel density did not vary systematically between central and peripheral regions of the tumor. There are many tumor types for which this is accurate, including some HNSCCs.[55–57] If a tumor with a necrotic or hypoxic core and a well-oxygenated rim is desired, multiple tumor growths with different vessel densities could be spatially pieced together. Note that the model does not currently simulate

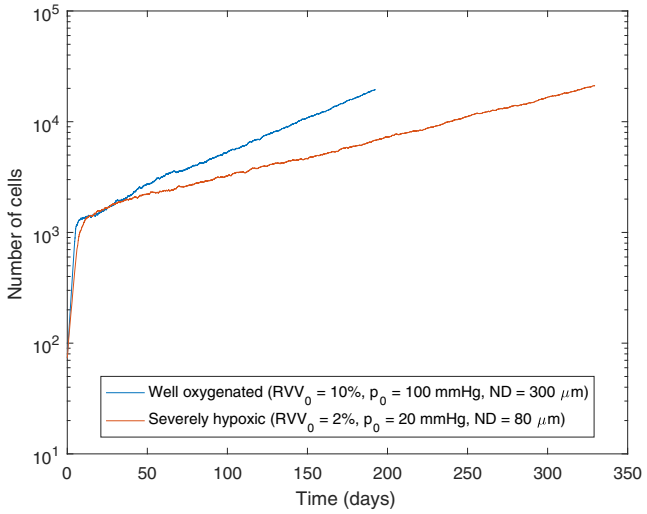

FIG. 14. Growth rates of well-oxygenated and severely hypoxic tumors. The stem cell symmetric division probability was 2% and the differentiated cell loss factor was 80%. Each simulation began with approximately 70 stem cells occupying the first two 21 μm shells of the tumor volume. [Color figure can be viewed at wileyonlinelibrary.com]

TABLE II. Computation times for a tumor growth simulation with a final tumor diameter of 1.5 mm.

Code segment	Cores	Run time
Generate 3D mesh	1	2.5 h
Identify neighborhoods	12	10 min
Grow vasculature + group cell pathways	1	15 min
Assign oxygen type & CCT	12	15 min
Grow tumor		
i) Stem cell symmetric division probability 2% and oxic (hypoxic)	1	190 (328) tumor days simulated in 316 (320) h
ii) Stem cell symmetric division probability 50% and oxic (hypoxic)	1	21 (32) tumor days simulated in 93 (40) h

acute (transient) hypoxia, which can be important in some tumors.[39]

The model parameters that determine the oxygenation of the simulated tumor are RVV_0, p_0, and ND. A strength of the model is that there is clinical data available for each of these parameters, enabling tumors to be generated with realistic oxygenations. Note that the simulated tumor will only have $RVV=RVV_0$ if it is spherical. In the simulation, the tumor naturally grows asymmetrically, with cells preferentially growing along the blood vessels. Thus, the tumor RVV is typically a percentage or so larger than RVV_0.

For HNSCC, there are wide ranges of biologically plausible RVV_0, p_0, and ND values, producing tumors ranging from well oxygenated to severely hypoxic. The presence of hypoxia and necrosis in the tumor markedly slowed the growth rate in simulated tumors. The doubling times obtained for well-oxygenated tumors were consistent with values in the literature for HNSCC, which average 45 days.[58] The proportion of stem cells in the tumor population was 6%, in agreement with clinical studies of HNSCC. These typically report cancer stem cell proportions less than 10%.[59–61]

A limitation of the current model is the large computation time, particularly for the "GROW TUMOR" section of the code which can only be run sequentially. Ideally, the tumor growth simulation would begin with a tumor size of approximately 1 mm^3, which is the size at which a tumor acquires its own vasculature,[62] and end with a clinically detectable volume of 1 cm^3. The issue of computation time has been a common problem for spatio-temporal models. For some models, it meant limiting the tumor to a subclinical size.[8,11] Others have used strategies to reach clinical tumor sizes. For example, Kansal et al.[19] and Antipas et al.[12] developed models in which the tumor was divided into geometrical cells, each of which represented a large number of real cells. For the current model, future work may involve conducting multiple tumor growth simulations in parallel and then piecing them together to form a clinically relevant tumor size. The computation time is less of a concern when simulating tumor growth during a course of radiotherapy, as accelerated repopulation occurs and a high stem cell symmetric division probability (possibly 50%) is favorable.[30–32] Furthermore, in this case only several weeks of tumor growth (equal to the total treatment time) need to be simulated.

5. CONCLUSIONS

A 4D computational tumor growth model with angiogenesis was developed. It was used to evaluate the tumor volume doubling time for well-oxygenated and hypoxic tumors of HNSCC. The model is unique in that it features randomized cell positions and grows a connected vasculature structure in the tumor. The doubling times and cancer stem cell proportions obtained are consistent with clinical data for HNSCC.

In future work, the tumor growth model will be used to generate 3D tumors that will be spatially irradiated using Monte Carlo track structure methods. The DNA damage to each cell will be determined by clustering the ionization events that occur in the cell nucleus to estimate the number of DNA double-strand breaks. The cellular pO_2 will affect the amount of damage incurred and the cell's ability to repair the damage. The current tumor model provides accurate localization of hypoxic cells and therefore cellular radiosensitivity to microscopic regions beyond some distance from the blood vessels, as well as accurate amounts of hypoxia in relation to the degree of tumor vascularity. As the blood vessels are modeled as serial structures, damages to the tumor vasculature can be studied, which are considerable in high-dose treatments such as stereotactic body radiation therapy.[63,64] Ultimately, the tumor growth model will be used in conjunction with the tumor irradiation model to simulate fractionated external beam radiotherapy for HNSCC. Early results presented herein of tumor doubling times indicate that the amount of hypoxia and necrosis as well as the stem cell symmetric division probability will have a large effect on the rate at which tumors regrow during a course of radiotherapy.

CONFLICTS OF INTEREST

The authors have no relevant conflicts of interest to disclose.

[a)]Author to whom correspondence should be addressed. Electronic mail: Jake.Forster@adelaide.edu.au.

REFERENCES

1. McElwain DLS, Pettet GJ. Cell migration in multicell spheroids: swimming against the tide. *Bull Math Biol.* 1993;55:655–674.
2. Tracqui P, Cruywagen GC, Woodward DE, Bartoo GT, Murray JD, Alvord EC Jr. A mathematical model of glioma growth: the effect of chemotherapy on spatio-temporal growth. *Cell Proliferat.* 1995;28:17–31.
3. Pescarmona GP, Scalerandi M, Delsanto PP, Condat CA. Non-linear model of cancer growth and metastasis: a limiting nutrient as a major determinant of tumor shape and discussion. *Med Hypotheses.* 1999;53:497–503.
4. Harriss-Phillips WM, Bezak E, Yeoh EK. Monte carlo radiotherapy simulations of accelerated repopulation and reoxygenation for hypoxic head and neck cancer. *Br J Radiol.* 2011;84:903–918.
5. Harriss-Phillips WM, Bezak E, Yeoh EK. The hyp-rt hypoxic tumour radiotherapy algorithm and accelerated repopulation dose per fraction study. *Comput Math Methods Med.* 2012;2012.
6. Harriss-Phillips WM, Bezak E, Yeoh EK. Altered fractionation outcomes for hypoxic head and neck cancer using the hyp-rt monte carlo model. *Br J Radiol.* 2013;86.
7. Appleton DR, Thomson PJ, Donaghey CE, Potten CS, McGurk M. Simulation of cell proliferation in mouse oral epithelium, and the action of epidermal growth factor: evidence for a high degree of synchronization of the stem cells. *Cell Proliferat.* 2002;35:68–77.
8. Duchting W, Vogelsaenger T. Three-dimensional pattern generation applied to spheroidal tumour growth in a nutrient medium. *Int J Bio Med Comput.* 1981;12:377–392.
9. Qi S, Zheng X, Du CY, An BS. A cellular automaton model of cancerous growth. *J Theor Biol.* 1993;161:1–12.
10. Kocher M, Treuer H, Voges, J, Hoevels M, Sturm V, Muller RP. Computer simulation of cytotoxic and vascular effects of radiosurgery in solid and necrotic brain metastases, Radiotherapy. *Oncol.* 2000;54:149–156.
11. Patel AA, Gawlinski ET, Lemieux SK, Gatenby RA. A cellular automaton model of early tumor growth and invasion. *J Theor Biol.* 2001;213:315–331.
12. Antipas VP, Stamatakos GS, Uzunoglu NK, Dionysiou DD, Dale RG. A spatio-temporal simulation model of the response of solid tumours to radiotherapy in vivo: parametric validation concerning oxygen enhancement ratio and cell cycle duration. *Phys Med Biol.* 2004;49:1485–1504.
13. Borkenstein K, Levegrun S, Peschke P. Modeling and computer simulations of tumor growth and tumor response to radiotherapy. *Radiat Res.* 2004;162:71–83.
14. Harting C, Peschke P, Borkenstein K, Karger CP. Single-cell-based computer simulation of the oxygen-dependent tumour response to irradiation. *Phys Med Biol.* 2007;52:4775–4789.
15. Cai Y, Xu S, Wu J, Long Q. Coupled modelling of tumour angiogenesis, tumour growth and blood perfusion. *J Theor Biol.* 2011;279:90–101.
16. Douglass MJJ, Bezak E, Penfold S. Development of a randomized 3d cell model for monte carlo microdosimetry simulations. *Med Phys.* 2012;39:3509–3519.
17. Douglass MJJ, Bezak E, Penfold S. Monte carlo investigation of the increased radiation deposition due to gold nanoparticles using kilovoltage and megavoltage photons in a 3d randomized cell model. *Med Phys.* 2013;40.
18. Douglass MJJ, Bezak E, Penfold S. Development of a radiation track structure clustering algorithm for the prediction of dna dsb yields and radiation induced cell death in eukaryotic cells. *Phys Med Biol.* 2015;60:3217–3236.
19. Kansal AR, Torquato S, Harsh GRIV, Chiocca EA, Deisboeck TS. Simulated brain tumor growth dynamics using a three-dimensional cellular automaton. *J Theor Biol.* 2000;203:367–382.
20. Tannock IF. The relation between cell proliferation and the vascular system in a transplanted mouse mammary tumour. *Br J Cancer.* 1968;22:258–273.
21. Hirst DG, Denekamp J. Tumour cell proliferation in relation to the vasculature. *Cell Tissue Kinet.* 1979;12:31–42.
22. Thomlinson RH, Gray LH. The histological structure of some human lung cancers and the possible implications for radiotherapy. *Br J Cancer.* 1955;9:539–549.
23. Tannock IF. Oxygen diffusion and the distribution of cellular radiosensitivity in tumours. *Br J Radiol.* 1972;45:515–524.
24. Beasley NJ, Wykoff CC, Watson PH, et al. Carbonic anhydrase ix, an endogenous hypoxia marker, expression in head and neck squamous cell carcinoma and its relationship to hypoxia, necrosis, and microvessel density. *Cancer Res.* 2001;61:5262–5267.
25. Carlson DJ, Keall PJ, Loo BW Jr, Chen ZJ, Brown JM. Hypofractionation results in reduced tumor cell kill compared to conventional fractionation for tumors with regions of hypoxia. *Int J Radiat Oncol Biol Phys.* 2011;79:1188–1195.
26. Harriss WM. Monte Carlo modelling of tumour growth, hypoxia and radiotherapy in head and neck squamous cell carcinoma, Ph.D. thesis, University of Adelaide 2011.
27. Douglass MJJ. Development of an Integrated Stochastic Radiobiological Model for Electro-magnetic Particle Interactions in a 4D Cellular Geometry, Ph.D. thesis, University of Adelaide 2014.
28. Vlad RM, Alajez NM, Giles A, Kolios MC, Czarnota GJ. Quantitative ultrasound characterization of cancer radiotherapy effects in vitro. *Int J Radiat Oncol Biol Phys.* 2008;72:1236–1243.
29. Huber MD, Gerace L. The size-wise nucleus: nuclear volume control in eukaryotes. *J Cell Biol.* 2007;179:583–584.
30. Withers HR, Elkind MM. Radiosensitivity and fractionation response of crypt cells of mouse jejunum. *Radiat. Res.* 1969;38:598–613.
31. Trott KR, Kummermehr J. Rapid repopulation in radiotherapy: a debate on mechanism. Accelerated repopulation in tumours and normal tissues. *Radiother Oncol.* 1991;22:159–160.
32. Dorr W. Three a's of repopulation during fractionated irradiation of squamous epithelia: asymmetry loss, acceleration of stem-cell divisions and abortive divisions. *Int J Radiat Biol.* 1997;72:635–643.
33. Zatterstrom UK, Kallen A, Wennerberg J. Cell cycle time, growth fraction and cell loss in xenografted head and neck cancer. *In Vivo.* 1991;5:137–142.
34. Marcu L. Tumour repopulation and the role of abortive division in squamous cell carcinomas during chemotherapy. *Cell Prolif.* 2014;47:318–325.
35. Amelink A, Sterenborg HJCM, Bard MPL, Burgers SA. In vivo measurement of the local optical properties of tissue by use of differential path-length spectroscopy. *Opt Lett.* 2004;29:1087–1089.
36. Amelink A, Kaspers OP, Sterenborg HJCM, Roodenburg JEvJN, Witjes MJH. Non-invasive measurement of the morphology and physiology of oral mucosa by use of optical spectroscopy. *Oral Oncol.* 2008;44:65–71.
37. Carmeliet P, Jain RK. Angiogenesis in cancer and other diseases. *Nature.* 2000;407:249–257.
38. Pazouki S, Chisholm DM, Adi MM, et al. The association between tumour progression and vascularity in the oral mucosa. *J Pathol.* 1997;183:39–43.
39. Wyffels KIEM, Kaanders JHAM, Rijken PFJW, et al. Vascular architecture and hypoxic profiles in human head and neck squamous cell carcinomas. *Br J Cancer.* 2000;83:674–683.
40. Carreau A, Hafny-Rahbi BE, Matejuk A, Grillon C, Kieda C. Why is the partial oxygen pressure of human tissues a crucial parameter? Small molecules and hypoxia. *J Cell Mol Med.* 2011;15:1239–1253.
41. Gardner LB, Li Q, Park MS, Flanagan WM, Semenza GL, Dang CV. Hypoxia inhibits g1/s transition through regulation of p27 expression. *J Biol Chem.* 2001;276:7919–7926.
42. Koritzinsky M, Wouters BG, Amellem O, Pettersen EO. Cell cycle progression and radiation survival following prolonged hypoxia and re-oxygenation. *Int J Radiat Biol.* 2001;77:319–328.

43. Webster L, Hodgkiss RJ, Wilson GD. Cell cycle distribution of hypoxia and progression of hypoxic tumour cells in vivo. *Br J Cancer.* 1998;77:227–234.
44. Wilson GD, Dische S, Saunders MI. Studies with bromodeoxyuridine in head and neck cancer and accelerated radiotherapy. *Radiother Oncol.* 1995;36:189–197.
45. Alarcon T, Byrne HM, Maini PK. A mathematical model of the effects of hypoxia on the cell-cycle of normal and cancer cells. *J Theor Biol.* 2004;229:395–411.
46. Amellem O, Pettersen EO. Cell inactivation and cell cycle inhibition as induced by extreme hypoxia: the possible role of cell cycle arrest as a protection against hypoxia-induced lethal damage. *Cell Prolif.* 1991;24:127–141.
47. Douglas RM, Farahani R, Morcillo P, Kanaan A, Xu T, Haddad GG. Hypoxia induces major effects on cell cycle kinetics and protein expression in drosophila melanogaster embryos. *Am J Physiol Regul Integr Comp Physiol.* 2005;288:R511–521.
48. Royds JA, Dower SK, Qwarnstrom EE, Lewis CE. Response of tumour cells to hypoxia: role of p53 and nfkb. *Mol Pathol.* 1998; 51:55–61.
49. Gross MW, Karbach U, Groebe K, Franko AJ, Mueller-Klieser W. Calibration of misonidazole labeling by simultaneous measurement of oxygen tension and labeling density in multicellular spheroids. *Int J Cancer.* 1995;61:567–573.
50. Chou SC, Azuma Y, Varia MA, Raleigh JA. Evidence that involucrin, a marker for differentiation, is oxygen regulated in human squamous cell carcinomas. *Br J Cancer* 2004;90:728–735.
51. Algire GH, Chalkley HW. Vascular reactions of normal and malignant tissues in vivo. i. vascular reactions of mice to wounds and to normal and neoplastic transplants. *J Natl Cancer Inst.* 1945;6:73–85.
52. Eddy HA, Casarett GW. Development of the vascular system in the hamster malignant neurilemmoma. *Microvascular Res.* 1973;6:63–82.
53. The University of Adelaide, Phoenix high performance computing, 2016.
54. del Monte U. Does the cell number 10^9 still really fit one gram of tumor tissue?. *Cell Cycle.* 2009;8:505–506.
55. Porschen R, Classen S, Piontek M, Borchard F. Vascularization of carcinomas of the esophagus and its correlation with tumor proliferation. *Cancer Res.* 1994;54:587–591.
56. Wijffels KIEM, Hoogsteen IJ, Lok J, et al. No detectable hypoxia in malignant salivary gland tumours: preliminary results. *Int J Rad Onc Biol Phys.* 2009;73:1319–1325.
57. Ljungkvist ASE, Bussink J, Rijken PFJW, et al. Vascular architecture, hypoxia, and proliferation in first-generation xenografts of human head-and-neck squamous cell carcinomas. *Int J Rad Onc Biol Phys.* 2002;54:215–228.
58. Tannock IF, Hill RP. *The Basic Science of Oncology*, 2nd edn. New York: McGraw-Hill; 1992:155–176.
59. Yu D, Jin C, Liu Y, et al. Clinical implications of cancer stem cell-like side population cells in human laryngeal cancer. *Tumour Biol.* 2013;34:3603–3610.
60. Chinn SB, Darr OA, Owen JH, et al. Cancer stem cells: mediators of tumorigenesis and metastasis in head and neck squamous cell carcinoma. *Head Neck.* 2015;37:317–326.
61. Wu J, Mu Q, Thiviyanathan V, Annapragada A, Vigneswaran N. Cancer stem cells are enriched in fanconi anemia head and neck squamous cell carcinomas. *Int J Oncol.* 2014;45:2365–2372.
62. Gimbrone MA Jr, Leapman SB, Cotran RS, Folkman J. Tumor dormancy in vivo by prevention of neovascularization. *J Exp Med.* 1972;136:261–276.
63. Park HJ, Griffn RJ, Hui S, Levitt SH, Song CW. Radiation-induced vascular damage in tumors: implications of vascular damage in ablative hypofractionated radiotherapy (sbrt and srs). *Rad Res.* 2012;177:311–327.
64. El Kaffas A, Giles A, Czarnota GJ. Dose-dependent response of tumor vasculature to radiation therapy in combination with sunitinib depicted by three-dimensional high-frequency power doppler ultrasound. *Angiogenes.* 2013;16:443–454.

Table 4.1: Revised computation times for a tumour growth simulation with a final tumour diameter of 1.5 mm.

Code segment	Cores	Run time	Memory (GB)[1]
Generate 3D mesh	1	2 h	0.5
Identify neighbourhoods	12	5 min	9
Grow vasculature and group cell pathways	1	11 min	0.4
Assign oxygen type and CCT	12	6 min	6
Grow tumour			
i) Stem cell SDP[2] 2% and oxic (hypoxic)	1	280 (481) tumour days simulated in 44 (37) h	1 (0.9)
ii) Stem cell SDP[2] 50% and oxic (hypoxic)	1	21 (34) tumour days simulated in 80 (40) min	0.6 (0.6)

[1]total memory shared between cores if multicore
[2]symmetric division probability

4.3 Discussion and Conclusion

The tumour growth model was developed after conceiving of a method based on "pathways". The stochastic, randomised cell/vessel unit positions were grouped into "curvy" pathways, some of which were selected to become blood vessels (and the positions in the pathways were assigned to blood vessel units), such that a connected, branching and chaotic vasculature was generated in the tumour. The remaining positions were cell positions and were grouped into radial pathways. After a cell division, cells were transported outward along their radial pathway to make room for the additional daughter cell. Similarly, after a cell death (e.g. differentiated or necrotic cell death), cells were transported inward along their radial pathway to fill the gap.

Shortly after this article was accepted for publication, a more efficient way of running Matlab code on Phoenix was discovered (see Appendix - previously the Matlab compiler `mcc` was used to generated an executable). Revised computation times are shown in Table 4.1.

5

Simulation of head and neck cancer oxygenation and doubling time in a 4D cellular model with angiogenesis

The publication [92] forms the basis of this chapter:

Forster JC, Douglass MJJ, Harriss-Phillips WM, Bezak E. Simulation of head and neck cancer oxygenation and doubling time in a 4D cellular model with angiogenesis. *Sci Rep.* 2017 Sep 8; 7(1):11037. doi: 10.1038/s41598-017-11444-1.

5.1 Introduction and Motivation

This paper explores the behaviour of the tumour growth model in more detail. For example, how do the model parameters $\{RVV, p_0, ND\}$ map to the hypoxic proportions and necrotic volume in the tumour? How do the stem cell symmetric division probability and tumour oxygenation affect the tumour doubling time and proportion of cancer stem cells in the tumour? What combinations of $\{RVV, p_0, ND\}$ give a typical HNSCC tumour oxygenation?

5.2 Statement of Contribution

5.2.1 Conception

All authors felt it necessary to rigorously explore the tumour growth model behaviour. The study methodology was conceived by Jake Forster under the supervision of Michael Douglass, Wendy Phillips and Eva Bezak.

5.2.2 Realisation

Jake Forster wrote the code to run the simulations to acquire data, wrote the code to run the simulations on a supercomputer, ran the simulations on a supercomputer, analysed the data and made the plots for visualising data. The manuscript was evaluated by Eva Bezak, Wendy Phillips and Michael Douglass for data accuracy, critical appraisal, conclusions reached and general structure and flow.

5.2.3 Documentation

The manuscript was primarily written by Jake Forster, who also prepared the figures. Wendy Phillips, Michael Douglass and Eva Bezak provided input, feedback and revisions.

Statement of Authorship

Title of Paper	Simulation of head and neck cancer oxygenation and doubling time in a 4D cellular model with angiogenesis
Publication Status	☑ Published ☐ Accepted for Publication ☐ Submitted for Publication ☐ Unpublished and Unsubmitted work written in manuscript style
Publication Details	Forster JC, Douglass MJJ, Harriss-Phillips WM, Bezak E. *Sci Rep*. 2017; 7(1):11037. doi: 10.1038/s41598-017-11444-1.

Principal Author

Name of Principal Author (Candidate)	Jake Cameron Forster		
Contribution to the Paper	Conceived of the study methodology, wrote the code to run the simulations to acquire data, wrote the code to run the simulations on a supercomputer, ran the simulations on a supercomputer, analysed the data, made the plots for visualising data, wrote the manuscript, prepared the figures and acted as the corresponding author.		
Overall percentage (%)	80%		
Certification:	This paper reports on original research I conducted during the period of my Higher Degree by Research candidature and is not subject to any obligations or contractual agreements with a third party that would constrain its inclusion in this thesis. I am the primary author of this paper.		
Signature		Date	3-10-2018

Co-Author Contributions

By signing the Statement of Authorship, each author certifies that:

i. the candidate's stated contribution to the publication is accurate (as detailed above);

ii. permission is granted for the candidate in include the publication in the thesis; and

iii. the sum of all co-author contributions is equal to 100% less the candidate's stated contribution.

Name of Co-Author	Prof. Eva Bezak		
Contribution to the Paper	General guidance and supervision and manuscript revision.		
Overall percentage (%)	10%		
Signature		Date	3-10-2018

Name of Co-Author	Dr Wendy Phillips		
Contribution to the Paper	General guidance and supervision and manuscript revision.		
Overall percentage (%)	5%		
Signature		Date	3-10-2018

Name of Co-Author	Dr Michael Douglass		
Contribution to the Paper	General guidance and supervision and manuscript revision.		
Overall percentage (%)	5%		
Signature		Date	4-10-2018

SCIENTIFIC REPORTS

OPEN

Simulation of head and neck cancer oxygenation and doubling time in a 4D cellular model with angiogenesis

Received: 24 May 2017
Accepted: 18 August 2017
Published online: 08 September 2017

Jake C. Forster[1,2], Michael J. J. Douglass[1,2], Wendy M. Harriss-Phillips[1,2] & Eva Bezak[1,3]

Tumor oxygenation has been correlated with treatment outcome for radiotherapy. In this work, the dependence of tumor oxygenation on tumor vascularity and blood oxygenation was determined quantitatively in a 4D stochastic computational model of head and neck squamous cell carcinoma (HNSCC) tumor growth and angiogenesis. Additionally, the impacts of the tumor oxygenation and the cancer stem cell (CSC) symmetric division probability on the tumor volume doubling time and the proportion of CSCs in the tumor were also quantified. Clinically relevant vascularities and blood oxygenations for HNSCC yielded tumor oxygenations in agreement with clinical data for HNSCC. The doubling time varied by a factor of 3 from well oxygenated tumors to the most severely hypoxic tumors of HNSCC. To obtain the doubling times and CSC proportions clinically observed in HNSCC, the model predicts a CSC symmetric division probability of approximately 2% before treatment. To obtain the doubling times clinically observed during treatment when accelerated repopulation is occurring, the model predicts a CSC symmetric division probability of approximately 50%, which also results in CSC proportions of 30–35% during this time.

While tumors are typically more vascularized than normal tissue, hypoxia will still arise in many tumors due to heterogeneity in the vascularity and depleted levels of blood oxygenation that occur when blood moves sluggishly through constricted and malformed vessels[1,2]. Radiotherapy is a primary treatment modality for head and neck squamous cell carcinoma (HNSCC) and tumor oxygenation has been correlated with treatment outcome[3–5]. Another key factor influencing the treatment outcome is the rate of tumor regrowth during treatment. Radiotherapy is typically delivered over several weeks (an example of a conventional fractionation schedule for the treatment of HNSCC with X-rays is 2 Gy fractions, 5 days/week over 6 weeks), and after a certain time (the "kick-off time") the tumor initiates accelerated repopulation[6–8]. One of the key mechanisms responsible for accelerated repopulation is reportedly an increase in the symmetric division of cancer stem cells (CSCs). CSCs make up only a small proportion of the tumor cells[9], but each has the potential to regenerate the tumor and must be inactivated to achieve 100% local tumor control probability.

In previous work, a computational model was developed that simulates HNSCC tumor growth[10]. This is a 4D cellular model that includes the simulation of tumor angiogenesis. In the first part of the current work, this model was used to quantitatively map tumor properties, such as vascularity and blood oxygenation, to tumor oxygenation descriptors, such as the proportion of hypoxic cells, the mean cellular pO_2 and the necrotic volume. By constraining the vascularity and blood oxygenation to values that have been clinically observed in HNSCC, values of tumor oxygenation descriptors were obtained for HNSCC and compared with clinical data.

In the second part of the work presented here, the effect of tumor oxygenation on the tumor volume doubling time for HNSCC was quantitatively assessed. The effect of the CSC symmetric division probability on the doubling time was also explored. The CSC symmetric division probability also affects the proportion of CSCs in the tumor and this relationship was investigated. Finally, doubling times and CSC proportions were compared with

[1]Department of Physics, University of Adelaide, North Terrace, Adelaide, South Australia, 5005, Australia. [2]Department of Medical Physics, Royal Adelaide Hospital, North Terrace, Adelaide, South Australia, 5000, Australia. [3]Sansom Institute for Health Research and the School of Health Sciences, University of South Australia, Adelaide, South Australia, Australia. Correspondence and requests for materials should be addressed to J.C.F. (email: Jake.Forster@adelaide.edu.au)

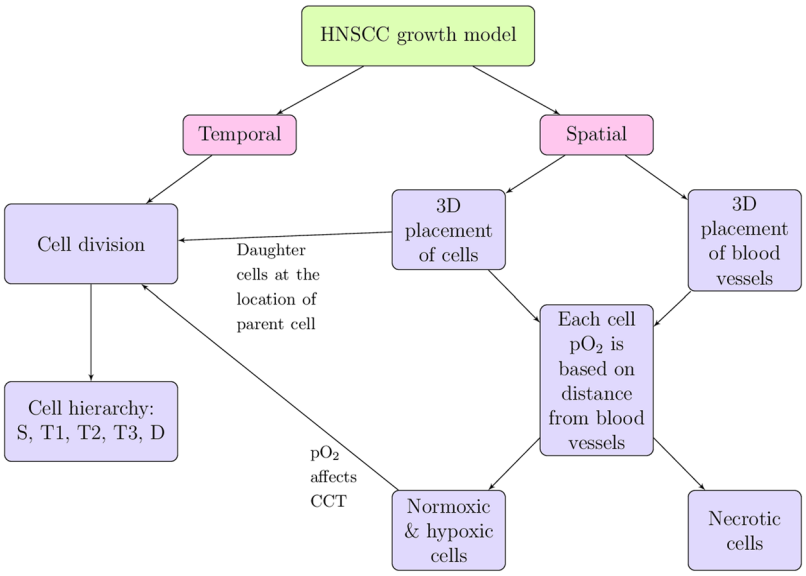

Figure 1. Main features of the HNSCC tumor growth model. Adapted with permission from ref. 10.

clinical data for HNSCC. While tumor irradiation was not simulated, tumor growth kinetics during accelerated repopulation were obtained by increasing the CSC symmetric division probability.

Methods

The tumor growth model. Simulations of HNSCC tumor growth were performed using a computational model that was developed in-house using Matlab (version R2017a, The MathWorks, Inc.) and has been previously described[10]. The flow chart in Fig. 1 outlines the spatial and temporal features of the model and how they are related. Briefly, each tumor cell is modeled as an ellipsoid and packed into randomized positions in 3D space without overlap (Fig. 2a). The tumor grows over time by cell division, wherein a cell upon reaching the end of its cell cycle time (CCT) divides into two daughter cells, consequently pushing neighbouring cells outward towards the tumor periphery. A hierarchy of cell types is simulated, including CSCs, three generations of transit cells (T1-3) and differentiated cells (Fig. 2b). The probability for CSCs to undergo symmetric division (i.e., divide into two CSCs as opposed to one CSC and one transit cell) is set by the user. The sloughing of differentiated cells, which is characteristic of epithelial tissue, is also simulated.

Angiogenesis is modeled reflecting a connected and chaotic tumor vasculature that grows out with the cells (Fig. 2c,d), with blood vessels represented by consecutive discrete vessel units. Tumors can be grown with different vascularities which are quantified by the relative vascular volume, *RVV*. Cellular pO_2 is modeled dynamically as a function of distance from the nearest vessel using a diffusion equation (Table 1), with key parameters being the blood oxygenation, p_0, and the distance from vessels to the onset of necrosis (the necrosis distance, *ND*). The tumor vascularity (*RVV*) and the blood oxygenation (p_0 and *ND*) affect the amount of hypoxia in the tumor (Fig. 2e,f). Hypoxic cells have longer CCTs and cells that become necrotic are gradually resorbed by the tumor. Table 1 summarises the main parameters of the model and their values for HNSCC.

Simulations entail the following. First, a unique 3D mesh of non-overlapping cell/vessel unit positions is generated using Monte Carlo methods. The cell density reached is 2×10^8 cells/cm^3. A connected network of blood vessels is then generated. As a result, a selection of the mesh positions are designated as vessel unit positions. A unique vasculature is generated each time using Monte Carlo methods. The vasculature is chaotic and tortuous, representative of tumor vasculature[1,2]. As the tumor grows larger, the vasculature grows out by activating more of the vessel unit positions. Mesh positions that are not designated as vessel unit positions are cell positions, meaning tumor cells may occupy them during tumor growth simulation.

Once a blood vessel network has been generated and prior to tumor growth simulation, the oxygen tension at each cell position is determined and used to calculate the CCT. Cells push one another around when a cell divides, a differentiated cell is lost or a necrotic cell is resorbed. When a cell changes position, it retains its age (the time since it last divided), but its CCT changes to the CCT at its new position. When the age of the cell equals its position dependent CCT, it divides. When a cell divides, it pushes a neighbouring cell outward towards the tumor periphery, causing a chain of cell movement outward, making room for the additional daughter cell. Thus, one daughter cell occupies the position where the parent cell used to be, and the other daughter cell occupies an adjacent position.

The daughter cells are always one generation more differentiated than the parent cell (CSC → T1 → T2 → T3 → differentiated), except in the case of CSC symmetric division. A differentiated cell loss frequency of 80% is simulated to model the natural cell death of these cells, i.e., apoptosis. When a cell becomes differentiated, after a time equal to the CCT, there is an 80% likelihood that the differentiated cell is removed from the tumor. If it is not removed, it remains for another period of time equal to the CCT, then there is again an 80% likelihood that

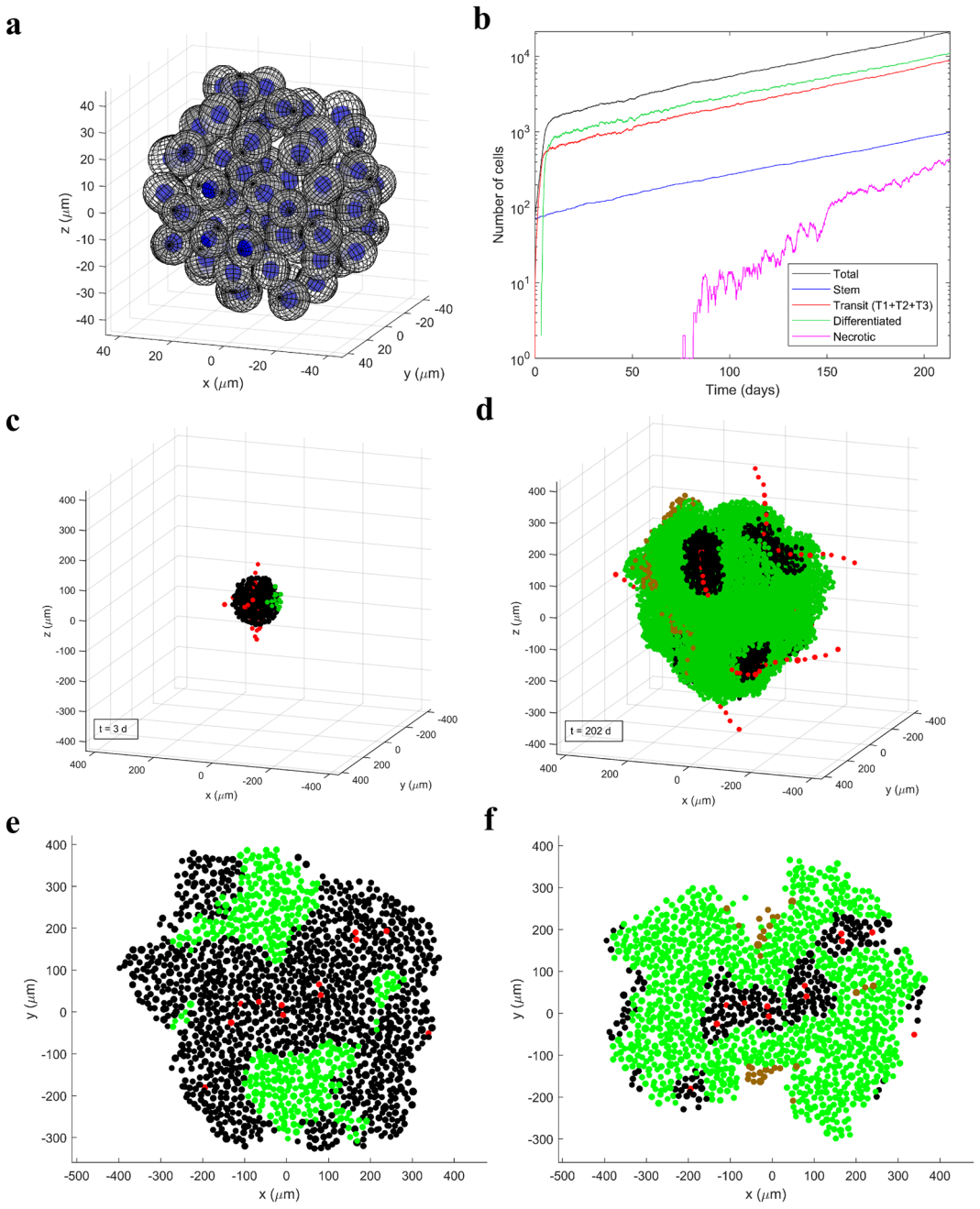

Figure 2. HNSCC tumor growth model. (**a**) Tumor cells are modeled as non-overlapping ellipsoids in randomized positions in 3D. (**b**) Cell kinetics for the different types of cells in an example simulation. (**c**,**d**) The tumor in the example simulation after 3 days and 202 days of growth. Vessel units are shown in red, normoxic cells in black, hypoxic cells ($pO_2 < 10$ mmHg) in green and necrotic cells in brown. Vessel units "string" together to form whole vessels that undergo branching in a chaotic fashion. Tumor cells close to vessels are normoxic, cells further from vessels are hypoxic and cells pushed further than *ND* from a vessel become necrotic. This example simulation started with approximately 70 CSCs and ended with $RVV = 0.4\%$, using $p_0 = 40$ mmHg, $ND = 180$ μm and CSC symmetric division probability = 2%. (**e**,**f**) Sections of tumors with the same vasculature structure but different blood oxygenation (via p_0 and *ND*) ((**e**) $p_0 = 60$ mmHg and $ND = 220$ μm; (**f**) $p_0 = 30$ mmHg and $ND = 120$ μm). (**e**,**f**) were adapted with permission from ref. 10.

it is removed, and so on. When a differentiated cell is removed, there is a chain of cell movement inward to fill the vacant position. The same occurs when a necrotic cell is resorbed from the tumor, which occurs when its age reaches the necrotic cell resorption time (Table 1).

For a more in-depth description of the computational model methods, please refer to ref. 10.

Input parameter	Values	Type	References
Cell (and blood vessel) diameter	14–20 μm	Distribution	11, 36, 37
RVV	2–10%	Single value	11, 12
Oxygen tension	$p(r) = p_0 \frac{ND^2}{R_0^2}\left(2\ln\left(\frac{ND}{r}\right) - 1 + \frac{r^2}{ND^2}\right)$ where, $a = 10$ μm	Distribution	38, 39
p_0	20–100 mmHg	Single value	11, 13
ND	80–300 μm	Single value	14, 15
CCT under normoxia	33 ± 5.9 h (Gaussian)	Distribution	40, 41
CCT adjustment factor with hypoxia	$y(\mathrm{pO_2}) = 1 + 1.8e^{-0.2\mathrm{pO_2}}$	Distribution	40, 42, 43
Hypoxia-induced quiescence	$\mathrm{pO_2} < 1$ mmHg	Single value	44–46
Necrotic cell resorption time	3–6 days depending on local necrotic volume	Distribution	47, 48
CSC symmetric division probability	~2% pre-treatment, possibly >50% during accelerated repopulation	Single value	6–8, 30, 40
Differentiated cell loss frequency	80%	Single value	40, 41

Table 1. Tumor growth model input parameters and values for HNSCC.

Study of tumor oxygenation. The HNSCC tumor model was used in this work to quantify how the vascularity (*RVV*) and the blood oxygenation (p_0 and *ND*) affect the tumor oxygenation. Noting that HNSCC exhibit *RVV* from 2–10%[11,12], p_0 from 20–100 mmHg[11,13] and *ND* from 80–300 μm[14,15], three combinations of (p_0, *ND*) were considered, namely (20 mmHg, 80 μm), (40 mmHg, 180 μm) and (100 mmHg, 300 μm), depicting scenarios of poor, moderate and high blood oxygenation, respectively. In each case, the model input parameter RVV_0 (which would be equal to the tumor *RVV* if the tumor grew with spherical symmetry, but due to preferential growth along the vessels, *RVV* ends up larger than RVV_0) was varied from 0–10% in 1% increments (for the (20 mmHg, 80 μm) combination, RVV_0 values of 0.25% and 0.5% were also used), yielding values of tumor *RVV* from 0–16%. The tumor *RVV* was determined at the end of the growth simulation as the ratio of the number of vessel units to the number of living cells + necrotic cells + vessel units (×100%). Tumor growth simulations began with approximately 70 CSCs and ended with a final tumor diameter of 1 mm (10^4–10^5 cells). A CSC symmetric division probability of 50% was used in the tumor oxygenation study for fast computations, since this affects the doubling time and CSC proportion but does not greatly affect the tumor oxygenation.

The tumor oxygenation at the end of the growth simulation was evaluated using several different descriptors. The hypoxic proportions HP_{10}, HP_5, $HP_{2.5}$ and HP_1 were determined, which were the proportions of living cells with $\mathrm{pO_2}$ <10, 5, 2.5 and 1 mmHg, respectively. The mean and median cellular $\mathrm{pO_2}$ in living cells were also calculated. The volume proportion of necrosis (necrotic volume) was evaluated as the ratio of the number of necrotic cells to the number of living cells + necrotic cells + vessel units (×100%).

Study of tumor growth rate and CSC proportion. The HNSCC tumor model was then used to explore the effects of tumor oxygenation and CSC symmetric division on the doubling time and the CSC proportion. The doubling time, T_d, in the final days (in "tumor time") of the tumor growth simulation was evaluated as follows. Let *N(t)* denote the number of living and necrotic cells in the tumor at time *t*. Then the average slope, *k*, of the curve ln*N* vs *t* in the final few days of the simulation was used to calculate the final doubling time according to:

$$T_d = \ln 2/k$$

The effect of tumor hypoxia and necrosis on doubling time was observed in the simulations from the tumor oxygenation study. Since these simulations all used a CSC symmetric division probability of 50%, the relative variation in the doubling time was reported.

To investigate the effects of the CSC symmetric division probability on the doubling time and the CSC proportion, CSC symmetric division probabilities of 2%, 5%, 10%, 25%, 50%, 75% and 100% were simulated for the two extremes of HNSCC tumor oxygenation. The most oxygenated case was *RVV* = 10%, p_0 = 100 mmHg and *ND* = 300 μm and the most hypoxic case was *RVV* = 2%, p_0 = 20 mmHg and *ND* = 80 μm. In order to achieve approximately these *RVV*s, the model parameter RVV_0 was set to 8.2% and 0.75% respectively. Again, the simulations began with approximately 70 CSCs and ended with a final tumor diameter of 1 mm. Three simulations (n = 3) were conducted for each value of CSC symmetric division probability for both well oxygenated and severely hypoxic cases (with the exception of the severely hypoxic case with CSC symmetric division probability 10%, for which n = 4 was used). The CSC proportion was calculated as the ratio of the number of CSCs to the number of living cells (×100%). The doubling times and CSC proportions were plotted using the mean value of the 3 (or 4) simulation runs and with error bars corresponding to the standard error of the mean (SEM). Prism (version 7, GraphPad Software, Inc.) was used to determine whether statistical significance had been reached.

Equipment. Simulations were performed on the Phoenix cluster at the University of Adelaide[16] using as many as 12 cores and 10 GB of RAM.

Data availability. The data that support the finding of this study are available from the corresponding author upon reasonable request.

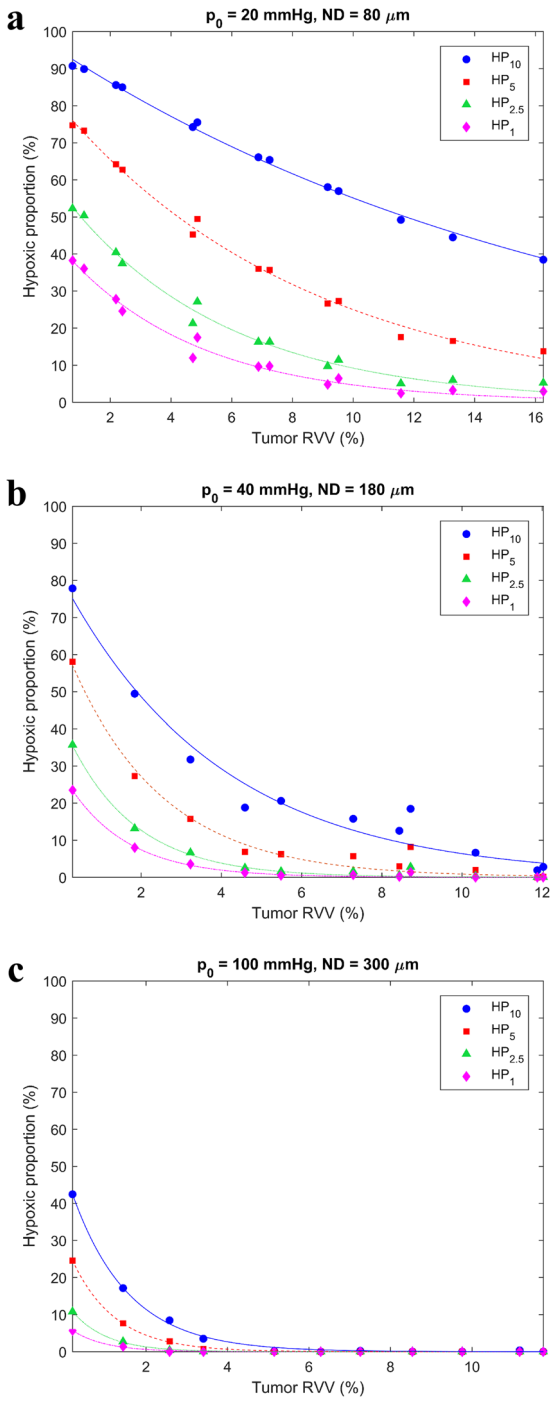

Figure 3. Variation of hypoxic proportions with tumor vascularity for (**a**) poor blood oxygenation ($p_0 = 20$ mmHg and $ND = 80$ µm), (**b**) moderate blood oxygenation ($p_0 = 40$ mmHg and $ND = 180$ µm) and (**c**) high blood oxygenation ($p_0 = 100$ mmHg and $ND = 300$ µm).

Code availability. The code used to analyze the data is available from the corresponding author upon reasonable request. The code used to perform tumor growth simulations has not been made publicly available at this time.

Results

The effects of tumor vascularity and blood oxygenation on tumor oxygenation. With increasing tumor vascularity (*RVV*) and increasing blood oxygenation (p_0 and *ND*), the hypoxic proportions and necrotic volume decreased, while the mean and median cellular pO_2 increased (Figs 3 and 4). According to clinical data, HNSCC exhibit *RVV* from 2–10%[11,12], p_0 from 20–100 mmHg[11,13] and *ND* from 80–300 µm[14,15]. With these constraints, the tumor growth model predicted values of HP_1 from 0–29%, $HP_{2.5}$ from 0–42%, HP_5 from 0–65%, HP_{10}

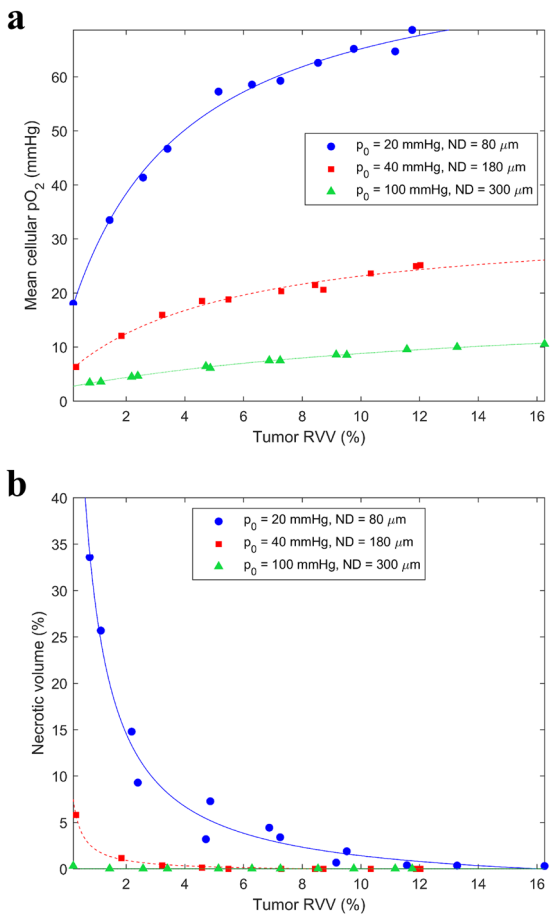

Figure 4. Variation of (**a**) mean cellular pO_2 and (**b**) necrotic volume with tumor vascularity for poor, moderate and high blood oxygenation.

from 0–86%, mean cellular pO_2 from 4.4–65.2 mmHg, median cellular pO_2 from 2.9–67.5 mmHg and necrotic volume from 0–15% for HNSCC.

For poor blood oxygenation ($p_0 = 20$ mmHg and $ND = 80$ μm), there was necrosis present even at 10% *RVV*. Note that the same hypoxic proportion could arise from different combinations of *RVV*, p_0 and *ND*. For example, (*RVV*, p_0, *ND*) combinations of (11.8%, 20 mmHg, 80 μm), (2.7%, 40 mmHg, 180 μm) and (0.4%, 100 mmHg, 300 μm) each yielded a HP_5 of 20%.

The effects of hypoxia and CSC symmetric division on the tumor growth rate and the CSC proportion. The doubling time decreased with increasing tumor vascularity (*RVV*) and increasing blood oxygenation (p_0 and *ND*) (Fig. 5a). For HNSCC (*RVV* = 2–10%, $p_0 = 20$–100 mmHg, $ND = 80$–300 μm), the doubling time increased by a factor of 3 from well oxygenated tumors to the most hypoxic tumors. The doubling time was considerably affected, even without the presence of necrosis, by low cellular pO_2 effects such as increased CCTs and cell quiescence (Fig. 5b,c).

The doubling time decreased with increasing probability of CSC symmetric division probability (Fig. 6a). The mean doubling time was 2.6–3.3 times larger for the most hypoxic tumors than for well oxygenated tumors of HNSCC across all values of CSC symmetric division probability. The difference in doubling time between severely hypoxic and well oxygenated conditions was significant (p-value < 0.05 using unpaired t-test with Welch's correction) at every value of CSC symmetric division probability.

The CSC proportion increased with CSC symmetric division probability (Fig. 6b). The mean CSC proportion was 1–1.14 times larger for the most hypoxic tumors than for well oxygenated tumors across all values of CSC symmetric division probability. The difference in CSC proportion between severely hypoxic and well oxygenated conditions was significant (p-value < 0.05 using unpaired t-test with Welch's correction) at every value of CSC symmetric division probability except 2%.

A CSC symmetric division probability of 2% yielded a mean ± SEM doubling time of 44.5 ± 0.8 days (n = 3) for well oxygenated tumors and 129 ± 16 days (n = 3) for the most hypoxic tumors. The CSC proportion was approximately 6% in each case (6.11 ± 0.01% (n = 3) and 6.3 ± 0.2% (n = 3) respectively). An increase in the CSC symmetric division probability to 50% yielded a doubling time of 2.28 ± 0.03 days (n = 3) for well oxygenated tumors and 6.3 ± 0.6 days (n = 3) for the most hypoxic tumors. The CSC proportions were 30.49 ± 0.06% (n = 3) and 34.8 ± 0.3% (n = 3) respectively.

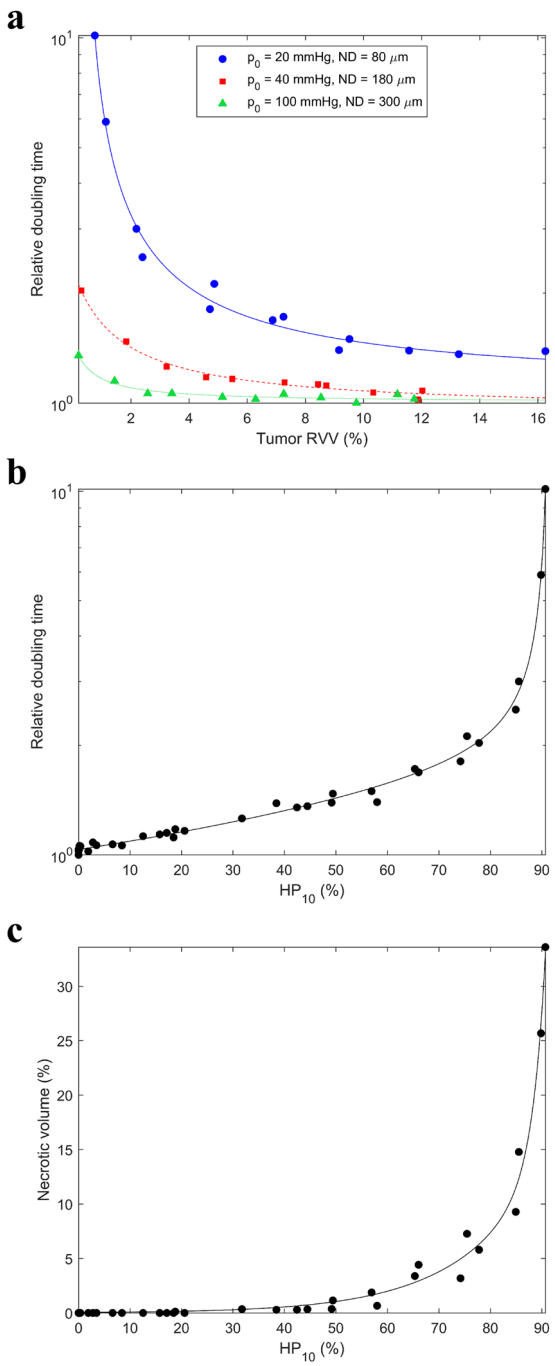

Figure 5. Relative variation in the doubling time with (**a**) tumor vascularity and (**b**) HP_{10}. (**c**) Variation in the necrotic volume with HP_{10}.

Discussion

Several studies have reported pO_2 measurements in human HNSCC using invasive polarographic needle electrodes. The results from some of these studies are collated in Table 2. Since accessing a tissue block from the HNSCC primary tumor can be difficult, these studies often took measurements from sufficiently large lymph node metastases originating from a primary HNSCC. The table also lists measurements of necrotic volume in HNSCCs, as assessed by CT scan or MRI. The results from the current study are included at the bottom for comparison.

The values of median pO_2, mean pO_2, $HP_{2.5}$, HP_5 and HP_{10} produced by the tumor growth model using *RVV* from 2–10%, p_0 from 20–100 mmHg and *ND* from 80–300 µm are in line with these clinical measurements. This assists in model validation since these values for *RVV*, p_0 and *ND* are based on clinical data for HNSCC. The clinical tumor oxygenation data overall indicate well oxygenated tumors are rare and lower values of *RVV*, p_0 and *ND* are typical.

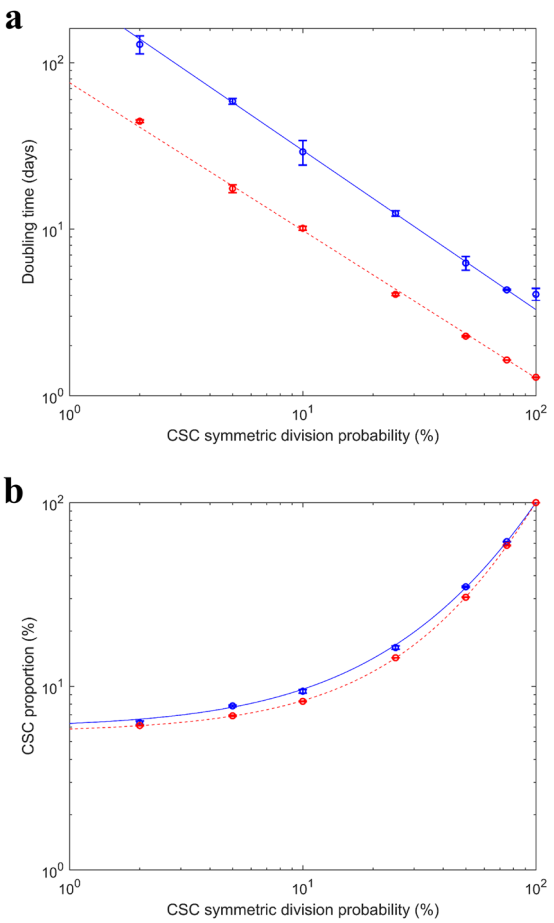

Figure 6. Variation of (**a**) doubling time and (**b**) CSC proportion with CSC symmetric division probability for severely hypoxic tumors (mean ± SD $RVV = 2.2 \pm 0.2\%$ (n = 22), $p_0 = 20$ mmHg, $ND = 80\,\mu m$) (blue) and well oxygenated tumors (mean ± SD $RVV = 10.5 \pm 0.6\%$ (n = 21), $p_0 = 100$ mmHg, $ND = 300\,\mu m$) (red) of HNSCC.

The clinical studies sometimes reported large values of necrotic volume outside the range produced by the tumor growth model. This is likely because the clinical studies observed macroscopic regions of necrosis. Macroscopic necrosis occurs when tumors become large and whole macroscopic regions of the tumor lose blood supply. The tumor growth model only produced necrosis at the microscopic scale (between distant blood vessels) in the sub-clinical sized tumors used in this study.

Pre-treatment doubling times of HNSCC have been obtained in studies that measured tumor growth while patients waited for treatment. Jensen *et al.*[17] found that in the time between diagnostic scan (MR or CT) and treatment planning CT scan (median 28 days, range 5–95 days), the median doubling time was 99 days (range 15 to > 234 days) for 61 patients with HNSCC. Waaijer *et al.*[18] found that in the time between diagnostic and treatment planning CT scans (mean 34 days), the mean doubling time was 96 days (range 21–256 days) in 13 patients with oropharyngeal SCC. Murphy *et al.*[19] found that in the time between diagnostic (MRI or CT) and planning or interval CT scan (median 35 days, range 8–314 days), the median doubling time was 94 days (range 16–6931 days) in 85 oropharyngeal SCC. These average clinically measured pre-treatment doubling times are similar to those produced by the presented tumor growth model under moderately hypoxic conditions and with a CSC symmetric division probability of approximately 2% (recall the doubling times obtained with the tumor model using 2% CSC symmetric division averaged 45 days for well oxygenated tumors and 130 days for severely hypoxic tumors).

In the current work, a CSC symmetric division probability of 2% yielded a proportion of CSCs in the tumor of approximately 6% for all HNSCC tumor oxygenation levels. Methods have been established for identifying CSCs in HNSCC. For example, cells that express markers such as ALDH1, CD133 and CD44 exhibit CSC-like properties, while others do not[9,20–24]. Cells that efficiently efflux Hoechst 33342 dye, termed side-population (SP) cells, are also CSC-like[25,26]. Chinn *et al.*[27] reported a mean $CD44^{high}$ content of 10.8% (range 0–84.5%) for 40 patient-derived primary HNSCCs. In 10 human oral SCC tissue samples, Zhang *et al.*[28] found $CD133^+$ content of 1–3%. Lu *et al.*[29] identified approximately 2.1% SP cells in 7 human primary HNSCC samples, and all SP cells were also $CD133^+$. The CSC proportion of 6% obtained by the tumor growth model using 2% CSC symmetric division, is close to these clinical estimates for HNSCC pre-treatment and results from other models (e.g. 5.9% from Marcu & Marcu[30]).

	Tumor site	Median pO_2 (mmHg) in the tumor	Mean pO_2 (mmHg) in the tumor	$HP_{2.5}$ (%)	HP_5 (%)	HP_{10} (%)	Necrotic volume (%)
King *et al.*[49]	Metastastic cervical nodes from HNSCC	—	—	—	—	—	mean ± SD 19.09 ± 13.94 (n = 106)
Kong *et al.*[50]	Primary HNSCC	mean 14.0 (n = 82)	—	—	—	—	—
Gagel *et al.*[51]	lymph node metastases from HNSCC	mean ± SD 12.5 ± 10.3; range 0.1–41.1 (n = 38)	mean ± SD 17.6 ± 7.3; range 8.8–36.0 (n = 38)	mean ± SD 29.3 ± 18.4; range 0.0–58.5 (n = 38)	mean ± SD 38.4 ± 18.1; range 7.0–73.6 (n = 38)	mean ± SD 48.9 ± 18.2; range 13.0–78.7 (n = 38)	—
Nordsmark *et al.*[3]	Neck node metastases from HNSCC or primary HNSCC	median 9; range 0–62 (n = 397)	—	median 19; range 0–97 (n = 397)	median 38; range 0–100 (n = 397)	—	—
Kuhnt *et al.*[52]	Primary HNSCC	—	—	—	—	—	mean ± SD 18 ± 30 (n = 51)*
Gagel *et al.*[53]	neck lymph node metastases from HNSCC	mean 10.7; 95% CI of mean 5.2–16.1; range 0.4–22.4 (n = 16)	mean 16.3; 95% CI of mean 12.1–20.5; range 9.0–27.4 (n = 16)	mean 35.9; 95% CI of mean 24.1–47.6; range 0.5–58.1 (n = 16)	mean 44.3; 95% CI of mean 34.0–54.5; range 27.6–66.5 (n = 16)	mean 52.5; 95% CI of mean 42.2–62.9; range 33.7–77.5 (n = 16)	—
Terris *et al.*[54]	cervical lymph node metastases from HNSCC	—	mean ± SD 20.8 ± 13.7 (n = 50)*	mean ± SD 20.8 ± 25.7 (n = 42)	—	—	mean ± SD 14.5 ± 11.2 (n = 42)
Brizel *et al.*[55]	Primary HNSCC or cervical lymph node from HNSCC	mean 4.5; range 0–60 (n = 63)*	—	—	—	—	—
Brizel *et al.*[5]	Primary HNSCC or neck node metastases from HNSCC	mean 11.2; range 0.4–60 (n = 28)	—	—	—	—	—
Nordsmark *et al.*[4]	Lymph node metastases from HNSCC (n = 34) or primary HNSCC (n = 1)	mean ± SD 14.7 ± 10.8; median 14; range 1–35 (n = 35)	—	mean ± SD 22 ± 24; median 15; range 0–95 (n = 35)	mean ± SD 35 ± 29; median 29; range 0–100 (n = 35)	—	—
The current work		range 2.9–67.5	range 4.4–65.2	range 0–42	range 0–65	range 0–86	range 0–15

Table 2. Clinical data for tissue pO_2 and necrotic volume in human HNSCC. *Mean ± SD of two or more subgroups were combined with appropriate error propagation.

Tumors respond to treatment by undergoing accelerated repopulation. In an analysis of 5 clinical trials containing a total of 2653 patients, Pedicini *et al.*[31] using an analytical/graphical method arrived at a best estimate of 3.5 days (95% CI 3.1–3.9 days) for the doubling time of HNSCC during radiotherapy. The loss of asymmetric division by CSCs is believed to be a key mechanism behind accelerated repopulation[6–8, 30, 32, 33]. In the tumor growth model, a CSC symmetric division probability of 50% yielded doubling times from 2.3 to 6.1 days, depending on the tumor oxygenation, which are in line with the estimate by Pedicini *et al.* A 50% CSC symmetric division probability yielded CSC proportions from 30–35% in the current work. To the authors' knowledge, there are no clinical studies in the literature that measured the CSC proportion in HNSCC in patients during accelerated repopulation. In the model by Marcu & Marcu[30], the CSC proportions obtained were higher than in the current work for the same CSC symmetric division probability. For example, in their work, 10%, 20% and 30% symmetric division yielded 25%, 35% and 45% CSCs, respectively (recall in the current work, 10% and 25% symmetric division yielded approximately 9% and 15% CSCs, respectively). Conversely, the CSC proportions were slightly lower in the HYP-RT model by Harriss-Phillips *et al.*[33] than in the current work. In that model, 30% symmetric division yielded just 10% CSCs. Most *in vitro* studies of various cancer types show a 3–5 times increase in CSCs post single irradiation[24].

Conclusion

The current work established how the tumor oxygenation varies with vascularity and blood oxygenation, how the doubling time varies with tumor oxygenation and CSC symmetric division probability, and how the CSC proportion varies with CSC symmetric division probability in a 4D cellular model of HNSCC tumor growth. The doubling time varied by a factor of ~3 from well oxygenated tumors to the most severely hypoxic tumors of HNSCC. A CSC symmetric division probability of 2% yielded clinically relevant doubling times and CSC proportions for HNSCC before treatment, while a value of 50% produced the doubling times observed in the clinic for HNSCC undergoing accelerated repopulation. This 50% probability yielded CSC proportions from 30–35%.

In future work, the tumor growth model will be extended to a radiotherapy simulation tool for both low and high LET beams. The cellular geometry will be imported into Geant4[34] and irradiated in Monte Carlo track structure simulations. Radiolysis will be simulated along the particle tracks. Ionisation events and generated $^{\bullet}OH$ species will be clustered in the cell nuclei to predict the complexity and extent of DNA damage to each cell. The cellular pO_2 will affect how efficiently $^{\bullet}OH$ attack to the base of DNA is translated to strand breakage[35]. Irradiation will be simulated in fractions separated by time intervals, during which the tumor growth model will translate DNA damage to cell death while also regrowing the tumor.

References

1. Carmeliet, P. & Jain, R. K. Angiogenesis in cancer and other diseases. *Nature* **407**, 249–257 (2000).
2. Forster, J. C., Harriss-Phillips, W. M., Douglass, M. J. & Bezak, E. A review of the development of tumor vasculature and its effects on the tumor microenvironment. *Hypoxia (Auckl)* **5**, 21–32 (2017).
3. Nordsmark, M. *et al*. Prognostic value of tumor oxygenation in 397 head and neck tumors after primary radiation therapy. An international multi-center study. *Radiother. Oncol.* **77**, 18–24 (2005).
4. Nordsmark, M., Overgaard, M. & Overgaard, J. Pretreatment oxygenation predicts radiation response in advanced squamous cell carcinoma of the head and neck. *Radiother. Oncol.* **41**, 31–39 (1996).
5. Brizel, D. M., Sibley, G. S., Prosnitz, L. R., Scher, R. L. & Dewhirst, M. W. Tumor hypoxia adversely affects the prognosis of carcinoma of the head and neck. *Int. J. Radiat. Oncol. Biol. Phys.* **38**, 285–289 (1997).
6. Dörr, W. Three A's of repopulation during fractionated irradiation of squamous epithelia: Asymmetry loss, Acceleration of stem-cell divisions and Abortive divisions. *Int. J. Radiat. Biol.* **72**, 635–643 (1997).
7. Trott, K. R. & Kummermehr, J. Rapid repopulation in radiotherapy: a debate on mechanism. Accelerated repopulation in tumours and normal tissues. *Radiother. Oncol.* **22**, 159–160 (1991).
8. Withers, H. R. & Elkind, M. M. Radiosensitivity and fractionation response of crypt cells of mouse jejunum. *Radiat. Res.* **38**, 598–613 (1969).
9. Krishnamurthy, S. & Nör, J. E. Head and neck cancer stem cells. *J. Dent. Res.* **91**, 334–340 (2012).
10. Forster, J. C., Douglass, M. J., Harriss-Phillips, W. M. & Bezak, E. Development of an in silico stochastic 4D model of tumor growth with angiogenesis. *Med. Phys.* **44**, 1563–1576 (2017).
11. Amelink, A. *et al*. Non-invasive measurement of the morphology and physiology of oral mucosa by use of optical spectroscopy. *Oral Oncol.* **44**, 65–71 (2008).
12. Pazouki, S. *et al*. The association between tumour progression and vascularity in the oral mucosa. *J. Pathol.* **183**, 39–43 (1997).
13. Carreau, A., El Hafny-Rahbi, B., Matejuk, A., Grillon, C. & Kieda, C. Why is the partial oxygen pressure of human tissues a crucial parameter? Small molecules and hypoxia. *J. Cell. Mol. Med.* **15**, 1239–1253 (2011).
14. Beasley, N. J. *et al*. Carbonic anhydrase IX, an endogenous hypoxia marker, expression in head and neck squamous cell carcinoma and its relationship to hypoxia, necrosis, and microvessel density. *Cancer Res.* **61**, 5262–5267 (2001).
15. Wijffels, K. I. *et al*. Vascular architecture and hypoxic profiles in human head and neck squamous cell carcinomas. *Br. J. Cancer* **83**, 674–683 (2000).
16. Phoenix High Performance Computing. *University of Adelaide* https://www.adelaide.edu.au/phoenix/ (2017)
17. Jensen, A. R., Nellemann, H. M. & Overgaard, J. Tumor progression in waiting time for radiotherapy in head and neck cancer. *Radiother. Oncol.* **84**, 5–10, doi:10.1016/j.radonc.2007.04.001 (2007).
18. Waaijer, A. *et al*. Waiting times for radiotherapy: consequences of volume increase for the TCP in oropharyngeal carcinoma. *Radiother. Oncol.* **66**, 271–276 (2003).
19. Murphy, C. T. *et al*. Pre-treatment tumor-specific growth rate as a temporal biomarker that predicts treatment failure and improves risk stratification for oropharyngeal cancer. *Oral Oncol.* **51**, 1034–1040 (2015).
20. Islam, F., Gopalan, V., Wahab, R., Smith, R. A. & Lam, A. K. Cancer stem cells in oesophageal squamous cell carcinoma: Identification, prognostic and treatment perspectives. *Crit. Rev. Oncol. Hematol.* **96**, 9–19 (2015).
21. Zhang, Z., Filho, M. S. & Nör, J. E. The biology of head and neck cancer stem cells. *Oral Oncol.* **48**, 1–9 (2012).
22. Albers, A. E. *et al*. Stem cells in squamous head and neck cancer. *Crit. Rev. Oncol. Hematol.* **81**, 224–240 (2012).
23. Prince, M. E. & Ailles, L. E. Cancer stem cells in head and neck squamous cell cancer. *J. Clin. Oncol.* **26**, 2871–2875 (2008).
24. Reid, P., Wilson, P., Li, Y., Marcu, L. G. & Bezak, E. Current Understanding of Cancer Stem Cells: Review of their Radiobiology and role in Head and Neck Cancers. *Head Neck* (2017).
25. Tabor, M. H. *et al*. Head and neck cancer stem cells: the side population. *Laryngoscope* **121**, 527–533 (2011).
26. Sun, G. *et al*. Identification of stem-like cells in head and neck cancer cell lines. *Anticancer Res.* **30**, 2005–2010 (2010).
27. Chinn, S. B. *et al*. Cancer stem cells: mediators of tumorigenesis and metastasis in head and neck squamous cell carcinoma. *Head Neck* **37**, 317–326 (2015).
28. Zhang, Q. *et al*. A subpopulation of CD133(+) cancer stem-like cells characterized in human oral squamous cell carcinoma confer resistance to chemotherapy. *Cancer Lett.* **289**, 151–160 (2010).
29. Lu, B. C. *et al*. Elevated expression of Nrf2 mediates multidrug resistance in CD133 + head and neck squamous cell carcinoma stem cells. *Oncol. Lett.* **12**, 4333–4338 (2016).
30. Marcu, L. G. & Marcu, D. In silico modelling of a cancer stem cell-targeting agent and its effects on tumour control during radiotherapy. *Sci. Rep.* **30**, 32332 (2016).
31. Pedicini, P., Caivano, R., Fiorentino, A. & Strigari, L. Clinical radiobiology of head and neck cancer: the hypothesis of stem cell activation. *Clin. Transl. Oncol.* **17**, 469–476 (2015).
32. Harriss-Phillips, W. M., Bezak, E. & Yeoh, E. K. Monte Carlo radiotherapy simulations of accelerated repopulation and reoxygenation for hypoxic head and neck cancer. *Br. J. Radiol.* **84**, 903–918 (2011).
33. Harriss-Phillips, W. M., Bezak, E. & Yeoh, E. The HYP-RT Hypoxic Tumour Radiotherapy Algorithm and Accelerated Repopulation Dose per Fraction Study. *Comput. Math. Methods Med.* **2012**, 363564 (2012).
34. Allison, J. *et al*. Recent developments in GEANT4. *Nucl. Instrum. Methods Phys. Res. A* **835**, 186–225 (2016).
35. Wardman, P. The importance of radiation chemistry to radiation and free radical biology (The 2008 Silvanus Thompson Memorial Lecture). *Br. J. Radiol.* **82**, 89–104 (2009).
36. Vlad, R. M., Alajez, N. M., Giles, A., Kolios, M. C. & Czarnota, G. J. Quantitative ultrasound characterization of cancer radiotherapy effects *in vitro*. *Int. J. Radiat. Oncol. Biol. Phys.* **72**, 1236–1243 (2008).
37. Amelink, A., Sterenborg, H. J., Bard, M. P. & Burgers, S. A. *In vivo* measurement of the local optical properties of tissue by use of differential path-length spectroscopy. *Opt. Lett.* **29**, 1087–1089 (2004).
38. Tannock, I. F. Oxygen diffusion and the distribution of cellular radiosensitivity in tumours. *Br. J. Radiol.* **45**, 515–524 (1972).
39. Carlson, D. J., Keall, P. J., Loo, B. W. Jr., Chen, Z. J. & Brown, J. M. Hypofractionation results in reduced tumor cell kill compared to conventional fractionation for tumors with regions of hypoxia. *Int. J. Radiat. Oncol. Biol. Phys.* **79**, 1188–1195 (2011).
40. Harriss, W. M. Monte Carlo Modelling of Tumour Growth, Hypoxia and Radiotherapy in Head and Neck Squamous Cell Carcinoma (PhD Thesis). University of Adelaide, Adelaide (2011).
41. Marcu, L. G. Tumour repopulation and the role of abortive division in squamous cell carcinomas during chemotherapy. *Cell Prolif.* **47**, 318–325 (2014).
42. Hirst, D. G. & Denekamp, J. Tumour cell proliferation in relation to the vasculature. *Cell Tissue Kinet.* **12**, 31–42 (1979).
43. Alarcón, T., Byrne, H. M. & Maini, P. K. A mathematical model of the effects of hypoxia on the cell-cycle of normal and cancer cells. *J. Theor. Biol.* **229**, 395–411 (2004).
44. Amellem, O. & Pettersen, E. O. Cell inactivation and cell cycle inhibition as induced by extreme hypoxia: the possible role of cell cycle arrest as a protection against hypoxia-induced lethal damage. *Cell Prolif.* **24**, 127–141 (1991).
45. Douglas, R. M. *et al*. Hypoxia induces major effects on cell cycle kinetics and protein expression in Drosophila melanogaster embryos. *Am. J. Physiol. Regul. Integr. Comp. Physiol.* **288**, R511–R521 (2005).
46. Royds, J. A., Dower, S. K., Qwarnstrom, E. E. & Lewis, C. E. Response of tumour cells to hypoxia: role of p53 and NFkB. *Mol. Pathol.* **51**, 55–61 (1998).

47. Borkenstein, K., Levegrün, S. & Peschke, P. Modeling and computer simulations of tumor growth and tumor response to radiotherapy. *Radiat. Res.* **162**, 71–83 (2004).
48. Harting, C., Peschke, P., Borkenstein, K. & Karger, C. P. Single-cell-based computer simulation of the oxygen-dependent tumour response to irradiation. *Phys. Med. Biol.* **52**, 4775–4789 (2007).
49. King, A. D. *et al.* Cervical nodal metastases from head and neck squamous cell carcinoma: MRI criteria for treatment assessment. *Head Neck* **38**, E1598–E1604 (2016).
50. Kong, C. S. *et al.* The relationship between human papillomavirus status and other molecular prognostic markers in head and neck squamous cell carcinomas. *Int. J. Radiat. Oncol. Biol. Phys.* **74**, 553–561 (2009).
51. Gagel, B. *et al.* pO polarography, contrast enhanced color duplex sonography (CDS), [18F] fluoromisonidazole and [18F] fluorodeoxyglucose positron emission tomography. *BMC Cancer* **7**, 113 (2007).
52. Kuhnt, T. *et al.* Impact of tumor control and presence of visible necrosis in head and neck cancer patients treated with radiotherapy or radiochemotherapy. *J. Cancer Res. Clin. Oncol.* **131**, 758–764 (2005).
53. Gagel, B. *et al.* pO(2) Polarography versus positron emission tomography ([(18)F] fluoromisonidazole, [(18)F]-2-fluoro-2′-deoxyglucose). *An appraisal of radiotherapeutically relevant hypoxia. Strahlenther. Onkol.* **180**, 616–622 (2004).
54. Terris, D. J. Head and neck cancer: the importance of oxygen. *Laryngoscope* **110**, 697–707 (2000).
55. Brizel, D. M., Dodge, R. K., Clough, R. W. & Dewhirst, M. W. Oxygenation of head and neck cancer: changes during radiotherapy and impact on treatment outcome. *Radiother. Oncol.* **53**, 113–117 (1999).

Author Contributions

J.F. conceptualized and developed the model under the supervision of M.D., W.H. and E.B., based on their previous work and the idea of a 4D spatial-temporal tumor model. All authors were involved in manuscript preparation. While J.F. wrote the bulk of the manuscript, M.D., W.H. and E.B. provided input, feedback and revisions.

Additional Information

Competing Interests: The authors declare that they have no competing interests.

Publisher's note: Springer Nature remains neutral with regard to jurisdictional claims in published maps and institutional affiliations.

5.3 Discussion and Conclusion

The behaviour of the tumour growth model was documented comprehensively. While HNSCC tumours can have RVV from 2 to 10%, p_0 from 20 to 100 mmHg and ND from 80 to 300 μm [56], they are typically very hypoxic, requiring these parameters to take values near their lower limits. Our attention now turns to the dose fraction module of the S^2RT model.

5.3.1 Erratum

- In the legend of Figure 4(**a**), the first and third entries were accidentally reversed.

6

Monte Carlo Simulation of the Oxygen Effect in DNA Damage Induction by Ionizing Radiation

The publication [93] forms the basis of this chapter:

Forster JC, Douglass MJJ, Phillips WM, Bezak E. Monte Carlo Simulation of the Oxygen Effect in DNA Damage Induction by Ionizing Radiation. *Radiat Res.* 2018 Sep; 190(3):248-261. doi: 10.1667/RR15050.1.

6.1 Introduction and Motivation

The aim was to deliver dose to the multicellular tumour via Monte Carlo tracks, so that DNA damage could be simulated from track segments through cell nuclei. For this to be possible, the tracks must be accurate down to eV electron energies. It is also important to simulate the indirect effect of ionising radiation, so the chemical tracks from water radiolysis should also be simulated. These were achieved using Geant4-DNA.

First, an algorithm was developed to predict DNA damage from physical and chemical tracks simulated in Geant4-DNA. This is presented in the publication that proceeds. The algorithm incorporates the oxygen (enhancement) effect, modelling the influence of pO_2 on the conversion of DNA radicals to strand breaks. This was

important to include, since tumour hypoxia is a focus and strength of the model (a connected vasculature was modelled, obtaining realistic spatial distributions of chronic hypoxia).

6.2 Statement of Contribution

6.2.1 Conception

The idea to develop an algorithm to predict DNA damage from Monte Carlo tracks originated from Michael Douglass and Eva Bezak. This model and its methods, including the way the indirect effect and the oxygen effect were modelled, were conceived by Jake Forster under the supervision of Eva Bezak, Wendy Phillips and Michael Douglass.

6.2.2 Realisation

Jake Forster developed the model (i.e. wrote the code), wrote the code to run the simulations to acquire data, wrote the code to run the simulations on a supercomputer, ran the simulations on a supercomputer, analysed the data and made the plots for visualising data. The manuscript was evaluated by Eva Bezak, Wendy Phillips and Michael Douglass for data accuracy, critical appraisal, conclusions reached and general structure and flow.

6.2.3 Documentation

The manuscript was primarily written by Jake Forster, who also prepared the figures. Wendy Phillips, Michael Douglass and Eva Bezak provided input, feedback and revisions.

Statement of Authorship

Title of Paper	Monte Carlo Simulation of the Oxygen Effect in DNA Damage Induction by Ionizing Radiation
Publication Status	☑ Published ☐ Accepted for Publication ☐ Submitted for Publication ☐ Unpublished and Unsubmitted w ork w ritten in manuscript style
Publication Details	Forster JC, Douglass MJJ, Phillips WM, Bezak E. *Radiat Res.* 2018; 190(3):248-261. doi: 10.1667/RR15050.1.

Principal Author

Name of Principal Author (Candidate)	Jake Cameron Forster
Contribution to the Paper	Conceived of the model methods, developed the model (i.e. wrote the code), wrote the code to run the simulations to acquire data, wrote the code to run the simulations on a supercomputer, ran the simulations on a supercomputer, analysed the data, made the plots for visualising data, wrote the manuscript, prepared the figures and acted as the corresponding author.
Overall percentage (%)	80%
Certification:	This paper reports on original research I conducted during the period of my Higher Degree by Research candidature and is not subject to any obligations or contractual agreements with a third party that would constrain its inclusion in this thesis. I am the primary author of this paper.
Signature	Date: 3-10-2018

Co-Author Contributions

By signing the Statement of Authorship, each author certifies that:

i. the candidate's stated contribution to the publication is accurate (as detailed above);

ii. permission is granted for the candidate in include the publication in the thesis; and

iii. the sum of all co-author contributions is equal to 100% less the candidate's stated contribution.

Name of Co-Author	Prof. Eva Bezak
Contribution to the Paper	Initial idea, general guidance and supervision and manuscript revision.
Overall percentage (%)	10%
Signature	Date: 3-10-2018

Name of Co-Author	Dr Wendy Phillips
Contribution to the Paper	General guidance and supervision and manuscript revision.
Overall percentage (%)	5%
Signature	Date: 3-10-2018

Name of Co-Author	Dr Michael Douglass		
Contribution to the Paper	Initial idea, general guidance and supervision and manuscript revision.		
Overall percentage (%)	5%		
Signature		Date	4-10-2018

RADIATION RESEARCH **190**, 248–261 (2018)
0033-7587/18 $15.00

DOI: 10.1667/RR15050.1

Monte Carlo Simulation of the Oxygen Effect in DNA Damage Induction by Ionizing Radiation

Jake C. Forster,[a,b,1,2] Michael J. J. Douglass,[a,b] Wendy M. Phillips[a,b] and Eva Bezak[a,c]

[a] *Department of Physics, University of Adelaide, North Terrace, Adelaide, South Australia 5005, Australia;* [b] *Department of Medical Physics, Royal Adelaide Hospital, North Terrace, Adelaide, South Australia 5000, Australia; and* [c] *Cancer Research Institute and School of Health Sciences, University of South Australia, Adelaide, South Australia, Australia*

Forster, J. C., Douglass, M. J. J., Phillips, W. M. and Bezak, E. Monte Carlo Simulation of the Oxygen Effect in DNA Damage Induction by Ionizing Radiation. *Radiat. Res.* 190, 248–261 (2018).

DNA damage induced by ionizing radiation exposure is enhanced in the presence of oxygen (the "oxygen effect"). Despite its practical importance in radiotherapy, the oxygen effect has largely been excluded from models that predict DNA damage from radiation tracks. A Monte Carlo-based algorithm was developed in MATLAB software to predict DNA damage from physical and chemical tracks through a cell nucleus simulated in Geant4-DNA, taking into account the effects of cellular oxygenation (pO_2) on DNA radical chemistry processes. An initial spatial distribution of DNA base and sugar radicals was determined by spatially clustering direct events (that deposited at least 10.79 eV) and hydroxyl radical ($^{\bullet}OH$) interactions. The oxygen effect was modeled by increasing the efficiency with which sugar radicals from direct-type effects were converted to strand breaks from 0.6 to 1, the efficiency with which sugar radicals from the indirect effect were converted to strand breaks from 0.28 to 1 and the efficiency of base-to-sugar radical transfer from $^{\bullet}OH$-mediated base radicals from 0 to 0.03 with increasing pO_2 from 0 to 760 mmHg. The DNA damage induction algorithm was applied to tracks from electrons, protons and alphas with LET values from 0.2 to 150 keV/μm under different pO_2 conditions. The oxygen enhancement ratio for double-strand break induction was 3.0 for low-LET radiation up to approximately 15 keV/μm, after which it gradually decreased to a value of 1.3 at 150 keV/μm. These values were consistent with a range of experimental data published in the literature. The DNA damage yields were verified using experimental data in the literature and results from other theoretical models. The spatial clustering approach developed in this work has low memory requirements and may be suitable for particle tracking simulations with a large number of cells.

INTRODUCTION

Ionizing radiation can damage DNA through direct-type effects and the indirect effect (*1, 2*). Direct-type effects refer to ionizations and excitations of DNA (direct effect) and water in its first hydration layer (quasi-direct effect) that produce radical anions/cations (electrons/holes). Electron/hole transfer can occur from the water to DNA or from one DNA component to another before the electrons/holes are trapped by protonation/deprotonation, producing neutral DNA radicals (*3–6*). DNA radicals ultimately give rise to various forms of DNA damage including single- and double-strand breaks (SSBs and DSBs), oxidized bases, abasic sites and crosslinks (DNA-protein, inter- and intra-strand) (*1, 7–11*). The indirect effect refers to the interaction of radiation with bulk water, producing radical species that in turn react with DNA. Of the radical species generated, the hydroxyl radical ($^{\bullet}OH$) is the most reactive with DNA (*8*). $^{\bullet}OH$ reacts with DNA by hydrogen atom abstraction, forming a DNA radical with an $^{\bullet}OH$-adduct.

The ''oxygen effect'' is the increase in radiation-induced cell killing under oxic conditions compared to anoxic conditions. This occurs because, through reactions with oxygen, the initial DNA radicals are more likely to follow chemical pathways that end in strand breaks (SBs) (*1, 12–15*). Oxygen reacts with base radicals to form base peroxyl radicals and reacts with sugar (2′-deoxyribose) radicals to produce sugar peroxyl radicals (*2*). Noting that a sugar radical is required to produce a strand break (*2*), there are thought to be two primary mechanisms driving the oxygen effect (*15*). The first is that sugar peroxyl radicals convert to strand breaks with greater efficiency than the native sugar radicals (*14*). The second is that $^{\bullet}OH$-mediated base peroxyl radicals more selectively abstract hydrogen atoms from the sugar (base-to-sugar radical transfer, BSRT) than the native base radicals, yielding more sugar radicals and thus ultimately more strand breaks (*1, 13, 16–18*).

A Monte Carlo-based algorithm was developed to predict DNA damage from physical and chemical tracks through a cell nucleus simulated in Geant4-DNA, taking into account

[1] Address for correspondence: Department of Physics, University of Adelaide, Physics Building, Room G16, North Terrace, Adelaide, South Australia 5005, Australia; email: Jake.Forster@adelaide.edu.au.

[2] Scholar-in-Training, Radiation Research Society.

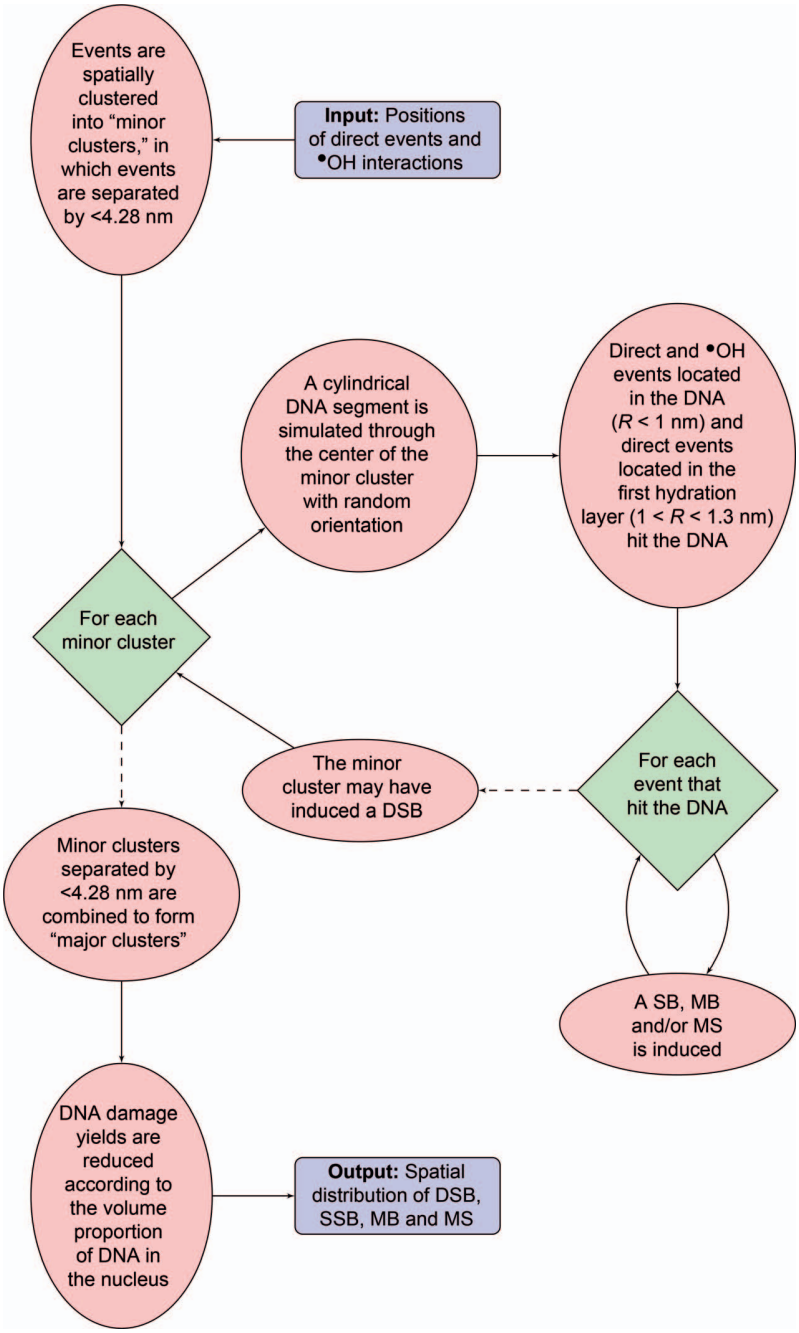

FIG. 1. Flowchart illustrating the DNA damage induction algorithm for processing Monte Carlo physical and chemical tracks generated in Geant4-DNA based on a spatial clustering approach.

the effect of cellular oxygenation (pO_2) on the efficiencies of sugar radical-to- strand break conversion and BSRT from $^{\bullet}$OH-mediated base radicals. Other DNA damage models using radiation track structure have typically focused on simulating DNA geometry at the molecular level [e.g., Friedland *et al*. (PARTRAC) (*19*), Liang *et al*. (*20*), Watanabe *et al*. (*21*), Štepán and Davídková (RADAMOL) (*22*) and Moiseenko *et al*. (*23*)], whereas the current work was concerned with simulating the oxygen effect. To our knowledge, no other model for predicting DNA damage from radiation tracks has simulated the effect of pO_2 on DNA radical chemistry. The primary objectives of this work were: 1. to predict yields of DNA damage with reasonable accuracy using a less sophisticated and less memory-intensive approach than is conventional; and 2. to achieve experimentally observed values of the oxygen enhancement ratio (OER) for DSB induction (OER_{DSB}) for both low- and high-LET radiation.

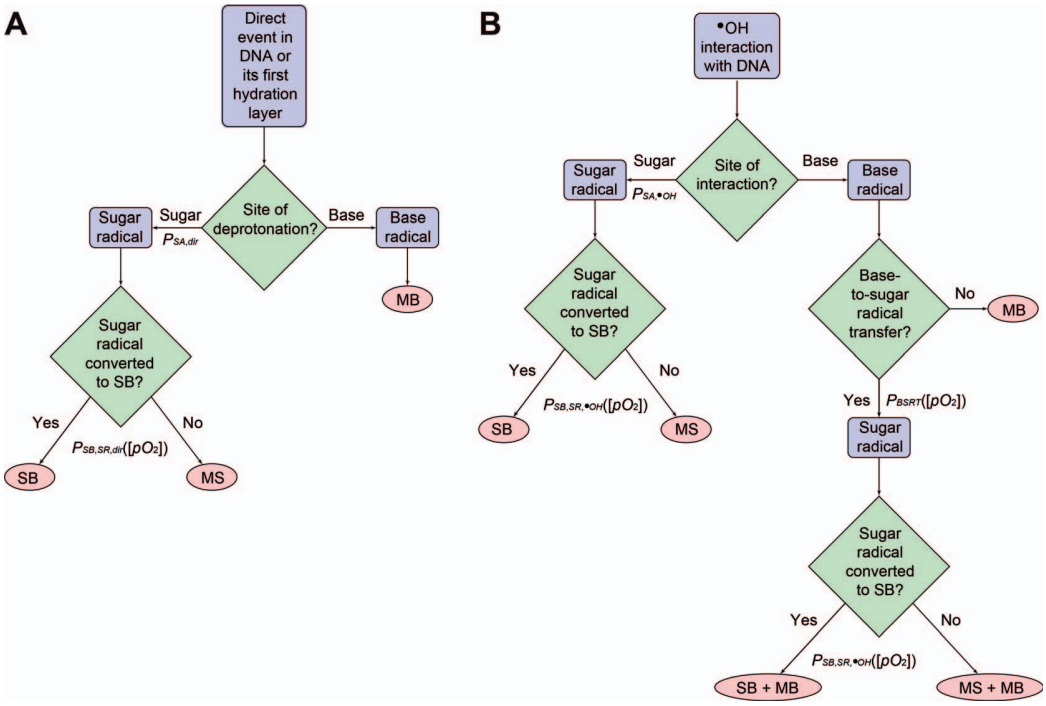

FIG. 2. Pathways to different types of DNA damage from direct events (panel A) and •OH interactions (panel B).

METHODS

Nucleus Irradiation Simulation

Physical tracks and subsequent chemical tracks from water radiolysis were simulated inside a cell nucleus region using Geant4-DNA (*24–28*) from the Monte Carlo Geant4 toolkit (version 10.3 patch-03) (*29–31*). The nucleus material was approximated by water with mass density 1 g/cm^3. To simulate the direct-type effects of radiation, the positions of direct events with energy deposition $\geq$ (E_{min} =) 10.79 eV (the ionization threshold of liquid water) were recorded. Then, as described in the next section, if such an event coincided with DNA or its primary hydration layer, it induced a DNA radical and subsequently DNA damage. There is evidence that sub-ionization energy electrons can induce DNA sugar radicals (and thus strand breaks) by resonant attachment (*32*), but this was neglected. For comparison, 10.79 eV was the energy threshold for strand break induction by direct events on the sugar moiety used by previous iterations of PARTRAC (*33, 34*) and more recently by Liang *et al.* (*20*). The current model differs in that a direct event may lead to a sugar radical but then the probability that the sugar radical is converted to a strand break depends on the pO_2 (next section). The physical processes constituting direct events for electrons were electron ionization, electron excitation, electron vibrational excitation and electron attachment. If protons were used, there was also proton ionization, proton charge decrease (electron capture), proton excitation, hydrogen ionization and hydrogen excitation. If alphas were used, there was also alpha ionization, alpha charge decrease, alpha excitation, alpha$^+$ ionization, alpha$^+$ charge decrease, alpha$^+$ excitation, helium ionization and helium excitation.

To simulate the indirect effect of radiation, •OH species were diffused for $t_{•OH} = 2.5$ ns before they were assumed to interact (unlike modeling a scavenging probability for each •OH along each time step). Spatial coordinates of •OH interactions were recorded. •OH interactions that spatially coincided with DNA induced DNA radicals and subsequently induced DNA damage (next section). This •OH lifetime corresponded to a scavenging capacity of 4×10^8 s^{-1}, which is similar to estimates for the cellular environment (*35, 36*). For diffusion in 3D, the root-mean-square displacement (*RMSD*) in time t is (*37*):

$$RMSD = \langle r^2 \rangle^{1/2} = (6Dt)^{1/2}, \quad (1)$$

where D is the diffusion coefficient. Geant4-DNA uses •OH diffusion coefficient $D_{OH} = 2.8 \times 10^{-9}$ m^2 s^{-1} (*28*). Thus, the $RMSD_{•OH}$ before interaction was 6.48 nm. This is consistent with most experimental estimates for the diffusion distance of •OH in biological material, which include $<$ 8.6 nm (*38*), ~5.4 nm (*39*), $<$ 2.6 nm (*40*) and 6–9 nm (*41*). •OH was the only species that contributed to indirect DNA damage, neglecting the minor contributions from H• and e_{aq}^- (*8, 42*). Reactions between radiolytic species and oxygen during the chemical stage (10^{-12} to 10^{-6} s) were not simulated. This was deemed acceptable because pO_2 has been shown to have only a small or negligible effect on the •OH yield in experimental (*43*) and theoretical models (*22, 44–46*). In one such model by Štepán and Davídková (*22*), the •OH yields under pO_2s of 0 and 760 mmHg only began to diverge after approximately 10 ns, which is after we assume they interact (2.5 ns).

DNA Damage Induction Algorithm

The current model algorithm, developed using MATLAB® version R2016b (MathWorks® Inc., Natick, MA), predicted DNA damage from the Geant4-DNA physical and chemical tracks. It simulated the DNA dimensions and biochemical processes after irradiation. The algorithm proceeded as follows (illustrated schematically in Fig. 1 and visualized in Results):

1. The positions of direct events (with energy deposition $\geq$10.79 eV) and •OH interactions were imported from the Geant4-DNA simulation.
2. The in-built MATLAB function ''clusterdata'' (*47*) with ''complete'' linkage was used to spatially cluster these events into ''minor clusters''. Complete linkage ensured any two events in the same minor cluster were not farther apart than some distance, d_1,

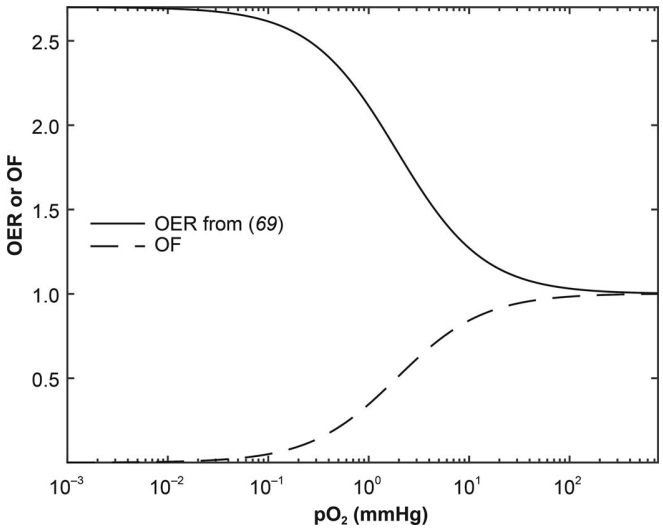

FIG. 3. *OER*($[pO_2]$) from Carlson *et al.* (*69*), defined as the ratio of cell killing under full oxia (pO_2 of 760 mmHg) to the cell killing under pO_2, and the oxygen function *OF*($[pO_2]$) derived from *OER*($[pO_2]$). *OF*($[pO_2]$) was used to map the probabilities of sugar radical-to-strand break conversion and BSRT from $^{\bullet}$OH-mediated base radicals from their minimum values under anoxia to their maximum values under full oxia.

set by the user; otherwise the events were allocated to different minor clusters. The following expression was used for this maximum distance between events in the same minor cluster:

$$d_1 = \sqrt{{L_{DSB}}^2 + \left(D_{DNA} + 2T_{hyd}\right)^2}. \quad (2)$$

Here, L_{DSB} is the maximum separation between two strand breaks on opposite strands of DNA that constitutes a DSB and is conventionally taken to be 3.4 nm, corresponding to 10 base pairs (bp) or one turn of the DNA double helix (*33*). $D_{DNA} = 2$ nm is the diameter of DNA and T_{hyd} is the thickness of the first hydration layer of DNA. Estimations for this thickness include 0.4–0.8 nm (*48*), 0.3 nm in experiments (*49, 50*) and 0.5 nm in theoretical simulations (*51–53*). Here it was taken to be 0.3 nm, choosing the low end of estimates because it was assumed that direct event-mediated radicals in the first hydration layer were transferred to DNA with 100% efficiency (*5, 6*), neglecting possible processes in which the radical is not transferred to DNA (*54*). Thus, this maximum separation between events in the same minor cluster was $d_1 \approx 4.28$ nm. This represents the limiting case for DSB production by two direct events located on opposite boundaries of the first hydration layer, 10 bp apart.

3. For each minor cluster, a cylinder of 1.3 nm radius representing a segment of DNA and its first hydration layer were placed through the center of the minor cluster with a random orientation. The cylinder was as long as necessary to contain as many events in the minor cluster as possible for the given cylinder orientation, with a maximum length of $d_1 \approx 4.28$ nm. Direct events in the DNA (radius $R < 1$ nm from the cylindrical axis) or in the first hydration layer ($1 < R < 1.3$ nm) and $^{\bullet}$OH interactions in the DNA each induced a modified base (MB), modified sugar (MS), MS + MB, SB or SB + MB (next section). If the number of strand breaks in the minor cluster, n_{SB}, was ≥ 2, the minor cluster was classified as a ''DSB minor cluster,'' provided not all strand breaks were on the same strand, i.e., the probability of a DSB minor cluster was:

$$P(n_{SB}) = 1 - 2(0.5^{n_{SB}}) \quad (3)$$

4. If a minor cluster contained an event less than ($L_{DSB,DSB} \approx$) 4.28 nm from an event in another minor cluster, the minor clusters were separated by too few undamaged bp (less than approximately 10) and were considered to be a part of the same ''major cluster''. This minimum DSB separation of ~10 bp was used by Štepán and

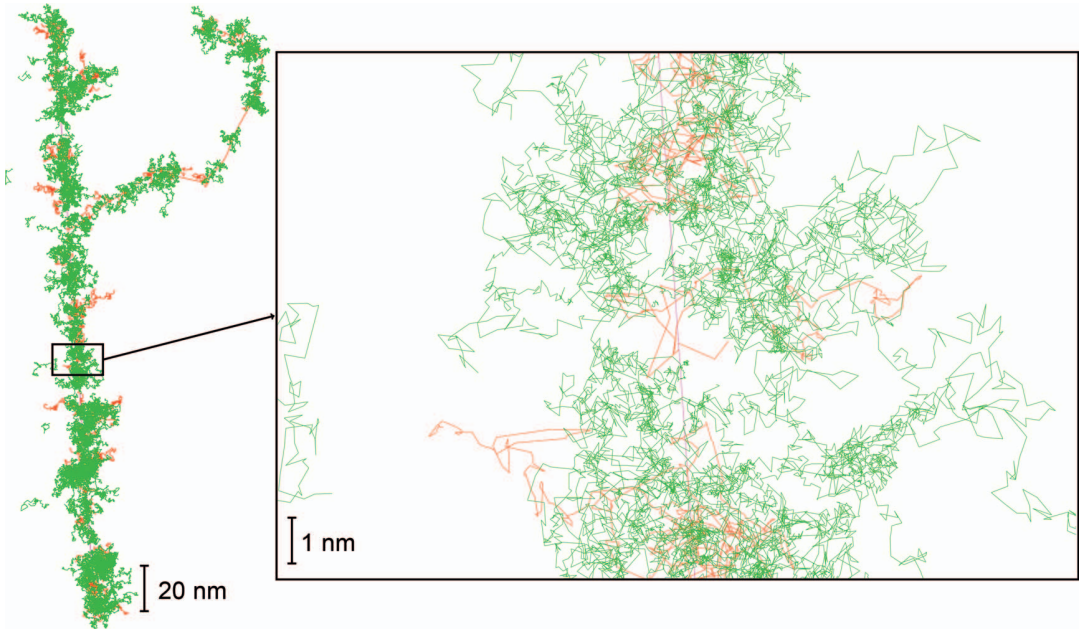

FIG. 4. Alpha (12 MeV) tracked for 10 keV of energy loss in Geant4-DNA. The alpha is shown in magenta, secondary electrons in red and $^{\bullet}$OH species in green. Tracks of other chemical species ($H^{\bullet}$, e_{aq}^{-}, H_2O_2, OH^{-}, H_3O^{+}) are not shown. $^{\bullet}$OH species diffused for $t_{^{\bullet}OH} = 2.5$ ns before they were assumed to interact.

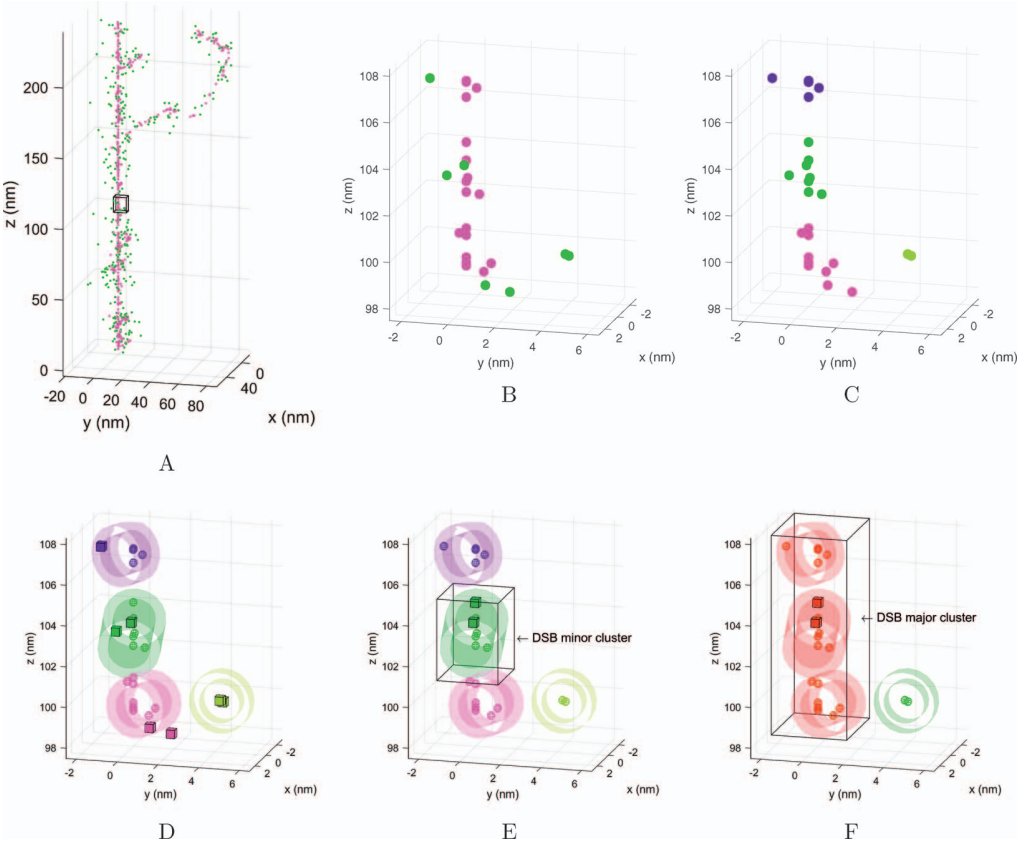

FIG. 5. Visualization of the spatial clustering approach used to estimate DNA damage, applied to the tracks in Fig. 4. Panel A: Sites of direct events (magenta) and •OH interactions (green). Panel B: A subsection of the tracks. Panel C: Direct and indirect events are spatially clustered into minor clusters. Events in the same minor cluster are shown in the same color. Panel D: DNA segments and their first hydration layers are placed. Direct events are shown with spheres and •OH interactions are shown with cubes. Panel E: Events that induced a DNA radical and subsequently caused a modified base, modified sugar, modified sugar and modified base, strand break or strand break and modified base. Events that caused a strand break are shown with cubes and events that did not are shown with spheres. One of the DNA segments contains a DSB and constitutes a DSB minor cluster. Panel F: Nearby minor clusters separated by less than 4.28 nm are joined to form major clusters. Minor clusters belonging to the same major cluster are shown in the same color. The major cluster containing a DSB minor cluster is called a DSB major cluster. The DNA damage yields are then reduced according to the volume proportion of DNA in the nucleus.

Davídková (RADAMOL) (*22*), but other models have used larger values [e.g., 25 bp in PARTRAC (*19*)]. To group minor clusters into major clusters, the MATLAB function ''clusterdata'' with ''single'' linkage was used. To begin with, single linkage grouped events into major clusters, ensuring any two events in different major clusters were not closer together than ($L_{DSB,DSB} \approx$) 4.28 nm, otherwise the events were allocated to the same major cluster. Since $d_1 = L_{DSB,DSB} \approx$ 4.28 nm, events in the same minor cluster belonged to the same major cluster, thus minor clusters were grouped into major clusters. A major cluster containing N DSB minor clusters was scored as a single DSB with multiplicity N. A DSB was classified as ''complex'' if it contained more than two strand breaks in total. If a major cluster did not contain a DSB minor cluster, all strand breaks within were scored as SSBs and all MBs and MSs were scored as ''isolated'' (in the sense that they were not part of a DSB).

5. The DNA damage yields were reduced by a factor that may be interpreted as the volume proportion of DNA in the nucleus, since it was assumed that all minor clusters coincided with DNA. This volume proportion has been estimated to be from 0.3% to 2% in yeast cells (*55*). In practice, this factor was tuned to bring the DSB yield into line with the DSB yield obtained by Štepán and Davídková (*22*) (see Results).
6. A spatial distribution of SSBs, DSBs, MBs and MSs was output.

pO_2-Dependent DNA Damage

The pathways to various forms of DNA damage by direct events and •OH interactions are shown in Fig. 2.

Experiments conducted by Purkayastha *et al.* (*4*) using hydrated plasmid DNA films showed that a direct event in DNA or its first hydration layer produced an electron or hole that was trapped on the sugar, forming a (neutral) sugar radical, 11% of the time and on a base, forming a (neutral) base radical, the remainder of the time. The probability of sugar attack (SA) by a direct event in DNA or its first hydration layer is denoted by $P_{SA,dir} = 0.11$. Experiments conducted by Scholes *et al.* (*56, 57*) on aqueous solutions of DNA and simulations by Chatterjee *et al.* (*58*), both found that •OH interactions with DNA occurred with the sugar, producing a sugar radical 20% of the time ($P_{SA,\bullet OH} = 0.2$) and the remainder of the time with a base, producing a base radical.

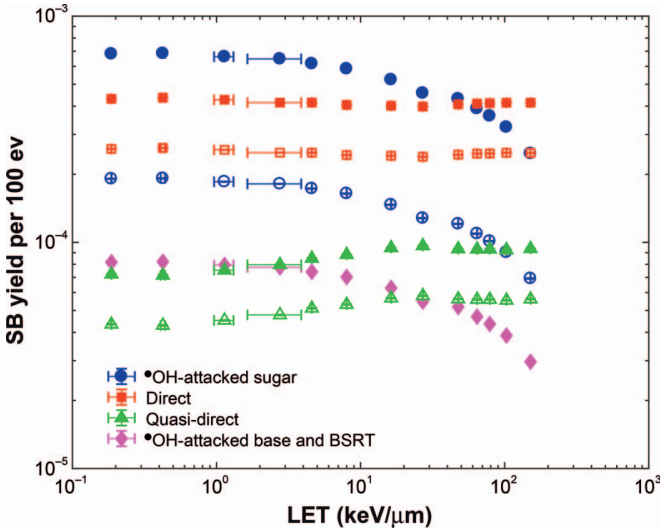

FIG. 6. Calculated yields of strand breaks from direct-type effects and the indirect effect under full oxia (pO_2 of 760 mmHg; filled symbols) and anoxia (pO_2 of 0 mmHg; unfilled symbols).

Each base radical resulted in a modified base. In addition, there was a small, pO_2-dependent chance for an $^{\bullet}OH$-mediated radical on a base to be transferred to the sugar moiety to form a sugar radical. This probability, $P_{BSRT}([pO_2])$, was made to increase from 0 to 0.03 for increasing pO_2 from 0 to 760 mmHg, so that the contribution from this mechanism to strand breakage was at most 7% (see Results), an upper limit indicated by experiments with single-stranded DNA (*59, 60*).

Each sugar radical resulted in either a strand break or a modified sugar. A sugar radical (SR) from a direct event and one from an $^{\bullet}OH$ interaction (either by $^{\bullet}OH$ attacking the sugar or by $^{\bullet}OH$ attacking the base followed by BSRT) were converted to a strand break with separate pO_2-dependent probabilities $P_{SB,SR,dir}([pO_2])$ and $P_{SB,SR,^{\bullet}OH}([pO_2])$, respectively. The efficiency of strand break induction by direct events in DNA and its first hydration layer, $P_{SB,dir}([pO_2])$, and the efficiency of strand break induction by $^{\bullet}OH$ interactions with DNA, $P_{SB,^{\bullet}OH}([pO_2])$, can be expressed as:

$$P_{SB,dir}([pO_2]) = P_{SA,dir}P_{SB,SR,dir}([pO_2]) \tag{4}$$

$$P_{SB,\bullet OH}([pO_2]) = P_{SA,\bullet OH}P_{SB,SR,\bullet OH}([pO_2]) + (1 - P_{SA,\bullet OH})P_{BSRT}([pO_2])P_{SB,SR,\bullet OH}([pO_2]) \tag{5}$$

The OER for cell killing by direct-type effects can be measured experimentally from the ratio of cell survival in air and a high concentration of $^{\bullet}OH$ scavenger to cell survival in nitrogen and a high concentration of $^{\bullet}OH$ scavenger. Estimates from the literature include 1.32 (AA8 cells) and 2.01 (CHO cells) (*61*), 1.66 (glutathione+ haploid yeast cells) (*62*), 1.9 (CHO cells) (*63*), 1.8 (V79-379-A cells) (*64*) and 1.6 (V79-379-A cells) (*35*). The OER for cell killing by the indirect effect has been estimated in experiments to be 4.11 (AA8 cells) and 3.75 (CHO cells) (*61*) and 4.24 (glutathione+ haploid yeast cells) (*62*). As a first approximation, equate the OER for cell killing by direct-type effects with the OER for the probability of strand break induction by a direct event in DNA or its first hydration layer. Similarly, equate the OER for cell killing by the indirect effect with the OER for the probability of strand break induction by an $^{\bullet}OH$ interaction with DNA [recall that, to a good approximation, the indirect effect can be attributed to $^{\bullet}OH$ alone (*8, 42*)]:

$$OER_{dir} = \frac{P_{SB,dir}(760\text{ mmHg})}{P_{SB,dir}(0\text{ mmHg})} = \frac{P_{SB,SR,dir}(760\text{ mmHg})}{P_{SB,SR,dir}(0\text{ mmHg})} \tag{6}$$

$$OER_{indir} = \frac{P_{SB,\bullet OH}(760\text{ mmHg})}{P_{SB,\bullet OH}(0\text{ mmHg})} = \frac{P_{SA,\bullet OH}P_{SB,SR,\bullet OH}(760\text{ mmHg}) + (1-P_{SA,OH})P_{BSRT}(760\text{ mmHg})P_{SB,SR,\bullet OH}(760\text{ mmHg})}{P_{SA,\bullet OH}P_{SB,SR,\bullet OH}(0\text{ mmHg}) + (1-P_{SA,\bullet OH})P_{BSRT}(0\text{ mmHg})P_{SB,SR,\bullet OH}(0\text{ mmHg})} = \frac{(0.2)P_{SB,SR,\bullet OH}(760\text{ mmHg}) + (0.8)(0.03)P_{SB,SR,\bullet OH}(760\text{ mmHg})}{(0.2)P_{SB,SR,\bullet OH}(0\text{ mmHg})}. \tag{7}$$

Taking an approximate OER_{dir} of 5/3, an approximate OER_{indir} of 4, and assuming sugar radicals from both direct events and $^{\bullet}OH$ interactions are converted to strand breaks with 100% efficiency under full oxia, i.e., $P_{SB,SR,dir}(760\text{ mmHg}) = P_{SB,SR,^{\bullet}OH}(760\text{ mmHg}) = 1$, Eqs. (6) and (7) were applied to obtain $P_{SB,SR,dir}(0\text{ mmHg}) = 0.6$ and $P_{SB,SR,^{\bullet}OH}(0\text{ mmHg}) = 0.28$. Note that under anoxia the majority of $^{\bullet}OH$-mediated sugar radicals were not converted to strand breaks. From Eqs. (4) and (5), the efficiency of strand break induction by direct events in DNA and its first hydration layer increased from 6.6% to 11% for pO_2 from 0 to 760 mmHg and the efficiency of strand break induction by $^{\bullet}OH$ interactions with DNA increased from 5.6% to 22.4% for pO_2 from 0 to 760 mmHg. Experimental estimates for this efficiency for $^{\bullet}OH$ range from 11–44% in DNA (*65–67*) and 41% in the polynucleotide poly(U) (*68*).

As for the functional form of the pO_2 dependency in probabilities $P_{SB,SR,dir}([pO_2])$, $P_{SB,SR,^{\bullet}OH}([pO_2])$ and $P_{BSRT}([pO_2])$, a goal of this work was to make these probabilities vary with pO_2 in the same manner as experimentally observed cell killing. An ''oxygen function'' $OF([pO_2])$ was defined with domain (0,760) mmHg and range (0,1) to map these probabilities from their minimum values under anoxia to their maximum values under full oxia:

TABLE 1
Summary of Model Parameters

Model parameter	Value	Refs.
E_{min}	10.79	(*20*, *33*, *34*)
$t^{\bullet}_{OH}/RMSD^{\bullet}_{OH}$	2.5 ns/6.48 nm	(*35*, *36*)/(*38–41*)
L_{DSB}	3.4 nm (10 bp)	(*33*)
T_{hyd}	0.3 nm	(*48–53*)
$L_{DSB,DSB}$	4.28 nm	(*22*)
$P_{SA,dir}$	0.11	(*4*)
$P_{SA,^{\bullet}OH}$	0.2	(*56–58*)
$P_{BSRT}([pO_2])$	$0 \rightarrow 0.03$ for pO_2 from $0 \rightarrow 760$ mmHg	(*59*, *60*)
$P_{SB,SR,dir}([pO_2])$	$0.6 \rightarrow 1$ for pO_2 from $0 \rightarrow 760$ mmHg	To achieve OER_{dir} of 5/3 (*35*, *61–64*)
$P_{SB,SR,^{\bullet}OH}([pO_2])$	$0.28 \rightarrow 1$ for pO_2 from $0 \rightarrow 760$ mmHg	To achieve OER_{indir} of 4 (*61*, *62*)

TABLE 2
Particles, Energies and LET Simulated in Geant4-DNA

Particle	Initial energy	Initial (final) LET (keV/μm)
Electron	999 keV	0.186 (0.187)
	100 keV	0.41 (0.439)
	30 keV	0.962 (1.312)
	15 keV	1.64 (3.874)
Proton	10 MeV	4.59 (4.59)
	5 MeV	8 (8.01)
	2 MeV	16.26 (16.32)
	1 MeV	26.94 (27.13)
Alpha	12 MeV	47.57 (47.6)
	8 MeV	64.31 (64.37)
	6 MeV	78.79 (78.88)
	4 MeV	102.79 (102.95)
	2 MeV	151.02 (151.39)

$$P_{SB,SR,dir}([pO_2]) = P_{SB,SR,dir}(0\,\text{mmHg}) + OF([pO_2])[P_{SB,SR,dir}(760\,\text{mmHg}) - P_{SB,SR,dir}(0\,\text{mmHg})] \quad (8)$$

$$P_{SB,SR,\bullet OH}([pO_2]) = P_{SB,SR,\bullet OH}(0\,\text{mmHg}) + OF([pO_2])[P_{SB,SR,\bullet OH}(760\,\text{mmHg}) - P_{SB,SR,\bullet OH}(0\,\text{mmHg})] \quad (9)$$

$$P_{BSRT}([pO_2]) = OF([pO_2])P_{BSRT}(760\,\text{mmHg}). \quad (10)$$

$OF([pO_2])$ was derived from experimentally measured $OER([pO_2])$ for cell killing, defined as the ratio of cell killing under full oxia to the cell killing under oxygenation pO_2 (in units of mmHg). The following formula for $OER([pO_2])$ was presented by Carlson *et al.* (*69*) as a good fit to experimental data from Spiro *et al.* (V79 cells) (*70*):

$$OER([pO_2]) = \frac{(5.13\,\text{mmHg}) + [pO_2]}{(1.9\,\text{mmHg}) + [pO_2]}. \quad (11)$$

To obtain $OF([pO_2])$ from $OER([pO_2])$, one may subtract the *OER* of 1 (let $f = OER$; $f \rightarrow f - 1$), invert ($f \rightarrow f_{max} - f$) and then normalize ($f \rightarrow f/f_{max}$; $OF = f$), thus obtaining Eq. (12):

$$OF([pO_2]) = \frac{1.0025[pO_2]}{1.9\,\text{mmHg} + [pO_2]}. \quad (12)$$

$OER([pO_2])$ and $OF([pO_2])$ are plotted in Fig. 3. As with cell killing, $OF([pO_2])$ and thus, these probabilities, vary most from 0.1 to 10 mmHg.

The key model parameters are summarized along with their values in Table 1.

Simulations and Analysis

Using Geant4-DNA, electrons, protons and alphas with various initial energies and LET values (Table 2) were tracked for 10 keV of energy loss before simulating radiolysis. Depending on the LET, this corresponded to track lengths from approximately 66 nm to 54 μm. Since the purpose of this work was to verify the DNA damage induction algorithm, it was assumed that the entire length of the track was inside a nucleus region. N = 100 tracks were generated for each particle/energy combination (n = 13).

For each track, the DNA damage induction algorithm was applied n = 1,000 times. This combination of sample sizes was sufficient to produce vertical error bars, equal to the SEM of the dependent variable, that were not visible in plots. For the thousand runs of the algorithm for track i of particle/energy combination p/E, the means ($mean_{p,E,i}$) and standard deviations ($SD_{p,E,i}$) of, for example, the number of SSBs, DSBs, MBs and MSs were recorded. This was repeated for different pO_2. To obtain the mean and standard deviation of the ratio of two quantities A/B (e.g. SSB/DSB or OER_{DSB}) for track i of particle/energy combination p/E:

$$mean_{\frac{A}{B},p,E,i} = \frac{mean_{A,p,E,i}}{mean_{B,p,E,i}}; \quad (13)$$

$$SD_{\frac{A}{B},p,E,i} = mean_{\frac{A}{B},p,E,i} \times \sqrt{\left(\frac{SD_{A,p,E,i}}{mean_{A,p,E,i}}\right)^2 + \left(\frac{SD_{B,p,E,i}}{mean_{B,p,E,i}}\right)^2}. \quad (14)$$

The means and standard deviations of the n = 100 tracks for particle/energy combination p,E were then combined as:

$$mean_{p,E} = \frac{1}{100}\sum_{i=1}^{100} mean_{p,E,i} \quad (15)$$

$$SD_{p,E} = \frac{1}{100}\sqrt{\sum_{i=1}^{100} SD_{p,E,i}^2} \quad (16)$$

$$SEM_{p,E} = \frac{SD_{p,E}}{\sqrt{100}}. \quad (17)$$

Note that OER_{DSB} compared full oxia (pO_2 of 760 mmHg) with anoxia (pO_2 of 0 mmHg). For the plotted figures in this report, the LET plotted was (initial LET + final LET)/2, with error bars equal to (final LET – initial LET)/2. The error bars for the dependent quantities were equal to the SEM. Statements of statistical significance were from statistical analysis (linear regression) performed in MATLAB.

Equipment

Simulations were performed on the Phoenix supercomputer cluster (University of Adelaide, Adelaide, Australia). Each track of 10 keV

TABLE 3
Contributions (%) to the Calculated Strand Break Yield by Different Mechanisms for Low- and High-LET Radiation under Full Oxia and Anoxia

	999 keV electron (0.19 keV/μm)		2 MeV alpha (151 keV/μm)	
	760 mmHg	0 mmHg	760 mmHg	0 mmHg
Direct	34.1	52.5	52.9	66.5
Quasi-direct	5.7	8.8	12.0	15.0
$^{\bullet}$OH-attacked sugar	53.8	38.7	31.4	18.5
$^{\bullet}$OH-attacked base and BSRT	6.4	0	3.8	0

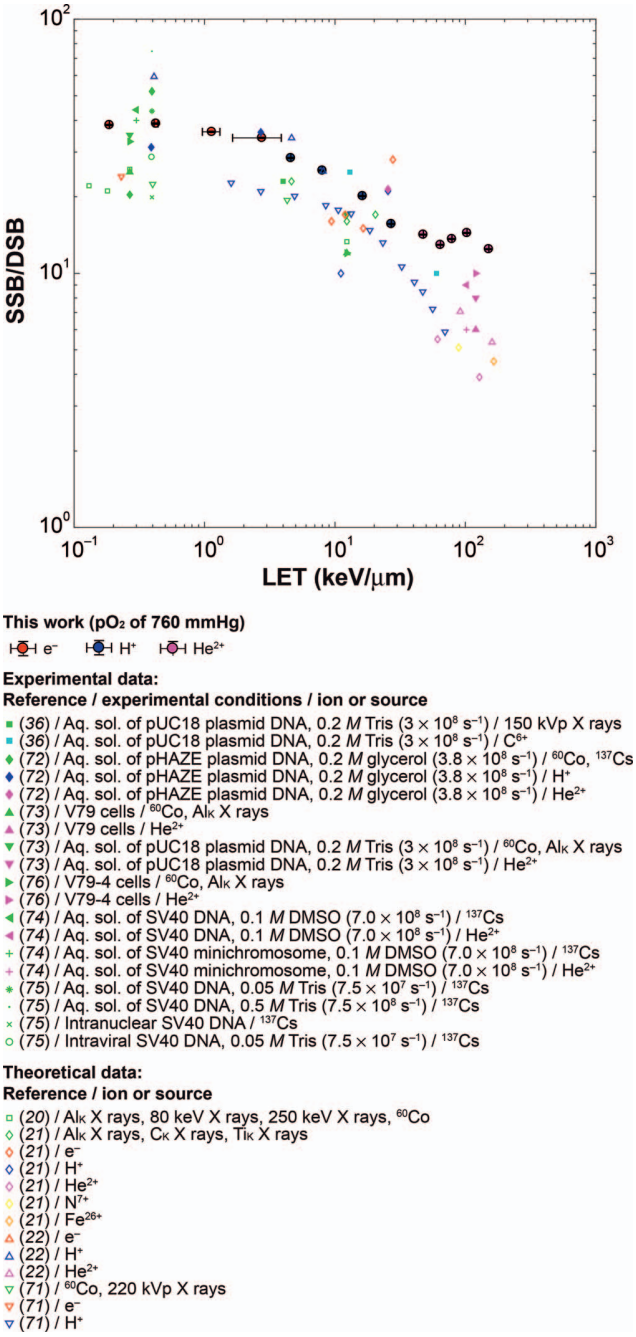

FIG. 7. Ratio of calculated SSB and DSB yields under full oxia, compared with experimental data in the literature and results from other theoretical models. Most experiments used DNA in aqueous solution with an $^{\bullet}OH$ scavenger such as Tris, glycerol or dimethylsulfoxide (DMSO) (*36, 72–75*). In such experiments, SSB/DSB decreased with increasing concentration of $^{\bullet}OH$ scavenger (*73*), so the data shown are for cell mimetic scavenging capacities of approximately 4×10^8 s^{-1} (*35, 36*). Data are also shown from experiments with DNA in cells (*73, 75, 76*). The theoretical data were from the models by Liang *et al*. (*20*), and Watanabe *et al*. (*21*) as well as from RADAMOL (*22*) and PARTRAC (*71*).

TABLE 4
Contribution (%) of Direct-Type Effects to the Calculated SSB Yield for Low- and High-LET Radiation under Full Oxia and Anoxia

	999 keV electron (0.19 keV/μm)		2 MeV alpha (151 keV/μm)	
	760 mmHg	0 mmHg	760 mmHg	0 mmHg
Direct-type	36.6	59.5	13.8	35.0

energy loss in Geant4-DNA ($n = 13 \times 100 = 1300$) took less than 2 min on a single core with 1 GB of RAM. The DNA damage induction algorithm was run millions of times, taking a total of approximately 15 h using parallel processing with 12 cores and at most 14 GB of RAM total.

RESULTS

The approach used to estimate DNA damage from physical and chemical tracks through a nucleus involved spatially clustering direct events (that deposited at least 10.79 eV) and $^{\bullet}OH$ interactions (Figs. 4 and 5).

The strand break yields due to different mechanisms are shown in Fig. 6. Similar to the PARTRAC model (*19, 71*), the strand break yield due to direct-type effects was approximately the same for all LETs simulated, while the strand break yield from the indirect effect decreased with increasing LET (water radiolysis products were generated closer together, so more chemical reactions occurred and there were fewer $^{\bullet}OH$ to react with DNA). The LET at which direct-type effects and the indirect effect contributed equally to the strand break yield was approximately 36 keV/μm under full oxia, while direct-type effects were dominant for all LETs under anoxia [in PARTRAC this LET was 70 keV/μm for protons and 140 keV/μm for alphas (*19*)]. The strand break yield from the indirect effect was more sensitive to pO_2, by design (see Methods). The relative contributions of the different mechanisms to the total strand break yield are presented quantitatively in Table 3 for the lowest and highest LETs. The strand break contribution by direct-type effects was 40% for the lowest LET under full oxia, in agreement with the 35–40% in PARTRAC (*19, 71*).

The ratio of the calculated SSB and DSB yields under full oxia was reasonably consistent across all LETs with experimental data in the literature and results from other theoretical models (Fig. 7). Pooling the experimental data together, there was a significant negative correlation between SSB/DSB and LET (one-sided P value 0.0002 using linear regression). The calculated SSB/DSB decreased from approximately 38 to 12 for increasing LET from 0.2 to 150 keV/μm.

Figure 8 shows the calculated yields of different types of DNA damage. The yield reduction factor, interpreted as the volume proportion of DNA in the nucleus (see Methods), was adjusted to 0.1% to best match the DSB yield with that of Štepán and Davídková (RADAMOL) (*22*). This value is similar to estimates of 0.3% to 2% for the volume

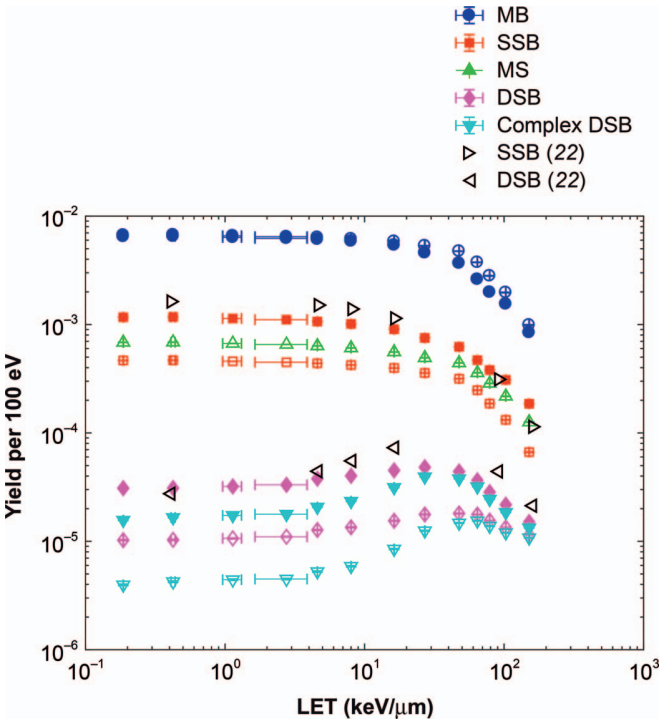

FIG. 8. Calculated DNA damage yields under full oxia (pO_2 of 760 mmHg; filled symbols) and anoxia (pO_2 of 0 mmHg; unfilled symbols). The calculated SSB and DSB yields from RADAMOL (*22*) are shown for comparison.

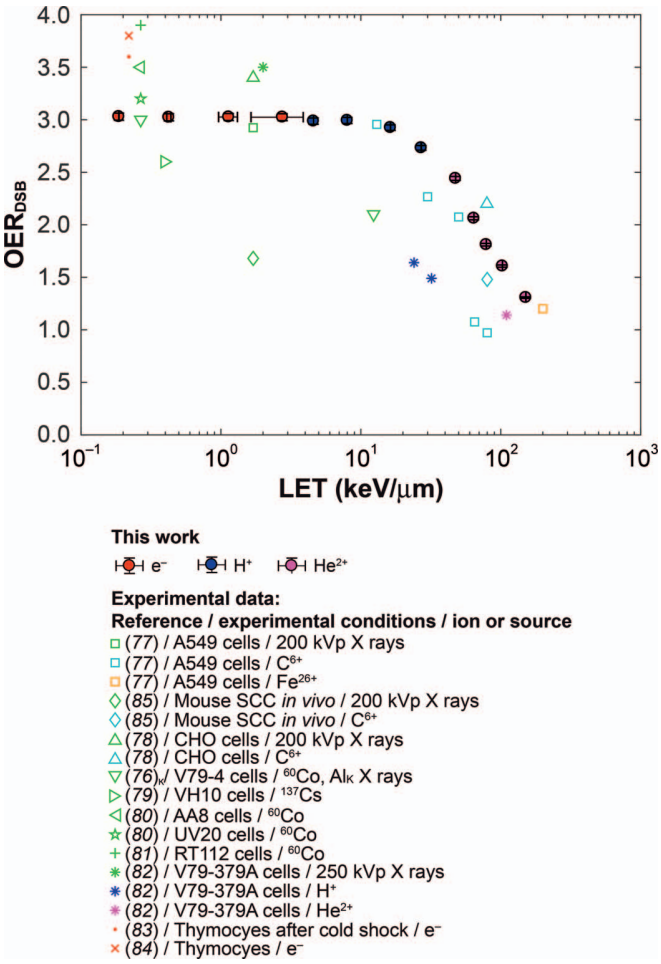

FIG. 9. Calculated OER_{DSB}, compared with experimental data found in the literature. Experimental data were for DNA in cells, typically irradiated *in vitro* under 95% air vs. 95% nitrogen (*76–84*), except for the *in vivo* experiment by Hirayama *et al.* (*85*), which used clamping to achieve hypoxia.

proportion of DNA in the nucleus of a yeast cell (*55*). As in RADAMOL, the DSB yield peaked at an LET of approximately 30 keV/μm. The peak is due to DSB clustering, wherein DSBs separated by less than 4.28 nm were scored as a single DSB.

The calculated OER_{DSB} was in reasonable agreement with experimental data in the literature (Fig. 9). The calculated OER_{DSB} was 3.0 for low LET up to approximately 15 keV/μm, then decreased with increasing LET to 1.3 at 150 keV/μm. Therefore, the additional strand breaks produced under full oxia, compared to under anoxia, did not produce additional DSBs as often for high LET as for low LET. The experimental OER_{DSB} data were highly scattered, but when pooled together, there was a significant negative correlation with LET (one-sided P value < 0.0001 using linear regression).

The variation of DNA damage yields with pO_2 is shown in Fig. 10. The variation was caused by the pO_2-dependent probabilities of sugar radical-to-strand break conversion and BSRT from $^{\bullet}OH$-mediated base radicals. Thus, the yields varied in the same way as these probabilities, which were constructed to vary like cell killing (see Methods), i.e., most of the change occurred between pO_2s of 0.1 and 10 mmHg. SSB, DSB and complex DSB yields increased with increasing pO_2. Conversely, the modified sugar yield decreased with increasing pO_2 as more sugar radicals were converted to strand breaks. The (isolated) modified base yield also decreased with increasing pO_2, particularly for high LET, as more modified bases were a part of DSBs.

As previously mentioned, the DSB yield peaked at approximately 30 keV/μm due to DSB clustering. This was evident by the mean DSB multiplicity increasing from unity at around this LET (Fig. 11A). If DSBs in clusters were counted separately, the DSB yield would continue to rise, as shown in Fig. 11B. The OER for the mean DSB multiplicity varied with LET inversely to OER_{DSB}. In PARTRAC (*19*), the mean DSB multiplicity was 2 for low LET and began to increase after approximately 100 keV/μm for alphas. This discrepancy may be due in part to PARTRAC combining DSBs separated by less than 25 bp, whereas the current work combined DSBs separated by less than approximately 10 bp. PARTRAC reported only a small increase in mean DSB multiplicity for alphas at 200 keV/μm.

The indirect effect contributed to SSBs more than direct-type effects under full oxia, but the situation was reversed

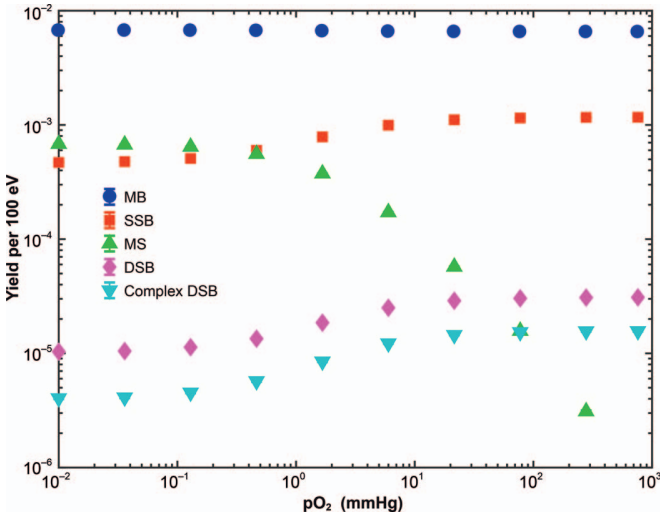

FIG. 10. Variation in calculated DNA damage yields with pO_2 for low-LET radiation (999 keV electrons).

under anoxia for all but the highest LET (Fig. 12 and Table 4). The direct-type contribution to SSBs of 36.6% under full oxia for low LET is comparable to values of 40% from Liang *et al.* (*20*) for ^{60}Co and 32% from Moiseenko *et al.* (*23*) for ^{137}Cs. Liang *et al.* found the direct-type contribution remained approximately 40% for LETs from 5 keV/μm to 170 keV/μm, whereas it decreased with increasing LET in the current work.

If DSBs were classified according to whether direct-type or indirect effects produced their strand breaks, the results are shown in Fig. 13A and B. For low LET, the majority of DSBs contained strand breaks from direct-type effects only. For high LET, the majority of DSBs contained strand break contributions from both direct-type and indirect effects. However, the fraction of DSBs that required an indirect contribution decreased with increasing LET (a DSB was said to require an indirect contribution if every DSB minor cluster in the DSB contained less than 2 SBs from direct-type effects). Therefore, the increasing indirect contribution to DSBs with increasing LET was associated with increasing DSB complexity, rather than the formation of additional DSBs.

The DSB fractions according to all elementary damage sites in the DSB, rather than just strand breaks, are shown in Fig. 13C and D. The majority of DSBs contained damages from both direct-type and indirect effects and this fraction increased with increasing LET. Moiseenko *et al.* (*23*) reported that 39% of DSBs for ^{137}Cs were from direct-type effects only and 30% were from the indirect effect only. These fractions are smaller in the current work. Watanabe *et al.* (*21*) found that the direct-type-only fraction increased with increasing LET, whereas it decreased in the current work.

DISCUSSION

Štepán and Davídková (*22*) simulated the effect of pO_2 on scavenging of e_{aq}^-, $H^\bullet$ and O^- by oxygen during the

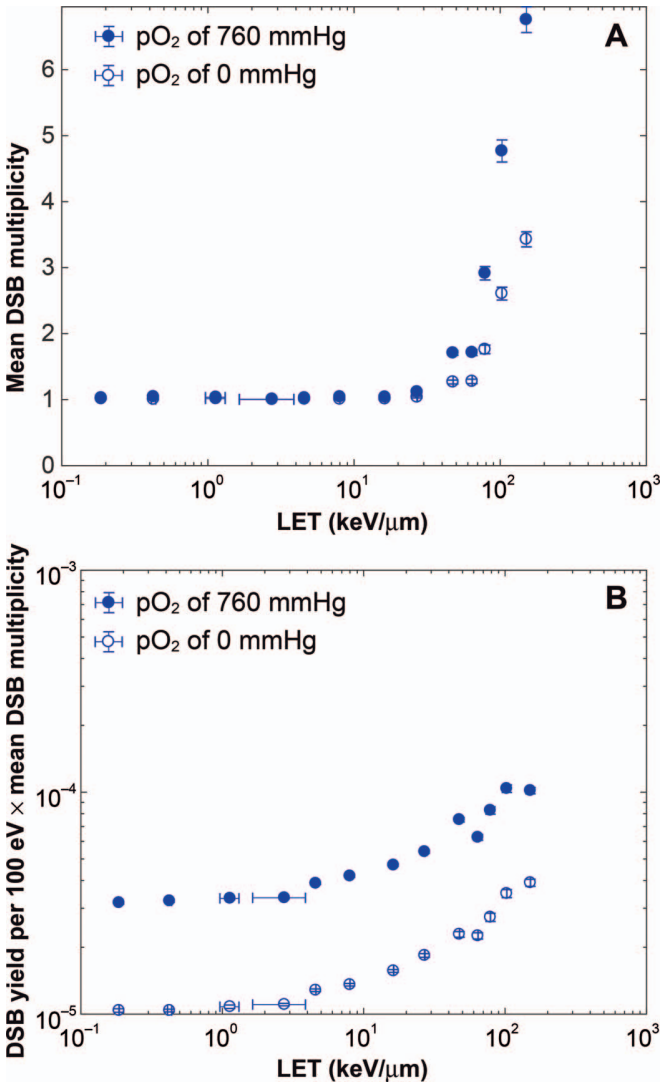

FIG. 11. Panel A: Mean DSB multiplicity. Recall that the DSB multiplicity is the number of DSB minor clusters contained in the DSB major cluster. Panel B: Yield of DSB minor clusters. This would be the DSB yield if nearby DSBs were not counted as a single DSB.

chemical stage (10^{-12} to 10^{-6} s). They found negligible oxygen enhancement of DSB induction ($OER_{DSB} < 1.2$) as a result. In the current work, the effect of pO_2 was simulated on DNA radical chemistry processes, in particular, on the efficiencies of sugar radical-to-strand break conversion and BSRT from $^\bullet$OH-mediated base radicals. In doing so, the values of OER_{DSB} obtained were consistent with experimental data in the literature, including a negative correlation with LET. To our knowledge, this is the first model to simulate the effect of pO_2 on DNA radical chemistry in the context of predicting DNA damage from radiation track structures.

The main sources of uncertainty in the current oxygen effect modeling were:

1. The OER for the probability of SB induction by a direct event in DNA or its first hydration layer was assumed to

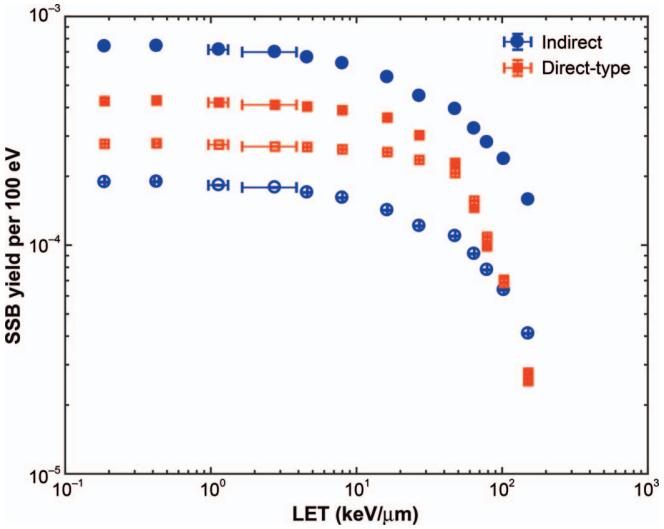

FIG. 12. Calculated yields of SSBs from direct-type effects and the indirect effect under full oxia (pO_2 of 760 mmHg; filled symbols) and anoxia (pO_2 of 0 mmHg; empty symbols).

be equal to the experimentally measured OER for cell killing by direct-type effects [Eq. (6)]. Likewise, the OER for the probability of SB induction by an $^{\bullet}OH$ interaction with DNA was assumed to be equal to the experimentally measured OER for cell killing by the indirect effect [Eq. (7)]. The experimental data (taken from the literature) were for cells *in vitro* and varied with cell type.

2. The probability that a sugar radical, from either direct event or $^{\bullet}OH$ interaction, was converted to a SB was assumed to be 100% under full oxia (pO_2 of 760 mmHg).
3. The probabilities of sugar radical-to-SB conversion and BSRT [Eqs. (8)–(10)] were assumed to vary with pO_2 in the same way as cell killing in experiments performed by Spiro *et al*. on V79 cells (*70*).
4. The theoretical fit [Eq. (11)] to this experimental data was performed by Carlson *et al*. (*69*) and carries some uncertainty.

The developed DNA damage algorithm spatially clustered direct events and $^{\bullet}OH$ interactions in volumes representing 10-bp segments of DNA to generate the initial DNA radical distribution. This approach differed from the one typically used in models of DNA damage induction by radiation (*19, 21–23*). The conventional approach is to first superimpose the physical tracks with a molecular DNA geometry. Direct events located within one van der Waals radius of a water molecule in the first hydration layer or a molecule

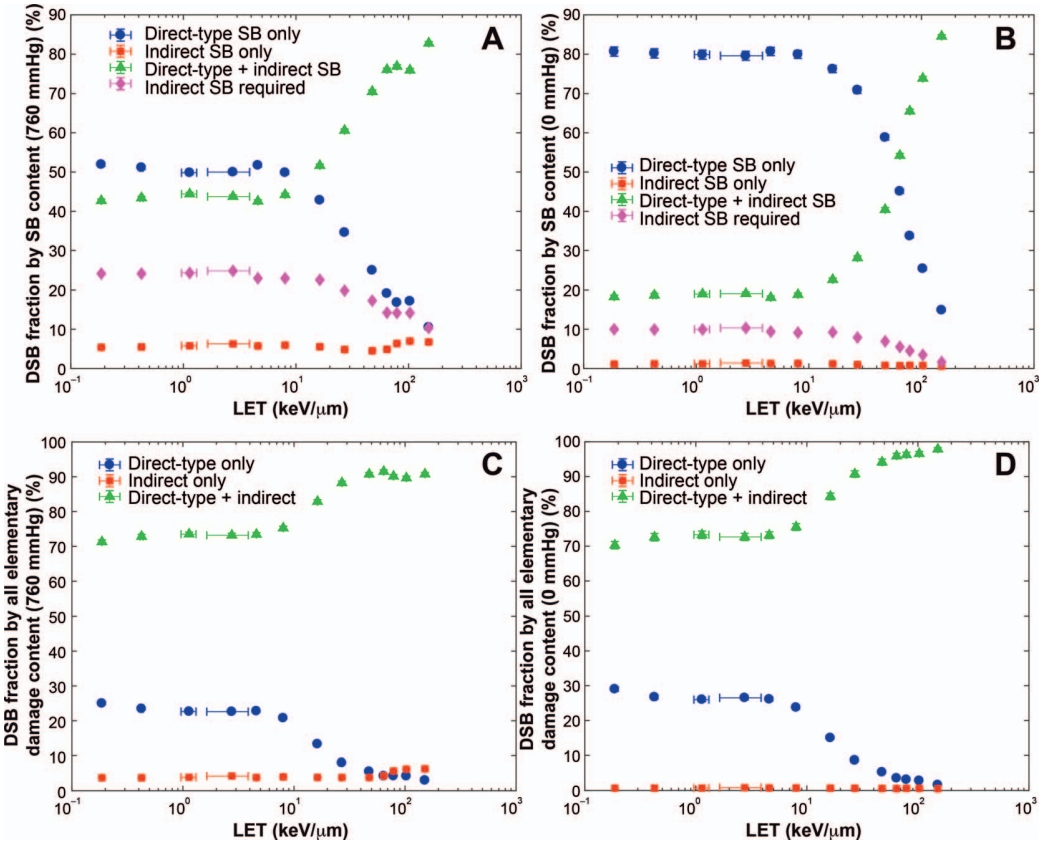

FIG. 13. Contribution of direct-type effects and the indirect effect to DSBs. DSB fractions according to strand break content under full oxia (panel A) and anoxia (panel B). DSB fractions according to all elementary damage content (SBs, MBs and MSs) under full oxia (panel C) and anoxia (panel D).

belonging to the sugar moiety may induce strand breaks. Then the physicochemical and chemical stages are simulated amidst the DNA geometry. If an $^{\bullet}OH$ species diffuses to within one van der Waals radius of a sugar molecule then it reacts and may induce a strand break. Models that take this approach have used increasingly rich geometrical structures to represent the contents of the cell nucleus. This approach may be too memory intensive (with current hardware) to use in track structure simulations of thousands to millions of cells. The developed spatial clustering approach has low memory requirements and may be suitable for this kind of task, having now validated the DNA damage yields using both experimental data and results from other theoretical models. Since the algorithm also simulates the oxygen effect, it could foreseeably be applied to radiation tracks through a large cluster of cells with nonuniform pO_2. This is an important situation to model, since many tumors contain microscopic regions of hypoxia, which impacts the efficacy of radiotherapy.

CONCLUSION

An algorithm was developed to predict DNA damage from physical and chemical tracks through a cell nucleus simulated in Geant4-DNA, taking into account the effect of pO_2 on DNA radical chemistry processes. An experimentally viable OER_{DSB} was achieved for both low- and high-LET radiation. DNA damage yields were verified using experimental data in the literature and results from other theoretical models. The developed algorithm was based on a spatial clustering approach. While this approach is a first order approximation, it is useful for radiation track structure simulations with large cell clusters due to its low memory requirements.

ACKNOWLEDGMENTS

We thank M. Karamitros for advice on the chemistry module of Geant4-DNA. This work was supported with supercomputing resources provided by the Phoenix HPC service at the University of Adelaide.

Received: January 30, 2018; accepted: May 29, 2018; published online: June 28, 2018

REFERENCES

1. Dizdaroglu M, Jaruga P. Mechanisms of free radical-induced damage to DNA. Free Radic Res 2012; 46:382–419.
2. von Sonntag C. Free-radical-induced DNA damage and its repair: a chemical perspective. Berlin: Springer; 2006.
3. Purkayastha S, Milligan JR, Bernhard WA. On the chemical yield of base lesions, strand breaks, and clustered damage generated in plasmid DNA by the direct effect of X rays. Radiat Res 2007; 168:357–66.
4. Purkayastha S, Milligan JR, Bernhard WA. The role of hydration in the distribution of free radical trapping in directly ionized DNA. Radiat Res 2006; 166:1–8.
5. Swarts SG, Becker D, Sevilla M, Wheeler KT. Radiation-induced DNA damage as a function of hydration. II. Base damage from electron-loss centers. Radiat Res 1996; 145:304–14.
6. Swarts SG, Sevilla MD, Becker D, Tokar CJ, Wheeler KT. Radiation-induced DNA damage as a function of hydration. I. Release of unaltered bases. Radiat Res 1992; 129:333–44.
7. Cadet J, Wagner JR, Shafirovich V, Geacintov NE. One-electron oxidation reactions of purine and pyrimidine bases in cellular DNA. Int J Radiat Biol 2014; 90:423–32.
8. Cadet J, Davies KJ, Medeiros MH, Di Mascio P, Wagner JR. Formation and repair of oxidatively generated damage in cellular DNA. Free Radic Biol Med 2017; 107:13–34.
9. Cadet J, Ravanat JL, TavernaPorro M, Menoni H, Angelov D. Oxidatively generated complex DNA damage: tandem and clustered lesions. Cancer Lett 2012; 327:5–15.
10. Cadet J, Wagner JR. DNA base damage by reactive oxygen species, oxidizing agents, and UV radiation. Cold Spring Harb Perspect Biol 2013; 5.
11. Cadet J, Delatour T, Douki T, Gasparutto D, Pouget JP, Ravanat JL, et al. Hydroxyl radicals and DNA base damage. Mutat Res 1999; 424:9–21.
12. Wardman P. Time as a variable in radiation biology: the oxygen effect. Radiat Res 2016; 185:1–3.
13. Wardman P. The importance of radiation chemistry to radiation and free radical biology (The 2008 Silvanus Thompson Memorial Lecture). Br J Radiol 2009; 82:89–104.
14. Pogozelski WK, Tullius TD. Oxidative strand scission of nucleic acids: routes initiated by hydrogen abstraction from the sugar moiety. Chem Rev 1998; 98:1089–107.
15. Jones GD, O'Neill P. Kinetics of radiation-induced strand break formation in single-stranded pyrimidine polynucleotides in the presence and absence of oxygen; a time-resolved light-scattering study. Int J Radiat Biol 1991; 59:1127–45.
16. von Sonntag C. Carbohydrate radicals: from ethylene glycol to DNA strand breakage. Int J Radiat Biol 1984; 46:507–19.
17. Melvin T, O'Neill P, Jones GD. Influence of nucleic acid base composition on radiation-induced strand breakage in single stranded DNA: a time resolved study. Int J Radiat Biol 1994; 66:499–503.
18. Osman R, Pardo L, Banfelder J, Mazurek AP, Shvartzman L, Strauss R, et al. Molecular mechanisms of radiation induced DNA damage: H-addition to bases, direct ionization and double strand break. Free Radic Res Commun 1991; 12–13 Pt 2:465–7.
19. Friedland W, Schmitt E, Kundrat P, Dingfelder M, Baiocco G, Barbieri S, et al. Comprehensive track-structure based evaluation of DNA damage by light ions from radiotherapy-relevant energies down to stopping. Sci Rep 2017; 7:45161.
20. Liang Y, Yang G, Liu F, Wang Y. Monte Carlo simulation of ionizing radiation induced DNA strand breaks utilizing coarse grained high-order chromatin structures. Phys Med Biol 2016; 61:445–60.
21. Watanabe R, Rahmanian S, Nikjoo H. Spectrum of radiation-induced clustered non-DSB damage - a Monte Carlo track structure modeling and calculations. Radiat Res 2015; 183:525–40.
22. Stepan V, Davídkova M. Impact of oxygen concentration on yields of DNA damages caused by ionizing radiation. J Phys Conf Ser 2008; 101:012015.
23. Moiseenko VV, Hamm RN, Waker AJ, Prestwich WV. Calculation of radiation-induced DNA damage from photons and tritium beta-particles. Part I: Model formulation and basic results. Radiat Environ Biophys 2001; 40:23–31.
24. Bernal MA, Bordage MC, Brown JM, Davídkova M, Delage E, El Bitar Z, et al. Track structure modeling in liquid water: a review of the Geant4-DNA very low energy extension of the Geant4 Monte Carlo simulation toolkit. Phys Med 2015; 31:861–74.
25. Incerti S, Ivanchenko A, Karamitros M, Mantero A, Moretto P, Tran HN, et al. Comparison of GEANT4 very low energy cross section models with experimental data in water. Med Phys 2010; 37:4692–708.

26. Incerti S, Baldacchino G, Bernal M, Capra R, Champion C, Francis Z, et al. THE Geant4-DNA project. Int J Model Simul Sci Comput 2010; 1:157–78.

27. Karamitros M, Luan S, Bernal MA, Allison J, Baldacchino G, Davidkova M, et al. Diffusion-controlled reactions modeling in Geant4-DNA. J Comput Phys 2014; 274:841–82.

28. Karamitros M, Mantero A, Incerti S, Friedland W, Baldacchino G, Barberet P, et al. Modeling radiation chemistry in the Geant4 toolkit. Prog Nucl Sci Technol 2011; 2:503–8.

29. Allison J, Amako K, Apostolakis J, Arce P, Asai M, Aso T, et al. Recent developments in GEANT4. Nucl Instrum Methods Phys Res A 2016; 835:186–225.

30. Allison J, Amako K, Apostolakis J, Araujo H, Dubois PA, Asai M, et al. Geant4 developments and applications. IEEE Trans Nucl Sci 2006; 53:270–8.

31. Agostinelli S, Allison J, Amako K, Apostolakis J, Araujo H, Arce P, et al. GEANT4 - A simulation toolkit. Nucl Instrum Methods Phys Res A 2003; 506:250–303.

32. Michael BD, O'Neill P. Molecular biology. A sting in the tail of electron tracks. Science 2000; 287:1603–4.

33. Friedland W, Jacob P, Paretzke HG, Merzagora M, Ottolenghi A. Simulation of DNA fragment distributions after irradiation with photons. Radiat Environ Biophys 1999; 38:39–47.

34. Dingfelder M, Hantke D, Inokuti M, Paretzke HG. Electron inelastic-scattering cross sections in liquid water. Radiat Phys Chem 1999; 53:1–18.

35. Chapman JD, Reuvers AP, Borsa J, Greenstock CL. Chemical radioprotection and radiosensitization of mammalian cells growing in vitro. Radiat Res 1973; 56:291–306.

36. Shiina T, Watanabe R, Shiraishi I, Suzuki M, Sugaya Y, Fujii K, et al. Induction of DNA damage, including abasic sites, in plasmid DNA by carbon ion and X-ray irradiation. Radiat Environ Biophys 2013; 52:99–112.

37. Berg HC. Random walks in biology. Princeton: Princeton University Press; 1993.

38. Guo Q, Yue Q, Zhao J, Wang L, Wang H, Wei X, et al. How far can hydroxyl radicals travel? An electrochemical study based on a DNA mediated electron transfer process. Chem Commun (Camb) 2011; 47:11906–8.

39. Chu BC, Orgel LE. Nonenzymatic sequence-specific cleavage of single-stranded DNA. Proc Natl Acad Sci U S A 1985; 82:963–7.

40. Dreyer GB, Dervan PB. Sequence-specific cleavage of single-stranded DNA: oligodeoxynucleotide-EDTA X Fe(II). Proc Natl Acad Sci U S A 1985; 82:968–72.

41. Roots R, Okada S. Estimation of life times and diffusion distances of radicals involved in x-ray-induced DNA strand breaks of killing of mammalian cells. Radiat Res 1975; 64:306–20.

42. Onal AM, Lemaire DG, Bothe E, Schulte-Frohlinde D. Gamma-radiolysis of poly(A) in aqueous solution: efficiency of strand break formation by primary water radicals. Int J Radiat Biol 1988; 53:787–96.

43. Kong S, Davison AJ. The role of interactions between O2, H2O2, $^{\bullet}$OH,e– and O2– in free radical damage to biological systems. Arch Biochem Biophys 1980; 204:18–29.

44. Colliaux A, Gervais B, Rodriguez-Lafrasse C, Beuve M. Simulation of ion-induced water radiolysis in different conditions of oxygenation. Nucl Instr Meth Phys Res B 2015; 365:596–605.

45. Tomita H, Kai M, Kusama T, Ito A. Monte Carlo simulation of physicochemical processes of liquid water radiolysis. The effects of dissolved oxygen and OH scavenger. Radiat Environ Biophys 1997; 36:105–16.

46. Turner JE, Hamm RN, Wright HA, Ritchie RH, Magee JL, Chatterjee A, et al. Studies to link the basic radiation physics and chemistry of liquid water. Radiat Phys Chem 1988; 32:503–10.

47. Douglass MJ. Development of an integrated stochastic radiobiological model for electromagnetic particle interactions in a 4D cellular geometry [dissertation]. Adelaide (SA): University of Adelaide; 2013. (https://digital.library.adelaide.edu.au/dspace/bitstream/2440/84965/8/02whole.pdf)

48. Bagchi B. Water dynamics in the hydration layer around proteins and micelles. Chem Rev 2005; 105:3197–219.

49. Egli M, Tereshko V, Teplova M, Minasov G, Joachimiak A, Sanishvili R, et al. X-ray crystallographic analysis of the hydration of A- and B-form DNA at atomic resolution. Biopolymers 1998; 48:234–52.

50. Guerri A, Simpson IJ, Neidle S. Visualisation of extensive water ribbons and networks in a DNA minor-groove drug complex. Nucleic Acids Res 1998; 26:2873–8.

51. Bandyopadhyay S, Chakraborty S, Balasubramanian S, Pal S, Bagchi B. Atomistic simulation study of the coupled motion of amino acid residues and water molecules around protein HP-36: fluctuations at and around the active sites. J Phys Chem B 2004; 108:12608–16.

52. Chakraborty S, Bandyopadhyay S. Correlation between the dynamics of hydrogen bonds and the local density reorganization in the protein hydration layer. J Phys Chem B 2007; 111:7626–30.

53. Chakraborty S, Sinha SK, Bandyopadhyay S. Low-frequency vibrational spectrum of water in the hydration layer of a protein: a molecular dynamics simulation study. J Phys Chem B 2007; 111:13626–31.

54. Becker D, La Vere T, Sevilla MD. ESR detection at 77 K of the hydroxyl radical in the hydration layer of gamma-irradiated DNA. Radiat Res 1994; 140:123–9.

55. Milo R, Phillips R. Cell biology by the numbers. 1st ed. New York: Garland Science; 2015.

56. Scholes G, Ward JF, Weiss J. Mechanism of the radiation-induced degradation of nucleic acids. J Mol Biol 1960; 2:379–91.

57. Scholes G, Willson RL, Ebert M. Pulse radiolysis of aqueous solutions of deoxyribonucleotides and of DNA: reaction with hydroxy-radicals. J Chem Soc D 1969:17–8.

58. Chatterjee A, Koehl P, Magee JL. Theoretical consideration of the chemical pathways for radiation-induced strand breaks. Adv Space Res 1986; 6:97–105.

59. Rao PJ, Bothe E, Schulte-Frohlinde D. Reaction of dithiothreitol and para-nitroacetophenone with different radical precursors of $^{\bullet}$OH radical-induced strand break formation of single-stranded DNA in anoxic aqueous solution. Int J Radiat Biol 1992; 61:577–91.

60. Adinarayana M, Bothe E, Schulte-Frohlinde D. Hydroxyl radical-induced strand break formation in single-stranded polynucleotides and single-stranded DNA in aqueous solution as measured by light scattering and by conductivity. Int J Radiat Biol 1988; 54:723–37.

61. Hirayama R, Ito A, Noguchi M, Matsumoto Y, Uzawa A, Kobashi G, et al. OH radicals from the indirect actions of X-rays induce cell lethality and mediate the majority of the oxygen enhancement effect. Radiat Res 2013; 180:514–23.

62. Frankenberg D, Frankenberg-Schwager M, Harbich R. Mechanisms of oxygen radiosensitization in irradiated yeast. I. DNA double-strand breakage. Int J Radiat Biol 1993; 64:511–21.

63. Skov KA. The contribution of hydroxyl radical to radiosensitization: a study of DNA damage. Radiat Res 1984; 99:502–10.

64. Chapman JD, Gillespie CJ, Reuvers AP, Dugle DL. The inactivation of Chinese hamster cells by x rays: the effects of chemical modifiers on single- and double-events. Radiat Res 1975; 64:365–75.

65. Milligan JR, Aguilera JA, Ward JF. Variation of single-strand break yield with scavenger concentration for plasmid DNA irradiated in aqueous solution. Radiat Res 1993; 133:151–7.

66. LaVerne JA, Pimblott SM. Yields of hydroxyl radical and hydrated electron scavenging reactions in aqueous solutions of biological interest. Radiat Res 1993; 135:16–23.

67. van Rijn K, Mayer T, Blok J, Verberne JB, Loman H. Reaction rate of OH radicals with phi X174 DNA: influence of salt and scavenger. Int J Radiat Biol 1985; 47:309–17.

68. Lemaire DG, Bothe E, Schulte-Frohlinde D. Yields of radiation-induced main chain scission of poly U in aqueous solution: strand break formation via base radicals. Int J Radiat Biol 1984; 45:351–8.

69. Carlson DJ, Stewart RD, Semenenko VA. Effects of oxygen on intrinsic radiation sensitivity: a test of the relationship between aerobic and hypoxic linear-quadratic (LQ) model parameters. Med Phys 2006; 33:3105–15.

70. Spiro IJ, Ling CC, Stickler R, Gaskill J. Oxygen radiosensitisation at low dose rate. Br J Radiol 1985; 58:357–63.

71. Friedland W, Jacob P, Bernhardt P, Paretzke HG, Dingfelder M. Simulation of DNA damage after proton irradiation. Radiat Res 2003; 159:401–10.

72. Leloup C, Garty G, Assaf G, Cristovao A, Breskin A, Chechik R, et al. Evaluation of lesion clustering in irradiated plasmid DNA. Int J Radiat Biol 2005; 81:41–54.

73. Fulford J, Nikjoo H, Goodhead DT, O'Neill P. Yields of SSB and DSB induced in DNA by Al(K) ultrasoft X-rays and alpha-particles: comparison of experimental and simulated yields. Int J Radiat Biol 2001; 77:1053–66.

74. Jones GD, Milligan JR, Ward JF, Calabro-Jones PM, Aquilera JA. Yield of strand breaks as a function of scavenger concentration and LET for SV40 irradiated with 4He ions. Radiat Res 1993; 136:190–6.

75. Krisch RE, Flick MB, Trumbore CN. Radiation chemical mechanisms of single- and double-strand break formation in irradiated SV40 DNA. Radiat Res 1991; 126:251–9.

76. Botchway SW, Stevens DL, Hill MA, Jenner TJ, O'Neill P. Induction and rejoining of DNA double-strand breaks in Chinese hamster V79-4 cells irradiated with characteristic aluminum K and copper L ultrasoft X rays. Radiat Res 1997; 148:317–24.

77. Sunada S, Hirakawa H, Fujimori A, Uesaka M, Okayasu R. Oxygen enhancement ratio in radiation-induced initial DSBs by an optimized flow cytometry-based gamma-H2AX analysis in A549 human cancer cells. Radiat Res 2017; 188:591–4.

78. Hirayama R, Furusawa Y, Fukawa T, Ando K. Repair kinetics of DNA-DSB induced by X-rays or carbon ions under oxic and hypoxic conditions. J Radiat Res 2005; 46:325–32.

79. Nygren J, Ahnström G. The oxygen effect in permeabilized and histone-depleted cells: an enhanced OER for DNA double-strand breaks, compared to single-strand breaks, is abolished by soluble scavengers. Int J Radiat Biol 1997; 72:163–70.

80. Murray D, Macann A, Hanson J, Rosenberg E. ERCC1/ERCC4 5′-endonuclease activity as a determinant of hypoxic cell radiosensitivity. Int J Radiat Biol 1996; 69:319–27.

81. Whitaker SJ, McMillan TJ. Oxygen effect for DNA double-strand break induction determined by pulsed-field gel electrophoresis. Int J Radiat Biol 1992; 61:29–41.

82. Prise KM, Folkard M, Davies S, Michael BD. The irradiation of V79 mammalian cells by protons with energies below 2 MeV. Part II. Measurement of oxygen enhancement ratios and DNA damage. Int J Radiat Biol 1990; 58:261–77.

83. Lennartz M, Coquerelle T, Bopp A, Hagen U. Oxygen-effect on strand breaks and specific end-groups in DNA of irradiated thymocytes. Int J Radiat Biol 1975; 27:577–87.

84. Lennartz M, Coquerelle T, Hagen U. Effect of oxygen on DNA strand breaks in irradiated thymocytes. Int J Radiat Biol 1973; 24:621–5.

85. Hirayama R, Uzawa A, Matsumoto Y, Noguchi M, Kase Y, Takase N, et al. Induction of DNA DSB and its rejoining in clamped and non-clamped tumours after exposure to carbon ion beams in comparison to X rays. Radiat Prot Dosimetry 2011; 143:508–12.

6.2.4 Discussion and Conclusion

An algorithm was developed to translate track structure through nucleus material into DNA damage. The algorithm used a spatial clustering approach, wherein direct events (e.g. ionisations and excitations) and indirect events ($^{\bullet}$OH interactions) were spatially clustered into volumes that each represented 10 base pairs of DNA. Direct events on DNA and its first hydration layer and indirect events on DNA produced DNA sugar and base radicals. The oxygen effect was simulated by making two biochemical processes depend upon the cellular pO_2: i) the chance for a base radical from an indirect event to transfer to a sugar radical and ii) the chance for a sugar radical to convert to a strand break.

It was remarkable that this model achieved not only the correct relationship for OER_{DSB} with LET, but also approximately correct values of OER_{DSB}, i.e., OER_{DSB} was 3.0 for low-LET and decreased with increasing LET to 1.3 at 150 keV/μm. For comparison, a model by Stewart et al [94] introduced a "chemical repair" variable which was a function of LET in order to produce the LET-dependence of OER_{DSB}. This was equivalent to making the efficiency of DNA radical-to-strand break conversion depend upon LET, which there is no evidence or theoretical basis for, that I know of. The current model achieved the correct LET dependence of OER_{DSB} naturally as a by-product of the spatial clustering approach.

7

Stochastic multicellular modeling of x-ray irradiation, DNA damage induction, DNA free-end misrejoining and cell death

The unpublished and unsubmitted manuscript [95] forms the basis of this chapter:

Forster JC, Douglass MJJ, Phillips WM, Bezak E. Stochastic multicellular modeling of x-ray irradiation, DNA damage induction, DNA free-end misrejoining and cell death. 2018 Oct; Manuscript in preparation.

7.1 Introduction and Motivation

An entire multicellular tumour is now irradiated and tracks are simulated in Geant4 using the Geant4-DNA physics and chemistry modules. The DNA damage algorithm was used to translate tracks through cell nuclei into DNA damage. But the bulk of this paper is concerned with another topic: how can we predict the likelihood that a cell survives, given its DNA damage? This question is explored and a stochastic algorithm is developed to simulate DNA free-end misrejoining and subsequent cell death. The algorithm is applied in a multicellular tumour following simulation of Monte Carlo tracks and DNA damage induction.

7.2 Statement of Contribution

7.2.1 Conception

Jake Forster conceived of the method of voxelisation to import the multicellular tumour into Geant4, the way of using Geant4-DNA physics and chemistry in the context of a multicellular tumour, and the idea to simulate DNA free-end misrejoining and predict cell death from it, under the supervision of Michael Douglass, Wendy Phillips and Eva Bezak.

7.2.2 Realisation

Jake Forster developed the model (i.e. wrote the code), wrote the code to run the simulations to acquire data, wrote the code to run the simulations on a supercomputer, ran the simulations on a supercomputer, analysed the data and made the plots for visualising data. The manuscript was evaluated by Eva Bezak, Wendy Phillips and Michael Douglass for data accuracy, critical appraisal, conclusions reached and general structure and flow.

7.2.3 Documentation

The manuscript was primarily written by Jake Forster, who also prepared the figures. Wendy Phillips, Michael Douglass and Eva Bezak provided input, feedback and revisions.

Statement of Authorship

Title of Paper	Stochastic multicellular modeling of x-ray irradiation, DNA damage induction, DNA free-end misrejoining and cell death
Publication Status	☐ Published ☐ Accepted for Publication ☐ Submitted for Publication ☑ Unpublished and Unsubmitted work written in manuscript style
Publication Details	Forster JC, Douglass MJJ, Phillips WM, Bezak E. 2018; Manuscript in preparation.

Principal Author

Name of Principal Author (Candidate)	Jake Cameron Forster		
Contribution to the Paper	Conceived of the model and its methods, developed the model (i.e. wrote the code), wrote the code to run the simulations to acquire data, wrote the code to run the simulations on a supercomputer, ran the simulations on a supercomputer, analysed the data, made the plots for visualising data, wrote the manuscript, prepared the figures and acted as the corresponding author.		
Overall percentage (%)	80%		
Certification:	This paper reports on original research I conducted during the period of my Higher Degree by Research candidature and is not subject to any obligations or contractual agreements with a third party that would constrain its inclusion in this thesis. I am the primary author of this paper.		
Signature		Date	3-10-2018

Co-Author Contributions

By signing the Statement of Authorship, each author certifies that:

i. the candidate's stated contribution to the publication is accurate (as detailed above);

ii. permission is granted for the candidate in include the publication in the thesis; and

iii. the sum of all co-author contributions is equal to 100% less the candidate's stated contribution.

Name of Co-Author	Prof. Eva Bezak		
Contribution to the Paper	General supervision and guidance and manuscript revision.		
Overall percentage (%)	10%		
Signature		Date	3-10-2018

Name of Co-Author	Dr Wendy Phillips		
Contribution to the Paper	General supervision and guidance and manuscript revision.		
Overall percentage (%)	5%		
Signature		Date	3-10-2018

Name of Co-Author	Dr Michael Douglass		
Contribution to the Paper	General supervision and guidance and manuscript revision.		
	5%		
Signature		Date	4-10-2018

Stochastic multicellular modeling of x-ray irradiation, DNA damage induction, DNA free-end misrejoining and cell death

Jake C. Forster*

Department of Physics, University of Adelaide

Michael J. J. Douglass and Wendy M. Phillips

Department of Medical Physics, Royal Adelaide Hospital and

Department of Physics, University of Adelaide

Eva Bezak

Cancer Research Institute and the School of

Health Sciences, University of South Australia and

Department of Physics, University of Adelaide

(Dated: December 3, 2018)

Abstract

The repair or misrepair of DNA double-strand breaks (DSBs) largely determines whether a cell will survive radiation insult or die. A new computational model of radiation-induced cell death was developed and used to investigate the contribution of DNA free-end misrejoining to cell killing by low-LET radiation. A randomized cellular tumor of 1224 squamous cells in a cubic volume of side length 0.2 mm was irradiated with 6 MV x-rays using the Monte Carlo toolkit Geant4 and the low-energy Geant4-DNA physics and chemistry modules. DNA damage including DSBs were simulated from the tracks through cell nuclei, with the cellular pO_2 affecting the efficiency of DNA radical-to-strand break conversion. DNA free-ends produced by complex DSBs (cDSBs) were able to misrejoin and produce exchange-type chromosome aberrations. The misrejoining probability was modeled as a negative exponential of the initial distance between the cDSBs with scale parameter r_0 (e.g. 0.7 μm). It was assumed there were no unrejoined ends (i.e. no terminal deletions or incomplete exchanges). The cell survival probability from misrejoining was then predicted by assuming each misrejoining independently had a probability P_{nlmr} (e.g. 0.5) of producing an asymmetric (lethal) exchange-type chromosome aberration. A sensitivity analysis was performed for model parameters DSB yield, r_0 and P_{nlmr}, observing the dose response up to 1 Gy of the number of misrejoinings per cell and the mean cell survival probability from misrejoining. Conditions of full oxia and anoxia were simulated. The linear component of cell killing from misrejoining was consistently small compared to values in the literature for the linear component of cell killing for head and neck squamous cell carcinoma (HNSCC). This indicated that misrejoinings involving DSBs from the same x-ray (including all associated secondary electrons) were rare and that other mechanisms (e.g. unrejoined ends) may be important. The quadratic component of cell killing from misrejoining was much larger than values in the literature for the quadratic component of cell killing for HNSCC. This was likely due to modeling the nuclei too small. Ignoring the contribution by the indirect effect toward DNA damage caused the DSB yield to drop to a third of its original value and the cDSB yield to drop to a tenth of its original value. As an application, DNA damage and misrejoining were simulated in all 135306 viable cells of a 1 mm^3 tumor of HNSCC, that had a tumor oxygenation typical of HNSCC, for a uniform dose of 1 Gy.

* Jake.Forster@adelaide.edu.au

I. INTRODUCTION

One of the tasks of radiobiological modeling is to predict whether a cell that received ionizing radiation will ultimately die from the initial radiation-induced DNA damage, consisting of DNA double-strand breaks (DSBs), single-strand breaks, modified bases and modified sugars. Cell death (defined by the loss of replicative potential) after irradiation mainly occurs in the form of mitotic catastrophe, meaning it results from, or follows, aberrant mitosis [1–3]. This occurs when a chromosome aberration (CA) is present that is "asymmetric", preventing a large amount of the genetic material from being replicated.

This paper presents a new computational model of CA production and cell death from ionizing radiation. First, some background is provided on the mechanism of CA production by DSB misrepair and the relationship between CAs and cell death. Some other computational models of radiation-induced CAs and cell death from the literature are then reviewed in order to establish the gap (in the literature) that will be addressed by the current model.

A. Mechanism of CA production by DSB misrepair

CAs are formed by the misrepair of DSBs. Each DSB causes a break in a chromosome, producing two DNA free-ends (a.k.a. "sticky" ends). Unrelated (incongruent) DNA free-ends produced by different DSBs can be misrejoined (illegitimate/incorrect reunion or exchange), resulting in an exchange-type CA [4–7]. A DSB can also have both ends left unrejoined, resulting in a terminal deletion, or have one end misrejoined and the other end left unrejoined (an incomplete exchange) (Figure 1) [8].

"Simple" exchange-type CAs are those that are possible with just two DSBs (Figure 2) [9]. If the two DSBs are on different chromosomes, a symmetric translocation or a dicentric (plus an acentric fragment) can form. Two DSBs on opposite arms of a chromosome can give rise to a centric ring (plus an acentric fragment) or a pericentric inversion. If the two DSBs are on the same arm, an acentric ring (plus an interstitial deletion) or a paracentric inversion can occur. A plethora of "complex" exchange-type CAs are possible with three or more DSBs on two or more chromosomes.

Of the simple exchange-type CAs, dicentrics and rings (centric and acentric) are asymmetric. Since they cause a large amount of the genetic material to be lost at the next

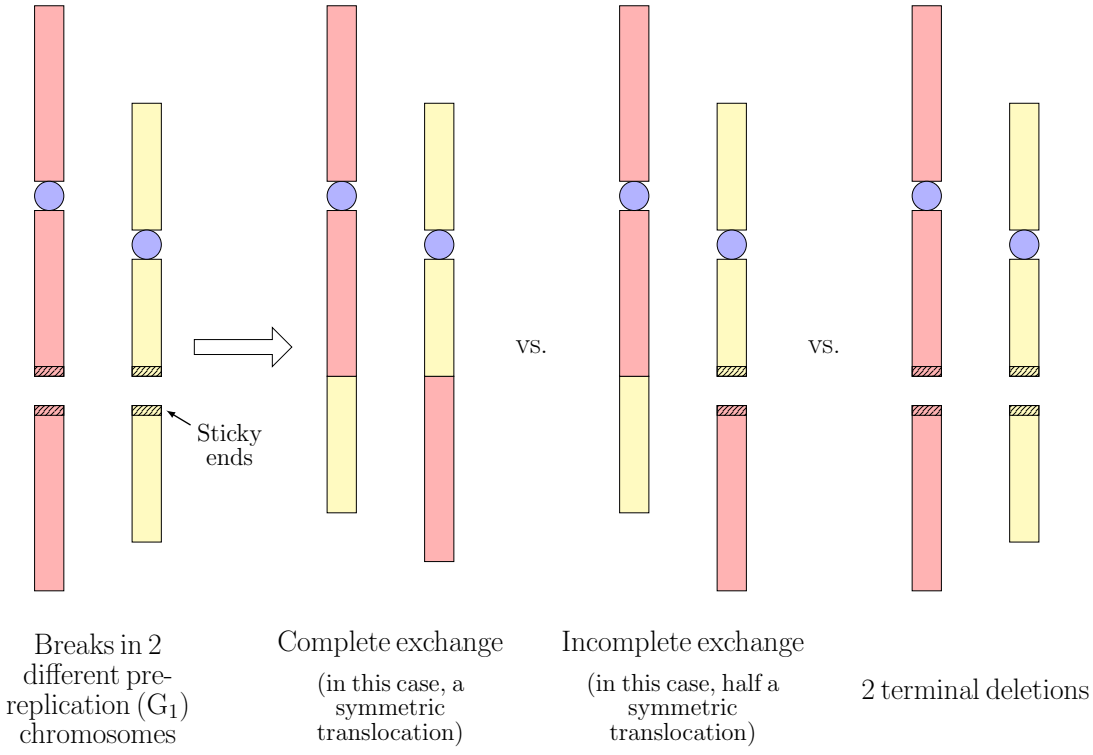

FIG. 1. DSB misrepair can be in the form of complete exchanges, incomplete exchanges and terminal deletions.

mitosis, they are unstable (lethal). On the other hand, symmetric translocations and inversions (pericentric and paracentric) are symmetric and stable (non-lethal). Large deletions due to unrejoined ends are also lethal.

The main repair pathway for DSBs in all cell cycle phases for mammalian cells is canonical-non-homologous end-joining (c-NHEJ) [6, 10–12]. There are two types of c-NHEJ in G_0/G_1: one fast (2-4 hrs) and one slow ($>$ 8 hrs). The fast one is resection-independent and the slow one is resection-dependent (and Artemis-dependent). The slow one is more error prone. For example, in G_1 human cells, resection-independent and resection-dependent c-NHEJ repaired 80% and 20% of DSBs, respectively, but each was responsible for half of the misrejoinings after a 7 Gy dose of 90 kV x-rays [13]. In G_2, resection-independent c-NHEJ is active but not resection-dependent c-NHEJ. The slow repair pathway in G_2 is homologous recombination (HR), which is error-free. HR is also active in S. There is also the alternative-NHEJ (alt-NHEJ) pathway, which involves enzymatically-driven resection. This is slow and error-prone (similar to resection-dependent c-NHEJ), but does not seem to

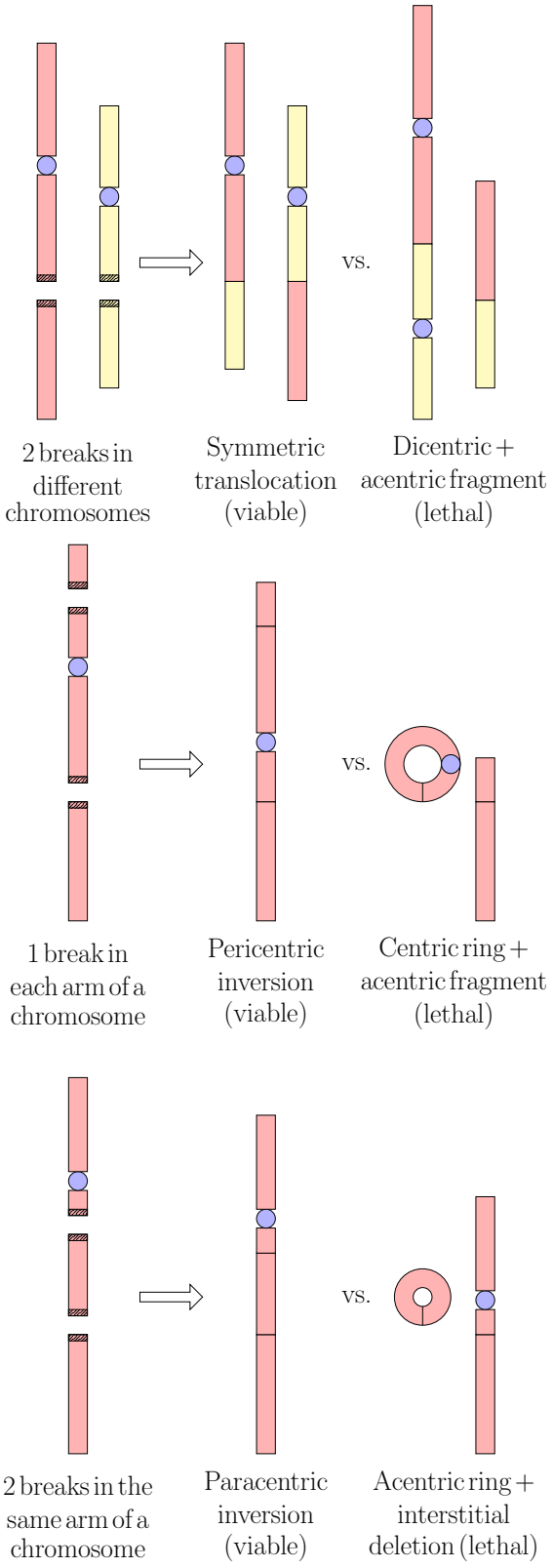

FIG. 2. Simple exchange-type CAs. Complete exchanges are shown.

contribute to repair in G_0/G_1-phase human cells (though it does appreciably in mice) [10].

Since DNA free-ends must spatio-temporally co-localize to either rejoin or misrejoin, it appears that the slowness of resection-dependent c-NHEJ and alt-NHEJ is what makes them more error-prone than resection-independent c-NHEJ, which is fast: the DNA free-ends have more time to move away from their initial location (possibly with Brownian motion [14]) and meet incongruent DNA free-ends. It follows that a misrejoining is more likely to occur if the DSBs are initially closer together.

The complexity of a DSB appears to affect the choice of repair pathway. Complex DSBs are repaired by slow pathways and simple DSBs by fast pathways [15, 16], though it is unclear why this is the case [11, 17]. Accordingly, DNA free-ends from complex DSBs are more likely to be misrejoined.

The average number of CAs per cell, N_{ca}, is typically linear-quadratic with dose [4, 7]:

$$N_{ca} = \alpha_{ca} D + \beta_{ca} D^2 \tag{1}$$

The linear component receives contributions from misrejoinings involving DSBs produced by the same primary (e.g. the same x-ray, including all associated secondary electrons) and from terminal deletions. The quadratic component corresponds to misrejoinings involving DSBs produced by two different primaries (thus it depends on dose rate and fractionation).

Let $f \leq 1$ be the fraction of lethal CAs, so the average number of lethal CAs per cell is:

$$N_{lca} = f N_{ca} \tag{2}$$

If the fraction of lethal CAs is independent of dose and lethal CAs are Poisson distributed in cells (the latter assumption may become less valid with increasing dose [18]), the surviving fraction from lethal CAs is:

$$S_{lca} = e^{-N_{lca}} \tag{3}$$

$$= e^{-f(\alpha_{ca} D + \beta_{ca} D^2)} \tag{4}$$

$$= e^{-\alpha_{\text{killing}(lca)} D - \beta_{\text{killing}(lca)} D^2} \tag{5}$$

Thus the surviving fraction inherits the linear-quadratic dependence from the CA yield [2]. The linear-quadratic model generally provides a good fit to experimental data from a clonogenic cell survival assay for doses up to about 10 Gy per fraction [19].

It is important to emphasise that S_{lca} is the contribution to the surviving fraction from the mechanism of lethal CA-driven mitotic catastrophe. While this appears to be the main mechanism of radiation-induced cell death for mammalian cells [1–3], there is evidence for additional sources of cell death. Sensitivity to apoptosis is often reduced in cancer compared to normal tissue [20], but apoptosis may be an important contributor to radiosensitvity in some tumors [1]. Apoptosis can occur in response to DNA damage [21]. In addition, damage to mitochondria (which can be enhanced by gold nanoparticles) can trigger cell death by apoptosis [22]. There are also non-targeted effects (bystander and cohort effects), i.e. signals emitted from nearby cells, that can elicit apoptosis [23]. In the approximation that the different mechanisms contribute independently (i.e. no synergistic or antagonistic effects), the overall surviving fraction is given by the product of all the contributions:

$$S = S_{lca} S_2 S_3 ... \tag{6}$$

Macroscopic cell death is the convolution of many microscopic processes. By modeling a microscopic process such as the production of CAs, its contribution to cell death can be investigated in isolation.

B. Computational models of radiation-induced CAs and cell death

Deterministic models of DSB repair and misrepair in the literature include [24–26]. There are also stochastic models, which stochastically generate a spatial distribution of DSBs in the nucleus (e.g. from Monte Carlo track structure) and then simulate the fate of each individual DSB using stochastic methods. The model in the current work is stochastic. Examples of stochastic models in the literature include the model by Henthorn et al [27], Friedland and Kundrát's model [28, 29], "BIophysical ANalysis of Cell death and chromosome Aberrations" (BIANCA) [30–32] and Brenner's model [33].

Brenner's model simulated track segments using the Monte Carlo code PROTON. A track was generated and then a cell nucleus was randomly superimposed over the track to score a segment of the track in the nucleus. This was repeated for a number of tracks (a certain number of tracks were expected to pass through the nucleus for a given dose), then it was assumed 1 in 1500 ionizations produced a DSB. The model simulated time-dependent diffusion and distant-dependent interaction of the DSBs to form exchange-type CAs, in

competition with faithful DSB repair.

The BIANCA model simulated cluster lesions (CLs), which were effectively DSBs whose free-ends were able to misrejoin, in a single cell nucleus. For sparsely-ionizing photons, the CLs were placed at random in the nucleus. For protons and alphas, there was an expected number of nucleus traversals (based on dose) and an expected number of CLs from each traversal (based on LET). Line segments representing traversals were randomly simulated through the nucleus and CLs were randomly distributed along the line segments. For higher LETs, some of the CLs were placed radially with respect to the line segments to account for high-energy secondary electrons. Proximity-based misrejoining of the DNA free-ends from CLs was simulated. The nucleus contained interphase chromosome territories and chromosome-arm domains, making it possible to determine the types of CAs produced (e.g. dicentrics, centric rings, etc.).

Friedland and Kundrát's model simulated Monte Carlo tracks through a single cell nucleus using the code PARTRAC (PARticle TRACks) and superimposed the tracks with a multiscale DNA target model to generate DNA damage. Spatio-temporal motion of DNA free-ends was simulated in addition to mechanistic modeling of NHEJ to achieve DSB repair and misrepair. The types of CAs produced were known due to modeling of chromosome territories in the nucleus. The model by Henthorn et al also simulated DNA free-end motion with mechanistic modeling of c-NHEJ. The DSBs were generated from Monte Carlo tracks simulated in Geant4 [34–36] using Geant4-DNA [37–39], using a spatial clustering approach. Chromosome territories were not modeled.

Compared with these other stochastic models, the current model has two unique properties: i) Monte Carlo tracks were simulated through a multicellular tumor volume (as opposed to a single cell nucleus) and ii) variable cellular pO_2 conditions were simulated. A multicellular tumor of head and neck squamous cell carcinoma (HNSCC) was irradiated with tracks using the Monte Carlo toolkit Geant4 (version 10.4) [34–36]. The physics and chemistry modules of Geant4-DNA [37–39] were used to accurately simulate low-energy physical interactions and the chemical tracks from water radiolysis. The tracks through cell nuclei were translated into spatial distributions of DNA damage, including DSBs, by spatially clustering the direct and indirect events into simulated DNA volumes. The DNA damage from the tracks was subject to the cellular pO_2: a higher pO_2 produces more efficient DNA radical-to-strand break conversion. Proximity-based DNA free-end misrejoining was simulated. Cell

death was predicted from the presence of lethal CAs.

The purpose of this work was two-fold: First, to present new stochastic modeling of radiation-induced CA production and cell killing, that befits a different purpose than other models in the literature. Namely, the simulation of a multicellular tumor and variable pO_2 conditions makes this model uniquely apt to be used as part of a radiotherapy model. Radiotherapy models often take the approach of simulating each cell in the tumor, but they typically simulate the radiation effect using the Linear-Quadratic equation or a variant thereof [40–45]. Greater accuracy and utility may be achieved if instead the radiation effect is simulated starting from Monte Carlo tracks. With improved accuracy and utility, radiotherapy models may find greater use in radiotherapy planning, helping to further individualize radiotherapy treatments to account for patient-specific radiobiology. The second aim of this work was to use the model to investigate the contribution of DNA free-end misrejoining to CA production and cell death by low-LET radiation for HNSCC.

II. MATERIALS AND METHODS

A. Model methods

A computational model was developed in-house to simulate a fraction of dose to a multicellular tumor of HNSCC, followed by DNA damage induction, DNA free-end misrejoining and cell death from misrejoining. The flowchart in Figure 3 summarises the components of the model, which are described in more detail below.

1. Tumor cell placement in 3D

A cubic volume of side length 0.2 mm was filled with 1224 non-overlapping cells (a tumor-mimetic density [46] of 1.53×10^8 cells/cm^3) using a previously developed algorithm (Figure 4(a)) [47, 48]. The cells were ellipsoid-shaped with random orientations and major axis lengths between 14 and 20 μm, representative of FaDu HNSCC cells [49]. Cells contained a concentric nucleus that occupied 8% of the cellular volume [50].

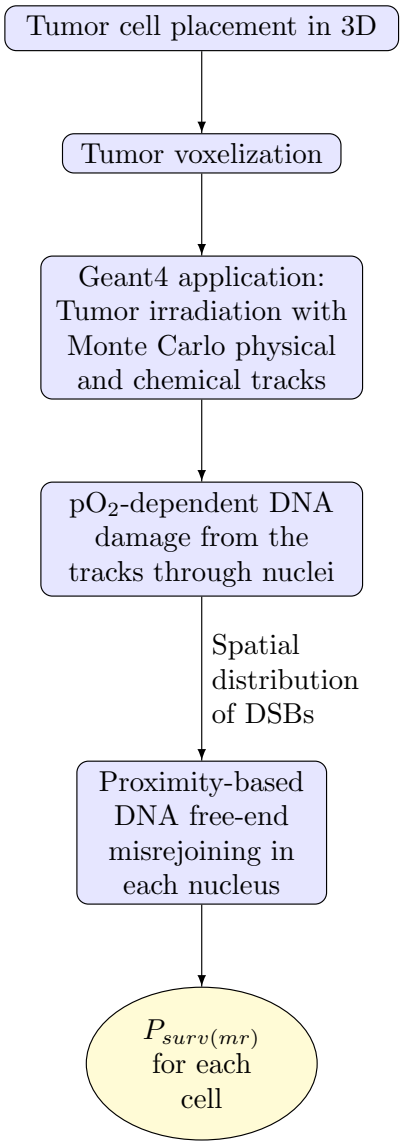

FIG. 3. Basic flowchart of the model. $P_{surv(mr)}$ is the probability of cell survival by the mechanism of misrejoining.

2. Tumor voxelization

In order to import the multicellular tumor (1224 cells) into Geant4 (version 10.4), it was first voxelized. Voxels were cubic volumes of side length 2 μm representing either nucleus, cytoplasm or intercellular material (Figure 4(b)). Voxelization was performed using an algorithm written in Matlab (R2016b, MathWorks® Inc., Natick, MA). The distance from the center of a voxel to the center of a cell was used to determine whether the center of the

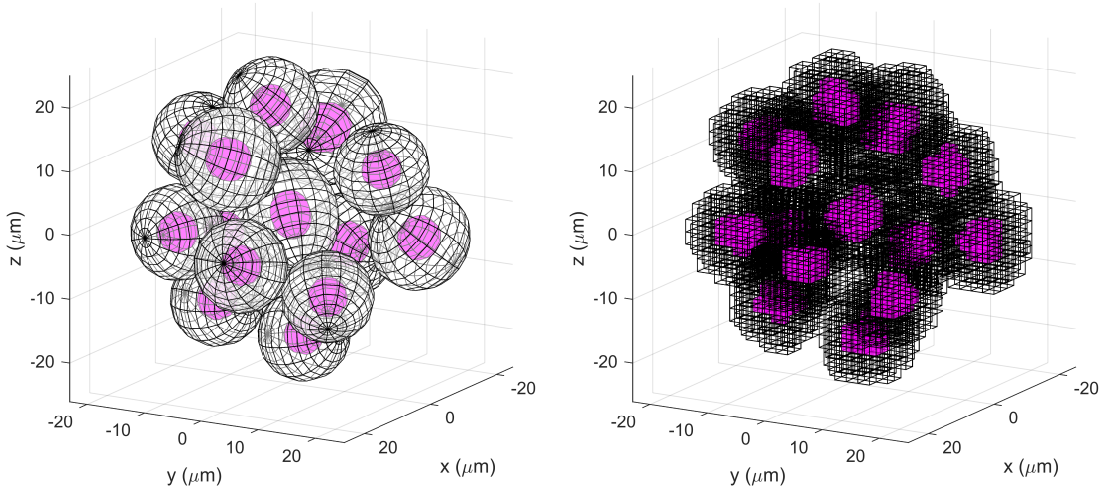

(a) (b)

FIG. 4. Example of a multicellular tumor with a small number of cells for demonstration. (a) Randomized ellipsoidal cells containing nuclei. (b) The corresponding voxel representation, showing nucleus and cytoplasm voxels.

voxel was located within the nucleus or cytoplasm of the cell (accounting for the ellipsoid-shaped cell and nucleus and their rotation). Voxels were assigned as nucleus or cytoplasm based on this criteria.

For the cubic volume of side length 0.2 mm, there were $100 \times 100 \times 100 = 10^6$ voxels. Two 3D arrays of size $100 \times 100 \times 100$ called *voxelType* and *voxelCell* were introduced. The element $\vec{i} = (i, j, k)$ of these arrays (where i, j and k took integer values from 0 to 99) corresponded to the voxel whose center had spatial coordinates:

$$\vec{X} = -99 + 2\vec{i} \ \ (\mu\text{m}) \tag{7}$$

The *voxelType* array contained the flag identifying the voxel type (0 for intercellular, 1 for nucleus and 2 for cytoplasm) and *voxelCell* contained the flag identifying the cell that the voxel belonged to (0 for intercellular voxels, 1-1224 for nucleus and cytoplasm voxels).

3. Tumor irradiation with track structure

The voxelized multicellular tumor (1224 cells) was imported into Geant4 as follows. A cubic volume (soon to accommodate the tumor) of side length 0.2 mm was placed in Geant4 and divided into $100 \times 100 \times 100$ voxels using "nested parametersiation". Nucleus, cytoplasm

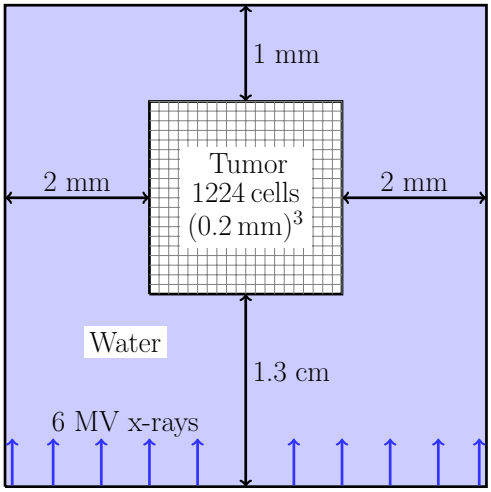

FIG. 5. Irradiation set-up in Geant4: the voxelized multicellular tumor encased in water.

and intercellular materials were defined equivalent to "G4_WATER" (as is required to use Geant4-DNA) with density 1 g/cm^3. The voxels were then assigned to nucleus, cytoplasm or intercellular material using the *voxelType* array.

X-rays with an energy distribution from a 6 MV linac model developed in the Philips Pinnacle treatment planning system were fired from a square 4.2 mm × 4.2 mm source with parallel beam, placed 1.3 cm from the tumor (Figure 5). The tumor was encased in water to achieve a uniform dose to tumor (see Results, Section III A). Relative to the beam direction, there was 1.3 cm of water in front of the tumor to achieve electronic equilibrium in the tumor (for 6 MV x-rays the mean electron energy is $\sim$ 2 MeV, which has a range of $\sim$ 1 cm in liquid water using the continuous slowing down approximation [51]), 2 mm of water either side of the tumor for lateral scattering and 1 mm of water behind the tumor to provide back scatter medium (MV x-rays mostly scatter forward).

Geant4-DNA physics models, which accurately simulate physical interactions down to eV energies, were used to simulate electron interactions in the tumor for electron energies $<$ 1 MeV (the models were not defined $\geq$ 1 MeV). The Livermore physics list (which is low-energy but not as low as Geant4-DNA) was used in the tumor for electron energies $\geq$ 1 MeV and for photon and positron interactions (Table I). Outside the tumor, Livermore physics was used exclusively (there was no need to simulate very low-energy physics outside the tumor) (Table II). For physical interactions in nucleus voxels that deposited $\geq$ 10.79 eV (the ionization energy for liquid water), the spatial coordinates of the interaction were

TABLE I. Physics interactions simulated in the tumor.

Particle	Interaction	Energy range[a]	Model
e^-	multiple scattering	≥ 1 MeV	Urban
	elastic scattering	(7.4 eV, 1 MeV)	DNA Champion
	ionization	≥ 1 MeV	Møller-Bhabha
		[10 keV, 1 MeV)	DNA Born
		[11 eV, 10 keV)	DNA Emfietzoglou
	excitation	[10 keV, 1 MeV)	DNA Born
		[8 eV, 10 keV)	DNA Emfietzoglou
	vibrational excitation	(7.4 eV, 100 eV)	DNA Sanche
	attachment	(7.4 eV, 11.2 eV)	DNA Melton
	electron solvation	≤ 7.4 eV	DNA one step thermalization
	bremsstrahlung		Livermore
γ	Compton		Livermore
	photoelectric effect		Livermore
	conversion		Livermore
	Rayleigh scattering		Livermore
e^+	multiple scattering		Urban
	ionization		Møller-Bhabha
	bremsstrahlung		Seltzer-Berger
	annihilation		

[a] Energies relevant to this application with 6 MV x-rays. Active for all relevant energies if not specified.

recorded, along with the flag identifying the cell in which it took place (via *voxelCell*). The total energy deposited in each voxel was also recorded.

Geant4-DNA chemistry was used to simulate water radiolysis following Geant4-DNA physics, but only inside nucleus voxels to save computation time (Figure 6). It was assumed that $^{\bullet}$OH molecules interacted after 2.5 ns of diffusion. This corresponded to an $^{\bullet}$OH scavenging capacity of 4×10^8 s^{-1}, and a root-mean-square displacement of 6.48 nm with the $^{\bullet}$OH diffusion coefficient of 2.8×10^{-9} $m^2 s^{-1}$ used in Geant4-DNA chemistry, which are

TABLE II. Physics interactions simulated outside the tumor.

Particle	Interaction	Energy range[a]	Model
e^-	multiple scattering		Urban
	ionization	≥ 100 keV	Møller-Bhabha
		< 100 keV	Livermore
	bremsstrahlung		Livermore
γ[b]			
e^+[b]			

[a] Energies relevant to this application with 6 MV x-rays. Active for all relevant energies if not specified.
[b] Same as in the tumor (Table I).

mimetic of the cellular environment [52–57]. When the virtual time of the chemistry simulation reached 2.5 ns, for each $^{\bullet}$OH molecule inside a nucleus voxel, the spatial coordinates of the $^{\bullet}$OH were recorded (taken to be the position of an $^{\bullet}$OH interaction) along with the flag identifying the cell it was located in. The chemistry simulation was ended after a virtual time of 2.5 ns to save computation time.

4. DNA damage induction algorithm

A spatial distribution of DNA damage including DSBs, single-strand breaks, modified bases and modified sugars was generated in each tumor cell nucleus from the track structure, using an algorithm that has previously been described [58]. Briefly, the algorithm spatially clustered the physical interactions that deposited ≥ 10.79 eV (direct events) and $^{\bullet}$OH interactions (indirect events) in the nucleus into cylindrical volumes representing 10 base-pair segments of DNA. Direct events on DNA and its first hydration layer and indirect events on DNA produced DNA sugar radicals and base radicals, some of which were subsequently converted to strand breaks with pO_2-dependent probabilities. Two or more strand breaks within 10 base-pairs constituted a DSB. If two DSBs were separated by less than 10 undamaged base-pairs, they were classified as the same DSB. Thus DSBs acquired a multiplicity. Only the spatial distributions of DSBs were used hence.

Note that the chemical stage of the Geant4-DNA chemistry simulation was ended at 2.5

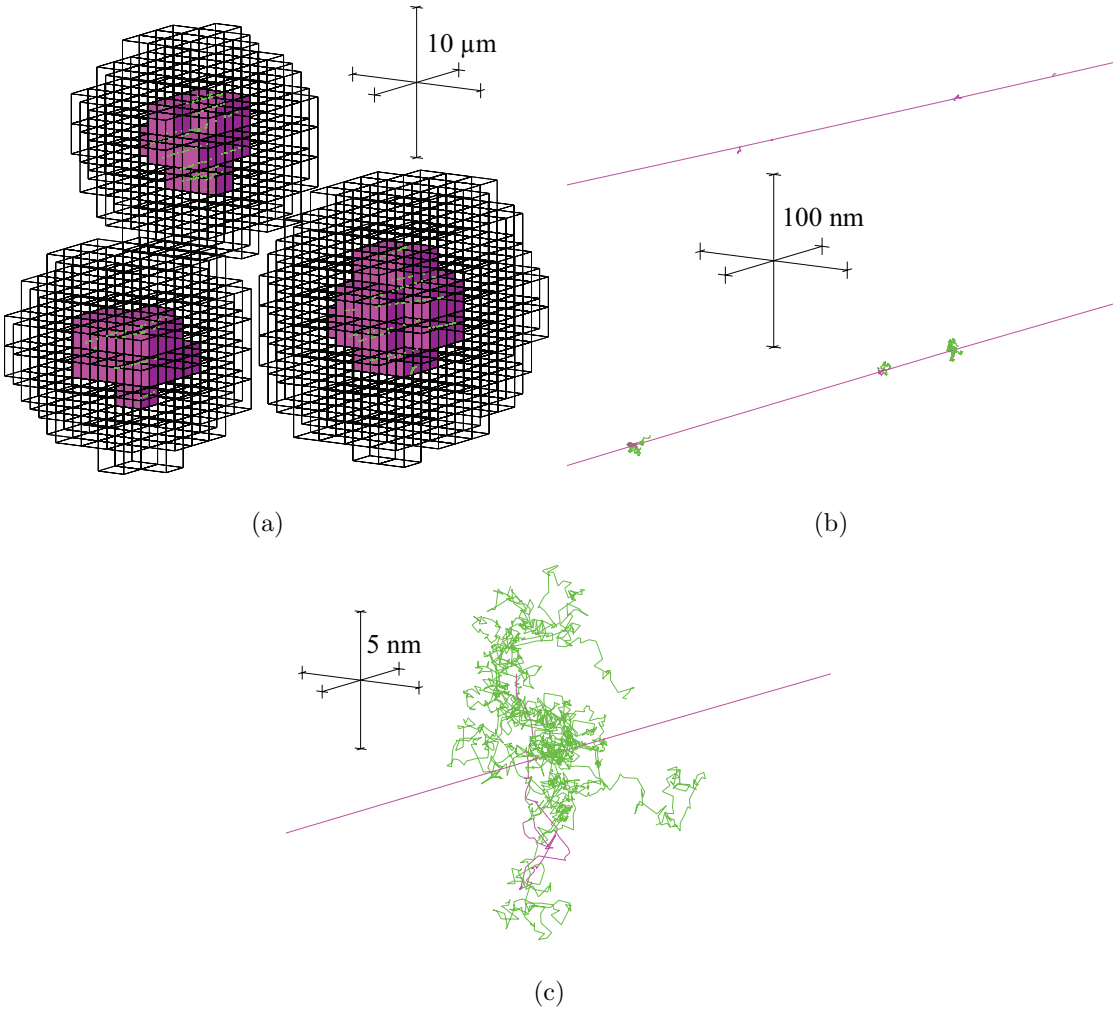

FIG. 6. Visualization of a few cells irradiated with 1 MeV electrons. (a) The electron tracks are not drawn, but their passage through cell nuclei is dotted by $^{\bullet}$OH tracks (green) (Geant4-DNA chemistry was only simulated in nucleus voxels). The three scale bars are mutually orthogonal and each 10 μm long. (b) A closer view (100 nm scale bars) shows the $^{\bullet}$OH tracks generated sporadically along the electron tracks (magenta). (c) A closer view again (5 nm scale bars) shows an $^{\bullet}$OH track in more detail, depicting 2.5 ns of diffusion by Brownian motion.

ns in the current work. In the previous work [58], in which the DNA damage induction algorithm was developed and verified, the chemical stage was continued to 1 μs. As a result, the relatively small number of $^{\bullet}$OH molecules formed during the chemical stage (by the reaction $e^{-}_{aq} + H_2O_2 \longrightarrow OH^{-} + {}^{\bullet}OH$, as opposed to during the physicochemical stage) were neglected in the current work. This was predicted to have a negligible effect on the DSB

yield, since these $^{\bullet}$OH molecules are typically formed away from the electron track and thus rarely contribute to clusters of damage (e.g. DSBs).

The DNA damage induction algorithm includes a parameter which may be interpreted as the volume proportion of DNA in the nucleus (DNA volume for short). The DNA damage yields, including the DSB yield, were scaled down according to this parameter. This meant that a fraction of the DSBs within the whole nucleus volume were removed from each cell, chosen at random and irrespective of DSB complexity. Estimates in the literature of the DNA volume in yeast cells vary from 0.3 to 2% [59]. In the current work, the DNA volume was adjusted to achieve realistic DSB yields. Experiments in the literature indicate that the DSB yield increases linearly with dose in the clinically relevant dose range < 100 Gy and is generally 20-40 /cell/Gy for mammalian haploid cells [7, 60–63]. For low-LET radiation and human HNSCC cell lines (in vitro) in particular, Saker et al [64], using colocalization of γH2AX and 53BP1 foci, measured an average of 36 DSBs/cell after 1 Gy with 200 kV x-rays for UTSCC15, FaDuDD and UTSCC14. El-Awady et al [65] with 220 kV x-rays measured a DSB yield of approximately 20 /cell/Gy for SCC4451 using graded-field gel electrophoresis. We aimed to achieve these yields; the current work includes a sensitivity analysis (see Section II B) using DSB yields of approximately 20, 30 and 40 /cell/Gy, which were achieved with DNA volumes of 13.3%, 20% and 26.7%, respectively (see Discussion for the likely reason for high DNA volumes).

5. DNA free-end misrejoining and cell death

In our simulation, DNA free-ends from complex DSBs (cDSBs) were able to participate in misrejoining events. To obtain a cDSB yield that was approximately 10% of the DSB yield (and therefore similar to the CL yields in the BIANCA model for x-rays, e.g. 4.0 /Gy/cell for a monolayer-shaped fibroblast and 3.1 /Gy/cell for a lymphocyte [32]), cDSBs were defined as DSBs with > 15 elementary damages (strand breaks, modified bases and modified sugars).

The probability of a misrejoining, P_{mr}, between two incongruent free-ends was modeled as a negative exponential function of the initial distance, d, between the two cDSBs that produced them (note that a negative exponential was used in the BIANCA model and the simulated CA yields for low-LET radiation achieved good agreement with experimental data

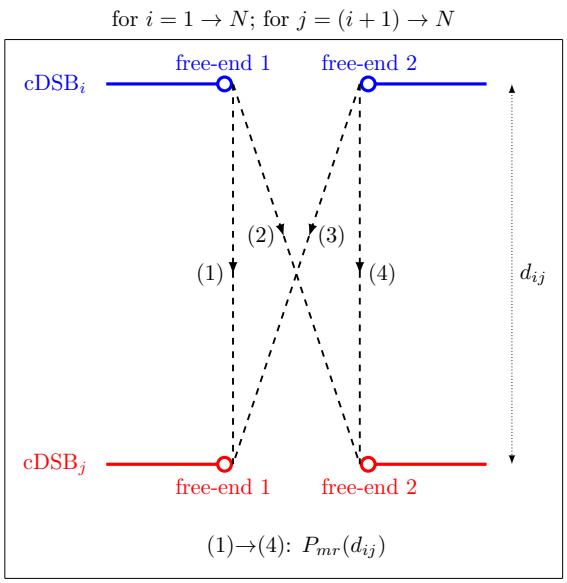

FIG. 7. Schematic of the stochastic, proximity-based DNA free-end misrejoining algorithm, based on the method in the BIANCA model [32]. A successful misrejoining event removed two free-ends from the pool. N is the total number of cDSBs, d_{ij} is the initial distance between cDSB$_i$ and cDSB$_j$, $P_{mr}(d_{ij})$ is the probability of a misrejoining between a free end of cDSB$_i$ and a free-end of cDSB$_j$.

for a monolayer-shaped fibroblast and a lymphocyte [32]):

$$P_{mr} = e^{-d/r_0}, \tag{8}$$

where r_0 is the characteristic interaction distance, which was an adjustable parameter (e.g. [32] used 0.7 μm for a monolayer-shaped fibroblast and 0.8 μm for a lymphocyte in BIANCA). For a nucleus containing N cDSBs (cDSB$_1$, cDSB$_2$, ..., cDSB$_N$), misrejoining was simulated as follows (Figure 7): The first free-end of cDSB$_1$ had a chance (with probability P_{mr}) to misrejoin with the first free-end of cDSB$_2$, then with the second free-end of cDSB$_2$. Then the second free-end of cDSB$_1$ had a chance to misrejoin with the first free-end of cDSB$_2$, then with the second free-end of cDSB$_2$. Then the first free-end of cDSB$_1$ had a chance to misrejoin with the first free-end of cDSB$_3$, then with the second free-end of cDSB$_3$, and so on. In general, each free-end of cDSB$_i$ had a chance to misrejoin with each free-end of cDSB$_{i+1}$, cDSB$_{i+2}$, ..., cDSB$_N$ (i.e. each combination of free-ends was tried only once). Successful misrejoinings removed free-ends from the "pool" of candidates.

To predict cell death from misrejoinings, the following assumptions were made:

1. No terminal deletions: cDSBs with both ends unrejoined were rejoined faithfully/correctly.

2. No incomplete exchanges: For cDSBs with only one end misrejoined, assume the other end misrejoined with the same cDSB as the first, or if that cDSB has no free ends, with the other available end in the misrejoining "chain" (e.g. if $cDSB_1$ and $cDSB_2$ each have an end misrejoined with an end from $cDSB_3$, then the remaining end of $cDSB_1$ was assumed to misrejoin with the remaining end of $cDSB_2$).

3. If two cDSBs misrejoined both of their ends together during the original misrejoining simulation, the second misrejoining was not counted, as this was assumed (from the previous assumption).

With these assumptions in place, each counted misrejoining independently had a 50% chance of resulting in an asymmetric exchange-type CA and thus causing cell death (Appendix). Accordingly, the probability of cell survival from misrejoining, $P_{surv(mr)}$, was related to the total number of counted misrejoinings, N_{mr}, by (similar to Brenner's model [33]):

$$P_{surv(mr)} = 0.5^{N_{mr}} \tag{9}$$

In the sensitivity analysis (see Section II B), values other than 0.5 were also considered for the probability that a misrejoining was non-lethal, P_{nlmr}; in which case:

$$P_{surv(mr)} = (P_{nlmr})^{N_{mr}} \tag{10}$$

The parameter r_0 (from Equation 8) was also included in the sensitivity analysis.

B. Simulations performed

1. Sensitivity analysis

Doses to the tumor (1224 cells) of up to 1 Gy were simulated (1 mGy, 3 mGy, 10 mGy, 30 mGy, 60 mGy, 0.1 Gy, 0.3 Gy, 0.5 Gy, 0.7 Gy and 1 Gy). For each dose, DNA damage induction and DNA free-end misrejoining were simulated in all 1224 cells under conditions

of full oxia (pO_2 of 760 mmHg) and anoxia (pO_2 of 0 mmHg). The number of DSBs per cell vs dose and the number of cDSBs per cell vs dose were fit (using Matlab) to:

$$N_{\text{DSB}} = m_{\text{DSB}} D \tag{11}$$

$$N_{\text{cDSB}} = m_{\text{cDSB}} D \tag{12}$$

The number of misrejoinings per cell vs dose was fit to:

$$N_{mr} = \alpha_{mr} D + \beta_{mr} D^2 \tag{13}$$

If $\alpha_{mr} < 0$, the fit was reperformed to:

$$N_{mr} = \beta_{mr} D^2 \tag{14}$$

The mean probability of cell survival from misrejoining was fit to:

$$P_{surv(mr)} = e^{-\alpha_{\text{killing}(mr)} D - \beta_{\text{killing}(mr)} D^2} \tag{15}$$

If $\alpha_{\text{killing}(mr)} < 0$, the fit was reperformed to:

$$P_{surv(mr)} = e^{-\beta_{\text{killing}(mr)} D^2} \tag{16}$$

The oxygen enhancement ratios (OERs) for DSB and cDSB induction were obtained by:

$$\text{OER}_{\text{DSB}} = \frac{m_{\text{DSB}}(pO_2 \text{ of 760 mmHg})}{m_{\text{DSB}}(pO_2 \text{ of 0 mmHg})} \tag{17}$$

$$\text{OER}_{\text{cDSB}} = \frac{m_{\text{cDSB}}(pO_2 \text{ of 760 mmHg})}{m_{\text{cDSB}}(pO_2 \text{ of 0 mmHg})} \tag{18}$$

The surviving fraction from misrejoining after a dose of 2 Gy, $\text{SF}_{2(mr)}$, was obtained by extrapolation using the fit for $P_{surv(mr)}$. The OER for cell killing by misrejoining was measured as:

$$\text{OER}_{\text{killing}(mr)} = \frac{D_{10}(pO_2 \text{ of 0 mmHg})}{D_{10}(pO_2 \text{ of 760 mmHg})} \tag{19}$$

where the dose to achieve 10% survival, D_{10}, was obtained by extrapolation using the fit for $P_{surv(mr)}$.

A sensitivity analysis was performed for the model parameters DSB yield $\in$ {20.1, 30.1, 40.2} /cell/Gy, $r_0 \in \{0.5, 0.7, 0.9\}$ μm and $P_{nlmr} \in$ {0.25, 0.5, 0.75}, using the endpoints OER_{DSB}, OER_{cDSB}, α_{mr}, β_{mr}, $\alpha_{\text{killing}(mr)}$, $\beta_{\text{killing}(mr)}$, $\text{SF}_{2(mr)}$ and $\text{OER}_{\text{killing}(mr)}$.

Simulations were performed on the Phoenix supercomputer (University of Adelaide, Adelaide, Australia). To irradiate the tumor (1224 cells) with tracks to a uniform dose of 1 Gy required 637 runs of 5×10^7 x-rays each. Each run required 5 cores sharing 30 GB of memory for 1.25 hours (4000 core hours total). The amount of resources required to run the the DNA damage induction algorithm was non-linear with dose. For a dose of 1 Gy, the DNA damage algorithm required 1 core with 35 GB for 8 hours, followed by 5 cores sharing 110 GB for 32 hours, once for full oxia and once for anoxia (328 core hours total). For comparison, for a dose of 0.7 Gy, it used 1 core with 25 GB for 3 hours, followed by 5 cores sharing 50 GB for 13 hours, once for full oxia and once for anoxia (29 core hours total). The misrejoining algorithm required almost no resources.

2. Isolation of the indirect effect

DNA damage induction and DNA free-end misrejoining were repeated for each dose, but without including the indirect effect ($^{\bullet}$OH interactions with DNA) in the induction of DNA damage. A DSB yield of 30.1 /Gy/cell, r_0 of 0.7 μm and P_{nlmr} of 0.5 were used. Without the indirect events, the DNA damage algorithm required approximately half as many core hours and GB of memory.

3. HNSCC tumor of volume 1 mm^3

The voxelized tumor (the cubic volume of side length 0.2 mm containing 1224 cells) was replicated 125 times to form a cubic volume of side length 1 mm^3 containing $1224 \times 125 = 153000$ cells. A previously developed model for cellular HNSCC tumor growth with angiogenesis [47, 66] was used to generate a connected network of blood vessels through the 1 mm^3 tumor and then assign each cell with a pO_2 according to its proximity to blood vessels.

The relevant model parameters were the relative vascular volume (RVV), the blood oxygenation (p_0) and the distance from a vessel to the onset of necrosis (ND). While HNSCC can have RVV from 2-10%, p_0 from 20-100 mmHg and ND from 80-300 μm [67], a typical HNSCC is very hypoxic, requiring these parameters to take values near their lower limits [66]. In order to achieve a typical HNSCC oxygenation (see Results; Section III C),

an RVV of 2.1%, p_0 of 30 mmHg and ND of 130 μm were chosen.

The same physical and chemical tracks through the original 1224 cells from 1 Gy were used for all 125 "copies" of the $(0.2\text{ mm})^3$ tumor. The positions that were occupied by viable cells (as opposed to necrotic cells or blood vessel units) and their pO_2 values differed between copies. Stochastic DNA damage induction and subsequent DNA free-end misrejoining were simulated for each viable (non-necrotic) cell in each copy. While the spatial distributions of direct and indirect events in nuclei were the same between copies, the DNA targets were moved each time, affecting which direct and indirect events hit the DNA. Furthermore, the same event on DNA may have produced the DNA radical on the sugar moiety one time and on a base the next. Most importantly, a higher cellular pO_2 made it more likely for a DNA radical to be converted to a strand break. For all of these reasons, the spatial distribution of DSBs in each nucleus was different between copies.

For the 1 mm^3 tumor of HNSCC, bivariate frequency distributions were generated of i) the cellular pO_2 and the number of DSBs in the nucleus, ii) the cellular pO_2 and the number of cDSBs in the nucleus, iii) the cellular pO_2 and the number of misrejoinings in the nucleus and iv) the cellular pO_2 and the cell survival probability from misrejoining.

The DNA damage algorithm required 1 core with 35 GB for 8 hours, followed by 5 cores sharing 110 GB for 32 hours for each of the 125 copies (20,008 core hours total).

III. RESULTS

A. Sensitivity analysis

Variations with dose of the number of DSBs per cell, the number of cDSBs per cell, the number of misrejoinings per cell and the cell survival probability from misrejoining, under full oxia and anoxia, are shown in Figure 8. These results used a DSB yield of 30.1 /Gy/cell, r_0 of 0.7 μm and P_{nlrm} of 0.5. The number of misrejoinings per cell and the cell survival probability from misrejoining were mostly quadratic with dose under full oxia ($\alpha_{mr} = 0.02$ Gy^{-1} and $\beta_{mr} = 0.37$ Gy^{-2}; $\alpha_{\text{killing}(mr)} = 0.02$ Gy^{-1} and $\beta_{\text{killing}(mr)} = 0.17$ Gy^{-2}) and purely quadratic under anoxia ($\beta_{mr} = 0.03$ Gy^{-2}; $\beta_{\text{killing}(mr)} = 0.02$ Gy^{-2}).

The results of a sensitivity analysis for the parameters DSB yield, r_0 and P_{nlrm} are presented in Tables III-V, respectively. The amount of misrejoining and hence cell killing

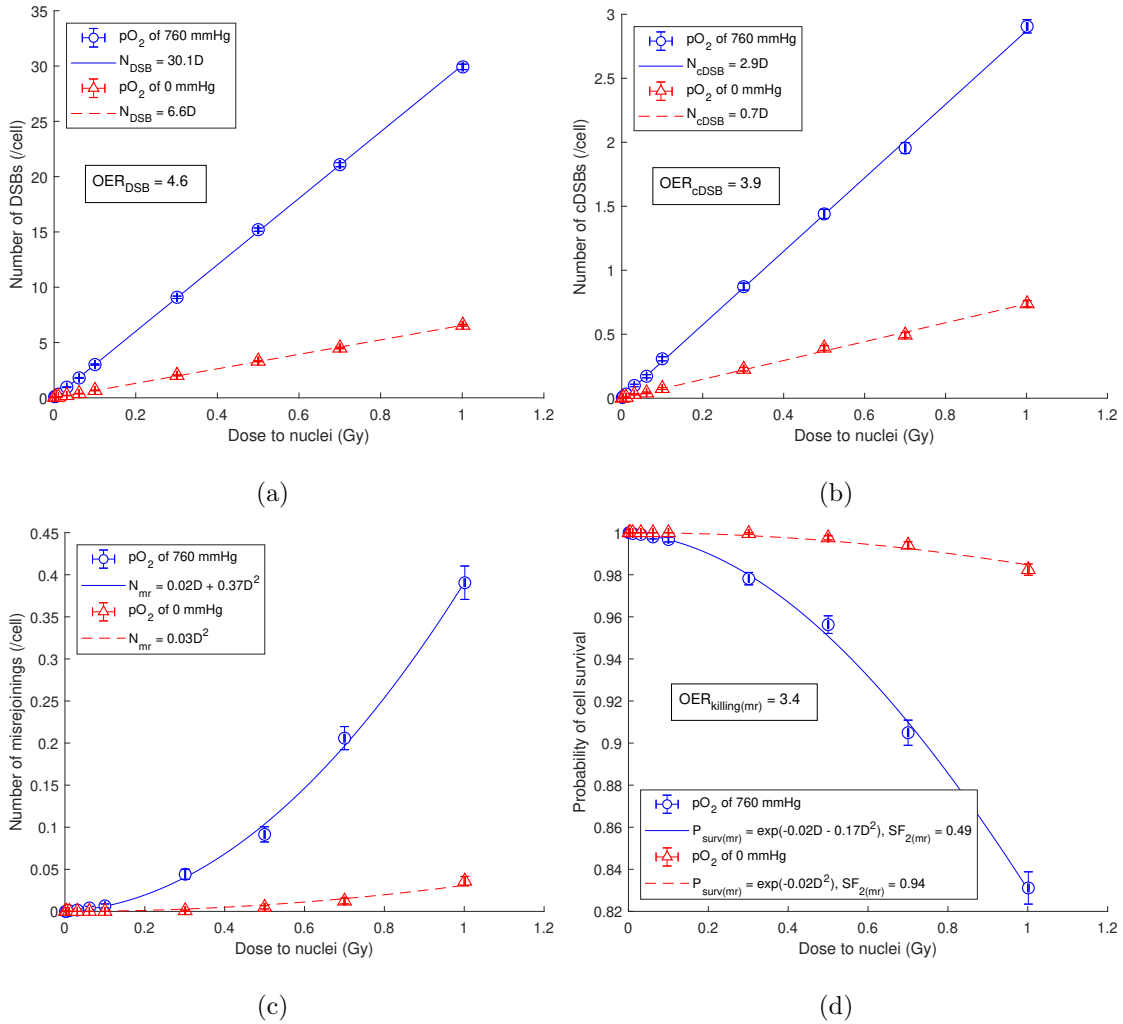

FIG. 8. (a) Number of DSBs per cell vs dose. (b) Number of cDSBs per cell vs dose. (c) Number of misrejoinings per cell vs dose. (d) Cell survival probability from misrejoining vs dose. The mean values for $n = 1224$ cells were plotted with error bars equal to the SEM. The model parameters used were a DSB yield of 30.1 /Gy/cell, r_0 of 0.7 μm and P_{nlrm} of 0.5.

increased with increasing DSB yield and r_0 while the amount of cell killing decreased with increasing P_{nlrm}, as expected. Note that misrejoining and cell killing consistently had small linear components (i.e. the α_{mr} and $\alpha_{\text{killing}(mr)}$ values). Also consistently observed were $\text{OER}_{\text{cDSB}} < \text{OER}_{\text{DSB}}$ and $\text{OER}_{\text{killing}(mr)} < \text{OER}_{\text{DSB}}$. For the remainder of the results, a DSB yield of 30.1 /Gy/cell, r_0 of 0.7 μm and P_{nlrm} of 0.5 were used.

For the 1 Gy irradiation, the dose to the tumor was uniform to within 1% (Figure 9(a)) and the dose to nuclei ($n = 1224$) was approximately normally distributed with a mean and

TABLE III. Effects of varying the DSB yield.

DSB / cDSB yields[a] (/Gy/cell) under full oxia	OER_{DSB}	OER_{cDSB}	α_{mr} (Gy^{-1})/β_{mr} (Gy^{-2}) under full oxia (anoxia)[bc]	$\alpha_{killing(mr)}$ (Gy^{-1})/ $\beta_{killing(mr)}$ (Gy^{-2}) under full oxia (anoxia)[de]	$SF_{2(mr)}$ under full oxia (anoxia)[fe]	$OER_{killing(mr)}$[ge]
20.1 / 1.9	4.6	3.9	0^{h}/0.19 (0^{h}/0.01)	0^{i}/0.09 (0^{i}/0.01)	0.70 (0.97)	3.6
30.1 / 2.9	4.6	3.9	0.02/0.37 (0^{h}/0.03)	0.02/0.17 (0^{i}/0.02)	0.49 (0.94)	3.4
40.2 / 3.9	4.6	4.0	0.07/0.56 (0.00/0.04)	0.04/0.25 (0.00/0.02)	0.34 (0.92)	3.6

[a] Using the slopes of the fits $N_{DSB} = m_{DSB}D$ and $N_{cDSB} = m_{cDSB}D$.

[b] Fit to $N_{mr} = \alpha_{mr}D + \beta_{mr}D^2$.

[c] Using $r_0 = 0.7$ μm.

[d] Fit to $P_{surv(mr)} = e^{-\alpha_{killing(mr)}D - \beta_{killing(mr)}D^2}$.

[e] Using $r_0 = 0.7$ μm and $P_{nlmr} = 0.5$.

[f] Using the fit to $P_{surv(mr)}$ and extrapolating to 2 Gy.

[g] Using $OER_{killing(mr)} = D_{10}(pO_2 \text{ of } 0 \text{ mmHg})/D_{10}(pO_2 \text{ of } 760 \text{ mmHg})$, where D_{10} was obtained by extrapolating the fit to $P_{surv(mr)}$.

[h] The fit gave $-0.01 \lesssim \alpha_{mr} < 0$, so the fit was reperformed to $N_{mr} = \beta_{mr}D^2$.

[i] The fit gave $-0.01 < \alpha_{killing(mr)} < 0$, so the fit was reperformed to $P_{surv(mr)} = e^{-\beta_{killing(mr)}D^2}$.

TABLE IV. Effects of varying the characteristic interaction distance, r_0 (from Equation 8). A DSB yield of 30.1 /Gy/cell (cDSB yield of 2.9 /Gy/cell) under full oxia was used.

r_0 (μm)	α_{mr} (Gy^{-1})/β_{mr} (Gy^{-2}) under full oxia (anoxia)[a]	$\alpha_{\mathrm{killing}(mr)}$ (Gy^{-1})/ $\beta_{\mathrm{killing}(mr)}$ (Gy^{-2}) under full oxia (anoxia)[bc]	$\mathrm{SF}_{2(mr)}$ under full oxia (anoxia)[dc]	$\mathrm{OER}_{\mathrm{killing}(mr)}$[ec]
0.5	0.01/0.17 (0[f]/0.01)	0.01/0.08 (0[g]/0.01)	0.71 (0.97)	3.5
0.7	0.02/0.37 (0[f]/0.03)	0.02/0.17 (0[g]/0.02)	0.49 (0.94)	3.4
0.9	0.04/0.54 (0[f]/0.04)	0.03/0.24 (0[g]/0.02)	0.36 (0.92)	3.4

[a] Fit to $N_{mr} = \alpha_{mr} D + \beta_{mr} D^2$.

[b] Fit to $P_{surv(mr)} = e^{-\alpha_{\mathrm{killing}(mr)} D - \beta_{\mathrm{killing}(mr)} D^2}$.

[c] Using $P_{nlmr} = 0.5$.

[d] Using the fit to $P_{surv(mr)}$ and extrapolating to 2 Gy.

[e] Using $\mathrm{OER}_{\mathrm{killing}(mr)} = D_{10}(\mathrm{pO_2}$ of 0 mmHg)/$D_{10}(\mathrm{pO_2}$ of 760 mmHg), where D_{10} was obtained by extrapolating the fit to $P_{surv(mr)}$.

[f] The fit gave $-0.01 \lesssim \alpha_{mr} < 0$, so the fit was reperformed to $N_{mr} = \beta_{mr} D^2$.

[g] The fit gave $-0.01 < \alpha_{\mathrm{killing}(mr)} < 0$, so the fit was reperformed to $P_{surv(mr)} = e^{-\beta_{\mathrm{killing}(mr)} D^2}$.

standard deviation of 1.00±0.06 Gy (Figure 9(b)).

Frequency distributions of the number of DSBs in nuclei, the number of cDSBs in nuclei, the number of misrejoinings in nuclei and the cell survival probability from misrejoining, under full oxia and anoxia, are shown in Figure 10 for the 1 Gy dose.

Figure 11 provides information about the complexity of the DSBs induced under full oxia and anoxia. While there were fewer DSBs under anoxia, the DSBs were on average more complex in terms of the number of elementary damages (strand breaks, modified bases and modified sugars). Given how cDSBs were defined (DSBs with > 15 elementary damages), this is consistent with $\mathrm{OER_{cDSB}} < \mathrm{OER_{DSB}}$. Almost all DSBs had unit multiplicity (98.3% of DSBs under full oxia and 99.6% of DSBs under anoxia).

TABLE V. Effects of varying the probability that a misrejoining was non-lethal, P_{nlmr} (from Equation 10). A DSB yield of 30.1 /Gy/cell (cDSB yield of 2.9 /Gy/cell) under full oxia and r_0 of 0.7 μm were used.

P_{nlmr}	$\alpha_{\text{killing}(mr)}$ (Gy^{-1})/ $\beta_{\text{killing}(mr)}$ (Gy^{-2}) under full oxia (anoxia)[a]	$\text{SF}_{2(mr)}$ under full oxia (anoxia)[b]	$\text{OER}_{\text{killing}(mr)}$[c]
0.25	0.03/0.25 (0^{d}/0.02)	0.35 (0.91)	3.3
0.5	0.02/0.17 (0^{d}/0.02)	0.49 (0.94)	3.4
0.75	0.01/0.09 (0^{d}/0.01)	0.69 (0.97)	3.4

[a] Fit to $P_{surv(mr)} = e^{-\alpha_{\text{killing}(mr)}D-\beta_{\text{killing}(mr)}D^2}$.

[b] Using the fit to $P_{surv(mr)}$ and extrapolating to 2 Gy.

[c] Using $\text{OER}_{\text{killing}(mr)} = D_{10}(\text{pO}_2 \text{ of 0 mmHg})/D_{10}(\text{pO}_2 \text{ of 760 mmHg})$, where D_{10} was obtained by extrapolating the fit to $P_{surv(mr)}$.

[d] The fit gave $-0.01 < \alpha_{\text{killing}(mr)} < 0$, so the fit was reperformed to $P_{surv(mr)} = e^{-\beta_{\text{killing}(mr)}D^2}$.

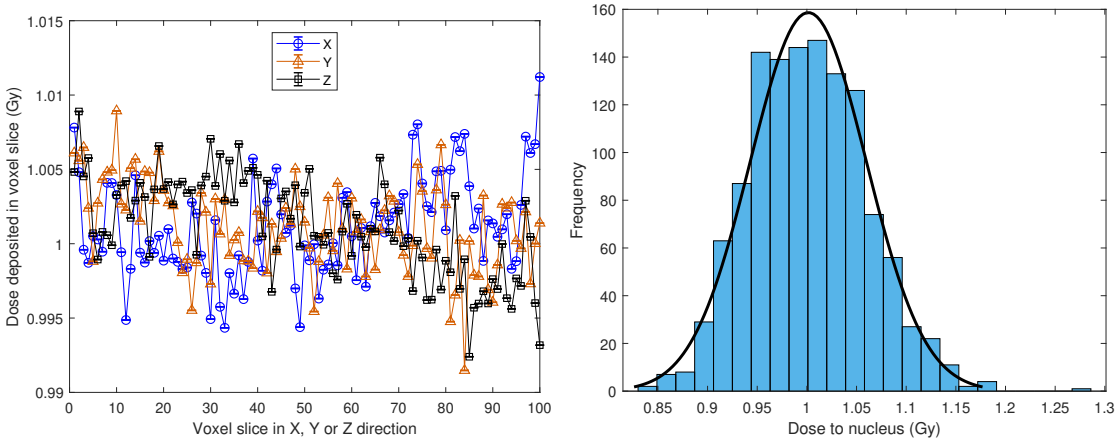

(a) (b)

FIG. 9. (a) Spatial dose profiles for the 1 Gy irradiation, using voxel slices in the X, Y and Z directions. The mean dose for $n = 10^4$ voxels in a voxel slice was plotted with vertical error bars equal to the SEM (which were smaller than the markers). (b) Frequency distribution of dose to nuclei ($n = 1224$) for the 1 Gy irradiation, with a normal distribution fit overlaid.

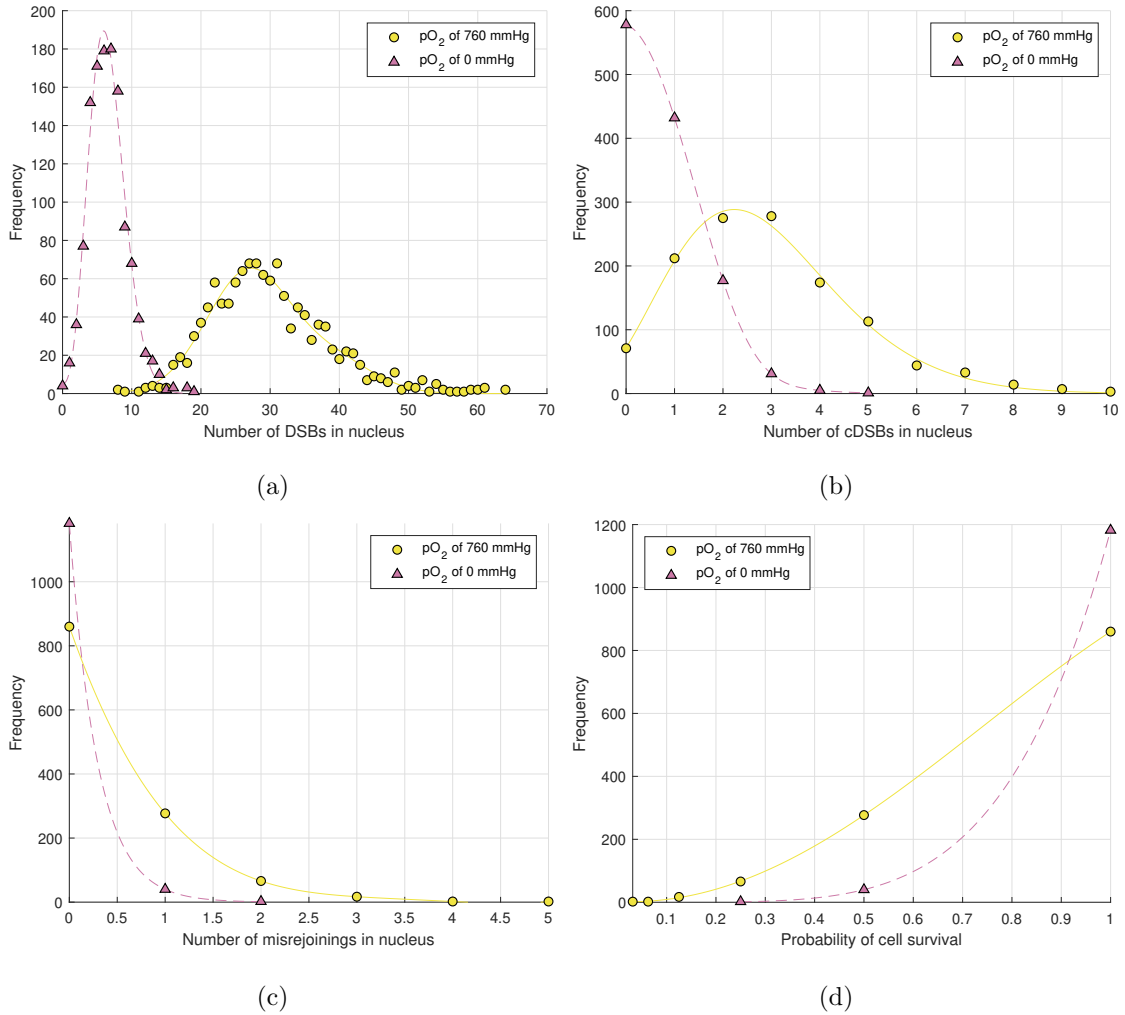

FIG. 10. Frequency distributions in $n = 1224$ cells for 1 Gy dose, under full oxia and anoxia: (a) Number of DSBs in nuclei. (b) Number of cDSBs in the nuclei. (c) Number of misrejoinings in the nuclei. (d) Cell survival probability from misrejoining.

B. Isolation of the indirect effect

If the indirect effect was not taken into account in the induction of DNA damage, the DSB yield was reduced to approximately a third of its original value and the cDSB yield to a tenth of its original value (Table VI).

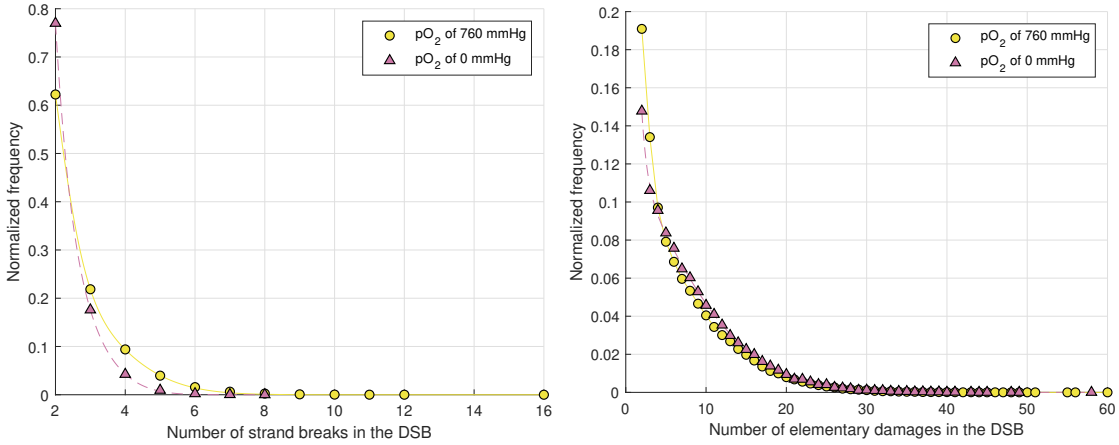

(a) (b)

FIG. 11. Frequency distributions for 1 Gy dose, under full oxia and anoxia: (a) Number of strand breaks in DSBs. (b) Number of elementary damages (strand breaks, modified bases and modified sugars) in DSBs. The total number of DSBs in 1224 cells was $n = 187518$ under full oxia and $n = 40886$ under anoxia. The frequency distributions were normalized for ease of comparison between full oxia and anoxia.

TABLE VI. The impact of neglecting the indirect effect.

	DSB / cDSB yields (/Gy/cell) under full oxia	OER_{DSB}	OER_{cDSB}
D^a+I^b	30.1 / 2.9	4.6	3.9
D^a only	12.3 / 0.3	2.6	2.2

[a] Direct-type effects
[b] Indirect effect

C. HNSCC tumor of volume 1 mm^3

A 1 mm^3 tumor was generated (Figure 12(a)) with a cellular pO_2 distribution (Figure 12(b)) characteristic of HNSCC [66]: the mean cellular pO_2 was 9.4 mmHg, the median cellular pO_2 was 8.2 mmHg, the HP_{10} (proportion of viable cells with $pO_2 < 10$ mmHg) was 58%, the HP_5 was 34%, the $HP_{2.5}$ was 20%, the HP_1 was 11% and the necrotic volume was 9.4%.

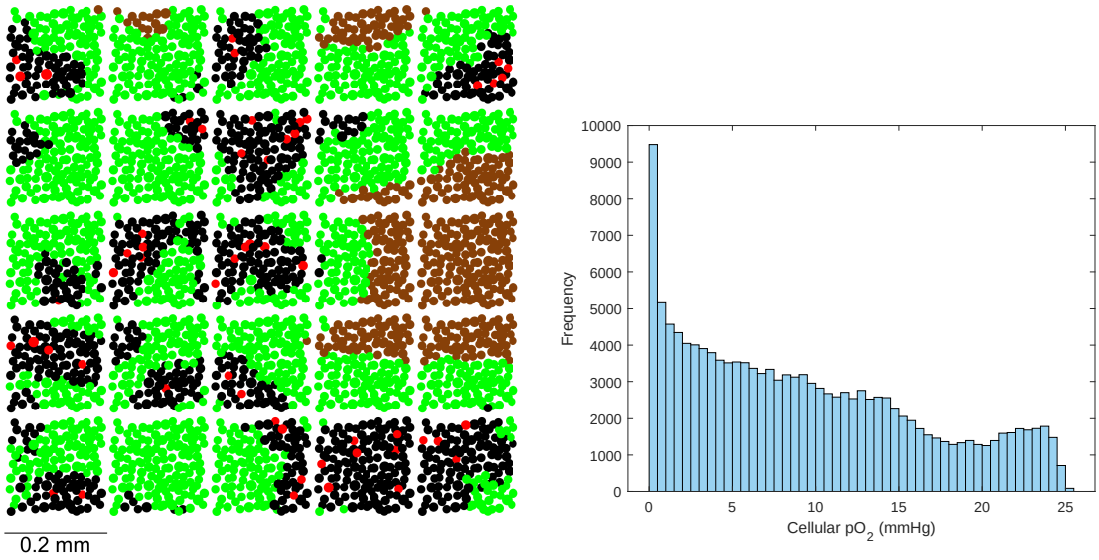

(a) (b)

FIG. 12. (a) Section (thickness 20 μm) of the 1 mm^3 tumor of HNSCC, showing blood vessel units (red), normoxic cells ($pO_2 > 10$ mmHg) (black) located near the blood vessels, hypoxic cells ($pO_2 \leq 10$ mmHg) (green) located further from the blood vessels and necrotic cells (brown) located further than $ND = 130$ μm from a blood vessel. It can be seen how the 1 mm^3 tumor was constructed by replicating the (0.2 mm)^3 tumor. (b) Frequency distribution of pO_2 for viable (non-necrotic) cells ($n = 135306$) in the 1 mm^3 tumor of HNSCC.

Figure 13 shows, for 1 Gy dose, bivariate frequency distributions of the cellular pO_2 and the number of DSBs in the nucleus, the cellular pO_2 and the number of cDSBs in the nucleus, the cellular pO_2 and the number of misrejoinings in the nucleus and the cellular pO_2 and the cell survival probability from misrejoining.

IV. DISCUSSION

DNA free-end misrejoining and its contribution to cell killing for MV x-rays was investigated. The linear components of misrejoining (α_{mr}) and cell killing from misrejoining ($\alpha_{\text{killing}(mr)}$) were consistently small in the sensitivity analysis. For example, for a DSB yield of 30.1 /Gy/cell, r_0 of 0.7 μm and P_{nlmr} of 0.5, $\alpha_{\text{killing}(mr)}$ was 0.02 Gy^{-1} under full oxia (and zero under anoxia). For comparison, a typical α_{killing} for HNSCC is 0.3 Gy^{-1} [68–73]. This indicated that i) misrejoinings involving DSBs from the same primary were a very rare

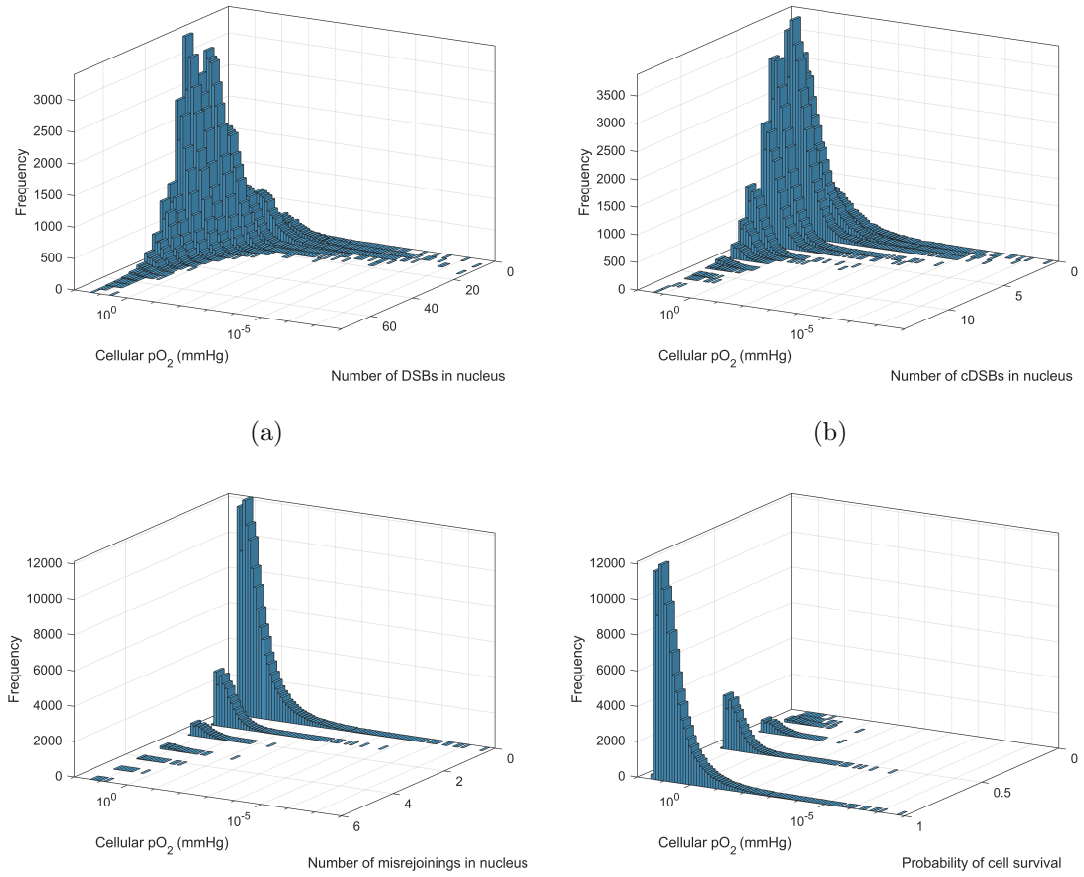

FIG. 13. Bivariate frequency distributions in $n = 135306$ viable cells of the 1 mm^3 HNSCC tumor for 1 Gy dose. (a) Cellular pO_2 and the number of DSBs in the nucleus. (b) Cellular pO_2 and the number of cDSBs in the nucleus. (c) Cellular pO_2 and the number of misrejoinings in the nucleus. (d) Cellular pO_2 and the cell survival probability from misrejoining.

occurrence, which is in agreement with deterministic modeling by Carlson et al [25], and ii) other mechanisms may be chiefly responsible for the linear components of CA production and cell killing by low-LET radiation for HNSCC. Unrejoined DNA free-ends (terminal deletions and incomplete exchanges) are likely candidates. It has been estimated that approximately 5% of DSBs end up as either terminal deletions or incomplete exchanges for low-LET radiation [8].

On the other hand, the quadratic components of misrejoining (β_{mr}) and cell killing from misrejoining ($\beta_{\text{killing}(mr)}$) were consistently large in the sensitivity analysis. For the aforementioned {DSB yield, r_0, P_{nlmr}}, $\beta_{\text{killing}(mr)}$ was 0.17 Gy^{-2} under full oxia (0.02 Gy^{-2} under

anoxia), whereas a typical value of β_{killing} for HNSCC is 0.03 Gy^{-2} [68–74]. This indicates that too much misrejoining was simulated (which makes the small linear component of cell killing by misrejoining look even smaller). This is to be expected given that the $\text{SF}_{2(mr)}$ under full oxia was already 49% without simulating terminal deletions and incomplete exchanges as sources of cell killing.

The amount of misrejoining could be reduced by decreasing the model parameter r_0 below 0.5 μm. However, this may not be optimal, since the BIANCA model obtained good results for the CA yields in a monolayer-shaped fibroblast using an r_0 of 0.7 μm and in a lymphocyte using an r_0 of 0.8 μm [32]. Alternatively, misrejoining could be reduced by increasing the size of the nuclei. This may be wise given that large DNA volumes from 13.3 to 26.7% were required to obtain DSB yields from 20 to 40 /Gy/cell (for reference, estimates of the DNA volume in yeast cells vary from 0.3 to 2% [59]). Increasing the nucleus volume would require a proportional decrease in the DNA volume to obtain the same DSB yield. The average nucleus volume in the current work was 142 μm^3 for squamous cells. For comparison, the fibroblast in the BIANCA model had a nucleus volume of 628 μm^3. Note that the fibroblast was modeled as monolayer-shaped and this reduced the amount of misrejoining compared to a more spherical shape.

It is also possible that some misrejoinings were counted that should not have been. If a group of $N \geq 3$ breaks involved N explicitly simulated misrejoinings (the maximum number), a value of $N_{mr} = N$ was mistakenly used in Equation 9 (or Equation 10) for the cell survival probability; the true probability in this case is obtained by using a value of $N_{mr} = N - 1$ (Appendix). However, for the largest dose simulated (1 Gy), only 1.7% of cells (22/1224 cells) under full oxia (and no cells under axoia) contained 3 or more misrejoinings (Figure 10(c)). Therefore, these erroneous cases could not have contributed appreciably to the current results. This oversight will be rectified in future iterations of the model, as it will be important for simulating hypofraction doses and high-LET proton and carbon beams, which are planned for future work.

A limitation of the model was the assumption of no incomplete exchanges. The model also did not simulate terminal deletions. There would be greater cell killing if these mechanisms were accounted for. Another limitation was that a negative exponential function was used to model the probability of misrejoining (Equation 8). This was an approximation of complex DSB repair processes (e.g. c-NHEJ), which involve a cascade of a large number of DNA

repair proteins [13]. Additionally, there can be DNA damage from non-targeted effects [23], which was not considered. The model also neglected cell death by apoptosis, when apoptosis is not a consequence of lethal CA-driven mitotic catastrophe [1, 21–23].

This work presented a new stochastic model of radiation-induced CA production and cell death that addressed a gap in the literature. Rather than focussing on simulating a complex DNA target model (e.g. Friedland and Kundrát's model [28, 29], the BIANCA model [30–32]), or the motion of DNA free-ends (Friedland and Kundrát, the model by Henthorn et al [27], Brenner's model [33]), or mechanistic modeling of NHEJ (Henthorn et al, Friedland and Kundrát), the current model uniquely simulated Monte Carlo tracks through a whole multicellular tumor volume, and converted the physical and chemical tracks in nuclei into DNA damage in a pO_2-dependent fashion. These novel properties make the model suitable for future amalgamation into a spatio-temporal multicellular radiotherapy model [47, 66], that simulates the radiation effect starting from whole-tumor Monte Carlo tracks and accurately simulates the effects of tumor hypoxia.

V. CONCLUSION

The current work achieved the stochastic simulation of i) x-ray irradiation of a multicellular tumor, ii) pO_2-dependent DNA damage induction from the tracks, iii) proximity-based DNA free-end misrejoining and iv) cell death from misrejoining. The model was used to investigate the contribution of misrejoining to cell killing in isolation for MV x-rays. A sensitivity analysis was conducted for the model parameters DSB yield, characteristic interaction distance and probability that a misrejoining was non-lethal. As an application, DNA damage and misrejoining were simulated in 135306 viable cells in a 1 mm^3 HNSCC tumor for a uniform dose of 1 Gy. The near absence of linear components of misrejoining and cell killing from misrejoining suggests that terminal deletions and incomplete exchanges may be important mechanisms for the linear components of CA production and cell killing by low-LET radiation for HNSCC, under the assumptions of the current model.

ACKNOWLEDGMENTS

This work was supported with supercomputing resources provided by the Phoenix HPC service at the University of Adelaide.

Appendix: Prediction of cell death from DNA free-end misrejoining

This appendix provides the justification for Equation 9:

$$P_{surv(mr)} = 0.5^{N_{mr}}$$

The assumptions that were made in this model are:

1. No terminal deletions: cDSBs with both ends unrejoined were rejoined faithfully/correctly.

2. No incomplete exchanges: For cDSBs with only one end misrejoined, assume the other end misrejoined with the same cDSB as the first, or if that cDSB has no free ends, with the other available end in the misrejoining "chain" (e.g. if $cDSB_1$ and $cDSB_2$ each have an end misrejoined with an end from $cDSB_3$, then the remaining end of $cDSB_1$ was assumed to misrejoin with the remaining end of $cDSB_2$).

3. If two cDSBs misrejoined both of their ends together during the original misrejoining simulation, the second misrejoining was not counted, as this was assumed (from the previous assumption).

Let the number of breaks (DSBs, or cDSBs in the current work) in the nucleus be $N \in [2, \infty)$. The number of misrejoinings involving these breaks is $N_{mr} \in [0, N]$. It will be demonstrated that this equation for $P_{surv(mr)}$ is true (given the assumptions above) for $N = 2$ and all $N_{mr} \in \{0, 1, 2\}$ and for $N \geq 3$ provided $N_{mr} \neq N$. For $N \geq 3$ and $N_{mr} = N$, one of the misrejoinings was counted that should not have been, i.e., $P_{surv(mr)}$ would have been correct if a value of $N_{mr} \rightarrow N_{mr} - 1$ had been used in the formula instead. Thus, the cell killing was overestimated in these cases (though they did not contribute appreciably in the current work - see Discussion). Lastly, it will be shown that the equation for $P_{surv(mr)}$ extends to a nucleus containing multiple independent groups of breaks with misrejoinings.

1. $N = 2$

a. 2 breaks on 2 chromosomes (1 break on each chromosome)

If there were no misrejoinings ($N_{mr} = 0$), both breaks were rejoined faithfully (assumption 1) and $P_{surv(mr)} = 1$, which the formula gives for $N_{mr} = 0$.

If there was 1 misrejoining ($N_{mr} = 1$), the options are:

- 1 dicentric (with no sticky ends) and 2 acentric fragments (each with 1 sticky end) (1 way)
- 1 acentric fragment (with no sticky ends) and 2 centric fragments (each with 1 sticky end) (1 way)
- 1 symmetric translocation (with no sticky ends), 1 centric fragment (with 1 sticky end) and 1 acentric fragment (with 1 sticky end) (2 ways)

A second misrejoining was then assumed (assumption 2), giving either:

- 1 dicentric (no sticky ends) and 1 acentric fragment (no sticky ends) (2 ways) → lethal
- 2 symmetric translocations (no sticky ends) (2 ways) → viable

Thus there were 2 equally likely outcomes (2 ways each): 1 lethal and 1 viable. Therefore $P_{surv(mr)} = 0.5$, which the formula gives for $N_{mr} = 1$.

If there were 2 misrejoinings simulated explicitly, the situation was described above and $P_{surv(mr)} = 0.5$. However, because the 2 simulated misrejoings were between the same 2 breaks, only the first misrejoining was counted toward N_{mr} (assumption 3), i.e., $N_{mr} = 1$ was used in the formula and thus the correct answer of $P_{surv(mr)} = 0.5$ was obtained.

b. 1 break on each arm of a chromosome

If $N_{mr} = 0$, same as in the previous example.

If there was one misrejoining ($N_{mr} = 1$), the options are:

- 1 centric ring and 2 acentric fragments (each with 1 sticky end) (1 way)
- 1 acentric fragment (no sticky ends) and 1 centric fragment (2 sticky ends) (1 way)

- half of a pericentric inversion, giving 1 centric fragment (1 sticky end) and 1 acentric fragment (1 sticky end) (2 ways)

A second misrejoining was then assumed (assumption 2), giving either:

- 1 centric ring and 1 acentric fragment (no sticky ends) (2 ways) → lethal
- pericentric inversion (2 ways) → viable

Lethal and viable outcomes were equally likely (2 ways each), so $P_{surv(mr)} = 0.5$, which the formula gives for $N_{mr} = 1$.

As in the previous example, if the 2 misrejoinings were simulated explicitly, the second misrejoining was not counted toward N_{mr} (assumption 3), so $N_{mr} = 1$ and the formula correctly gives $P_{surv(mr)} = 0.5$.

c. 2 breaks on the same arm of a chromosome

If $N_{mr} = 0$, same as above.

If there was one misrejoining ($N_{mr} = 1$), the options are:

- interstitial deletion, giving 1 acentric fragment (2 sticky ends) and 1 centric fragment (no sticky ends) (1 way)
- 1 acentric ring, 1 centric fragment (1 sticky end) and 1 acentric fragment (1 sticky end) (1 way)
- half of a paracentric inversion, giving 1 centric fragment (1 sticky end) and 1 acentric fragment (1 sticky end) (2 ways)

A second misrejoining was then assumed (assumption 3), giving either:

- interstitial deletion, with 1 acentric ring and 1 centric fragment (no sticky ends) (2 ways) → lethal
- paracentric inversion (2 ways) → viable

Lethal and viable outcomes were equally likely (2 ways each), so $P_{surv(mr)} = 0.5$, which the formula gives for $N_{mr} = 1$.

As above, if the 2 misrejoinings were simulated explicitly, the second misrejoining was not counted toward N_{mr} (assumption 3), so $N_{mr} = 1$ and the formula correctly gives $P_{surv(mr)} = 0.5$.

2. $N \geq 3$

a. 3 breaks on 3 chromosomes (1 break on each chromosome)

If there were no misrejoinings ($N_{mr} = 0$), all 3 breaks were rejoined faithfully (assumption 1) and $P_{surv(mr)} = 1$, which the formula gives for $N_{mr} = 0$.

If there was 1 misrejoining ($N_{mr} = 1$), the options are:

- 1 dicentric (no sticky ends), 1 centric fragment (1 sticky end) and 3 acentric framgents (each with 1 sticky end) (3 ways)
- 1 acentric fragment (no sticky ends), 3 centric fragments (each with 1 sticky end) and 1 acentric fragment (1 sticky end) (3 ways)
- 1 symmetric translocation (no sticky ends), 2 centric fragments (each with 1 sticky end) and 2 acentric framgents (each with 1 sticky end) (6 ways)

A second misrejoining was then assumed between the same two breaks as the first (assumption 2), giving options:

- 1 dicentric (no sticky ends), 1 acentric fragmemt (no sticky ends), 1 centric fragment (1 sticky end) and 1 acentric fragment (1 sticky end) (6 ways)
- 2 symmetric translocations (no sticky ends), 1 acentric fragment (1 sticky end) and 1 centric fragment (1 sticky end) (6 ways)

The break that was not involved in any misrejoinings was rejoined faithfully (assumption 1), giving options:

- 1 dicentric (no sticky ends), 1 acentric fragmemt (no sticky ends) and 1 repair (6 ways) $\rightarrow$ lethal
- 2 symmetric translocations (no sticky ends) and 1 repair (6 ways) $\rightarrow$ viable

Half of the outcomes are lethal and half are viable, giving $P_{surv(mr)} = 0.5$, which the formula gives for $N_{mr} = 1$.

Now consider if 2 misrejoinings were simulated explicitly. If the second misrejoining was between the same pair of breaks as the first, then the situation was described above, with $P_{surv(mr)} = 0.5$. However, because the second misrejoining was between the same pair of breaks as the first, the second misrejoining was not counted toward N_{mr} (assumption 3), so $N_{mr} = 1$ and the formula correctly gives $P_{surv(mr)} = 0.5$.

If the second misrejoining was not between the same pair of breaks as the first ($N_{mr} = 2$), then the options are (after the third misrejoining; by assumption 2):

- 1 dicentric (no sticky ends), 1 symmetric translocation (no sticky ends) and 1 acentric fragment (no sticky ends) (36 ways) → lethal
- 3 symmetric translocations (no sticky ends) (12 ways) → viable

There are 36 ways for a lethal outcome and 12 ways for a viable outcome, giving $P_{surv(mr)} = 0.25$, which the formula correctly gives for $N_{mr} = 2$.

If the 3 misrejoinings were simulated explicitly, the situation is as described above, with $P_{surv(mr)} = 0.25$. In the current algorithm, the third misrejoining was mistakenly counted ($N_{mr} = 3$), so the formula incorrectly gave $P_{surv(mr)} = 0.125$. This will be fixed in future iterations of the algorithm.

3. Independent groups of breaks in a nucleus

Consider a nucleus containing one group of breaks with $N_{mr,1}$ and corresponding $P_{surv(mr),1}$ and a second group of breaks with $N_{mr,2}$ and corresponding $P_{surv(mr),2}$:

$$P_{surv(mr),1} = 0.5^{N_{mr,1}} \tag{A.1}$$

$$P_{surv(mr),2} = 0.5^{N_{mr,2}} \tag{A.2}$$

For the cell to be viable, both groups of breaks must have a viable outcome:

$$P_{surv(mr)} = P_{surv(mr),1} P_{surv(mr),2} \tag{A.3}$$

$$= 0.5^{N_{mr,1}} 0.5^{N_{mr,2}} \tag{A.4}$$

$$= 0.5^{N_{mr,1}+N_{mr,2}} \tag{A.5}$$

So $P_{surv(mr)}$ is given by the same formula but using the total number of misrejoinings in the nucleus.

---

[1] B. G. Wouters, in *Basic clinical radiobiology*, edited by M. C. Joiner and A. van der Kogel (CRC Press, Boca Raton, 2009) 4th ed., Chap. 3, pp. 27–40.

[2] E. J. Hall and A. J. Giaccia, *Radiobiology for the radiologist*, 7th ed. (Lippincott Williams & Wilkins, Philadelphia, 2012) pp. 41–42.

[3] M. N. Cornforth and J. S. Bedford, Radiat. Res. **111**, 385 (1987).

[4] M. N. Cornforth, DNA Repair (Amst) **5**, 1182 (2006).

[5] M. S. Sasaki, Int. J. Radiat. Biol. **85**, 26 (2009).

[6] M. Durante, J. S. Bedford, D. J. Chen, S. Conrad, M. N. Cornforth, A. T. Natarajan, D. C. van Gent, and G. Obe, Mutat. Res. **756**, 5 (2013).

[7] E. J. Hall and A. J. Giaccia, *Radiobiology for the radiologist*, 7th ed. (Lippincott Williams & Wilkins, Philadelphia, 2012) pp. 25–34.

[8] B. D. Loucas and M. N. Cornforth, Radiat. Res. **179**, 393– (2013).

[9] R. K. Sachs, A. M. Chen, and D. J. Brenner, Int. J. Radiat. Biol. **71**, 1 (1997).

[10] M. Löbrich and P. Jeggo, Trends. Biochem. Sci. **42**, 690 (2017).

[11] A. S. A and G. Iliakis, Nucleic Acids Res. **41**, 7589 (2013).

[12] T. Le Guen, S. Ragu, J. Guirouilh-Barbat, and B. S. Lopez, Mol. Cell. Oncol. **2**, e968020 (2015).

[13] R. Biehs, M. Steinlage, O. Barton, S. Juhász, J. KÜnzel, J. Spies, A. Shibata, P. A. Jeggo, and M. Löbrich, Mol. Cell. **65**, 671 (2017).

[14] B. Jakob, J. Splinter, M. Durante, and G. Taucher-Scholz, Proc. Natl. Acad. Sci. U. S. A. **106**, 3172 (2009).

[15] P. Reynolds, J. A. Anderson, J. V. Harper, M. A. Hill, S. W. Botchway, A. W. Parker, and P. O'Neill, Nucleic Acids Res. **40**, 10821 (2012).

[16] Y. Li, P. Reynolds, P. O'Neill, and F. A. Cucinotta, PLoS One **9**, e85816 (2014).

[17] Y. Liang, Q. Fu, X. Wang, F. Liu, G. Yang, C. Luo, Q. Ouyang, and Y. Wang, Phys. Med. Biol. **62**, 2153 (2017).

[18] I. Shuryak, B. D. Loucas, and M. N. Cornforth, Front. Oncol. **7**, 318 (2017).

[19] D. J. Brenner, Semin. Radiat. Oncol. **18**, 234– (2008).

[20] D. Hanahan and R. A. Weinberg, Cell **144**, 646 (2011).

[21] W. P. Roos and B. Kaina, Trends Mol. Med. **12**, 440 (2006).

[22] M. Kodiha, Y. M. Wang, E. Hutter, D. Maysinger, and U. Stochaj, Theranostics **5**, 357 (2015).

[23] R. Wang, T. Zhou, W. Liu, and L. Zuo, Oncotarget **9**, 18637 (2018).

[24] J. Besserer and U. Schneider, Z. Med. Phys. **25**, 168 (2015).

[25] D. J. Carlson, R. D. Stewart, V. A. Semenenko, and G. A. Sandison, Radiat. Res. **169**, 447 (2008).

[26] R. D. Stewart, Radiat. Res. **156**, 365 (2001).

[27] N. T. Henthorn, J. W. Warmenhoven, M. Sotiropoulos, R. I. Mackay, N. F. Kirkby, K. J. Kirkby, and M. J. Merchant, Sci. Rep. **8**, 2654 (2018).

[28] W. Friedland and P. Kundrát, Radiat. Prot. Dosimetry **166**, 71 (2015).

[29] W. Friedland and P. Kundrát, Mutat. Res. **756**, 213 (2013).

[30] J. J. Tello Cajiao, M. P. Carante, M. A. Bernal Rodriguez, and F. Ballarini, DNA Repair (Amst) **64**, 45 (2018).

[31] M. P. Carante, C. Aimè, J. J. T. Cajiao, and F. Ballarini, Phys. Med. Biol. **63**, 075007 (2018).

[32] J. J. Tello Cajiao, M. P. Carante, M. A. Bernal Rodriguez, and F. Ballarini, DNA Repair (Amst) **58**, 38 (2017).

[33] D. J. Brenner, Radiat. Res. **124**, S29 (1990).

[34] J. Allison, K. Amako, J. Apostolakis, P. Arce, M. Asai, T. Aso, E. Bagli, and et al., Nucl. Instrum. Methods Phys. Res. A. **835**, 186 (2016).

[35] J. Allison, K. Amako, J. Apostolakis, H. Araujo, P. A. Dubois, and e. a. M. Asai M, IEEE Trans. Nucl. Sci. **53**, 270 (2006).

[36] S. Agostinelli, J. Allison, K. Amako, J. Apostolakis, H. Araujo, and e. a. P. Arce, Nucl. Instrum. Methods Phys. Res. A **506**, 250 (2003).

[37] M. A. Bernal, M. C. Bordage, J. M. Brown, M. Davídková, E. Delage, Z. El Bitar, S. A. Enger, and et al., Phys. Med. **31**, 861 (2015).

[38] S. Incerti, A. Ivanchenko, M. Karamitros, A. Mantero, P. Moretto, H. N. Tran, B. Mascialino, and et al., Med. Phys. **37**, 4692 (2010).

[39] S. Incerti, G. Baldacchino, M. Bernal, R. Capra, C. Champion, and e. a. Z. Francis, Int. J. Model. Simul. Sci. Comput. **1**, 157 (2010).

[40] E. Lindblom, I. Toma-Dasu, and A. Dasu, Adv. Exp. Med. Biol. **1072**, 183 (2018).

[41] W. M. Harriss-Phillips, E. Bezak, and E. K. Yeoh, Br. J. Radiol. **86**, 20120443 (2013).

[42] C. Harting, P. Peschke, K. Borkenstein, and C. P. Karger, Phys. Med. Biol. **52**, 4775 (2007).

[43] V. P. Antipas, G. S. Stamatakos, N. K. Uzunoglu, D. D. Dionysiou, and R. G. Dale, Phys. Med. Biol. **49**, 1485 (2004).

[44] K. Borkenstein, S. Levegrün, and P. Peschke, Radiat. Res. **162**, 71 (2004).

[45] M. Kocher, H. Treuer, J. Voges, M. Hoevels, V. Sturm, and R. P. Müller, Radiother. Oncol. **54**, 149 (2000).

[46] U. Del Monte, Cell Cycle **8**, 505 (2009).

[47] J. C. Forster, M. J. Douglass, W. M. Harriss-Phillips, and E. Bezak, Med. Phys. **44**, 1563 (2017).

[48] M. J. J. Douglass, *Development of an Integrated Stochastic Radiobiological Model for Electromagnetic Particle Interactions in a 4D Cellular Geometry*, PhD dissertation, University of Adelaide, School of Chemistry and Physics (2014).

[49] R. M. Vlad, N. M. Alajez, A. Giles, M. C. Kolios, and G. J. Czarnota, Int. J. Radiat. Oncol. Biol. Phys. **72**, 1236 (2008).

[50] M. D. Huber and L. Gerace, J. Cell. Biol. **179**, 583 (2007).

[51] M. J. Berger, J. S. Coursey, M. A. Zucker, and J. Chang, "ESTAR, PSTAR, and ASTAR: Computer programs for calculating stopping-power and range tables for electrons, protons, and helium ions (version 1.2.3)," `http://physics.nist.gov/Star` (2005), accessed: 17-09-2018.

[52] J. D. Chapman, A. P. Reuvers, J. Borsa, and C. L. Greenstock, Radiat. Res. **56**, 291 (1973).

[53] T. Shiina, R. Watanabe, I. Shiraishi, M. Suzuki, Y. Sugaya, K. Fujii, and et al., Radiat. Environ. Biophys. **52**, 99 (2013).

[54] Q. Guo, Q. Yue, J. Zhao, L. Wang, H. Wang, X. Wei, and et al., Chem. Commun. (Camb) **47**, 11906 (2011).

[55] B. C. Chu and L. E. Orgel, Proc. Natl. Acad. Sci. U. S. A. **82**, 963 (1985).

[56] G. B. Dreyer and P. B. Dervan, Proc. Natl. Acad. Sci. U. S. A. **82**, 968 (1985).

[57] R. Roots and S. Okada, Radiat. Res. **64**, 306 (1975).

[58] J. C. Forster, M. J. J. Douglass, W. M. Harriss-Phillips, and E. Bezak, Radiat. Res. (2018), doi: 10.1667/RR15050.1. (Epub ahead of print).

[59] R. Milo and R. Phillips, *Cell biology by the numbers*, 1st ed. (Garland Science, New York, 2015) pp. 55–58.

[60] K. H. Karlsson, I. Radulescu, B. Rydberg, and B. Stenerlöw, Radiat. Res. **169**, 506 (2008).

[61] M. Pinto, K. M. Prise, and B. D. Michael, Int. J. Radiat. Biol. **78**, 375 (2002).

[62] K. M. Prise, G. Ahnström, M. Belli, J. Carlsson, D. Frankenberg, J. Kiefer, M. Löbrich, B. D. Michael, J. Nygren, G. Simone, and B. Stenerlöw, Int. J. Radiat. Biol. **74**, 173 (1998).

[63] K. Rothkamm and M. Löbrich, Proc. Natl. Acad. Sci. U.S.A **100**, 5057 (2003).

[64] J. Saker, M. Kriegs, M. Zenker, J. M. Heldt, I. Eke, H. J. Pietzsch, R. Grénman, N. Cordes, C. Petersen, M. Baumann, J. Steinbach, E. Dikomey, and U. Kasten-Pisula, J. Nucl. Med. **54**, 416 (2013).

[65] R. A. El-Awady, E. Dikomey, and J. Dahm-Daphi, Br. J. Cancer **89**, 593 (2003).

[66] J. C. Forster, M. J. J. Douglass, W. M. Harriss-Phillips, and E. Bezak, Sci. Rep. **7**, 111037 (2017).

[67] J. C. Forster, W. M. Harriss-Phillips, M. J. Douglass, and E. Bezak, Hypoxia (Auckl) **5**, 21 (2017).

[68] X. S. Qi, Q. Yang, S. P. Lee, X. A. Li, and D. Wang, Cancers **4**, 566 (2012).

[69] M. B. Altman, M. A. Stinauer, D. Javier, B. D. Smith, L. C. Herman, M. L. Pytynia, B. Aydogan, C. A. Pelizzari, S. J. Chmura, and J. C. Roeske, Int. J. Radiat. Oncol. Biol. Phys. **75**, 1240 (2009).

[70] M. Stuschke and H. D. Thames, Int. J. Radiat. Oncol. Biol. Phys. **37**, 259 (1997).

[71] M. Stuschke, V. Budach, W. Budach, H. J. Feldmann, and H. Sack, Int. J. Radiat. Oncol. Biol. Phys. **24**, 119 (1992).

[72] A. Courdi, R. J. Bensadoun, J. Gioanni, and C. Caldani, Radiother. Oncol. **24**, 102 (1992).

[73] W. M. Harriss-Phillips, E. Bezak, and A. Potter, Int. J. Radiat. Oncol. Biol. Phys. **95**, 1290 (2016).

[74] M. C. Joiner, *Basic clinical radiobiology*, 4th ed., edited by M. C. Joiner and A. van der Kogel (CRC Press, Boca Raton, 2009).

7.2.4 Discussion and Conclusion

Cell death was predicted using the initial spatial distribution of complex DSBs (cDSBs) in the nucleus, which was obtained from the track structure. The distance between 2 cDSBs was used to predict the likelihood that a DNA free-end from one cDSB was misrejoined with a DNA free-end from the other cDSB. After running the misrejoining algorithm, assuming there were no unrejoined ends, the cell survival probability could be predicted: each misrejoining event had a 0.5 chance of producing an asymmetric chromosome aberration that would cause the cell to die via mitotic catastrophe.

Someone familiar with Michael Douglass' work may wonder why the multicellular tumour was imported into Geant4 in a voxelised representation, rather than using parameterised volumes, as Michael Douglass did. Since version 10 of Geant4, it is no longer possible to parameterise a volume plus its daughter volume (e.g. the cell membrane plus the cell nucleus). The voxelisation approach was devised as an alternative. The voxelisation approach happens to have some advantages over volume parameterisation. In particular, the voxel array was imported using a "Nested Parametersiation", which allows for fast particle navigation and reduces memory requirement.

In future work, a modeller could aim to grow out the multicellular tumour spatio-temporally, so that the cells have different types (stem, transit and differentiated), before delivering a dose fraction. Considerable computation time could be saved by only simulating DNA damage, DNA free-end misrejoining and cell death from misrejoining in stem cells. Then the surviving stem cells can regrow the tumour in the time before the next dose fraction is delivered. Thus fractionated radiotherapy can be simulated. Future work should also endeavour to account for incomplete exchanges and terminal deletions as sources of cell death, for the possibility that a non-zero linear component of cell killing is obtained for low-LET radiation.

8
Conclusion

Comprehensive application of radiobiology is underutilised in standard practice radiotherapy. There are well-established predictive biomarkers (e.g. hypoxia [33]) and many more that are promising (e.g. p53-status, HPV-status and a multitude of others [25, 27, 29, 37]), that are generally not taken into consideration during standard clinical radiotherapy planning [96]. These markers vary between patients and (by definition) indicate the response to a treatment. By taking them into account, patient outcomes could be improved (higher tumour control probabilities and reduced side-effects). The problem: it is not clear precisely how a given set of evaluated markers will interact to produce the overall effect (tumour response) for a particular fractionation schedule, type of cancer, radiation quality, combination of chemotherapy drugs, and so on. This is the large hurdle that must be overcome, i.e., patient-specific radiobiology must be predicted reliably before it can be used to further individualise radiotherapy treatment (and justify the expense of using biomarkers). Clinical trials are essential, but they are time-consuming and expensive and many of them will be required to consider the large number of variables involved. It is hoped that radiobiological modelling will help provide the answers and drive more individualised radiotherapy planning forward.

The complexity of radiobiology in radiotherapy, involving the interplay of physical, chemical and biological processes, demands increasingly complex radio-

biological models: from purely deterministic models to models that incorporate stochastic elements; from temporal models to spatio-temporal models. It may be possible to meet the demand with increases in computational power as a result of technological advancements.

This thesis set out to develop a new radiobiological model of HNSCC radiotherapy that would achieve a higher degree of complexity than previous models. In particular, the aim was to develop a model with the following unique combination of properties:

1. It would be a spatio-temporal model in which each tumour cell was modelled individually.
    - With the spatial component, each cell would have a physical volume of space that it occupied.
    - With the temporal component, each viable non-differentiated cell would progress through cell cycles and undergo cell division, thus growing the tumour spatio-temporally.
2. A tumour vasculature would grow (angiogenesis), from which cells would acquire their pO_2.
3. Finally, Monte Carlo particle tracks would be simulated through the cellular tumour to deliver the dose.

The developed model ultimately achieved all of this and more. Each component of the model was developed and verified as described in the thesis.

8.1 Summary of main findings

The literature review of tumour angiogenesis and the vasculature morphology in HNSCC in Chapter 2 [56] influenced the way the tumour vasculature and tumour hypoxia were modelled later in Chapter 4, which was a primary focus of the model. In particular, this review led to the formulation of model parameters: relative vascular volume (RVV), blood oxygenation (p_0) and necrosis distance (ND), for

which lower and upper limits were obtained for HNSCC (2-10%, 20-100 mmHg and 80-300 μm, respectively) using clinical notes and data from the literature. It was envisioned that these parameters, combined with a stochastically generated tumour vasculature, would give rise to the tumour oxygenation.

A key feature of the tumour growth model developed in Chapter 4 [91] was the "pathway"-based approach. Specifically, the randomised cell positions were grouped into i) "curvy" pathways to generate the connected, branching and chaotic tumour vasculature and ii) radial pathways to transport cells outward following a cell division and inward following a cell death. Other main features of the tumour growth model include:

- Cell positions within a distance ND of a vessel were viable; others were necrotic.
- Viable cells were assigned a cell type in the epithelial cell hierarchy (stem, transit and differentiated cells), a pO_2 based on their distance to the nearest blood vessel and a cell cycle time based on their pO_2.
- The probability for stem cells to undergo symmetric division was a parameter that could be increased to simulate accelerated repopulation.

Chapter 5 [92] rigorously explored and documented the behaviour of the tumour growth model. It was found that relatively small values of the model parameters RVV, p_0 and ND (e.g. 2.1%, 30 mmHg and 130 μm, respectively) were required to achieve the typical tumour oxygenation of HNSCC, which is very hypoxic. A notably large stem cell symmetric division probability of 50% (corresponding to stem cell proportions from 30 to 35%) was required to achieve doubling times from 2.3 to 6.1 days (from well oxygenated to severely hypoxic HNSCC), characteristic of an accelerated repopulation phase.

Geant4 [38–40] and Geant4-DNA [41–43, 86] were used to simulate low-energy physics interactions and the chemical tracks from water radiolysis. In Chapter 6 [93], an algorithm was developed to predict DNA damage from the track structure.

Direct events (ionisations and excitations) and indirect events ($^{\bullet}$OH interactions) in cell nucleus material were spatially clustered into cylindrical volumes representing 10 base-pair segments of DNA. Since tumour hypoxia was a major focus of the model, the mechanism of the oxygen enhancement effect was reviewed (see Introduction of [93]) to gain a sense of how to model it. The result was to model pO_2-dependent probabilities of DNA base radical-to-DNA sugar radical transfer and DNA sugar radical-to-strand break conversion. The resulting DNA damage yields and oxygen enhancement ratio (OER) for double-strand break (DSB) induction were verified for LETs up to 150 keV/μm. In particular, the OER for DSB induction was 3.0 for low-LET radiation up to approximately keV/μm and then decreased to 1.3 at 150 keV/μm. An important finding was that while the OER for DSB induction was close to unity at 150 keV/μm, there was oxygen enhancement of DSB complexity at this high LET, which was quantified.

The last Chapter 7 [95] reported on simulations of multicellular irradiation with track structure followed by DNA damage induction, DNA free-end misrejoining and cell death. The cellular tumour geometry was voxelised, imported into Geant4 and irradiated with 6 MV x-rays using Geant4-DNA physics and chemistry modules. The physical and chemical tracks through nuclei were translated into DNA damage, taking into account cellular pO_2, and then stochastic, proximity-based DNA free-end misrejoining was simulated, from which cell survival probabilities were obtained. The results indicated that the linear components of chromosome aberration production and cell survival are from unrejoined DSBs rather than from misrejoinings between DSBs produced by the same primary x-ray. For a 1 mm^3 tumour with oxygenation typical of HNSCC, DNA damage and misrejoining were simulated in all 135306 viable cells, following a uniform dose to the tumour of 1 Gy.

In this way, a new and unique computational radiotherapy model was developed and verified; one that is spatio-temporal, models each tumour cell individually, includes tumour angiogenesis and delivers dose to the tumour volume via Monte Carlo particle tracks, as required. Novel achievements are:

- the mechanism of cellular movement to accommodate new cells from proliferation and to remove cells after they die;

- stochastic growth of a connected and chaotic tumour vasculature, producing realistic spatial distributions of chronic hypoxia and necrosis;

- multicellular irradiation with Monte Carlo track structure, including low-energy physical interactions and chemical tracks from water radiolysis;

- stochastic conversion of track structure to spatially distributed DNA damage in each cell's nucleus in a way that takes into account the cell's pO_2; and,

- using the DSBs and their complexities, stochastic simulation of proximity-based DNA free-end misrejoining in each cell's nucleus to determine the likelihood of cell survival.

The added complexity of the model provides greater utility and potential for new radiobiological insights. However, it comes at the cost of greater computational load. A very large computation time would be required to grow a tumour to a clinically relevant diameter of $\sim$ 1 cm with pre-treatment cell kinetics (i.e. 2% symmetric stem cell division). Tumour irradiation in Geant4 would also be much more computationally efficient if Geant4-DNA physics was only simulated in nucleus voxels, rather than in all voxels, which is currently the case. This is not possible to achieve in the current version (10.4) of Geant4. The current model does not model DNA in complex geometries, such as nucleosome, chromatin and chromosome, as this was not appropriate/feasible for a multicellular tumour model. The DNA damage algorithm used a spatial clustering approach to work around this. While we can predict the event of a chromosome aberration, the absence of explicit chromosome structures meant that the specific type of chromosome aberration can not be known; one can only estimate the likelihood that it is lethal.

8.2 Future research

The ground work has now been laid and there is future work anticipated that will benefit from the framework that has been developed. The model can be extended in many directions. In the next work expected to follow, the dose fraction module (shorthand for irradiation, DNA damage induction, DNA free-end misrejoining and cell death components) will be combined with the cellular tumour growth model. After a dose fraction, the tumour will shrink (surviving cells will fall in along the radial pathways) and surviving stem cells will regrow the tumour, with or without the loss of asymmetric division, until the next dose fraction is delivered. Thus, fractionated radiotherapy treatments will be simulated. Different fractionation schedules may be simulated to investigate which are the most effective at combating tumour hypoxia and accelerated repopulation [97].

There are many options for further research applications using the S^2RT model. High fractional doses (i.e. hypofractionation and stereotactic body radiotherapy) could be simulated to probe the contribution of vascular damages to the tumour response. The current model is equipped to address this topic because of the connected tumour vasculature; damage to a single blood vessel unit can cause the inactivation of the entire length of the vessel and thus cause hundreds of surrounding cells to die by necrosis. Experimental data will be required to model the effects of vascular damage. Experiments that use a 3D vasculature would be particularly valuable, as the morphology may affect the radiosensitivity. For example, endothelial cells (e.g. human umbilical vein endothelial cells; HUVECs) could be grown and irradiated in 3D (e.g. using a tube formation assay [98] or 3D bioprinting [99]) followed by a clonogenic cell survival assay.

Since tumour irradiation is performed using track structure methods, the model can easily be extended to simulate hadrontherapy, including high-LET radiation. In particular, protons and carbon ions are well supported by Geant4-DNA. The DNA damage induction algorithm was demonstrated to have reasonably accurate behaviour up to 150 keV/μm [93]. As a first step, the simulations and analysis in [95] could be repeated with protons instead of MV x-rays.

Cancer types other than HNSCC could be simulated with minor modifications to the model. This may include changes to the size and shape of cells and nuclei, the cell hierarchy, the tumour oxygenation (RVV, p_0 and ND), the cell cycle times, the stem cell symmetric division probability, the cellular radiosensitivity (r_0), and so on. Similar adjustments could be made to model secondary cancers (which are typically more radioresistant than primary cancers) and normal tissue toxicity.

The code is currently written in Matlab for all components of the model other than the tumour irradiation in Geant4 (which is in C++). This includes: 4D cellular tumour growth with angiogenesis, tumour voxelisation, DNA damage induction and DNA free-end misrejoining (plus cell death). Matlab is excellent for developing models. It has robust in-built routines and toolboxes and enables convenient visualisation of data, making it easy to convert ideas into model methods and then verify the model behaviour. In the future, some time will be spent looking for opportunities to further vectorise the Matlab code in order to reduce computation time [100]. Some of the code may be translated into C++ to further improve computational performance.

There has recently been interest expressed from radiation oncology manufacturers to amalgamate and translate several radiobiological models, including this one, into a commercial product for clinical application. This product would be a tool that assists in identifying the optimal treatment (fractionation, radiation quality, chemotherapy drugs, etc.) for a given cancer patient and their tumour based on various predictive markers (e.g. hypoxia, p53-status, HPV-status, etc.). This is something radiobiological modelling has long been building towards. As computation time is a factor in the current model, a first approach could be to perform benchmarking and then interpolate for a given patient's tumour. There would also need to be a graphical user interface (GUI) developed for a commercial product.

The field of radiobiological modelling, and in particular radiotherapy modelling, is at an exciting stage and brimming with opportunities. There is much work left to do, but we are now beginning the process of translating models into clinical tools that will better individualise and optimise radiotherapy treatments. The

current lack of patient-specific radiobiological considerations in standard practice radiotherapy limits potential clinical benefit to patients. It is understandable if clinicians were hesitant in the past to go down this path, for example, due to limitations of deterministic models [66]. But with the more accurate and reliable stochastic approaches in newer models, and speed improvements to make them clinically viable, perhaps there can be a larger investment made into pursuing the integration of new and innovative radiobiology-based radiotherapy planning models in the clinical setting.

Appendices

A

Parallel and high performance computing with Matlab and Geant4

This work made extensive use of parallel computing. This appendix provides practical tips for using parallel computing in Matlab and Geant4 and running parallel Matlab code and Geant4 applications on a supercomputer.

A.1 Parallel computing

Some computational tasks consist of performing a similar subtask many times, with each subtask independent of the others. In parallel computing, such subtasks are executed simultaneously on multiple workers (e.g. cores in multicore processing).

A.1.1 Matlab

In Matlab, the parallel analogue of the `for`-loop is the `parfor`-loop. A `parfor`-loop can be used instead of a `for`-loop if the iterations are capable of running independently. A call to `parfor` will automatically create a "parallel pool", unless one is already active. The parallel pool contains the workers that will execute the `parfor`-loop iterations in parallel. Parallel pools can be manually created and deleted (Listing A.1).

Listing A.1: Parallel pools in Matlab (Matlab code)

```
nworkers = 4; % declare a variable for the number of workers in the
    parallel pool
poolobj = parpool(nworkers); % create a parallel pool with nworkers
delete(poolobj) % delete the parallel pool
parpool(nworkers, 'IdleTimeout', Inf) % create a parallel pool that
    never times out due to inactivity
poolobj = gcp(); % get current pool
```

A.1.2 Geant4

Primary particles (events) are independent, so they can be simulated in parallel on different workers (event-level parallelism). Geant4 offers this capability with "multithreaded mode" (Listing A.2). Note that to use multithreaded mode, when installing Geant4 the Geant4 library must be built with the CMAKE option:

```
-DGEANT4_BUILD_MULTITHREADED=ON
```

Listing A.2: To run a Geant4 application in multithreaded mode, create a multithreaded run manager in the main file (C++).

```
#ifdef G4MULTITHREADED // was the Geant4 library built with
    multithreaded option?
  G4MTRunManager * runManager = new G4MTRunManager; // create
    multithreaded run manager
  runManager->SetNumberOfThreads(4); // use e.g. 4 cores
  runManager->SetNumberOfThreads(G4Threading::G4GetNumberOfCores());
    // use all the cores you have
#else
  G4RunManager * runManager = new G4RunManager; // otherwise create
    serial run manager
#endif
```

It is recommended to score data in Geant4 simulations using G4AnalysisManager, which is thread-safe (i.e., compatible with multithreaded mode) [101]. The data is written in the form of "ntuples", which are like the rows of a table. For example, an ntuple may be generated for an event (or track or step) and the elements of the ntuple (i.e., the columns of the table) contain information about the event (or track or step). Listings A.3, A.4 and A.5 show how to create an ntuple, score data in it and properly close the output file, respectively. Several output formats are available including CSV (comma-separated values) and ROOT. Listing A.6 shows how to specify the output format. Note that in multithreaded mode, each thread

writes its ntuples on a separate output file (e.g. "output_nt_output_t0.csv" for thread 0, "output_nt_output_t1.csv" for thread 1, etc.). Examples of analysis manager can be found at <g4src>/examples/extended/analysis.

Listing A.3: Create an ntuple in the RunAction constructor (not in BeginOfRunAction) (C++)

```
#include "Analysis.hh"
...
// Create analysis manager
auto analysisManager = G4AnalysisManager::Instance();

// Create ntuple
analysisManager->CreateNtuple("output", "my title"); // file name,
    title of the file
analysisManager->CreateNtupleIColumn("flagParticle"); // I for integer
    , column name
analysisManager->CreateNtupleIColumn("flagProcess");
analysisManager->CreateNtupleDColumn("totalEnergyDeposit"); // D for
    double precision
analysisManager->FinishNtuple();
```

Listing A.4: Score data in an ntuple (C++). This is usually in a user action class, e.g. in the UserSteppingAction of SteppingAction.cc.

```
#include "Analysis.hh"
...
// Create analysis manager
auto analysisManager = G4AnalysisManager::Instance();

// Fill the ntuple
analysisManager->FillNtupleIColumn(0, flagParticle); // column index
    starts at 0
analysisManager->FillNtupleIColumn(1, flagProcess);
analysisManager->FillNtupleDColumn(2, Edep);
analysisManager->AddNtupleRow();
```

Listing A.5: Close the output file properly in the EndOfRunAction in RunAction.cc (C++)

```
#include "Analysis.hh"
...
// Create analysis manager
auto analysisManager = G4AnalysisManager::Instance();

analysisManager->Write(); // For ROOT histogram output, merges thread
    histograms into a single histogram
analysisManager->CloseFile();
```

Listing A.6: In the "include" folder of your application, you need an "Analysis.hh" file that specifies the output format (C++).

```
#ifndef Analysis_h
```

```
#define Analysis_h 1
#include "g4csv.hh"      // for CSV output
//#include "g4root.hh"     // for ROOT output
#endif
```

A.2 High performance computing

You get the most out of parallel code by using a high performance computer (HPC) (a.k.a a supercomputer). HPCs provide access to many more cores and much higher memory than a personal computer.

A.2.1 Job script

Code and software are ran on a HPC in the form of "jobs". A job is submitted to a HPC using a job script. The job script includes details of the resources to be assigned to the job, set-up of notifications and execution of the code (Listing A.7). The cores in a HPC are grouped into "nodes". If you only use one node, the number of cores is limited to the number of cores in one node. If you want to use more than one node, you should check that your software/code can do that. A job is then submitted with the command:

```
sbatch my_job_script.sh
```

Listing A.7: Example of a job script (bash).

```
#!/bin/bash

#SBATCH -p batch       # partition (others: test, highmem)
#SBATCH -N 1           # number of nodes
#SBATCH -n 1           # number of cores
#SBATCH --time=0-01:00     # time allocation (format D-HH:MM)
#SBATCH --mem=30GB       # memory pool for all cores

# Notification configuration
#SBATCH --mail-type=END   # Send email when the job ends
#SBATCH --mail-type=FAIL  # Send email when the job fails
#SBATCH --mail-user=jake.forster@adelaide.edu.au  # Email address

# Execute the script
module load matlab/2016b # Load the Matlab module
matlab -nodisplay -nodesktop -r "try run('my_script.m'); catch; end;
    quit" # Execute a Matlab script
```

A.2.2 Matlab

The last part of the above job script (Listing A.7) shows how to execute a sequential Matlab script. Listing A.8 shows how to execute a sequential Matlab function with variables. In each case, the Matlab module is loaded prior to calling the Matlab file. The Matlab file is called with the options `-nodisplay`, `-nodesktop` and `-r`, which are suitable for running a job in batch mode on a HPC. The `try/catch` wrapper ensures that a Matlab error is recognised as such by the HPC (a Matlab error is reported as a successful job otherwise). To run a `parfor`-loop in parallel on a HPC, modify the job script as shown in Listing A.9. Make no reference to the parallel pool in the Matlab file; simply call `parfor`.

Listing A.8: Executing a Matlab function in the job script (bash).

```
# Execute the script
VAR1=3          # variables for the Matlab function
VAR2=5
module load matlab/2016b
matlab -nodisplay -nodesktop -r "try my_matlab_function($VAR1,$VAR2);
    catch; end; quit"
```

Listing A.9: Executing a parallel Matlab script in the job script (bash).

```
...
NCORES = 5          # variable for the number of cores
#SBATCH -n $NCORES     # number of cores
...
# Execute the script
module load matlab/2016b
matlab -nodisplay -nodesktop -r "max_pool=$NCORES; parpool(max_pool, '
    IdleTimeout', Inf); p=gcp(); try run('my_parallel_script.m');
    catch; end; quit"
```

A.2.3 Geant4

To use Geant4 on a HPC, you may have to request it to be installed (Geant4 is not as popular as Matlab), in which case notify the HPC user support staff of which version of Geant4 to install and ensure that they install it with the flags:

```
-DGEANT4_INSTALL_DATA=ON -DGEANT4_BUILD_MULTITHREADED=ON
```

The module will have a name like “Geant4/10.04-foss-2016b”. Here the version is 10.04. The “foss-2016b” part refers to the toolchain used to build the software. If you have a problem with Geant4 on the HPC, one thing to try is a different toolchain.

Normally to compile a Geant4 application (in a build directory located inside the source directory) on a personal computer or laptop with Geant4 installed, the commands are:

```
CMAKE -DGeant4_DIR=$G4COMP ..
make
```

On a HPC, compilation is slightly different, e.g.:

```
module load Geant4/10.04-foss-2016b
module load CMake/3.4.3
cmake -DCMAKE_C_COMPILER=gcc \
-DGeant4_DIR=$EBROOTGEANT4/lib64/Geant4-10.4 \
-DCMAKE_CXX_COMPILER=g++ ..
make
```

Listing A.10 shows how to modify the job script for a Geant4 application. The application will then run in multithreaded mode with `NCORES` (1 core works too). The `G4FORCENUMBEROFTHREADS` line prevents the job from using more cores than are allocated.

Listing A.10: Job script modifications for Geant4 (bash)

```
...
NCORES=5          # variable for the number of cores
#SBATCH -n $NCORES     # number of cores
...
# Execute the script
module load Geant4/10.04-foss-2016b
module load CMake/3.4.3
source $EBROOTGEANT4/bin/geant4.sh
export G4FORCENUMBEROFTHREADS=$NCORES
./my_g4exec my_macro.mac
```

A.2.4 Job array

Code can sometimes be modified to run more efficiently on a HPC. This is because a HPC is ran analogous to a game of Tetris: jobs that request less cores, memory and time start quicker because the resources are more readily available and these jobs are given higher priority by the Slurm Workload Manager.

One way to take advantage of this is to use a job array instead of a `parfor`-loop in Matlab, so that each iteration of the `parfor`-loop is submitted as a separate job. Because a job for a single iteration of the `parfor`-loop requires less resources (cores/memory/time) than a job for the entire loop, the job array method is more optimised for running on a HPC.

Listing A.11 shows how to modify the job script for a job array. The elements of the job array are called "tasks", equivalent to the iterations of the `parfor`-loop in this example. The variable `SLURM_ARRAY_TASK_ID` serves as the original `parfor`-loop index. Note that the time and memory specified in the job script are for individual tasks in the job array.

Listing A.11: Job script modifications for a job array (bash).

```
...
#SBATCH --array=3-8     # run tasks 3 to 8 of the job array
...
# Execute the script
module load matlab/2016b
matlab -nodisplay -nodesktop -r "try my_matlab_function(
   $SLURM_ARRAY_TASK_ID); catch; end; quit"
```

A.2.5 Slurm dependencies

You may want to submit multiple jobs to a HPC that depend upon each other. For example, you may want one job to only start running after another job has completed successfully. Slurm dependencies can be used to achieve this. A job can be submitted with syntax:

```
sbatch --dependency=<TYPE> my_job_script.sh
```

where <TYPE> can be:

- `after:<JOBID>[:<JOBID>...]` - the job can start after these jobs have started.
- `afterany:<JOBID>[:<JOBID>...]` - the job can start after these jobs have ended.

- `afternotok:<JOBID>[:<JOBID>...]` - the job can start after these jobs have failed.
- `afterok:<JOBID>[:<JOBID>...]` - the job can start after these jobs have completed successfully.
- `singleton` - the job can start if there are no jobs currently running with the same name by the same user.

Slurm dependencies can be used to build "pipelines" in a bash script (Listing A.12).

Listing A.12: A bash script to build a simple pipeline with a slurm dependency (bash). Note that the variable "jid1" is a string of the form "Slurm-1234567". The "-7" is to get only the job ID part.

```
#!/bin/bash
jid1=$(sbatch job_script1.sh)
jid2=$(sbatch --dependency=afterok:${jid1: -7} job_script2.sh) # job
    script 2 can only start running after job script 1 has completed
    successfully
```

Bibliography

NB: Does not include references in publications.

1. Wolfram, S. *A New Kind of Science* 1st ed. Freely accessible at `http://www.wolframscience.com/nks/` (Wolfram Media, Champaign, 2002).
2. *Complexity Labs. Computational Irreducibility* `http://complexitylabs.io/glossary/computational-irreducibility/`. Accessed: 24-09-2018.
3. Delaney, G., Jacob, S. & Barton, M. Estimation of an optimal external beam radiotherapy utilization rate for head and neck carcinoma. *Cancer* **103,** 2216–2227 (2005).
4. *Royal Australian and New Zealand College of Radiologists (RANZCR) Faculty of Radiation Oncology (FRO). FRO Response to MBS Consultation Paper 2015* `https://www.ranzcr.com/college/document-library/fro-response-to-mbs-consultation-paper`. Accessed: 29-11-2018.
5. Sanderson, R. J. & Ironside, J. A. Squamous cell carcinomas of the head and neck. *BMJ* **325,** 822–827 (2002).
6. Australian Institute of Health and Welfare. *Cancer in Australia 2017* Cancer series no. 101. Cat. no. CAN 100. (AIHW, Canberra, 2017).
7. Australian Institute of Health and Welfare. *Head and neck cancers in Australia* Cancer series no. 83. Cat. no. CAN 80. (AIHW, Canberra, 2014).
8. Döbrossy, L. Epidemiology of head and neck cancer: magnitude of the problem. *Cancer Metastasis Rev.* **24,** 9–17 (2005).
9. Aldalwg, M. A. & Brestovac, B. Human Papillomavirus Associated Cancers of the Head and Neck: An Australian Perspective. *Head Neck Pathol.* **11,** 377–384 (2017).
10. Grégoire, V., Lefebvre, J. L., Licitra, L. & Felip, E. Squamous cell carcinoma of the head and neck: EHNS-ESMO-ESTRO Clinical Practice Guidelines for diagnosis, treatment and follow-up. *Ann. Oncol.* **21.** On behalf of the EHNS-ESMO-ESTRO Guidelines Working Group, v184–v186 (2010).
11. Chin, D. *et al.* Head and neck cancer: past, present and future. *Expert Rev. Anticancer Ther.* **6,** 1111–1118 (2006).
12. Marta, G. N. & Saad, E. D. Assessment of quality of life in phase III trials of radiotherapy in localized or locally advanced head and neck cancer over the past 17 years. *Ann. Palliat. Med.* **6,** 73–80 (2017).
13. Kim, J. K. *et al.* Proton Therapy for Head and Neck Cancer. *Curr. Treat. Options Oncol.* **19,** 28 (2018).

14. *South Australian Health and Medical Research Institute (SAHMRI). Australian Bragg Centre for Proton Therapy* `https://www.australianbraggcentre.com`. Accessed: 15-08-2018.

15. Bishop, S. & Reed, W. M. The provision of enteral nutritional support during definitive chemoradiotherapy in head and neck cancer patients. *J. Med. Radiat. Sci.* **62,** 267–276 (2015).

16. Xia, P. & Murray, E. 3D treatment planning system-Pinnacle system. *Med. Dosim.* **43,** 118–128 (2018).

17. Clements, M., Schupp, N., Tattersall, M., Brown, A. & Larson, R. Monaco treatment planning system tools and optimization processes. *Med. Dosim.* **43,** 106–117 (2018).

18. Purdy, J. A. Dose to normal tissues outside the radiation therapy patient's treated volume: a review of different radiation therapy techniques. *Health. Phys.* **95,** 666–676 (2008).

19. Cho, B. Intensity-modulated radiation therapy: a review with a physics perspective. *Radiat. Oncol. J.* **36,** 1–10 (2018).

20. van der Veen, J. & Nuyts, S. Can Intensity-Modulated-Radiotherapy Reduce Toxicity in Head and Neck Squamous Cell Carcinoma? *Cancers (Basel)* **9,** pii: E135 (2017).

21. Begg, A. C. in *Basic clinical radiobiology* (eds Joiner, M. C. & van der Kogel, A.) 4th ed., 316–331 (CRC Press, Boca Raton, 2009).

22. Oldenhuis, C. N., Oosting, S. F., Gietema, J. A. & de Vries, E. G. Prognostic versus predictive value of biomarkers in oncology. *Eur. J. Cancer* **44,** 946–953 (2008).

23. Kang, H., Kiess, A. & Chung, C. H. Emerging biomarkers in head and neck cancer in the era of genomics. *Nat. Rev. Clin. Oncol.* **12,** 11–26 (2015).

24. Rieke, D. T., Klinghammer, K. & Keilholz, U. Targeted Therapy of Head and Neck Cancer. *Oncol. Res. Treat.* **39,** 780–786 (2016).

25. Akervall, J. *et al.* A novel panel of biomarkers predicts radioresistance in patients with squamous cell carcinoma of the head and neck. *Eur. J. Cancer* **50,** 570–581 (2014).

26. Licitra, L., Bergamini, C., Mirabile, A. & Granata, R. Targeted therapy in head and neck cancer. *Curr. Opin. Otolaryngol. Head Neck Surg.* **19,** 132–137 (2011).

27. Pardo-Reoyo, S., Roig-Lopez, J. L. & Yang, E. S. Potential biomarkers for radiosensitivity in head and neck cancers. *Ann. Transl. Med.* **4,** 524 (2016).

28. Tinhofer, I. *et al.* Next-generation sequencing: hype and hope for development of personalized radiation therapy? *Radiat. Oncol.* **10,** 183 (2015).

29. Lampri, E. S. *et al.* Biomarkers of head and neck cancer, tools or a gordian knot? *Int. J. Clin. Exp. Med.* **8,** 10340–10357 (2015).

30. Bossi, P. *et al.* Prognostic and predictive value of EGFR in head and neck squamous cell carcinoma. *Oncotarget* **7,** 74362–74379 (2016).

31. Yokota, T. Is biomarker research advancing in the era of personalized medicine for head and neck cancer? *Int. J. Clin. Oncol.* **19,** 211–219 (2014).

32. Bozec, A., Peyrade, F. & Milano, G. Molecular targeted therapies in the management of head and neck squamous cell carcinoma: recent developments and perspectives. *Anticancer Agents Med. Chem.* **13,** 389–402 (2013).

33. Clavo, B. *et al.* Predictive value of hypoxia in advanced head and neck cancer after treatment with hyperfractionated radio-chemotherapy and hypoxia modification. *Clin. Transl. Oncol.* **19,** 419–424 (2017).

34. Samuels, S. E. *et al.* Management of locally advanced HPV-related oropharyngeal squamous cell carcinoma: where are we? *Eur. Arch. Otorhinolaryngol.* **273,** 2877–2894 (2016).

35. Nordsmark, M., Overgaard, M. & Overgaard, J. Pretreatment oxygenation predicts radiation response in advanced squamous cell carcinoma of the head and neck. *Radiother. Oncol.* **41,** 31–39 (1996).

36. Dikomey, E., Borgmann, K., Peacock, J. & Jung, H. Why recent studies relating normal tissue response to individual radiosensitivity might have failed and how new studies should be performed. *Int. J. Radiat. Oncol. Biol. Phys.* **56,** 1194–1200 (2003).

37. Kim, K. Y., McShane, L. M. & Conley, B. A. Designing biomarker studies for head and neck cancer. *Head Neck* **36,** 1069–1075 (2014).

38. Allison, J. *et al.* Recent developments in Geant4. *Nucl. Instrum. Methods Phys. Res. A.* **835,** 186–225 (2016).

39. Allison, J. *et al.* Geant4 developments and applications. *IEEE Trans. Nucl. Sci.* **53,** 270–278 (2006).

40. Agostinelli, S. *et al.* GEANT4 - A simulation toolkit. *Nucl. Instrum. Methods Phys. Res. A* **506,** 250–303 (2003).

41. Bernal, M. A. *et al.* Track structure modeling in liquid water: A review of the Geant4-DNA very low energy extension of the Geant4 Monte Carlo simulation toolkit. *Phys. Med.* **31,** 861–874 (2015).

42. Incerti, S. *et al.* Comparison of GEANT4 very low energy cross section models with experimental data in water. *Med. Phys.* **37,** 4692–4708 (2010).

43. Incerti, S. *et al.* The Geant4-DNA project. *Int. J. Model. Simul. Sci. Comput.* **1,** 157–178 (2010).

44. Douglass, M. J. J. *Development of an Integrated Stochastic Radiobiological Model for Electromagnetic Particle Interactions in a 4D Cellular Geometry* PhD Dissertation (University of Adelaide, School of Chemistry and Physics, May 2014).

45. Harriss, W. M. *Monte Carlo modelling of tumour growth, hypoxia and radiotherapy in head and neck squamous cell carcinoma* PhD Dissertation (University of Adelaide, School of Chemistry and Physics, 2011).

46. Friedland, W. *et al.* Comprehensive track-structure based evaluation of DNA damage by light ions from radiotherapy-relevant energies down to stopping. *Sci. Rep.* **7,** 45161 (2017).

47. Friedland, W. & Kundrát, P. Track structure based modelling of chromosome aberrations after photon and alpha-particle irradiation. *Mutat. Res.* **756,** 213–223 (2013).

48. de la Fuente Rosales, L., Incerti, S., Francis, Z. & Bernal, M. A. Accounting for radiation-induced indirect damage on DNA with the Geant 4-DNA code. *Phys. Med.* Epub ahead of print (2018).

49. Liang, Y., Yang, G., Liu, F. & Wang, Y. Monte Carlo simulation of ionizing radiation induced DNA strand breaks utilizing coarse grained high-order chromatin structures. *Phys. Med. Biol.* **61,** 445–460 (2016).

50. Tajik, M., Rozatian, A. S. H. & Semsarha, F. Calculation of direct effects of 60 Co gamma rays on the different DNA structural levels: a simulation study using the Geant4-DNA toolkit. *Nucl. Instrum. Methods Phys. Res. B* **346,** 53–60 (2015).

51. Watanabe, R., Rahmanian, S. & Nikjoo, H. Spectrum of Radiation-Induced Clustered Non-DSB Damage - A Monte Carlo Track Structure Modeling and Calculations. *Radiat. Res.* **183,** 525–540 (2015).

52. Štepán, V. & Davídková, M. Impact of oxygen concentration on yields of DNA damages caused by ionizing radiation. *J. Phys.: Conf. Ser.* **101,** 012015 (2008).

53. Moiseenko, V. V., Hamm, R. N., Waker, A. J. & Prestwich, W. V. Calculation of radiation-induced DNA damage from photons and tritium beta-particles. Part I: Model formulation and basic results. *Radiat. Environ. Biophys.* **40,** 23–31 (2001).

54. Friedland, W., Schmitt, E., Kundrát, P., Baiocco, G. & Ottolenghi, A. Track-structure simulations of energy deposition patterns to mitochondria and damage to their DNA. *Int. J. Radiat. Biol.* Epub ahead of print (2018).

55. Nordsmark, M. *et al.* Prognostic value of tumor oxygenation in 397 head and neck tumors after primary radiation therapy. An international multi-center study. *Radiother. Oncol.* **77,** 18–24 (2005).

56. Forster, J. C., Harriss-Phillips, W. M., Douglass, M. J. & Bezak, E. A review of the development of tumor vasculature and its effects on the tumor microenvironment. *Hypoxia (Auckl)* **5,** 21–32 (2017).

57. Steel, G. G., McMillan, T. J. & Peacock, J. H. The 5Rs of radiobiology. *Int. J. Radiat. Biol.* **56,** 1045–1048 (1989).

58. Withers, H. R. The 4 R's of radiotherapy. *Adv. Radiat. Biol.* **5,** 241–247 (1975).

59. Joiner, M. C. & van der Kogel, A. *Basic clinical radiobiology* 4th ed., 201–213 (CRC Press, Boca Raton, 2009).

60. Hall, E. J. & Giaccia, A. J. *Radiobiology for the radiologist* 7th ed. (Lippincott Williams & Wilkins, Philadelphia, 2012).

61. Marcu, L. G., Toma-Dasu, I. & Dasu, A. in *Contemporary Issues in Head and Neck Cancer Management.* (ed Marcu, L. G.) 35–58 (InTech, Rijeka, 2015).

62. Hall, E. J. & Brenner, D. J. The dose-rate effect revisited: radiobiological considerations of importance in radiotherapy. *Int. J. Radiat. Oncol. Biol. Phys.* **21,** 1403–1414 (1991).

63. Chadwick, K. H. & Leenhouts, H. P. A molecular theory of cell survival. *Phys. Med. Biol.* **18,** 78–87 (1973).

64. Brenner, D. J. Point: The linear-quadratic model is an appropriate methodology for determining iso-effective doses at large doses per fraction. *Semin. Radiat. Oncol.* **18,** 234–239. (2008).

65. Astrahan, M. Some implications of linear-quadratic-linear radiation dose-response with regard to hypofractionation. *Med. Phys.* **35,** 4161–4172 (2008).

66. Park, C., Papiez, L., Zhang, S., Story, M. & Timmerman, R. D. Universal survival curve and single fraction equivalent dose: useful tools in understanding potency of ablative radiotherapy. *Int. J. Radiat. Oncol. Biol. Phys.* **70,** 847–852 (2008).

67. Park, H. J., Griffin, R. J., Hui, S., Levitt, S. H. & Song, C. W. Radiation-induced vascular damage in tumors: implications of vascular damage in ablative hypofractionated radiotherapy (SBRT and SRS). *Radiat. Res.* **177,** 311–327 (2012).

68. Shuryak, I., Loucas, B. D. & Cornforth, M. N. Straightening Beta: Overdispersion of Lethal Chromosome Aberrations following Radiotherapeutic Doses Leads to Terminal Linearity in the Alpha-Beta Model. *Front. Oncol.* **7,** 318 (2017).

69. Brenner, D. J., Hlatky, L. R., Hahnfeldt, P. J., Hall, E. J. & Sachs, R. K. A convenient extension of the linear-quadratic model to include redistribution and reoxygenation. *Int. J. Radiat. Oncol. Biol. Phys.* **32,** 379–390 (1995).

70. Friedland, W., Dingfelder, M., Kundrát, P. & Jacob, P. Track structures, DNA targets and radiation effects in the biophysical Monte Carlo simulation code PARTRAC. *Mutat. Res.* **711,** 28–40 (2011).

71. Kreipl, M. S., Friedland, W. & Paretzke, H. G. Time- and space-resolved Monte Carlo study of water radiolysis for photon, electron and ion irradiation. *Radiat Environ Biophys.* **48,** 11–20 (2009).

72. Plante, I. & Devroye, L. Considerations for the independent reaction times and step-by-step methods for radiation chemistry simulations. *Radiat. Phys. Chem.* **139,** 157–172 (2017).

73. Plante, I. & Cucinotta, F. A. Simulation of the radiolysis of water using Green's functions of the diffusion equation. *Radiat. Prot. Dosimetry* **166,** 24–28 (2015).

74. Nikjoo, H. *et al.* Radiation track, DNA damage and response-a review. *Rep. Prog. Phys.* **79,** 116601 (2016).

75. Wilson, W. E., Miller, J. H., Lynch, D. J., Lewis, R. R. & Batdorf, M. Analysis of low-energy electron track structure in liquid water. *Radiat. Res.* **161,** 591–596 (2004).

76. Semenenko, V. A., Turner, J. E. & Borak, T. B. NOREC, a Monte Carlo code for simulating electron tracks in liquid water. *Radiat. Environ. Biophys.* **42,** 213–217 (2003).

77. Emfietzoglou, K., Karava, K., Papamichael, G. & Moscovitch, M. Monte Carlo simulation of the energy loss of low-energy electrons in liquid water. *Phys. Med. Biol.* **48,** 2355–2371 (2003).

78. Bigildeev, E. A. & Michalik, V. Charged particle tracks in water of different phases. Monte Carlo simulation of electron tracks. *Radiat. Phys. Chem.* **47,** 197–207 (1996).

79. Terrissol, M. & Baudre, A. A simulation of space and time evolution of radiolytic species induced by electrons in water. *Radiat. Prot. Dosim.* **31,** 175–177 (1990).

80. Paretzke, H. G. in *Kinetics of Nonhomogeneous Processes: A Practical Introduction for Chemists, Biologists, Physicists and Materials Scientists.* (ed Freeman, G. R.) 1st ed., 89–170 (Wiley, New York, 1987).

81. Zaider, M., Brenner, D. J. & Wilson, W. E. The Applications of Track Calculations to Radiobiology I. Monte Carlo Simulation of Proton Tracks. *Radiat. Res.* **95,** 231–247 (1983).

82. *Geant4 collaboration. Geant4: a simulation toolkit* `https://geant4.web.cern.ch/`. Accessed: 15-08-2018.

83. *The ATLAS Collaboration.* `http://geant4.web.cern.ch/gallery`. Accessed: 15-08-2018.

84. *Khronos Group. OpenGL - The Industry Standard for High Performance Graphics* `https://www.opengl.org/`. Accessed: 25-09-2018.

85. *Tanaka, S. et al. Fukui Renderer DAWN (Drawer for Academic WritiNgs)* `http://geant4.kek.jp/~tanaka/DAWN/About_DAWN.html`. Accessed: 25-09-2018.

86. *The Geant4-DNA Collaboration. Geant4-DNA: Extending the Geant4 Monte Carlo simulation toolkit for radiobiology* `http://geant4-dna.org/`. Accessed: 15-08-2018.

87. Michael, B. D. & O'Neill, P. Molecular biology. A sting in the tail of electron tracks. *Science* **287,** 1603–1604 (2000).

88. Karamitros, M. *et al.* Modeling radiation chemistry in the Geant4 toolkit. *Prog. Nucl. Sci. Technol.* **2,** 503–508 (2011).

89. Colliaux, A., Gervais, B., Rodriguez-Lafrasse, C. & Beuve, M. Simulation of ion-induced water radiolysis in different conditions of oxygenation. *Nucl. Instr. Meth. Phys. Res. B* **365,** 596–605 (2015).

90. Karamitros, M. *et al.* Diffusion-controlled reactions modeling in Geant4-DNA. *J. Comput. Phys.* **274,** 841–882 (2014).

91. Forster, J. C., Douglass, M. J., Harriss-Phillips, W. M. & Bezak, E. Development of an in silico stochastic 4D model of tumor growth with angiogenesis. *Med. Phys.* **44,** 1563–1576 (2017).

92. Forster, J. C., Douglass, M. J. J., Harriss-Phillips, W. M. & Bezak, E. Simulation of head and neck cancer oxygenation and doubling time in a 4D cellular model with angiogenesis. *Sci. Rep.* **7,** 11037 (2017).

93. Forster, J. C., Douglass, M. J. J., Phillips, W. M. & Bezak, E. Monte Carlo Simulation of the Oxygen Effect in DNA Damage Induction by Ionizing Radiation. *Radiat. Res.* **190,** 248–261 (2018).

94. Stewart, R. D. *et al.* Effects of radiation quality and oxygen on clustered DNA lesions and cell death. *Radiat. Res.* **176,** 587–602 (2011).

95. Forster, J. C., Douglass, M. J. J., Phillips, W. M. & Bezak, E. Stochastic multicellular modeling of x-ray irradiation, DNA damage induction, DNA free-end misrejoining and cell death. Manuscript in preparation (2018).

96. Pryor, D. I., Solomon, B. & Porceddu, S. V. The emerging era of personalized therapy in squamous cell carcinoma of the head and neck. *Asia Pac. J. Clin. Oncol.* **7,** 236–251 (2011).

97. Corry, J. & Rischin, D. Strategies to overcome accelerated repopulation and hypoxia–what have we learned from clinical trials? *Semin. Oncol.* **31,** 802–808 (2004).

98. Irvin, M. W., Zijlstra, A., Wikswo, J. P. & Pozzi, A. Techniques and assays for the study of angiogenesis. *Exp. Biol. Med. (Maywood)* **239,** 1476–1488 (2014).

99. Sekiya, S. & Shimizu, T. Introduction of vasculature in engineered three-dimensional tissue. *Inflamm. Regen.* **37,** 25 (2017).

100. *The MathWorks, Inc. Vectorization* `https://au.mathworks.com/help/matlab/matlab_prog/vectorization.html`. Accessed: 4-09-2018.

101. Hřivnáčová, I. & Barrand, G. Analysis Tools in Geant4 10.2 and 10.3. *J. Phys.: Conf. Ser.* **898,** 042018 (2017).